The Development of a Membraneless Direct Borohydride Alkaline Fuel Cell

Ph.D.

Author *Scott Nash, MChem*

Supervisors *Dr Richard Dawson*

Dr Fabrice Andrieux

Lancaster University Engineering Department

(Date of submission: January 2017)

Acknowledgements

Firstly, I would like to thank my Supervisors, Dr Richard Dawson and Dr Fabrice Andrieux, for their seemingly endless knowledge of fuel cells, electrochemistry and chemical engineering which has guided me throughout the Ph.D. Their patience and understanding, especially when I often pestered them to ask a “quick question”, along with their friendly manner made them the perfect Supervisors. I’d also like to say thank you to Dr Anant Patel and Peter Jones for their support. Many a difficult problem I had was solved by talking and bouncing ideas off you both. I would like to thank Hui Choy for developing the initial fuel cell testing rig that I used in several experiments. Finally, I would like to thank Prof. Rob Poole at Liverpool University for the use of his rheometer.

My Ph.D. could not have happened without the support of the EPSRC and AFC Energy. I’d like to thank you both for your support and specifically AFC Energy for the use of their methods and materials.

I’d also like to thank the Chemistry lecturers at Kingston University, who are second to none with boundless energy, passion and knowledge of their subject. I would like to say a special thank you to Dr Neil Williams. Not only do you share these qualities, but as my Project Supervisor you constantly pushed me to do better, which I’ve continued to do. I owe you a great debt and a lot of my success I attribute to you.

I would like to thank Lauren Godfrey. You have supported and encouraged everything I’ve done and continuingly make me a better person every day.

Finally, I would like to thank my family, to whom I dedicate this thesis to for your endless support, especially my parents. Your continuing support throughout the years has made everything that much easier. I would like to say my most heartfelt thank you to my family for everything.

Abstract

Fuel cells offer the potential for the generation of clean, renewable energy source for a wide variety of applications. Low temperature fuel cells (< 150 °C) are most suitable for portable applications, out of these the alkaline fuel cell (AFC) shows increased electrode kinetics over other fuel cell types. The direct borohydride alkaline fuel cell (DBAFC), a derivative of the AFC, can provide increased power output and improved safety features afforded using borohydride in place of hydrogen gas. However, relatively little research has been conducted on DBAFC, particularly membraneless DBAFC. This work aims to address this and describes an investigation into every aspect of DBAFC to evaluate their deployment on an industrial scale.

As such, candidate electrocatalysts were assessed for their electrocatalytic activity towards the oxidation of borohydride in alkaline media for use in DBAFCs using cyclic voltammetry. The candidate electrocatalysts, including Pt, Pd and Ru on activated C and cathode electrocatalysts were then developed into a screen printable electrode ink, a method which could be easily upscaled for mass manufacture. A screen-printed anode developed outperformed commercially available AFC anodes with the developed cathode performing sufficiently when evaluated using electrochemical polarisation. Computer simulations were used to design individual components of a DBAFC, which were built and tested experimentally through operational use and electrochemical impendence analysis. The developed DBAFC performed well, with theoretically low ionic leakage when in a stack, good distribution of electrolyte and air and a low cell weight. Finally, a system was designed to evaluate different electrolyte flow methods and operating conditions and produced a flexible testing system for DBAFC suitable for scale up.

The results generated indicate that DBAFCs are a viable alternative to other low temperature fuel cells. Using an effective anode electrocatalyst and system design, DBAFC could be used for a variety of applications.

Declaration

The author declares that this thesis has not been previously submitted for the award of a higher degree to this or any university and that the contents, except where otherwise stated, are the author's own work.

Signed: 

Date: 17 Jan 2017

Contents

Figures

Notations

Abbreviations and Terminology

Abbreviation	Meaning	Definition
A_{act}	Active surface area	The surface area which is electrochemically active and used during reactions.
AEM	Anion-exchange membrane	An SPE used to conduct hydroxyl ions in AFCs.

AFC	Alkaline fuel cell	A hydrogen fuel cell which uses alkaline media as the electrolyte.
A_{geo}	Geometric surface area	The surface area associated with the electrode geometry.
AL	Active layer	The layer of an electrode containing the electrocatalyst.
A_{rea}	Real surface area	The surface area of the electrocatalytic material.
ASR	Area specific resistance	A method used to compare fuel cells. It is calculated based on the ohmic loss as a function of the fuel cell's A_{geo}.
A_{tot}	Total surface area	The surface area of the support material and the active material.
BLL	Borohydride lower limit	The lowest borohydride concentration that can be detected.
BOR	Borohydride oxidation reaction	The oxidation, both direct and indirect, reaction of borohydride to metaborate at the anode in a fuel cell.
BUL	Borohydride upper limit	The highest borohydride concertation that can be detected.
CAL	Cathode active layer	The cathode layer containing the electrocatalyst.
CALI	Cathode active layer ink	The electrocatalyst suspension used to screen print the cathode.
CP	Constant power	The generation of a continuous power, such as residential applications.
CV	Cyclic voltammetry	An electroanalytical technique used to determine the effect of applied potential on current of a material.
DBAFC	Direct borohydride alkaline fuel cell	A fuel cell which oxidises borohydride directly compared to using it as a hydrogen store. Limited to oxygen/air oxidant.

DBFC	Direct borohydride fuel cells	A fuel cell which oxidises borohydride directly compared to using it as a hydrogen store. This includes DBAFC and DBPFC.
DBPFC	Direct borohydride-peroxide fuel cell	A DBFC which uses hydrogen peroxide as the oxidant in place of air or oxygen.
DMFC	Direct methanol fuel cell	A fuel cell which oxidises methanol directly to generate power.
EIS	Electrochemical impedance spectroscopy	An electroanalytical technique used to determine the effect of applied sinusoidal phase shift on the resistance of a material or system.
FM	Flow meter	Equipment used to measure the flow of a fluid through a pipe.
GDE	Gas diffusion electrode	An electrode which is used in conjunction with a gaseous fluid.
GDL	Gas diffusion layer	A layer which has been designed to specifically allow the passage of gas but prevent liquid permeating through in a GDE.
GEIS	Galvano-electrochemical impedance spectroscopy	An EIS technique which determines the effect of changing the current on the resistance of a material or system.
HOR	Hydrogen oxidation reaction	The oxidation reaction of hydrogen, when used as the reductant, at the anode in a fuel cell.
IDBFC	Indirect borohydride fuel cell	A fuel cell which uses borohydride as a hydrogen store. Hydrogen is released and used in conjunction with another fuel cell.
IPA	Isopropyl alcohol (propan-2-ol, IPA)	An organic solvent.
LDL	Liquid diffusion layer	A layer which has been designed to specifically allow the passage of liquid.
MCFC	Molten carbonate fuel cell	A high temperature fuel cell which uses a liquid carbonate electrolyte.

MFC	Mass flow controller	Equipment used to control the volumetric flow rate of gas through a pipe.
MWCNT	Multi-walled carbon nanotubes	Multiple layers of cylindrical sheet of planar carbon atoms formed around each other.
NRV	Non-return/check valve	A valve which allows the flow of a fluid in a single direction.
OCP	Open circuit potential	The potential of a system at equilibrium when no current is drawn.
OCP_{real}	Real *OCP*	The measured *OCP* of a cell (also known as E_{cell} at I = 0 A).
OCP_{theo}	Theoretical *OCP*	The *OCP* calculated based on the redox thermodynamics.
ORR	Oxygen reduction reaction	The reduction of oxygen, when used as an oxidant, at the cathode in a fuel cell.
PAFC	Phosphoric acid fuel cell	A low temperature fuel cell which uses phosphoric acid as the electrolyte.
PEIS	Potentio- electrochemical impedance spectroscopy	An EIS technique which determines the effect of changing the applied potential on the resistance of a material or system.
PEM	Proton-exchange membrane	An SPE used to conduct protons in PEMFCs.
PEMFC	Proton exchange membrane fuel cell	A low temperature fuel cell which uses a solid proton conducting electrolyte.
PoD	Power on demand	The generation of power quickly when required.
PTFE	Polytetrafluoroethylene (Teflon®, PTFE)	A chemical which is used as a binder, increasing hydrophobicity and sealant. It is known for its high chemical corrosion resistance, low electrical conductivity and flexibility.
SCE	Saturated calomel electrode	A reference electrode, $Hg\|Hg_2Cl_2$, used in electroanalytical techniques.
SEM	Scanning electron microscopy	A microscopic technique used to image materials on a nano meter scale.

SM	Static mixer	A component which is placed in the flow of a liquid to aid mixing.
SOFC	Solid oxide fuel cell	A high temperature fuel cell which uses a solid ceramic oxide as the electrolyte.
SP	Syringe pump	A pump which has a relatively low volumetric flow rate and a volume limited to that of the syringe.
SPE	Solid polymer electrolyte	An electrolyte held in a polymer matrix.

Equations, Constants and Notations

Equation	Definition
$\dot{\eta} = \frac{iA}{nF}$	Faraday equation
$OCP_{theo} = -\frac{\Delta \overline{g}_f}{nF}$	Open circuit potential
$j_i = 1.544nFD^{\frac{2}{3}}v^{-\frac{1}{6}}f^{-\frac{1}{2}}C$	Levich equation
$P = I.V_{cell}$	Power as a function of current and potential.
$\frac{1}{j} = \frac{1}{j_K} + \frac{1}{j_L} = \frac{1}{B}f^{-\frac{1}{2}} + \frac{1}{j_K}$	Koutechy−Levich equation
$R_\Omega = \frac{E}{I}$	Resistance as a function of potential and current.
$\tau = \dot{\gamma}.\eta$	Shear stress as a function of shear rate and viscosity.

Symbol	Definition	Value
F	Faraday's Constant	96485 $C.mol^{-1}$ or $A.s^{-1}.mol^{-1}$
R	Universal gas constant	8.314 $J.K^{-1}.mol^{-1}$

Symbol	Definition	Units Used
E_a	Anode potential	V
E_c	Cathode potential	V
V_{cell}	Cell voltage	V
α	Charge coefficient	None
C	Concentration	M ($mol.dm^{-3}$)

I	Current	A
j	Current density	$A.cm^{-2}$
j_K	Kinetic-limited current density	$A.cm^{-2}$
j_L	Mass-transfer limited current density	$A.cm^{-2}$
ρ	Density	$g.cm^{-3}$
D	Diffusion coefficient	$m^2.s^{-1}$
j_0	Exchange current density	$A.cm^2$
$\Delta\overline{g}_f$	Gibbs energy of formation	$kJ.mol^{-1}$
$\dot{\eta}$	Molar flow rate	$mol.min^{-1}$
n	Number of electrons transferred	None
E	Potential	V
E_{cell}^{θ}	Potential of the cell at standard conditions	V
E_{cell}	Potential of the cell at non-standard conditions	V
R_{Ω}	Resistance	Ω
f	Rotation rate	Hz
$\dot{\gamma}$	Shear rate	s^{-1}
τ	Shear stress	Pa
A	Surface area	cm^2
T	Temperature	°C
v	Viscosity	$Pa.s^{-1}$
$\dot{v}$	Volumetric flow rate	$cm^3.min^{-1}$

1 Introduction

1.1 Context of Study

This section aims to discuss the gap in current knowledge and how the fuel cell designed and developed in this project can address and fill this niche.

1.1.1 The Energy Crisis and Global Warming

Modern lifestyles have become increasingly dependent on the use of electrical energy. From the development of the light bulb in the 1870's, through to televisions, portable music players, transport and computers, technology has developed over time to meet our needs. Through the development of wondrous electronic applications, it has changed the way people work every day. It has now become the norm to listen to music on your mobile phone or read your e-book on the way to work, to sit at a desk all day typing, analysing data and watching videos on your computer then to spend evenings watching a flat panel television for hours. Due to the development and extensive use of electronic devices, the demand on energy resources is higher than ever. The global consumption of primary energy, i.e. commercially traded fuels including modern renewables used to generate electricity, has increased by 28 % from 9,944 million tonnes (oil equivalent) in 2003 to 12,730 million tonnes in 2013 [1]. This increased demand for energy is only accelerated by the increase in global population which shows no signs of slowing down. The global population in 2015 reached 7.3 billion with a projected increase to 11.2 billion by 2100 [2]. The increase in energy consumption is disproportionally large in comparison to the increase in population which could be attributed to the increase in population in developing countries which expect a greater living standard, increasing their energy consumption.

Historically, the energy has been sourced from wood, coal and fossil fuels, such as petroleum, natural gas and oil produced by the natural decay of organic matter [3]. Although the Earth requires the greenhouse effect to support life, the enhanced greenhouse effect has started to warm up the Earth beyond its historical trend, which will continue to due in part to the combustion of fossil fuels [4], leading to climate change and a steady increase in the Earth's temperature. With fossil fuels damaging the environment, coupled with their reserves being depleted and low efficiency, it makes them a damaging and unsustainable energy source.

The growth in global energy demand and humanity's effect on the environment have led to an important challenge that is: the pressing need to discover energy sources which can supply the high global energy demand whilst having, at least, a neutral effect on the environment. This problem has caused a surge in the amount of research in various fields to help solve this complex problem.

1.1.2 Energy Generation and Storage

The generation and storage of energy are vital to modern life and has a long and established history. This section discusses these two types and uses of the current technology.

1.1.2.1 *Energy Generation*

The use of fossil fuels as a primary source of energy generates two main concerns: i) the depletion of limited reserves and ii) the environmentally damaging by-products from fossil fuel combustion. It is these concerns which have driven research into both renewable and green energy. Renewable energy sources replenish themselves over a short period of time whilst green energy sources have no negative impacts on the environment. Energy sources can be renewable but have a negative impact on the environment, for example, hydroelectric sources which can have a negative effect on local ecology [5]. Green energy, which is a sub-category of renewable energy, are sources which are deemed to have little or no impact on the environment in any aspect. The development of a high power output green energy sources would allow the production of energy, thus solving the energy crisis, whilst having no/negligible impact on the environment, although not solving the greenhouse effect issue, it will dramatically slow it down. Renewable energy comes from a variety of sources including solar, wind, tidal and geothermal energy. Although these technologies address some of the issues, they are not currently suitable for transportation/personal electronics purposes without the aid of a suitable energy storage system, i.e. a battery.

1.1.2.2 *Energy Storage*

Energy storage devices convert electrical energy from an external source into a form that can be stored and then converted back into electrical energy. These energy storage devices have applications that vary from small scale, i.e. watch batteries, to the large industrial uses, i.e. storing energy generated by wind power. Energy generated by renewable energy, such as wind turbines, are not always predictable and their power output will fluctuate depending on the

conditions. Should the energy generated exceed the amount required, the energy storage systems can be used to capture the energy for future use [6]. Furthermore, energy storage systems are used in small to medium size applications such as mobile phones and cars, with Li-ion batteries leading the way with their relatively high energy density compared to others. However, with consumers demanding longer life cycles and higher energy densities, the traditional Li-ion battery cannot keep up with the demand [7] leading to the increased research focus.

1.1.3 Fuel Cell Niche

Fuel cells are a technology which offers a potential solution to energy generation and storage for a variety of applications. They can be used to fill in various niches and, although they have many benefits, can be considered to provide a solution to the energy crisis and climate change in two ways, the first is for a wide range of power outputs. Depending on the type of fuel cell used, the power applications can range from small electronics such as torches through to residential homes. The size of the fuel cell can be considered customisable to suit the power requirements and the size of the application. For example, where a laptop battery would have to be charged from a potentially non-renewable energy source (which is supplied via a power socket), a fuel cell could convert hydrogen into its own green energy.

The second advantage is that fuel cells are environmentally friendly. Fuel cells utilise a wide variety of fuels, from the standard hydrogen gas through to organic and inorganic fuels. Such fuels can be supplied from green sources such as with direct ethanol fuel cells which use ethanol sourced from biomass [8] or green hydrogen production through the electrolysis of biodegradable material or water [9] used for proton exchange membrane fuel cells (PEMFCs) whereby fuels is the energy storage intermediate. This variety of fuel types make the use of potentially green and renewable fuel sources viable. Furthermore, the final product of fuel cells is water and produces no environmentally damaging chemicals with respect to fuel cells utilising hydrogen gas. This water by-product has a variety of uses within either the fuel cell stack and the system it's integrated into, i.e. being used as drinking water during NASA's Apollo missions. The wide range of power outputs whilst simultaneously utilising renewable/green fuels without producing any environmentally damaging chemicals makes fuel cells a promising future power supply.

1.1.4 Direct Borohydride Alkaline Fuel Cells

Although fuel cells offer a potential technology to help with the energy crisis and climate change, there are some challenges which need to be addressed. The most highly used fuel cells are arguably the solid oxide fuel cell (SOFC) and the proton exchange membrane fuel cell (PEMFC) which require the use of hydrogen gas or other organic gases containing hydrogen as a fuel source. This is problematic as the use of compressed hydrogen gas can be considered dangerous as it is highly explosive and logistically impractical as the system must be designed around the hydrogen containers. Furthermore, hydrogen has a low density meaning large quantities are required for useful applications leading to high cost in compression and liquefaction techniques. Metal hydrides and other materials can be used as hydrogen stores through the use of physisorbed hydrogen; however, challenges with each material have prevented a universal material to be developed [10]. There is potential for the direct borohydride alkaline fuel cell (DBAFC) to be used as a replacement. The DBAFC do not require containers of hydrogen gas (which are pressurised to approximately 70 MPa in the automotive sector) as the fuel is in the form of a liquid, which is incorporated into the liquid electrolyte already present. This fuel is used in the fuel cell to generate the power in a safer and more practical way. Furthermore, the use of borohydride as a fuel may potentially produce more power than using hydrogen gas, if completely utilised, due to the thermodynamic cell potential of a hydrogen and borohydride fuel cell being 1.23 and 1.64 V respectively. Therefore, the development of a working and optimised DBAFC may address some of the challenges currently experienced by other types of fuel cells.

1.2 Motivation for Project

With some of the background to fuel cell technology, its place and use in comparison to the current energy generating and storage technologies, the DBAFC can potentially be used as a more environmentally friendly alternative. This section discusses how this project addresses the various gaps in current knowledge.

1.2.1 History of issues

There has been a steady increase in the amount of research dedicated to technologies used to produce green renewable energy for a variety of applications, such as portable electronics and public transport. Although green renewable energy has been investigated for larger power outputs, such as wind turbines, little has been done for portable electronics such as laptops and mobile phones. These technologies rely on batteries as a method of energy storage.

Despite the energy generated from green renewable sources can charge portable electronics batteries, little has changed in the form of the historical lithium-based batteries which suffer from dendrite formation, leading to cathode degradation [11]. While much work has been dedicated to developing batteries, they are becoming increasingly unsuitable for high power requiring portable electronics as solutions to these issues have not yet been fully addressed and implemented. Public transport, such as cars, have also received an extensive amount of research to reduce the impact they have on the environment and people's health. This has led to the development of low emission cars such as battery powered (electric) and hybrid cars [12]. With electric cars succumbing to the same Li-ion battery issues and hybrids still requiring the use of fossil fuels, humanity is still relying on old technologies and unsuitable fuels. Fuel cells offer the opportunity to produce power for both portable electronics and transportation. However, the historically best fuel cells require hydrogen gas which is usually stored in bulky pressure vessels. This use of a hydrogen gas pressure vessels, from a practicality and safety point of view, is unsuitable for these applications. Furthermore, the fuel could potentially be replaced with other higher power density fuels, including borohydride.

1.2.2 Recent Increase in Issues

With the combination of fossil fuel reserve depletion and an increase in climate change severity, the Earth's environment could potentially deteriorate to a point where the effect cannot be reversed. This is a pressing issue which must be addressed immediately. Over the past few decades, many technologies have been developed to help solve this issue; however, there are still areas which can be improved upon. Of these technologies, fuel cells have received a lot of attention as a power source for a wide range of power demands.

1.2.3 Dissatisfaction with current knowledge

The specific type of fuel cell developed in this project is the DBAFC. These have not been researched as comprehensively as other types of fuel cells which have left a gap in our current knowledge. There are several reasons for the lack of research interest, mainly due to certain borohydride related challenges experienced in DBAFC. The first is the use of an effect electrocatalyst to obtain the maximum columbic efficiency from the borohydride fuel. Although there are known electrocatalysts which show high electrocatalytic activity, they are usually based on expensive precious metals, such as Pt, and so are difficult to commercialise. Furthermore, much of fuel cell research has been focused on electrocatalyst identification, not the manufacture of electrodes suitable for scale up. Little research has been conducted into

the development of a full stack, a series of fuel cells, which could be incorporated into portable devices or transport. Finally, the development of a flexible membraneless DBAFC system has not been developed for the use under a variety of operating conditions. If these challenges can be addressed and solved, the applications for DBAFC could be widely utilised.

1.2.4 Identification of specific factors

It is from the gaps in current knowledge previously stated that the identification of specific factors to be researched have been drawn. The electrocatalyst has an important role within the fuel cell and the correct material must be used to generate the large power outputs at a cost which is affordable to be made mainstream. The electrocatalyst must be developed into an effective electrode, which has the desired characters without hindering the electrochemical performance. Furthermore, the fuel cell stack architecture design must be evaluated to determine whether the fuel cell can be "scaled up" to a usable power output. Finally, a suitable fuel cell system would need to be developed to control all the operating conditions required for fuel cell operation and to evaluate various performance parameters. These four areas, the electrocatalyst identification, manufacturing method, stack architecture and system design are the basis for this project.

1.3 Aim and Scope

Each of the four research areas discussed has a wealth of potential solutions to the challenges mentioned. As such, the project had to have clear and specific aims and scope to accurately address the DBAFC challenges.

1.3.1 Aim

The aim of this project is to develop a DBAFC with increased power outputs compared to the current fuel cell standard for the potential use in portable electronics and transport.

1.3.2 Scope

This project is very broad and so it was split into four research areas; i) identification of anode electrocatalyst, ii) development of a scalable electrode manufacturing method, iii) designing a DBAFC fuel cell stack and iv) designing a flexible DBAFC system. Due to the potential for a variety of solutions in these research areas, the scope had to be defined.

- Electrode development –
  - Electrocatalysts: there's an abundance of possible types of materials which could be used as electrocatalysts for the anode as well as the materials varying from supplier to supplier, i.e. the same material from one supplier may not have the same properties as one from another. Furthermore, due to the different project objectives, electrocatalysts could not be specifically designed hence only a few commercially available electrocatalysts were evaluated.
  - Manufacturing: there are various methods for manufacturing electrodes such as screen printing and spray coating. Developing an electrode for each process and then optimising the manufacturing conditions would take a lot of time which could be invested more wisely in other areas. Therefore, only screen printing will be investigated as there are fewer parameters to optimise compared to other manufacturing methods.
  - Cathode: the electrode kinetics of the cathode electrocatalysts is well established in alkaline fuel cells (AFC); however, not in the presence of borohydride. A commercially used electrocatalyst was used as the candidate cathode electrocatalyst and was developed into a screen printable electrode.
- Stack architecture design – each of the components in the fuel cell stack requires a specific design to have a high performance during operation. These different components were designed using CAD software and the effect of different designs on fluid flow at different operating conditions was evaluated using computational simulation modelling. The designs were then manufactured and assessed experimentally for their ease of manufacture and suitability.
- System design – during the operation of a fuel cell, there are several parameters which must be controlled and various outputs which need to be measured. Different types of fuel cells and applications require different testing systems. As such, a flexible system was designed to be specifically used for a DBAFC for use with different operating conditions.

1.4 Overview of Study

Each of the research areas feeds into each other with the candidate electrocatalyst being developed into a full electrode, which would, in turn, be used in a designed fuel cell stack and system. Below is a summary of the individual phases and the research completed within them.

1.4.1 Anode Electrocatalyst

The kinetics of the anode in a DBAFC differ from that of an AFC due to the fuel being present in the form of a liquid rather than a gas. This difference in kinetics, along with current generation via a direct oxidation pathway of borohydride, have been assessed for several commercially available materials. Initially, the effect of different suppliers and manufacturing methods on the performance of the electrocatalyst was assessed. This identified three precious metals (platinum (Pt), palladium (Pd) and ruthenium(Ru)) on a carbon support as potential electrocatalysts. The effect of different carbon supports (carbon black and activated carbon) on performance were evaluated. Finally, once the candidate electrocatalysts were identified, their performance in borohydride, including material loading, mass transport, kinetics and peak current, were evaluated and compared using cyclic voltammetry.

1.4.2 Electrode Manufacture and Evaluation

Manufacturing electrodes for use in analytical techniques, such as cyclic voltammetry, is vastly different from manufacturing electrodes on an industrial scale. Therefore, new methods should be employed to produce high quality electrodes, quickly and at a low cost. One method is the use of screen printing. The candidate electrocatalysts were prepared into a suitable ink and printed onto an electrode substrate. The inks were evaluated for their printability using observational and rheological methods. Originally a commercially used cathode was to be used in conjunction with the developed anode. However, the cathode was discontinued but the cathode electrocatalyst was still available and was also developed into a screen printable ink. The effects of different manufacturing methods on electrode surface defects were determined using 3D SEM reconstruction and light microscopy techniques. A method was developed and used to quantify the amount of electrode degradation experienced during fuel cell operation. The removal of all surface defects by altering the ink formulation and manufacturing method was not possible; however, a method was developed to repair the electrode's surface. Finally, the electrochemical properties of the anode and cathode were compared to commercially used electrodes in both borohydride and hydrogen fuel cells.

1.4.3 Fuel Cell Stack Design and Architecture

This chapter focuses on the design of a suitable DBAFC fuel cell stack using CAD and simulation modelling software. The stack, which consisted of a single repeating cell unit, was split into different components and designed individually. Although all components needed to be designed to some extent, to ensure that the cell construction would align and there was a flow

of fluid through the stack, some component designs had a larger impact on the performance of the stack compared to others. This included the air and electrolyte distribution plates. A simple air plate, which distributed the air to the back of the cathode, was designed and evaluated using simulation software. Similarly, different electrolyte plates were designed to optimise the amount of electrolyte (and therefore fuel) distributed across the face of the electrodes whilst reducing ionic leakage. These were evaluated using simulation modelling for flow distribution under a variety of temperatures. Furthermore, these plates were manufactured using different methods as the material used for the plate, polytetrafluoroethylene (PTFE), was difficult to manufacture due to being thin and flexible. The manufacture plates were then experimentally assessed for their electrical resistance, used as an indicator for their effect on ionic leakage, using electrochemical impedance spectroscopy.

1.4.4 Fuel Cell System Design and Development

The DBAFC had to be assessed using different operating conditions, which required the development of a flexible testing system. As the electrode and stack were evaluated, the system developed through a series of iterations. Operating the fuel cell at increased temperatures and borohydride concentrations produced large quantities of hydrogen to be evolved, due to the hydrolysis of borohydride. This led to the final system being a single pass from the initial simple recirculating electrolyte with the intention of being a semi-recirculating. The system developed controlled all operating conditions, including temperature, flow rates and orientation. Furthermore, the system monitored the electrochemical properties of the cell, temperature fluctuations, pH, humidity, outlet borohydride concentration and discusses the prospect of determining the fuel cell fuel utilisation by monitoring the hydrogen gas evolved.

1.5 Significance of Study

Little is known about DBAFC's, with respect to suitable electrocatalysts, operating conditions and the development of a full stack. These gaps in knowledge are what this project hopes to fill. Currently, there are only two types of fuel cells which are considered the standard for ambient pressure and temperature power generation, the direct methanol proton exchange membrane fuel cell (DMFC) and anion exchange membrane fuel cell (AEMFC).

However, by developing the DBAFC it could be possible to produce a fuel cell which is not only safer and logistically better designed, with respect to the removal of a large hydrogen gas pressure vessel, compared to some SOFC and PEMFC, but it also potentially has greater power outputs. If developed and optimised correctly and assuming large power outputs, the DBAFC would be able to produce power for portable devices and transport. Currently, the fuel cells operated state-of-the-art fuel cell cars use hydrogen gas as a fuel source. This compressed hydrogen is bulky and presents challenges in terms of safety. DBAFC offer the possibility for a replacement of these fuel cells with a safer and potentially higher power output energy source. Furthermore, depending on the method in which the fuel cell is operated, the DBAFC could power portable electronics such as laptops. By replacing the battery with a DBAFC, the laptop would not succumb to the same issues as batteries do. To recharge the laptop, the borohydride concentration could just be increased with the addition of a borohydride tablet. Additionally, should the DBAFC offer higher power outputs, the time between laptop charging, i.e. replenishing the borohydride concentration, could be longer than hours as the current technology stands.

2 Background

2.1 A Brief Background of Fuel Cells

The basis of fuel cells can be traced back to the 1800's to Sir Humphry Davy, a British chemist who originally used electrolysis as a method to separate compounds in a mixture [13]. This theory was then developed into a fuel cell concept independently by two scientists. Christian Friedrich Schönbein investigated the idea fuel cells in 1838 whilst Sir William Grove developed the gas battery; two Pt electrodes separated by an electrolyte with $O_{2(g)}$ and $H_{2(g)}$ used as fuels to generate a current, which is essentially the fuel cell setup we know today [14]. Later in the 19th century, Ludwig Mond and Charles Langer developed Grove's work and coined the term "fuel cell" [13]. Moving forward into the 1900's, Francis Bacon developed the first alkaline fuel cell which was eventually used in the Apollo missions [13, 14]. Since then, many aspects of fuel cells have been investigated, from determining specific interactions between the reductant/oxidant and electrocatalyst to increasing the power output. The technology has been used in a wide range of applications and has notably been used in spacecrafts [15, 16], submarines [17, 18], cars [19, 20], buses [21, 22] and in residential homes [21, 23].

2.2 Basic Fuel Cell Theory

This section details the basic principles of fuel cells operation introduces the different types and describes their construction.

2.3 Hydrogen / Oxygen Fuel Cell

Hydrogen fuel cells are an electrochemical power source whereby hydrogen and oxygen react in a redox reaction to produce water, electricity and heat (see Equation 2.1). From small flashlights, laptops and mp3 players to cars, buses and even national power stations fuel cells can be used for a wide variety of applications. Different types of fuel cells, with varying power outputs, utilise different technologies to meet the demand of the user although all hydrogen/oxygen fuel cells have the same general equation:

$$2H_2 + O_2 \rightarrow 2H_2O + Electricity + Heat$$

Equation 2.1 - General fuel cell equation.

Table 2.1 below shows the target applications of different fuel cell technologies together with their advantages and the approximate power outputs they can deliver.

Table 2.1 - Difference fuel cells and their performance/applications [16].

Typical Applications	**Portable electronics equipment**			**Cars, boats and domestic CHP**		**Distributed power generation, CHP and buses**		
Power /W	1	10	100	1K	10K	100K	1M	10M
Advantages	Higher energy density than other batteries. Faster recharging.			Potential for zero emissions, higher efficiency.		Higher efficiency, less pollution, quiet.		
Range of applications	AFC						MFC	
	SOFC							
	PEMFC							
	PAFC							

The different fuel cell technologies cover a wide power range and offer a potentially more environmentally friendly alternative to current energy storage and generation devices.

2.3.1 Fuel Cell Architecture and Components

In its simplest form, a fuel cell consists of three main components (Figure 2.1):

- Anode – electrode responsible for the oxidation of hydrogen.
- Cathode – electrode responsible for the reduction of oxygen.
- Electrolyte – an ion conducting material (can be either solid or liquid depending on the type of fuel cell) which completes the circuit via charge transfer.

The fuel is fed to the anode where it is oxidised. For fuel cells which use hydrogen as the fuel, this is called the hydrogen oxidation reaction (HOR). The electrons travel from the anode, through an electronic load to the cathode, where they reduce the oxidant, in most cases this is oxygen and the reaction is known as the oxygen reduction reaction (ORR). The electrolyte connects the two electrodes together and allows the transfer of charge between them, with the mechanism and direction depending on the type of electrolyte used.

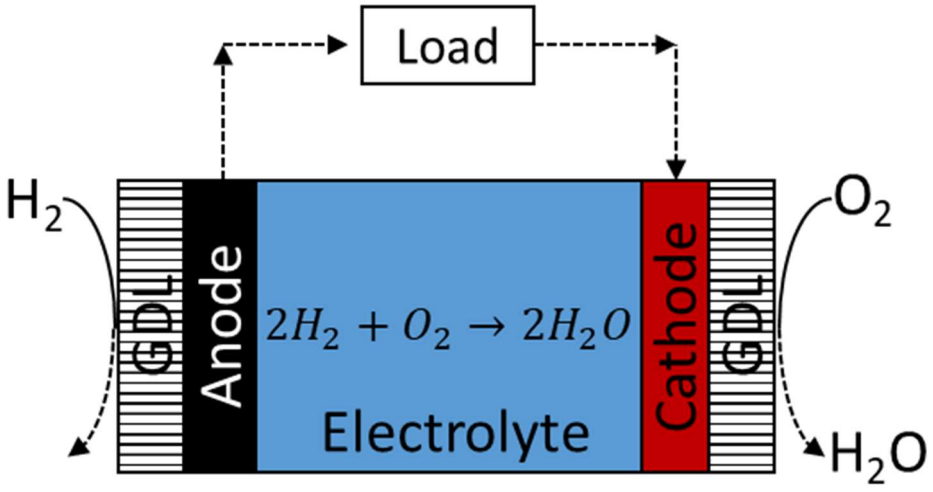

Figure 2.1 - A generic single fuel cell unit using hydrogen and oxygen.

The amount of voltage generated by a single cell is very low, with a maximum of approximately 1.2 V, depending on the reductant and oxidant used. However, due to efficiency and ohmic losses, the cell voltage is less. As such, they must be connected electrically in series to produce much larger and useful voltages. This arrangement then becomes a stack.

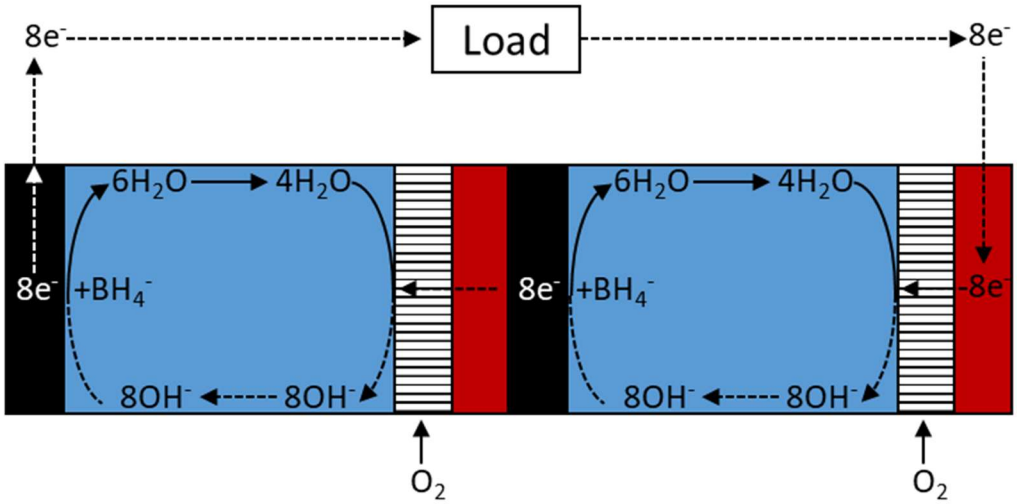

Figure 2.2 - Flow of electrons (dotted lines) through a two cell DBAFC stack and charged countered by transport of hydroxyl ions electrolyte.

The generation and flow of electrons through a two cell stack are highlighted in Figure 2.2. Electrons which are generated on the first anode travel through the load, much like in a single

cell. However, these electrons travel to the final cathode rather than the cathode in the first cell. This charge then moves through the entire stack, moving as electrons around the circuit and, in the case of AFC, via the hydroxyl ion charge carrier, accumulating energy and return to the first anode to complete the circuit. The voltage generated from a fuel cell stack can be represented as the sum of all thermodynamic voltages less cell and stack inefficiencies, which can include ionic leakages, resistances and generation of heat.

2.3.2 Alkaline Fuel Cells

The alkaline fuel cell (AFC), an example of which is being developed in this work, is a fuel cell which uses an alkaline electrolyte (see Equation 2.2). The AFC can be used with an electrolyte membrane separating the two electrodes, in this case, an anion exchange membrane (AEM), or be membraneless, utilising a flowing liquid electrolyte. Using an alkaline electrolyte has advantages over an acidic electrolyte such as improved oxygen reduction kinetics, low cost alternative electrocatalysts and operation at ambient temperatures. However, the use of alkaline electrolyte presents a challenge regarding carbonate formation due to carbon dioxide present in the air feed. Furthermore, precious metals are commonly used which are sensitive to carbon monoxide poisoning. Finally, AFCs have a relatively low power density compared to other types of fuel cells such as SOFCs. It is for these reasons that AFCs have dropped out of favour against other types of fuel cells.

Anode: $2H_2 + 4OH^- \rightarrow 4H_2O + 4e^-$

Cathode: $O_2 + 2H_2O + 4e^- \rightarrow 4OH^-$

Equation 2.2 - AFC redox reaction equation.

The concept of AFCs was first introduced in 1933 by Francis Bacon, with the suggestion that an alkaline electrolyte could replace the more common acid electrolyte [14, 24]. During World War II, he developed a fuel cell for submarines in the navy, and after the war began work on a fuel cell with usable voltage outputs and developed the “Bacon Cell” using a nickel electrode, moderate temperatures and high pressures [25]. The patent for the technology was then bought by Pratt & Whitney which was later developed and used in the Apollo space missions [14, 24]. Since then, AFCs have been used in a wide variety of applications, both stationary and

for transportation. Notably, AFC Energy PLC has developed an AFC, known as the KORE, which provided 200 kW of clean energy into the German grid in Stade. [26]

There are several advantages and disadvantages to AFCs which include:

Advantages:

- Enhanced cathode kinetics – a decreased voltage drop compared to an acidic electrolyte promotes increased cathode kinetics [27].
- Non-noble electrocatalysts – having the fuel cell under alkaline conditions allows for non-noble electrocatalyst materials to be used. This reduces the cost of fuel cells compared to the historic precious metal/Pt-based fuel cells [27-29].
- Low temperature and pressure – AFC can be used at low temperature and pressures (ambient and 1 atm). This makes them ideal for portable electronics.
- Circulating Electrolyte aids heat management – the production of energy is not 100 % efficient towards electricity generation (as with all fuel cells). A lot of energy is lost as heat and so this must be managed; however, this is relatively easy to do so due to the circulating electrolyte.

Challenges

- Formation of carbonate - using alkaline media produces a unique challenge to carbon dioxide degradation of the electrolyte. In alkaline conditions the carbon dioxide, which can be introduced through air, can react with the electrolyte to form solid carbonates (Equation 2.3), reducing the electrolyte conductivity by i) decrease in the concentration of KOH in the electrolyte below the optimal value of about 30 % [30] and ii) the lower conductivity of carbonate compared to the hydroxyl ion at ambient temperature [31] and iii) potentially causing cathode degradation as a result of crystal growth within the electrode and electrocatalyst channels, initiating electrode cracking or flaking . However, these issues can be resolved relatively easily by using a carbon dioxide scrubber on the cathode air inlet.
- The fuel cell electrocatalyst “gold standard” has historically been Pt based, making them expensive and susceptible to carbon monoxide poisoning.
- Water management – The loss of electrolyte in conjunction with the generation of water makes it necessary to have a water management system in place. Water is produced by the electrolyte degradation in the presence of carbon dioxide (Equation 2.3) as well as the anode surface in the electrooxidation process. It is also consumed at the cathode surface during

electroreduction. The net change in the amount of water present differs according to the reductants used (see Table 2.2).

$$2KOH + \quad _2 \rightarrow K_2CO_3 + H_2O$$

Equation 2.3 - Carbon dioxide poisoning on electrolyte.

Water content can be regulated via any gas which is pumped into the system. A high humidity gas will introduce additional water while a dry gas will remove water from the system, both via diffusion through the electrode). Inefficient water management can lead to several problems which include electrolyte dilution/increased concentration and a decrease in cathode performance (water deficiency will restrict the number of reduction reactions which can take place). Research has been conducted in the production of mathematical models to predict the movement of water through the fuel cell. A better understanding of the management of water in a fuel cell is of great importance since it can help develop more compact fuel cells [32].

AFCs can be differentiated according to the type of electrolyte they employ. In a static/immobilised electrolyte fuel cell, the electrolyte is held in a discrete channel filled with an electrolyte gel matrix between the anode and cathode. The electrolyte in the static electrolyte AFC remains within this channel and mass transport is only achieved through migration or diffusion between the two electrodes. Conversely, in a flowing electrolyte/membraneless AFC, the electrolyte is a liquid which is pumped through the fuel cell. The following sections consider the advantages and disadvantages of both designs.

2.3.2.1 *Alkaline Fuel Cell Components*

Although there are similar components to all fuel cells, there are some which are not used for all fuel cells. The components of an AFC are discussed in more detail in Chapter 5; however, a summary of each component are listed below:

- Anode – the site of HOR using an electrocatalyst.
- Electrolyte – an alkaline electrolyte, typically potassium or sodium hydroxide, which has a high ionic conductivity.

- Cathode – the site of ORR using an electrocatalyst.
- Bipolar plate (BBP) – a plate primarily used to distribute fluid throughout the cell and make an electrical connection between the adjacent electrodes.
- Gas diffusion layer (GDL) – a carbon based layer with an electrocatalyst impregnated onto one surface whilst being adhered onto the electrode substrate/BBP. It is responsible for making an electrical connection between the electrocatalyst and BBP, allow the diffusion of gas from the BBP to the electrocatalyst, controls the permeability of electrolyte through the electrode and provides a support for the electrocatalyst.

Although other balance of plant components may be present in an AFC, including pumps, fans and heat exchangers, the components above are common for all AFC applications.

2.3.2.2 *Membraneless Electrolyte Alkaline Fuel Cells*

An AFC is illustrated in Figure 2.3 which highlights the use of a liquid alkaline electrolyte along with the two fuel gas supplies [33].

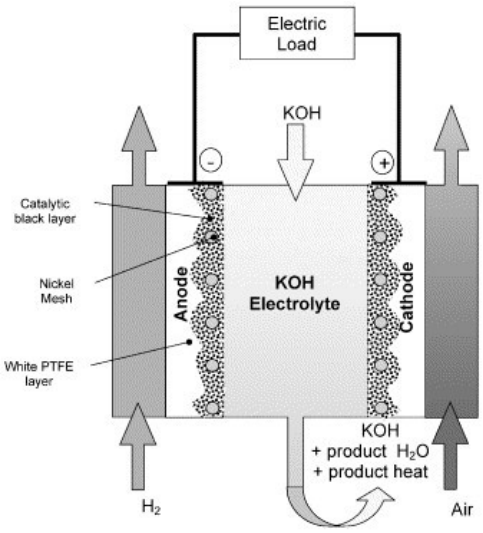

Figure 2.3 - Flow electrolyte alkaline fuel cell structure [33].

There are different types of membraneless fuel cells, one of which is the laminar flow fuel cell. During operation, the reductant and oxidant are flowing through the same domain; however,

the reductant flows in the opposite direction to the reductant between the electrodes [34]. Another is the flow of two liquids through the fuel cell; the electrolyte which carries the reductant fuel and a liquid on the cathode side with the oxidant (typically peroxide). Finally, there is the flow of a single liquid electrolyte between the electrodes with a gas flow on the outside of the cathode which is the type of fuel cell which has been developed in this thesis.

The advantages of membraneless flowing electrolyte AFCs are:

- Membrane degradation – the lack of membrane within the fuel cell removes any issues with membrane stability and degradation. Any electrolyte degradation experienced can be resolved by replacing the electrolyte.
- Water management – although it is possible for water to leak through the GDL due to a drop in hydrophobicity, known as weeping, water management is quite simple compared to membraned fuel cells. Water can be added and removed easily from the flowing electrolyte to keep concentrations of electrolyte constant. Furthermore, membranes that dehydrate can suffer irreversible degradation, increasing system resistance [35].
- Heat management – the temperature of the fuel cell can be regulated without the use of an external cooling system.

However, the absence of a membrane brings certain challenges which include:

- Orientation – due to the liquid electrolyte, specific fuel cell orientations must be used as it is not contained in a rigid matrix.
- Carbonate formation – having a liquid electrolyte gives rise to increased carbonate formation, leading to a decrease in electrical conductivity, electrode degradation and increased difficulties in water management. This is a challenge for both flowing and static electrolyte fuel cells but is less of a challenge for fuel cells containing a membrane.
- Increased weight – the liquid electrolyte weighs considerably more than membrane equivalents.
- Pumps – additional pumps are required to control the flow of electrolyte through the fuel cell. Though this is not a challenge it creates increased system complexity.

- Ionic leakage – flowing liquid electrolyte gives rise to ionic leakage challenges whereby the electrons migrate through the electrolyte from the last cathode to the first anode, by-passing all electrodes in-between, and reducing efficiency.

2.3.2.3 *Static Electrolyte Alkaline Fuel Cells*

There are two types of static electrolyte AFCs, one which the electrolyte is held within a saturate matrix, historically asbestos, and the other with a solid polymer electrolyte with an ion conducting functional groups. The saturated matrix is sealed between each pair of electrodes and so removes the requirement of having a pump to transport the electrolyte around the system. However, this results in water management issues as the matrix cannot be topped up as with flowing electrolytes. Furthermore, the obvious carcinogenic properties of the asbestos raise safety concerns [16].

The polymer electrolyte, known as the anion exchange membrane (AEM), acts as a solid electrolyte allowing the passage of hydroxyl ions between the two electrodes (see Figure 2.4). To do this, the AEM polymer consists of a polymer backbone (which is generally responsible for the mechanical and thermal properties of the AEM) and cationic functional groups (which act as the charge carriers) [36]. There are three types of AEMs which include homogeneous (containing a single type of polymer), heterogeneous (containing two integrated types of polymer) and interpenetrating polymer network (a polymer which has been doped with either a salt or an organic/inorganic segment) [36]. Although the hydroxyl ion transportation mechanism through the AEM is not fully understood, it is speculated that it is similar to that of PEMFC (Grotthus mechanism, convection, migration and diffusion) [36].

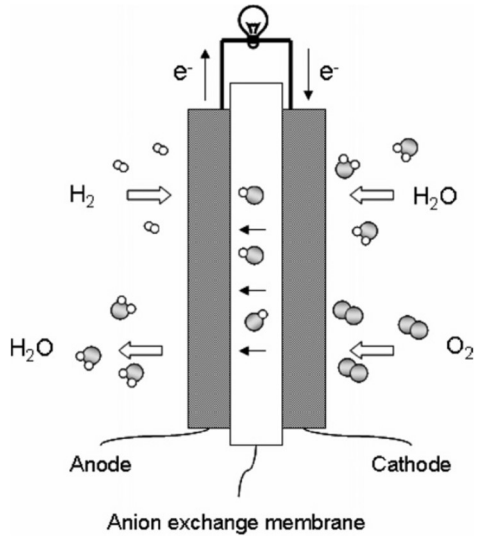

Figure 2.4 - AEM Alkaline Fuel Cell Schematic [36].

There are several benefits to using an AEM which include [36, 37]:

- Fuel cell orientation versatility – the electrolyte is immobilized within a rigid gel matrix within the fuel cell and therefore does not need to use pumps, unlike flow electrolyte fuel cells. This gives the benefit of being able to use the fuel cell in any orientation as no pumps and pipes will be required.
- No electrode weeping – due to the electrolyte being immobilized, it is unable to weep.
- Prevention of fuel crossover – the membrane can be used to segregate the fuel from the cathode.
- Easy handling – when the fuel cell is manufactured and used there is a vast reduction in the amount of corrosive liquid alkaline media.
- Weight reduction – the removal of large amounts of liquid.

There are still several challenges which need to be addressed regarding the use of AEM such as [37]:

- Additional coolant system – unlike the flow electrolyte AFC, the static electrolyte AFC requires an additional coolant system to regulate the temperature.
- Water management – as water is being produced at the anode, used at the cathode and evaporated in the air/oxygen supply, there must be a degree of water management. This is

to ensure that water is being removed from the anode, fed to the cathode and the air/oxygen supply does not remove too much/too little.

- AEM stability – a concern of using AEM is its stability. It is thought to be due to the substitution of the ammonium and methyl groups within the AEM with a hydroxyl group. This can cause them to crack easily.
- Carbonate sensitivity – due to the enclosed nature of the fuel cell, both for the AEM and the asbestos matrix, it is difficult to remove any carbon dioxide present within the system meaning that they are susceptible to carbon dioxide poisoning of the electrolyte.

2.3.3 Direct Fuel Alkaline Fuel Cells

A derivative of AFC is the direct fuel alkaline fuel cell (DFAFC). This section will explain the key differences between the standard AFC and its derivative form. The research conducted within this thesis is focused on the technologies which can be directly applied to DFAFCs.

2.3.3.1 *Direct Fuel Alkaline Fuel Cell Function*

A DFAFC is an AFC whereby one or more of the fuels are dissolved/incorporated into the electrolyte. For example, a DFAFC may use methanol as a hydrogen carrier, i.e. a chemical which contains hydrogen bound to another atom, and so would not require hydrogen gas. This offers up some exciting possible fuel sources such as methanol, ethanol and sodium borohydride, which will be discussed further in Sections 2.3.3.3. In this thesis, only the hydrogen supply will be replaced with dissolved hydrides, also known as direct oxidation alkaline fuel cells (DOAFC). It must be noted that the oxygen source can be replaced with a dissolved source such as hydrogen peroxide, H_2O_2; however, this is out of scope for this thesis.

This change in using dissolved fuel rather than the gas results in a different construction to other fuel cells. This is illustrated in Figure 2.5 which shows the difference between a static and membraneless DFAFC. In the static electrolyte DFAFC, the reductant flows on the outer interface of the anode (i.e. not between the anode and cathode for that cell). The reductant diffuses through the liquid diffusion layer (LDL) of the anode to the anode-membrane interface where it is oxidised in a similar process to the transport of oxygen through the gas diffusion layer (GDL) of the cathode. Conversely, in a membraneless FC, the oxidant, reductant or both flow between the electrodes.

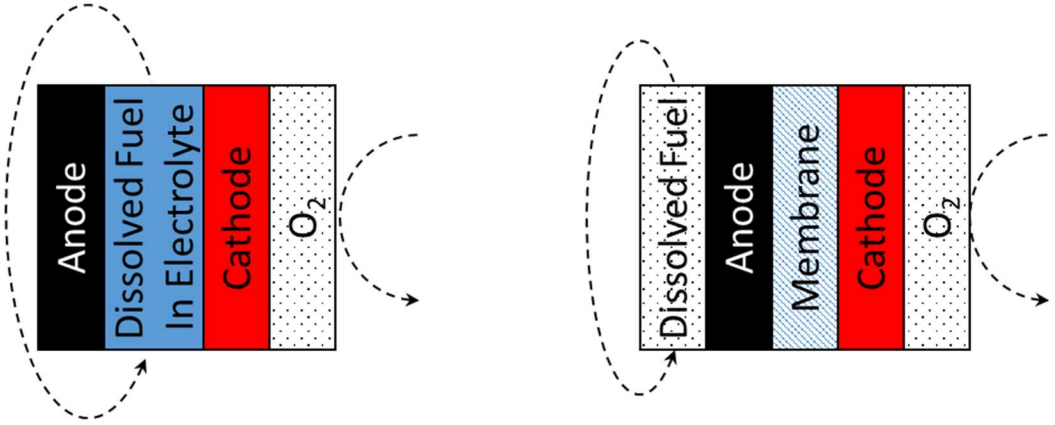

Figure 2.5 - The flow of dissolved fuel through a membraneless (left) and a static (right) fuel cell. Note that the dissolved fuel may also be on the cathode side.

The benefit of having a static electrolyte DFAFC are the advantages of using a membrane, with the benefits of using a dissolved fuel. The benefit of having a design based on being membraneless is the removal of a GLD on either of the electrode, depending on the gas which is being replaced, allowing for simpler electrode design and manufacture. However, this requires the electrocatalysts to be selective to either the oxidant or the reductant as it will be in the presence of both. It is speculated that the complexity of making the anode selective outweighs the benefit of designing a GDL.

2.3.3.2 *Advantages and Challenges of DFAFC*

There are two major advantages of a DFAFC over a traditional AFC, one of which is the flexibility of fuels which can be used. A wide variety of fuels can be used in place of hydrogen or oxygen gas and can lead to increased cell voltages, including peroxide and various alcohols for the reductant and oxidant respectively. Furthermore, replacing the hydrogen or oxygen gas with another dissolved oxidant or reductant respectively allows for the removal of hazardous gas storage cylinders. This increases the ease of logistics, especially in transportation applications, as well as safety. However, there are disadvantages to using a dissolved fuel such as the production of by-products, which can potentially inhibit the poison electrocatalyst's surface and electrolyte as well as cause challenges in the removal of the products from the fuel cell. Depending on which fuel is used there may also be challenges regarding water management (the net water change will differ between fuels see Table 2.2).

Having the fuel solely on chemically bound hydrogen in the electrolyte gives several advantages:

- Transportation – whilst the oxygen can be sourced from the air, hydrogen would historically be provided by compressing hydrogen gas at 35 and 70 MPa [38] or in heavy hydride containers. This would not be ideal for the public and for portable electronics as it would be bulky and hazardous. By having the fuel dissolved in the electrolyte this removes the need for a cylinder of compressed hydrogen. Once the fuel has been used, it can be pumped out of the system and replaced with a fresh new electrolyte.
- Multiple fuel sources – there are many different fuel sources for dissolved hydrogen fuel cells. This can be from organic fuels (such as alcohols) to inorganic fuels (such as hydrides) which makes DFAFC very diverse [39].
- Low cost fuels – certain fuels used to power DFAFC can be far low cost than current fuels, i.e. when compared to fossil fuels for cars. It has been estimated by Ogden *et al.* that a gasoline powered car would be approximately USD $850 - 1200 increase in capital costs compared to hydrogen versus a USD $500 - 650 increase of that of a methanol fuel one [40].
- Sustainable fuels – there is a big drive to find sustainable fuels for the future and DFAFC can make use of this. Fuels from biomass, i.e. biofuels, can be used in DFAFC and so be more sustainable than fossil fuels. This drive has increased the production of biofuels from 4.4 billion litres in 1980 to 50.1 billion litres in 2005 and is continuing to grow [41].
- AFC – along with the benefits mentioned above relating to the fuel, it also encompasses the benefits of being an AFC, i.e. enhanced cathode kinetics and the potential use of low cost electrocatalysts [27].

Unfortunately, there are some disadvantages to DFAFC:

- Fuel – each fuel has its own issues which need to be addressed before it can be utilised fully. This will be explained further, for the fuels which will be used within this thesis.
- Fuel crossover – due to the electrodes being submerged in the fuel, the cathode electrocatalyst must be selective only to the oxygen and not the hydrogen fuel source (and vice versa).
- AFC - the disadvantages of AFC (including carbon dioxide and carbon monoxide poisoning) also apply to DFAFC. However, this is more prominent in DFAFC using organic fuels

containing alcohol functional groups as the oxidation intermediates and by-products produced is carbon monoxide [42].

2.3.3.3 *DOAFC Fuels*

There are numerous fuels which can be used in DOAFC, including organic and inorganic materials with a wide range of power densities [39]. Each have their own advantages and challenges. Originally in this thesis, three fuels were meant to be investigated; methanol, ethanol and sodium borohydride. The advantages and challenges of their use as an oxidant in alkaline fuel cells are discussed below.

Table 2.2 - Different fuel cell fuels, reactions and net water.

Fuel	Overall Anodic Oxidation Reaction	Overall Cathodic Reduction Reaction	Net Water
Hydrogen	$2H_2 + 4OH^- \rightarrow 4H_2O + 4e^-$	$O_2 + 4e^- + 2H_2O \rightarrow 4OH^-$	+2
Methanol	$CH_4 + 6OH^- \rightarrow 5H_2O + 6e^- + CO_2$	$\frac{3}{2}O_2 + 3H_2O + 6e^- \rightarrow 6OH^-$	+2
Ethanol	$CH_3CH_2OH + 2OH^- \rightarrow CH_3COH + 2H_2O + 2e^-$	$3O_2 + 6H_2O + 12e^- \rightarrow 12OH^-$	-4
	$CH_3CH_2OH + 4OH^- \rightarrow CH_3COOH + 3H_2O + 4e^-$		-3
	$CH_3CH_2OH + 12OH^- \rightarrow 2CO_2 + 9H_2O + 12e^-$		+3
Sodium Borohydride	$BH_4^- + 8OH^- \rightarrow BO_2^- + 6H_2O + 8e^-$	$2O_2 + 4H_2O + 8e^- \rightarrow 8OH^-$	+2

Table 2.3 - Reactions, net water, cell potentials (vs SHE) and energy densities of different reductant fuels [39].

Fuel	Anode E^0 (V)	Cathode E^0 (V)*	Overall E^0 (V)*	Energy Density/ W.h.kg^{-1}
Hydrogen	-0.83	0.40	1.23	33,000
Methanol	-0.81	0.40	1.21	6100
Ethanol	-0.77	0.40	1.17	8030
Sodium Borohydride	-1.24	0.40	1.64	9,000

***Cathode potentials are based on oxygen gas reductant.**

Methanol

Methanol, CH_3OH, is the simplest alcohol and little research has been conducted for its use as a fuel in alkaline compared to acidic media and is referred to direct methanol alkaline fuel cells (DMAFC). Although methanol as a fuel has historically been sourced from natural gas, recent pushes in green, sustainable and environmentally friendly synthetic routes have allowed for much more ethical methods of production such as from glycerol and biomass [43, 44]. Methanol is relatively simple to oxidise at low temperatures and pressures which make it

valuable as a fuel for portable electronics applications. However, methanol has a relatively low energy density compared to other fuels (see Table 2.3) and the oxidation by-product, carbon monoxide, can poison electrocatalysts. Furthermore, methanol is toxic and although it's unlikely that persons will ingest it, this must be taken into consideration should the applications be used for the public.

Ethanol

Ethanol, CH_3CH_2OH, is another organic molecule; however, unlike methanol, it contains an important carbon-carbon bond. Like DMFC there has been extensive work conducted in relation to fuel cells, also known as direct ethanol fuel cells (DEFC). Historically ethanol has been produced from the fermentation of plants and biomass for the use in alcoholic beverages, antiseptics, solvents and other applications [8, 45]. Ethanol has a higher energy density compared to methanol due to the additional carbon-carbon bond, is less toxic than methanol, a low production cost and can be produced from green sustainable sources. However, ethanol still has a lower energy density compared to other fuels (see Table 2.3), it is difficult to use at lower temperatures and pressures, could potentially be appealing to public ingestion (due to ethanol being the alcohol used in alcoholic beverages) and has a complicated oxidation pathway [46]. Furthermore, much like methanol, the oxidation by-products can poison electrocatalysts.

Sodium Borohydride

Sodium borohydride, $[Na]^+[BH_4]^-$, is an inorganic hydride molecule which has a very high energy density (when compared to methanol and ethanol see Table 2.3). Unlike DMFC and DEFC, it has not received as much attention due to issues relating to its oxidation. Borohydride has been used extensively as both a reducing agent in chemical reactions as well as in hydrogen storage. Using borohydride gives rise to high energy densities with the by-products being potentially reformed back to borohydride [47]. Furthermore, unlike the use of some organic fuels, the by-products from the reduction of borohydride do not produce carbon monoxide and therefore will not poison precious metal electrocatalysts. However, the synthesis for borohydride can be costly, using the standard Brown-Schlesinger and the Bayer process, has a complicated oxidation reaction and the oxidation product (metaborate) has a significantly higher molecular mass of 42.8 $g.mol^{-1}$ compared to borohydride which is 14.84

$g.mol^{-1}$. This increase in molecular mass (nearly 3 times) results in the fuel's weight increasing during use which is undesirable for transportation uses.

Sodium borohydride, methanol and ethanol were potentially going to be investigated. Sodium borohydride seems promising, due to its high power density, and with the relatively low research interest, compared to other fuels, had the potential for novel research with respect to finding an appropriate anode electrocatalyst and used in conjunction with a membraneless electrolyte. It's for these reasons that sodium borohydride fuel was the one focused on in this work. In the following section, a more in-depth description of using borohydride as an oxidant.

2.3.4 Sodium Borohydride

Sodium borohydride has been focused as the fuel in this thesis and so it is important to know the role of borohydrides in the energy industry, how it's produced and its reaction mechanisms.

2.3.4.1 *Use of Sodium Borohydride in Energy*

There are arguably three major uses for sodium borohydride which are as a reducing agent in chemical reactions, hydrogen storage applications and as a fuel for fuel cells. This section will not be looking at the former as it is out of scope; however, it should be noted of its importance.

The main use of sodium borohydride in the energy sector is for the use of hydrogen storage. Hydrogen powered applications have been increasingly important due its low, albeit zero, impact on the environment is produced from green sustainable sources. One challenge for this is to find alternative methods to storing hydrogen as a gas in cylinders as this presents a safety concern due to hydrogen's extremely high flammability. One method of storing hydrogen is in solid materials such as hydride which, under specific conditions, liberate hydrogen which can be used for applications such as fuel cells [48, 49]. Borohydride is a common metal halide used as a hydrogen storage material. Out of the popular boron containing storage materials, including lithium borohydride, ammonia-borane and ammonia-triborane, sodium borohydride has received the most attention due to its high hydrogen capacity, approximately 10.8 wt.%, increased safety, stability and other characteristics [50]. Much like with other electrochemical

cells, one of the drives for sodium borohydride hydrogen storage is the stability and cost of electrocatalysts used to release the hydrogen [50, 51]. Research into low cost electrocatalysts has led to the development of non-precious metals such as nickel, cobalt, manganese and other materials [48-51]. Other work into increasing the amount of dissolved borohydride, and therefore increase the hydrogen storage density. As it stands, 20 wt.% sodium borohydride in water (which equates to approximately 4.5 - 6.5 wt.% hydrogen) is the upper limit of how much sodium borohydride can be dissolved before solid precipitate forms [52]. Although sodium borohydride contains approximately the same amount of hydrogen as required by the U.S. Department of Energy target (5.5 wt.%) the work carried out by Schubert *et al.* has increased the hydrogen capacity to approximately 6.5 wt.% in order to store more hydrogen within the dissolved fuel by altering the pH of the media [50, 52].

The other energy application for sodium borohydride is in the use of direct borohydride alkaline fuel cells (DBAFC). The current technologies and variations are discussed in detail in Section 3.

2.3.4.2 *Sodium Borohydride Synthesis*

Historically the most commonly used process for the production of sodium borohydride is via the Brown-Schlesinger process [53]. This is based on the reaction of sodium hydride and sodium trimethylborate (see Equation 2.4) at temperatures of around 250 °C and 93 % yield [54].

$$4NaH + B(OCH_3)_3 \rightarrow 4NaBH_4 + 3NaOCH_3$$

Equation 2.4 - Brown-Schlesinger process for sodium borohydride production.

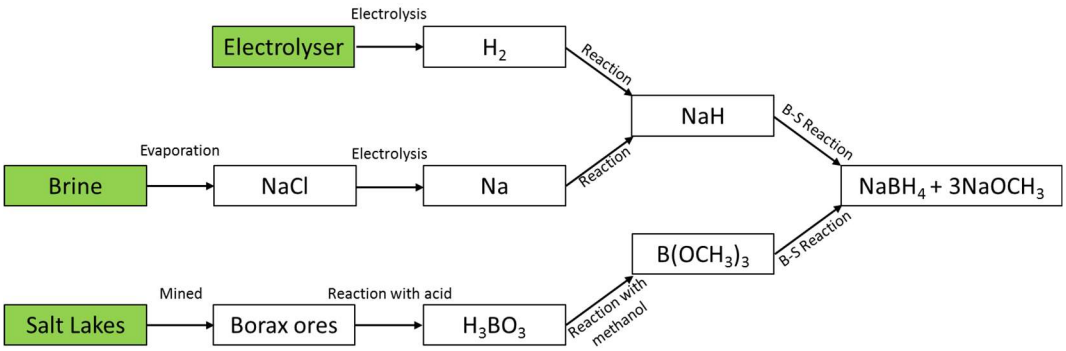

Equation 2.5 - The Brown-Schlesinger process and precursor sources [55].

Another process for the synthesis of sodium borohydride is via the Bayer Process which has similar precursors to the Brown –Schlesinger but with the addition of silicon dioxide [25].

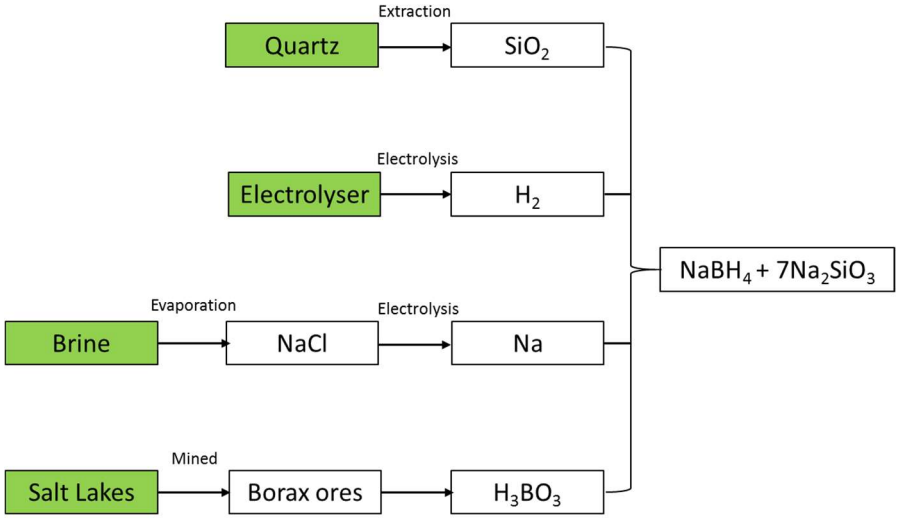

Equation 2.6 - The Bayer process and precursor sources.

All the precursors for the synthesis of sodium borohydride can potentially be produced from green sustainable sources, although historically this is not the case. Since the original production in the 1940's by Brown and Schlesinger there have been numerous more methods for its synthesis, with some quoting approximately 100 methods due to the drive of its use in energy storage [25].

2.3.4.3 *Sodium Borohydride Oxidation*

There are two challenges to using borohydride as a fuel with the first being its stability in the electrolyte. Borohydride is unstable at low pH's which is important for the use of hydrogen energy storage but is an issue when used in a fuel cell [56]. However, borohydride is very stable at increased pH's, i.e. electrolytes above pH 7, which is preferable in AFCs. The other, and arguably the main, challenge is the oxidation mechanism of borohydride which can proceed through two potential pathways; the direct and indirect oxidation route. The direct oxidation, which proceeds according to the anodic oxidation process as in Equation 2.7, utilizes the full 8 potential electrons within the borohydride molecule. The indirect pathway; however, proceeds first by a hydrolysis and subsequent oxidation process (shown in Equation 2.7) which leads to a reduction of approximately 25 % electrical energy [57]. Furthermore, the generation of hydrogen gas could lead to losses due to potentially leaving the fuel cell before being oxidised. To obtain the maximum amount of energy from the borohydride, an electrocatalyst must be used in which is specific to the direct oxidation pathway. Having an electrocatalyst specific to the direct oxidation pathway would not only increase the overall power generated, it would also remove the added potential complications relating to the generation of hydrogen gas in the electrolyte channel. Although the electrocatalyst which produces the gas would possibly be able to reduce the hydrogen and release the electrons, the physical presence of bubbles in a system could lead to a fault as well as the presence of localised explosive hydrogen gas.

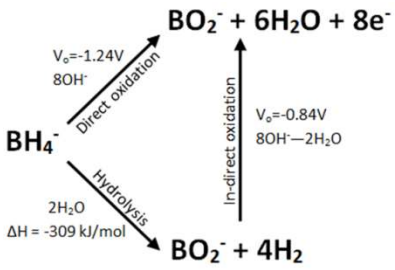

Equation 2.7 - Both the direct and in-direct oxidation of borohydride [57].

The oxidation pathways shown in Equation 2.7 are very simplified. In practice, the reaction mechanism is complex with different mechanisms and intermediates varying with depending on the electrocatalyst used [58].

Most electrocatalysts that can oxidise borohydride will do so via both pathways though research has been conducted to drive the reaction towards the direct oxidation pathway. Borohydride is commonly used as a hydrogen store and so materials are being developed to release as much of the hydrogen from the borohydride as possible with minimal further oxidation occurring. The desired electrocatalyst for DBAFC would be one that would progress exclusively through the direct oxidation pathway, such as gold. Gold has been known to progress through the direct oxidation pathway with minimal indirect oxidation occurring; however, challenges over its cost make it difficult to commercialise.

2.3.4.4 *Sodium Metaborate Recycling*

The oxidation product of sodium borohydride is sodium metaborate ($NaBO_2$), as seen in Equation 2.7. Research into recycling sodium metaborate back into sodium borohydride has begun due to the increased use of sodium borohydride in hydrogen storage and the potential for boron deposits to decrease and the increased cost of producing sodium borohydride. Sodium borohydride, as in the case of this thesis, can be used as a fuel and the potential for recycling or recharging this fuel would lead to new possibilities for using DBAFC in portable electronics. Methods for borohydride recycling include electrochemically reducing the sodium metaborate on precious metal electrodes, annealing sodium metaborate with manganese compounds under high temperatures and hydrogen pressures as well as the use of manganese hydride and other hydrides with reasonable success [47, 59, 60]. Other methods involve ball milling, thermal and electrochemical synthesis [61, 62]. Although good yields of over 95% have been produced at high temperatures and pressures, with low temperature methods producing much lower yields over long periods of time it makes recycling sodium borohydride difficult when used for portable electronics applications which this thesis is focused on. However, should DBAFC be used in the automotive industry these higher yielding methods could be used to recover borohydride from spent fuel when recovered from a vehicle.

2.4 Other Types of Fuel Cells

Several types of fuel cells are being developed for a variety of applications. These may be differentiated based on the nature of the electrolyte used. This section reviews the more common types of fuel cells and details the technology they employ, together with some of the advantages and challenges for each type.

The majority of the fuel cells discussed here use hydrogen as the fuel, with the exception of high temperature solid oxide fuel cells which utilise hydrocarbons such as methane [63].

2.4.1 Proton Exchange Membrane Fuel Cells

Proton exchange membrane fuel cells (PEMFC) were originally developed by General Electric in the early 1960's and use an acidic electrolyte immobilised in a gel matrix such as Nafion®, a proton-conducting polymer electrolyte which consists of a long hydrophobic fluorinated carbon chain with a cationic functional group such as a sulfonium ion. The proton generated by the oxidation of hydrogen in an acidic electrolyte (see Equation 2.8) is preferentially transferred from one of the cations in the polymer chain to another, allowing the transfer of protons from the anode to the cathode. Benefits of using a ridged polymer electrolyte include ease of fuel cell orientation and making the fuel cell lighter and more portable. Furthermore, PEMFC can be used between low (60 - 80 °C using Nafion® based membranes) and medium (110 - 180 °C using Nafion® composites or phosphoric acid doped polybenzimidazole membranes) temperatures [64]. However, the membrane may become degraded over time and when exposed to elevated temperatures.

Anode: $$H_2 \rightarrow 2H^+ + 2e^-$$

Cathode: $$\frac{1}{2}O_2 + 2H^+ + 2e^- \rightarrow H_2O$$

Equation 2.8 - PEMFC redox reaction equation.

2.4.2 Molten Carbonate Fuel Cells

Unlike other fuel cells where carbonate formation can be detrimental to the fuel cell performance, the molten carbonate fuel cell (MCFC) uses carbonates as their charge carrier. The carbonates, which are solid at room temperature, become a liquid at approximately 650 °C and allow for the charge transfer between the electrodes. The liquid carbonate, which is usually a mixture of lithium and potassium carbonates, saturates a porous ceramic matrix composed of lithium aluminate [65]. The increased operating temperatures allow the use of non-precious metal electrocatalysts and the generation of hydrogen within the fuel cell from methane to further reduce costs. However, the high operating temperature of MCFCs means

the electrodes suffer from poor stability as well as challenges regarding low power densities [64].

$$\text{Anode:} \quad CO_3^{2-} + H_2 \rightarrow H_2O + CO_2 + 2e^-$$

$$\text{Cathode:} \quad CO_2 + \frac{1}{2}O_2 + 2e^- \rightarrow CO_3^{2-}$$

Equation 2.9 - MCFC redox reaction equation.

2.4.3 Phosphoric Acid Fuel Cells

Phosphoric acid fuel cells (PAFC) use an acidic electrolyte similarly to PEMFCs and hence exploit the same redox reaction (see Equation 2.8). Unlike PEMFCs, PAFCs employ a liquid phosphoric acid (H_3PO_4) electrolyte and operate at high temperatures of around 200 °C [16]. Phosphoric acid displays better stability to carbon dioxide compared to other fuel cells and allows for simple water management due to the liquid electrolyte, which allows the addition or removal of water relatively simple compared to a gas reductant. While the lack of membrane removes the issues associated with membrane degradation, the overall weight of the fuel cell is increased. Additionally, as with PEMFCs, PAFCs require the use of expensive precious metals which increase costs.

2.4.4 Solid Oxide Fuel Cells

As the name suggests, solid oxide fuel cells (SOFC) uses a solid electrolyte to separate the electrodes. The electrolyte is a ceramic material, typically yttria-stabilised zirconia, which conducts charge using a similar mechanism to the MCFC. SOFCs also operate at high temperatures of approximately 600 - 1,000 °C depending on the support. An SOFC can contain a thick electrode or electrolyte component which gives the whole fuel cell structure [23, 66]. Anode electrocatalysts for SOFC are typically non-precious metals immobilised on a conductive ceramic substrate with cathodes consisting of conducting ceramics. SOFC are capable of high electrical efficiencies and offer fuel flexibility but suffer from durability issues and slow start-up times [64].

Anode: $2H_2 + 2O^{2-} \rightarrow 2H_2O + 4e^-$

Cathode: $O_2 + 4e^- \rightarrow 2O^{2-}$

Equation 2.10 - SOFC redox reaction equation.

There are many other fuel cell types, all with their own advantages and challenges. However, the relatively less developed DBAFC has the potential for high power outputs, when the borohydride is fully utilised, and can potentially be supplied from renewable sources. As such, the various strengths and current issues need to be identified, not just from an upstream perspective but for commercialisation. This work explores and develops methods for the commercialisation of borohydride fuel cells, from the electrocatalyst and electrode manufacture through to the stack and system design.

3 Anode Electrocatalyst

3.1 Background

This chapter focuses on the development of a suitable anode electrocatalyst for a DBAFC. The slower kinetics of the oxygen reduction reaction (ORR) at the cathode compared to that of the hydrogen oxidation reaction (HOR) at the anode has increased the interest in the research of the former [67]. However, two main differences between DBAFC and other fuel cell types have made the study of anode electrocatalyst relevant to this project; the use of borohydride and fuel crossover.

Borohydride can undergo oxidation via two distinct mechanisms and can also undergo hydrolysis, making the specificity of the anode electrocatalyst a critical factor. Fuel crossover is experienced by membraneless DBAFCs and other membraneless fuel cells, in the DBAFC developed in this study, it results from the dissolution of borohydride in the electrolyte rather than being isolated from the cathode. This means that both electrodes require a degree of specificity to the reaction they sustain i.e. the cathode must only reduce the oxygen and not interact with the borohydride. Using previously developed materials for the cathode allows the focus on the anode development.

The use of an unoptimised electrocatalyst can result in low efficiencies due to poor fuel utilisation, high polarisation losses or electrocatalyst degradation. Pt has historically been considered one of the most catalytically active materials available with high kinetics for ORR and HOR [21] and has therefore been used as an electrocatalyst. Its high cost and poisoning by fuel by-products and impurities such as carbon monoxide, has meant that full commercialisation of the technology has proven difficult [68]. To overcome these issues, methods have been developed to increase its surface area and decreasing the amount of material required to help drive down costs. This may be readily achieved through low cost, electrically conductive carbon supports such as high surface area carbon blacks. Furthermore, the development of carbon monoxide-tolerant Pt-composites has helped increased the stability of Pt as a plausible electrocatalyst [69].

In this work, Pt was set as a baseline catalyst because of its fast kinetics for borohydride oxidation, although full efficiency realisation is hindered by the predominance of the indirect mechanism and subsequent hydrolysis. This allows the comparison of the activities of low cost alternative electrocatalysts.

3.1.1 Types of Anode Electrocatalysts

It has been shown that the rate determining step occurs at the cathode and that the lifetime of a fuel cell is dependent on the reaction taking place at the cathode. As a result, the majority of research in the development of AFCs has focused on this area [70], with pure noble metals such as Pt, Pd and silver (Ag) being investigated as the main electrocatalyst choices. Pt has been shown to be the most catalytically active with multiple fuels and consequently has been the most used material for both the anode and cathode [71]. However, increases in the cost of Pt make it increasingly difficult to make Pt based electrocatalysts commercially viable, with recent research focusing on the development of non-noble metal electrocatalysts showing similar levels of catalytic activity and hybrid materials involving noble metals. The latter can be produced by immobilising smaller precious metal particles onto the surface of carbon substrate while increasing the surface area of the exposed catalyst (Figure 3.1).

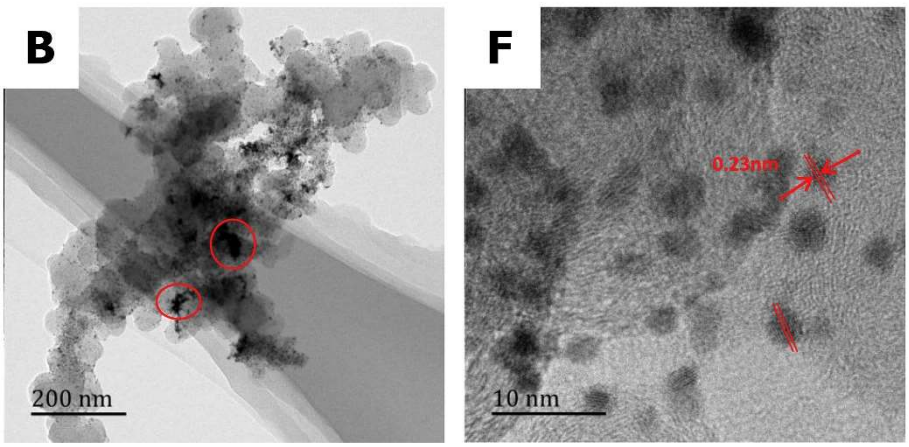

Figure 3.1 – Transmission electron microscopy of nano Pt on carbon black (Wang *et al.* [72]) highlighting particle agglomerates.

Electrocatalytic properties are dependent on the material, its particle size, loading and electrical conductivity. Precious metals, such as Pt, Pd and Ru, have been used extensively in

this work and immobilised on carbon black and activated carbon. This allows for improved kinetics, due to the increased active surface area, and a decrease in their cost. Other metals such as nickel (Ni) and gold (Au) have also been investigated. Pierre *et al.* [73] reviewed the DBAFC literature extensively and compiled a list featuring the electrocatalysts and setups used with the current and power density produced. The best DBAFC setups are discussed further in the electrode manufacturing chapter but highlighted in Table 3.1 are the leading Pt, Pd and Ru based electrocatalysts and their current densities.

Table 3.1 - Top performing DBAFC and their electrocatalysts [73-77].

Anode	Cathode	Separator	Reductant	Oxidant	T (°C)	P ($mW.cm^{-2}$)	j ($mA.cm^{-2}$)
Top Performing Setups							
Ni + Pd/C + Chitosan chemical hydrogel (CCH)	Pt/C	Chitosan binder (CS)	5 wt. % $NaBH_4$ in 10 wt. % NaOH	O_2	70	810	1680
Ni + Pd/C + Nafion + CCH	Pt/C	CS	5 wt. % $NaBH_4$ in 10 wt. % NaOH	Humidified O_2	60	685	1400
CoO powder + PTFE on Ni	$LaNiO_3$ + CNT	Poly Fibrous Membrane	0.8 M KBH_4 in 6 M KOH	O_2	65	663	1200
Top Pt, Pd and Ru Containing Anode Electrocatalyst Setups							
Ni powder + Pt/C + Zr-Ni AB alloy on Ni foam	$Co(OH_2)$-PPY-C	Nafion® 211	5 wt% $NaBH_4$ in 10 wt% NaOH	Humidified O_2	60	390	800
Ni + Pd/C + CCH	Pt/C	CS	5 wt. % $NaBH_4$ in 10 wt. % NaOH	O_2	70	810	1680
Pt-Ru/C (5 mg cm^{-2})	Pt/C	Polyvinyl alcohol	1 M KBH_4 in 4 M KOH	Humidified O_2	30	184	280

The literature data collected in Table 3.1 is based on full fuel cell setups which include the membrane used at a range of temperatures for a variety of anode electrocatalysts which makes comparing the results difficult. When comparing the electrocatalysts, the setups which produced the highest current densities use a combination of electrocatalysts. This indicates that there could be either a synergistic effect by using multiple elements, such as Ru is known to be used in conjunction with Pt to prevent CO poisoning and aid with borohydride oxidation [78]. The lack of single element electrocatalysts, which includes precious metals on carbons as the carbon is considered electrocatalytically inactive, may suggest that the development of an optimal DBAFC electrocatalyst may be more complex than evaluating various elements on the periodic table.

Fuel cell electrocatalysts include metal alloys [57, 79, 80], transition metal macrocycles [81-86], metal oxides [39, 87-93], ceramic perovskites and spinels (used as the cathode electrocatalyst for the work described in this thesis) [94-101], carbon doped with heteroatoms

[102-106], transition metal carbides and nitrides [107-113], transition metal chalcogenides (a transition metal with a group 16 atom) [114-118] and core-shell materials [119, 120]. This is by no means an exhaustive list. The design of an electrocatalyst specifically for the direct oxidation of borohydride presents a significant challenge that is out of scope for this work. For this reason, commercially available carbon-supported highly active precious metals have been evaluated for their electrocatalytic activity for direct borohydride oxidation.

3.1.2 Electrochemical and Physical Properties of Electrocatalysts

The performance of an electrocatalyst may be best assessed by considering its physical and crucially its electrochemical properties, which are often interlinked.

3.1.2.1 *Electrode Electrochemical Properties*

Catalysts play an important role in many chemical processes from synthetic chemistry to pharmaceuticals and polymer production to petroleum, where the catalyst accelerates or facilitate a reaction. An electrocatalyst is one that is specifically used for redox reactions of the general form shown in Equation 3.1.

$$Oxidant + ne^- \xrightarrow{electrocatalyst} Reductant$$

Equation 3.1 - A generic redox reaction between an oxidant, reductant and n number of electrons using an electrocatalyst.

Redox reactions involve the oxidation of a material, i.e. electron loss, coupled with a subsequent reduction of another material, i.e. electron gain. At equilibrium (no net electron movement), the potential difference between the electrodes is called the open circuit potential (*OCP*). For a DBAFC the redox reaction in alkali media is shown in Equation 3.2.

Anode:	$BH_4^- + 8OH^- \rightarrow BO_2^- + 6H_2O + 8e^-$	$E_a^0 = +1.24\,V$
Cathode:	$2O_2 + 4H_2O + 8e^- \rightarrow 8OH^-$	$E_c^0 = -0.40\,V$
Overall:	$BH_4^- + 2O_2 \rightarrow BO_2^- + 2H_2O$	$E_{cell}^0 = +1.64\,V$

Equation 3.2 - DBAFC redox reaction.

3.1.2.2 *Electrode Physical Properties*

The efficiency of the catalytic process and the overall electrode stability can be critically dependent on the electrocatalyst's physical properties and it is therefore of significant importance to characterise them accurately. Table 3.2 lists the main physical properties of interest and gives a brief definition while Figure 3.2 gives a graphical representation of the same concepts.

Table 3.2 - Table describing the different types of surface areas.

Surface Area Type	Description
Total Surface Area, A_{tot}	The area of the electrocatalyst including the support material, i.e. the surface area of Pt/C.
Real Surface Area, A_{rea}	The surface area of the electrocatalytically active material alone, i.e. the Pt on the Pt/C.
Active Surface Area, A_{act}	The electrocatalytically active surface area on the electrocatalyst material, i.e. sites on the Pt whereby electrooxidation occurs.
Geometric Surface Area, A_{geo}	The electrically conductive surface area of the electrode.

Each of the surface types listed in Table 3.2 influence the performance of the electrode in their own way. This is especially true for an increased active surface area (A_{act}) which increases the number of sites available to support the reaction, while an increased total surface area (A_{tot}) provides improved kinetics while reducing the overall amount of material needed and associated cost. To some extent, the active surface area is dependent on the real surface area (A_{rea}) although a cost-benefit analysis is required to limit the expense of producing such catalysts. In addition, the desired total surface area has important implications for the fabrication method. For example, the solvation of the catalyst is required for application purposes and a large A_{tot} requires an increase in the amount of solvent required to achieve this, decreasing the solid loading and increasing manufacturing costs. The geometric surface

area (A_{geo}) is the size of the deposited electrode and is used for calculating current density. This surface area is not a property of the electrocatalyst, but electrode produced and then electrode substrate which varies with the fuel cell application.

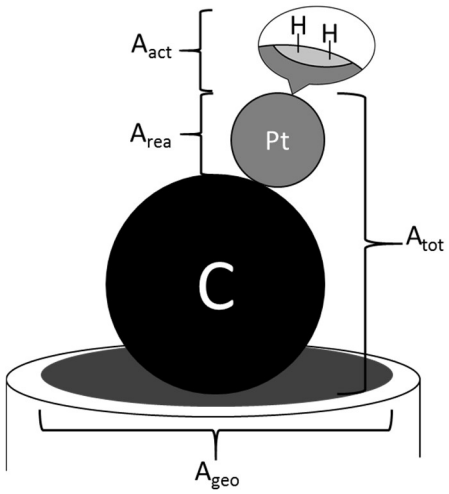

Figure 3.2 - A diagram depicting the different types of surface areas on a Pt/C (not to scale).

Unlike other types of fuel cells, due to the reductant borohydride being dissolved in the electrolyte, the boundary interfaces are different. Typically fuel cells have the reductant and oxidant on each side of the anode and cathode respectively whilst being separate by an, often solid, electrolyte. The use of a reductant dissolved in a liquid phase produces an electrode$_{(s)}$-electrolyte$_{(l)}$ double phase reactant boundary on the anode. In many fuel cells a double phase boundary is common, such as between the electrode$_{(s)}$-hydrogen$_{(g)}$ or anode$_{(s)}$-electrolyte$_{(l)}$. However, in a DBAFC the cathode has a triple phase boundary, electrode$_{(s)}$-electrolyte$_{(l)}$-air$_{(g)}$, shown in Figure 3.3. The double phase could potentially be relatively simple to produce as this only requires a porous electrode which allows the permeability of electrolyte through. However, the cathode is more complex as a balance between gas and electrolyte permeability would have to be achieved to create a high number of triple phase reactant boundary sites whilst preventing electrode weeping (the flooding of electrolyte through the back of the cathode).

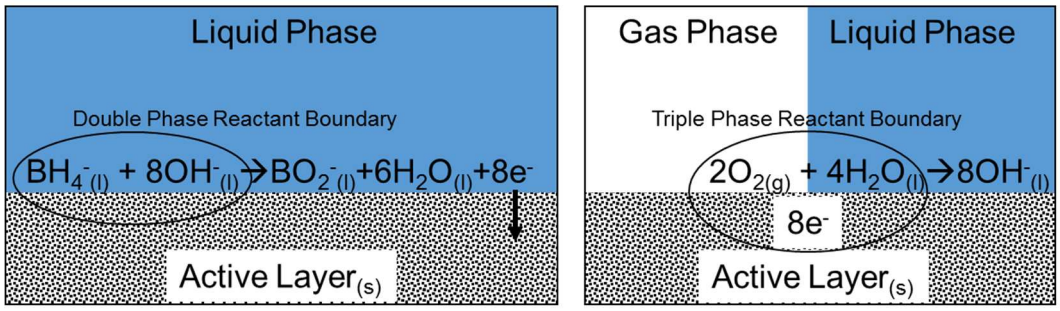

Figure 3.3 - Double phase anode (left) and triple phase cathode (right) reaction boundaries in a DBAFC.

There are numerous mechanisms involved in the generation of current at the electrocatalyst in a fuel cell. Convection is the flow of fluid resulting from mixing, in the case of DBAFCs, this applies to the borohydride-containing electrolyte between the electrodes and the air on the back of the cathode, and is controlled by the flow rate and design of the cell.

Variations in the concentration of borohydride (due to its consumption at the electrode surface) induce diffusion which is controlled by the Stokes-Einstein equation. The diffusion coefficient for borohydride in sodium hydroxide media has been determined by Chatenet *et al.* [121] (being 2.59×10^{-9} $m^2.s^{-1}$). Diffusion is also affected by the wettability and porosity of the electrode. Slow diffusion can lead to electrode starvation, reducing the current density generated, therefore a high diffusion coefficient is desirable. Migration occurs when a charged particle is transported due to the application of an electric field.

To ensure high efficiency of the fuel cell, many components must have a high electrical conductivity, limiting the use of some materials with high electrical resistance which would decrease the net current density generated. The exchange current density is the current density measured through the cell when no overpotential is applied. Ideally, the exchange current density would be high to generate as much current density as possible for the lowest overpotential. This property is controlled by the electrocatalyst, the electrode design (poor electrode design could potentially inhibit the electrocatalyst) and the chemicals used in the redox reaction.

The electrode structure plays a crucial role in determining the performance of a fuel cell and electrode structure properties which affect current density generation such as wettability, porosity, surface areas, electrical conductivity and pore size distribution must be studied. By optimising electrode materials, quantities and manufacturing process, the optimum electrode may be identified. This is discussed further in Chapter 4.

Understanding how these physical properties can impact the efficiency of the cell can help select and design a suitable electrocatalyst and electrode for a DBAFC.

3.1.3 Voltammetry

Voltammetric techniques are quick and simple methods that can be used to determine the kinetics of electrocatalysis (Figure 3.4). The setup requires a three electrode system which includes a working electrode (WE), the candidate material which is to be assessed and where a potential is applied, a counter electrode (CE), often made of Pt, and a reference electrode (RE). All electrodes are connected to a potentiostat which is used to control the potential of the cell and measure the current passed. The potential is applied between the working and reference electrodes. As the potential is swept, electrochemical reactions are triggered resulting in the generation of a current which is measured between the WE and CE.

To understand the effect of mass transport on an electrocatalyst, the amount of analyte flowing across the surface must be controlled. This may be achieved by using a rotating ring disc electrode (RRDE). The electrode is attached to a rotor/shaft which rotates at a controlled speed. The speed of rotation affects the mass transport of the electrolyte to the electrode and therefore the current density measured. This process is described by the Levich Equation (Equation 3.3).

As the potential is applied, an electrocatalyst with slow kinetics generates the peak current density at a larger overpotential compared to one with fast kinetics. Fast kinetics result in high current densities at low overpotentials, i.e. the potential applied past the *OCP*, which is beneficial in fuel cells as this increases the overall power output and potentially helps reduce electrode degradation.

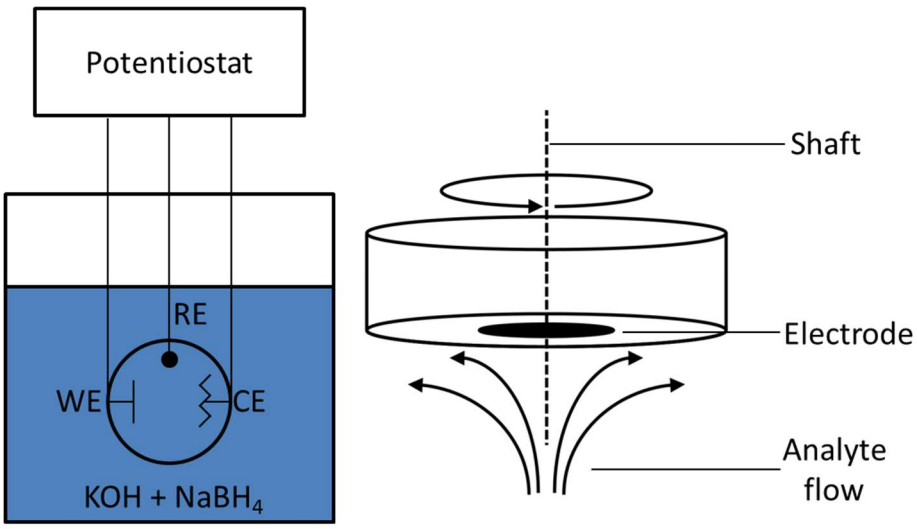

Figure 3.4 – Potentiostat electrode in analyte (left) and the flow of analyte across the RRDE during rotation (right).

Furthermore, the overall performance of the electrocatalyst can be evaluated by the magnitude of peak currents produced, with the desired electrocatalyst producing high currents at low overpotentials. Often, the current is converted to current density whereby the current produced is normalised using the A_{geo} which makes it simpler to compare different electrode systems. This also relates to the *OCP* of the electrocatalyst and the difference between the theoretical *OCP* (OCP_{theo}) and the measured *OCP* (OCP_{real}) whereby the OCP_{theo} is the *OCP* calculated based the reaction thermodynamics whilst the OCP_{real} is the *OCP* measured during experimentation/operation. The OCP_{theo} assumes that all the reactants are converted to products, including electrons, and experiences no losses. However, this is never the case as some losses are always experienced and often heat is produced as a by-product, reducing the OCP_{theo} to the OCP_{real}. The ideal electrocatalyst would have an OCP_{theo} equal to the OCP_{real} to obtain the maximum current density available. By identifying the *OCP* of a redox reaction, the point at which no current is generated, this can be used as a measure of an electrocatalysts performance.

3.1.3.1 *Levich Equation and Mass Transport*

The Levich equation (Equation 3.3) can be used to calculate important characteristics such as Levich peak currents (j_L), diffusion coefficients (D) and the number of electrons (n) being transferred using Faraday's constant (F), kinematic viscosity (v), rotational frequency (f) and

analyte concentration (c). The latter is of particular interest as it can be used as an indication of the efficiency of the material as an electrocatalyst. For example, if the oxidation reaction involves 8 electrons, such as in the theorised direct oxidation of borohydride [58], a calculated electron transfer value of 4 could be thought as having an efficiency of 50 %.

$$j_L = 1.554.n.F.D^{\frac{2}{3}}.v^{-\frac{1}{6}}.f^{\frac{1}{2}}.c$$

Equation 3.3 - The Levich equation [122].

This model can only be used when there is a constant flow of analyte across the electrode's surface, i.e. a constant rotation rate, and when the peak has plateaued (i.e. mass transport limit has been reached and the kinetics of the electrochemical reactions are controlled by the amount of analyte supplied to the electrode's surface). If this is the case, doubling the rotation rate will increase the peak current density by a factor of √2.

Another equation which can be used to assess the properties of an electrocatalyst, which is linked to the Levich equation, is the Koutechy–Levich equation shown in Equation 3.4 [123].

$$\frac{1}{j} = \frac{1}{j_K} + \frac{1}{j_L}$$

Equation 3.4 – The Koutechy–Levich equation whereby j_K = kinetic limited current density and j_L = mass transport limited current density.

Using the Koutechy-Levich equation, one can determine whether the electrocatalyst is limited by mass transport or kinetics. Essentially, the Koutechy-Levich equation attributes the variation between the measured current density and the Levich peak current density (or mass transport limited current density) as the effect of kinetic factors, known as the kinetic limited current density.

3.2 Methods

3.2.1 Cyclic Voltammetry

Cyclic voltammetry (CV) experiments were used to determine the electrochemical and physical characteristics of various electrocatalysts. This was achieved by depositing a suspension of the candidate electrocatalyst, onto a RRDE. The cyclic voltammogram was then recorded in the selected electrolyte, potassium hydroxide in deionised water ($KOH_{(aq.)}$), and analyte, sodium borohydride ($NaBH_{4(s)}$).

KOH was dissolved in DI water to produce the carrier electrolyte solution of a concentration 3 and 6 M $KOH_{(aq.)}$. 0.01 to 1 M analyte/reductant, sodium borohydride ($NaBH_4$), was dissolved in the carrier electrolyte. Both were produced at varying concentrations throughout the DBAFC development.

The electrocatalyst suspension was produced as follows:

1. 1 g Isopropyl alcohol (IPA, Sigma Aldrich) and 0.5 g electrocatalyst were mixed in a glass vial and sonicated for 10 minutes.
2. 1.05 g of IPA-electrocatalyst mix was pipetted into another glass vial and 0.1 g of Nafion® 1100 EW (Sigma Aldrich) was added. The resulting mix was sonicated for an additional 10 minutes.

The likely degradation of Nafion® in the suspension over time whilst in the suspension led to the preparation of fresh suspension every 5 days. Deposition of a thin uniform layer of electrocatalyst suspension was achieved by spin coating 5 µL of the suspension directly onto the RRDE while rotating it at 500 rpm for 20 minutes.

The prepared RRDE was mounted onto the rotor (Pine) and connected to the potentiostat (CompactStat, Ivium). All three electrodes (with the WE consisting of a glassy carbon disc and Pt-ring geometric surface area of 0.2475 and 0.1866 cm^2 respectively) were then submerged in the electrolyte Figure 3.5.

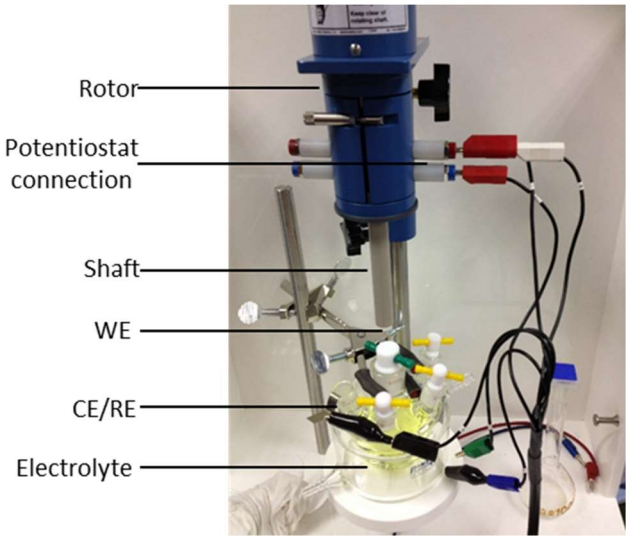

Figure 3.5 - Pine RRDE used to evaluate candidate electrocatalysts.

The hydrolysis of borohydride in the presence of the electrocatalysts lead to the production of hydrogen gas at the electrode surface, impeding electrolyte access (Figure 3.6).

The hydrogen bubbles formed remained trapped at the electrode surface and cannot be removed even at high rotation speeds (> 3,000 rpm). When this situation arose, the electrolyte container was moved manually, using a gentle swirling motion, to dislodge the trapped gas from the electrode surface.

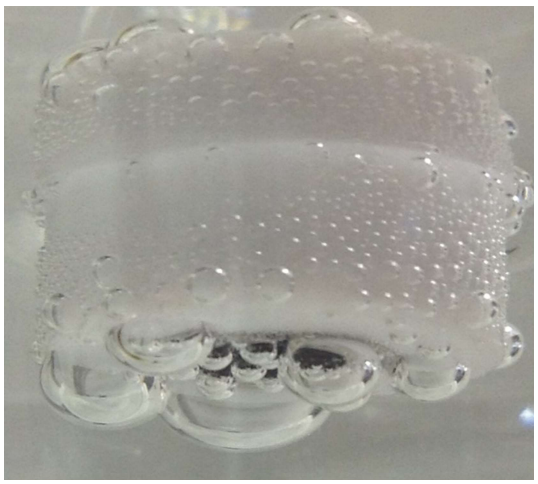

Figure 3.6 - Photo of hydrogen being generated during a voltammetry experiment and blocking access to the electrode.

3.2.2 Active Surface Area Determination using Underpotential Deposition of Hydrogen, H_{UPD}

Determining an electrocatalyst's surface area may be conducted electrochemically by measuring the adsorption and desorption of a monolayer of hydrogen atoms on the active surface of the material (A_{act}). This method replicates the environment of the electrode when used in the fuel cell setup and presents advantages over temperature/pressure based isotherms such as ChemBET. In this method, a CV was recorded at the candidate electrocatalyst on the RRDE substrate in a 0.5 M H_2SO_4 electrolyte at a scan rate of 50 $mV.s^{-1}$. Each peak in the voltammogram corresponds to a hydrogen interaction. Hydrogen adsorption results in peaks in the range -0.25 to 0.05 V (SCE). The active surface area of the electrode may be calculated from the charge passed from the H_2 adsorption process, which itself may be determined by the integration of the current-time curve (assuming a monolayer of $H_{2(ads)}$ gives a charge passed of 210 µC cm^{-2} [124]).

The active surface area of candidate electrocatalysts was measured before a series of CV experiments to determine electrocatalyst performance, followed by a repetition of the active surface area measurement. Any decrease in A_{act} was then attributed to the experimentation conducted to determine the electrocatalyst's performance. However, it must be noted that the nature of the experiment meant that measuring A_{act} may have decreased it.

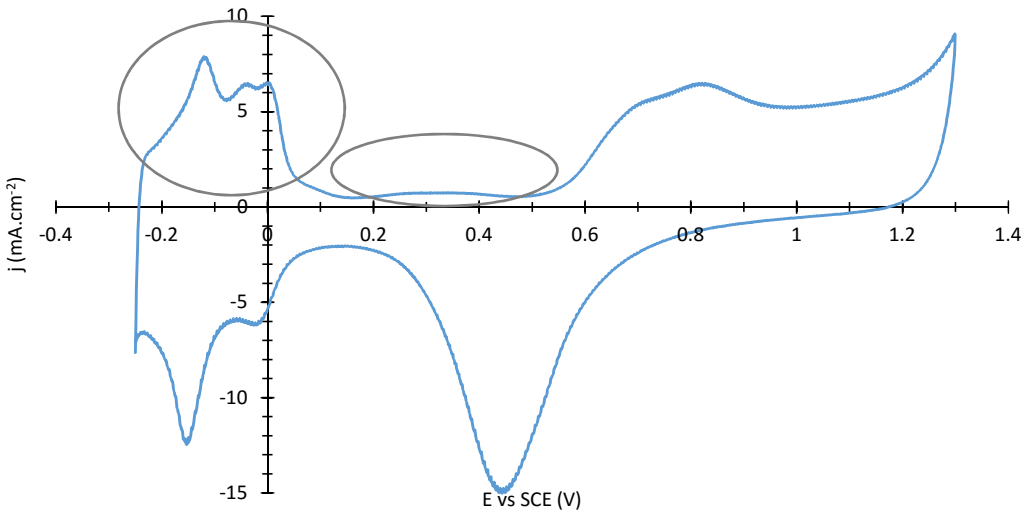

Figure 3.7 - Full voltammogram of the HUPD of 50 % Pt/C_b in 0.5 M $H_2SO_{4(aq.)}$ at 2,000 rpm and 50 $mV.s^{-1}$.

3.2.3 Deposition of Metals on Carbon Black

To compare the effect of different material loadings on the electrooxidation of borohydride, as well as performance with activated carbon (C_a), different weight percentages of Pd on carbon black (C_b) were assessed. However, Pd/C_b wasn't commercially available and was produced as follows:

- 0.641 g palladium (II) nitrate hydrate (~39% Pd, $PdN_2O_6.xH_2O$, Alfa Aesar) was dissolved in 20 mL nitric acid (Sigma Aldrich).
- 4.75 g Carbon black (Cabot Vulcan XC72R, 5wt. %) was then added to the solution.
- It was then mixed in a planetary centrifugal mixer (Thinky Mixer ARE-250) for one minute at 2,000 rpm.
- The Pd-C slurry was then decanted into a beaker and heat treated at 80 °C for 4 hours followed by 150 °C for 2 hours and 300 °C for 1.5 hours, resulting in the deposition of Pd onto the carbon black surface.

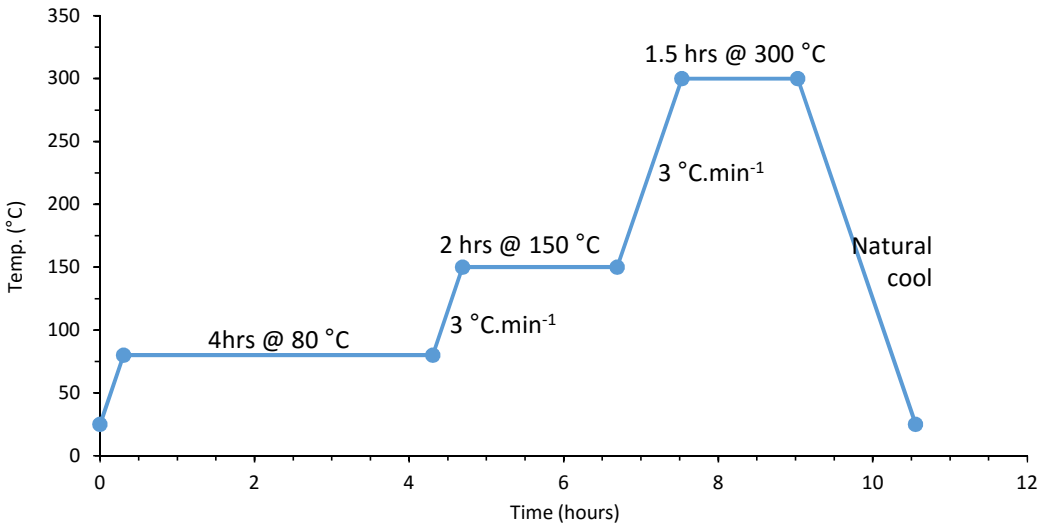

Figure 3.8 - The thermal treatment of metal deposition on carbon.

3.3 Results

Various methods were developed and used to evaluate the electrocatalyst's performance towards the BOR which is described in this section.

3.3.1 Method Development

3.3.1.1 *Effect of Experimentation on Electrocatalyst*

During the investigation into an appropriate CV potential range, a characteristic in the scan profiles was identified (shown in Figure 3.9). Although the literature has used ranges a large as -1.042 – 0.558 vs SCE [125], the lower the overpotential, i.e. the smaller the potential range, the more current can be drawn from the fuel cell. This indicated that there was an effect on the electrocatalyst by the experimentation used. Should the use of CV, and its associated potential range, be used as a method to evaluate candidate electrocatalysts, the effect of the experimentation on the electrocatalyst, specifically any decrease in A_{act} due to continuous redox cycling, had to be determined.

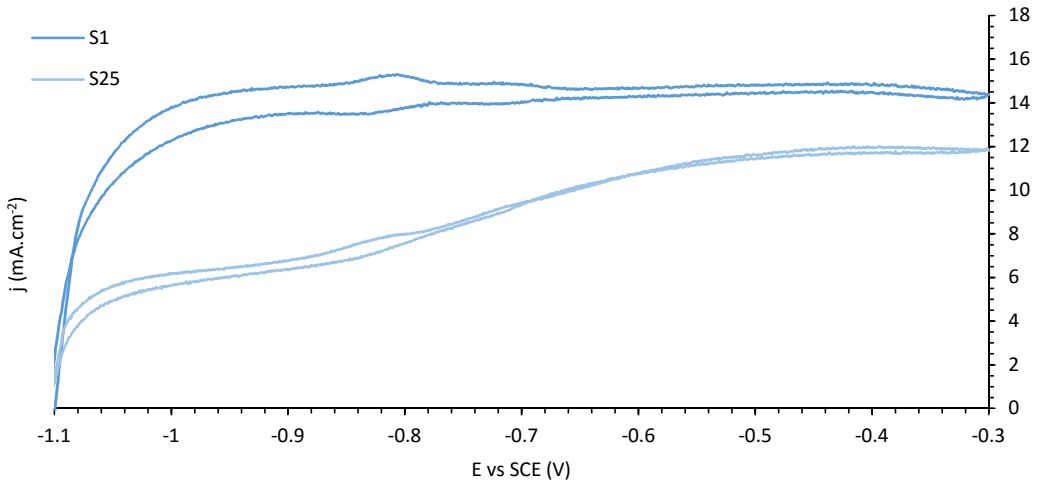

Figure 3.9 - Voltammogram showing the decrease in current density with scan number (scan 1 and 25) of 50 % Pd/C_a at 2,000 rpm and 5 mV.s^{-1} in 10 mM NaBH4/3M $KOH_{(aq.)}$.

To determine the effect of experimentation on the electrocatalyst with respect to the current density degradation, the A_{act} was measured before and after a Pt electrode was used in a CV scan. The active surface area of a 50 % Pt/C_b catalyst was measured in sulfuric acid, followed by a CV (25 scans) in 10 mM $NaBH_4$/3M $KOH_{(aq.)}$, before measuring A_{act} again. This was repeated at two different rotation speeds to determine if the results varied with mass transport. A higher material loading of 50 % Pt was chosen to ensure a higher initial A_{act} and enable straightforward observation of any decrease in this value. The voltammogram obtained from both the pre-CV and post-CV experiments are presented in Figure 3.10.

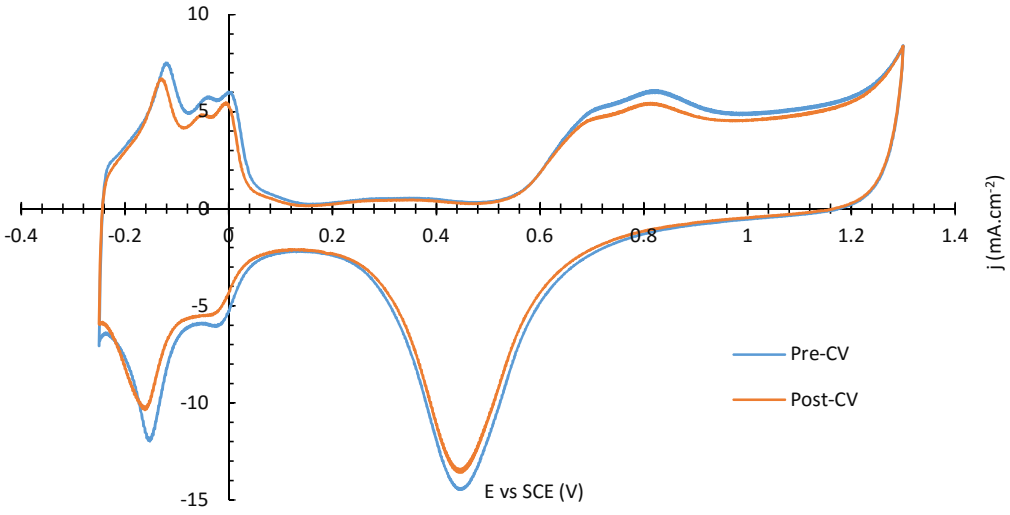

Figure 3.10 - Voltammogram of 50 % Pt/C_b in 0.5 M $H_2SO_{4(aq.)}$ at 1,000 rpm and 50 mV.s^{-1} before (pre-) and after (post) CVs.

Isolating and integrating the hydrogen adsorption peaks (Figure 3.11) give the amount of charge passed which is then converted into the electrochemically active surface area, A_{act}.

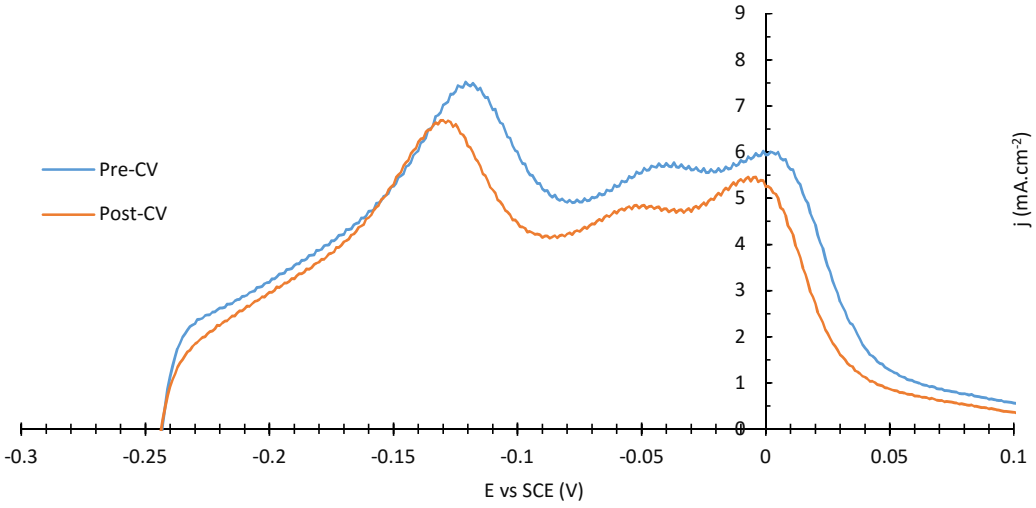

Figure 3.11 - The hydrogen adsorption region of the H_{UPD} of 50 % Pt/C_b in sulfuric acid from Figure 3.10.

The adsorption peaks show that there was a decrease in the A_{act} of the 50 % Pt/C_b electrocatalyst, as shown by the reduction in the three hydrogen adsorption peaks in the voltammogram. This was then converted into A_{act} using the amount of charge passed per surface area, shown in Figure 3.12.

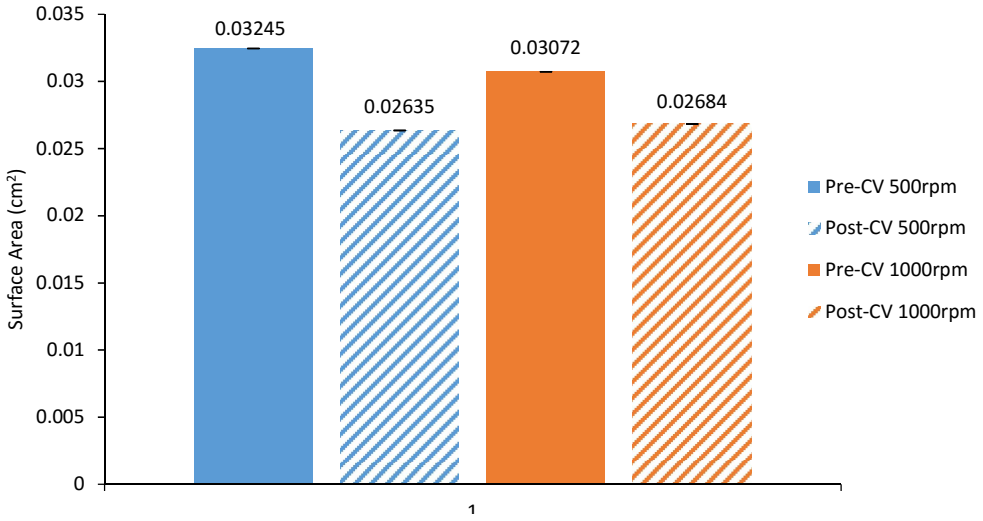

Figure 3.12 - The change in A_{act} due to experimentation taken from the integration of the hydrogen adsorption peaks at 500 and 1,000 rpm in 0.5 M $H_2SO_{4(aq.)}$ at 1,000 rpm and 50 $mV.s^{-1}$.

The results show a decrease in A_{act} of 19 and 13 % for 500 and 1,000 rpm respectively. This indicates that there is surface fouling on the Pt/C electrocatalyst surface. However, this does not indicate the cause of the fouling. i.e. the specific chemical species or mechanisms. The surface area obtained varied slightly with the pre-CV 1,000 rpm being 5 % less and the post-CV 500 rpm being 2 % less. This could be due to small variations in experimental conditions or the dissociation of the adsorbed hydrogen due to the higher rotation rate.

The surface area measurements show that the experimentation used to evaluate the candidate electrocatalysts can potentially alter and foul the electrocatalyst's surface. This was important to understand as the results suggest that fresh electrocatalyst and electrodes were required to get a true representation of an electrocatalyst's potential during the CVs. Continuous use of the same electrode over a series of experiments would degrade it, producing unreliable results.

3.3.2 Comparison of Electrocatalyst Suppliers

Nickel (Ni) has been used as a low cost non-noble alternative electrocatalyst in AFCs, and in DBAFC [33]. However, performances of Ni-based electrocatalysts are not yet comparable with precious metals. As such, Ni was not evaluated as a candidate electrocatalyst in this work

although due to it having some electrocatalyst activity it was used to assess the effect of different suppliers as a low cost alternative to using precious metal electrocatalysts. Several Ni electrocatalyst suppliers were assessed for their electrocatalytic activity towards the BOR. The manufacturing method of electrocatalysts can have a dramatic effect on their performance and it is necessary to investigate and compare each commercially available product. For this study, three Ni materials from different suppliers, Hongwu Nanometer (HN), Quantum Sphere (QS) and Skyspring Nanomaterials (SS), were deposited onto the RRDE and assessed by CV in 10 mM $NaBH_4$/3 M $KOH_{(aq.)}$. Although surface areas for the Ni electrocatalysts were unavailable, the particles sizes for HN, QS and SS were approximately 40, 25 and 60 nm respectively as given by the suppliers. Due to the electrocatalyst being in bulk form, the entire surface of the material could be considered active (i.e. $A_{tot} = A_{rea} = A_{act}$). As such, it could be theorised that the smaller the Ni particle size, the higher A_{tot} and the higher the A_{act} which would result in the order of A_{act} being SS < HN < QS. Thus, the QS Ni could be considered to potentially have the highest electrocatalytic activity. Their performance is shown in Figure 3.13.

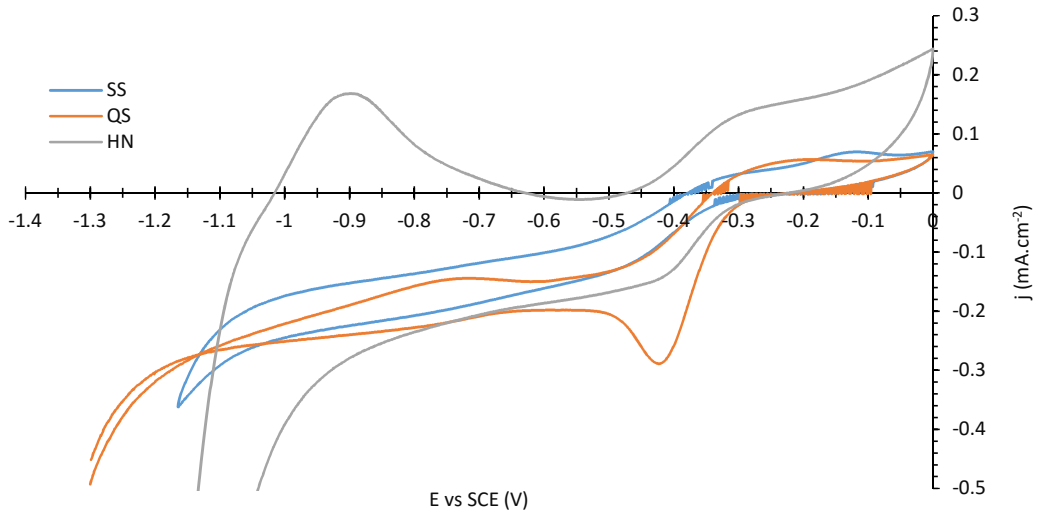

Figure 3.13- Comparison of different Ni suppliers at in 10 mM $NaBH_4$/3 M $KOH_{(aq.)}$ at 20 $mV.s^{-1}$ and 2,000 rpm.

Low peak currents were generated with QS and SS showing little or no catalytic activity. However, Ni from HN showed enhanced current density generation (Figure 3.13). Although the Ni has produced small currents compared to those observed at Pt electrocatalyst electrodes, the very low cost of the material allows for much higher material loading. To

enable further study of the HN Ni, another electrode was prepared and further CV was conducted in 1 M $NaBH_4$/3 M $KOH_{(aq.)}$. Increasing the amount of borohydride may have identified other processes which may have occurred.

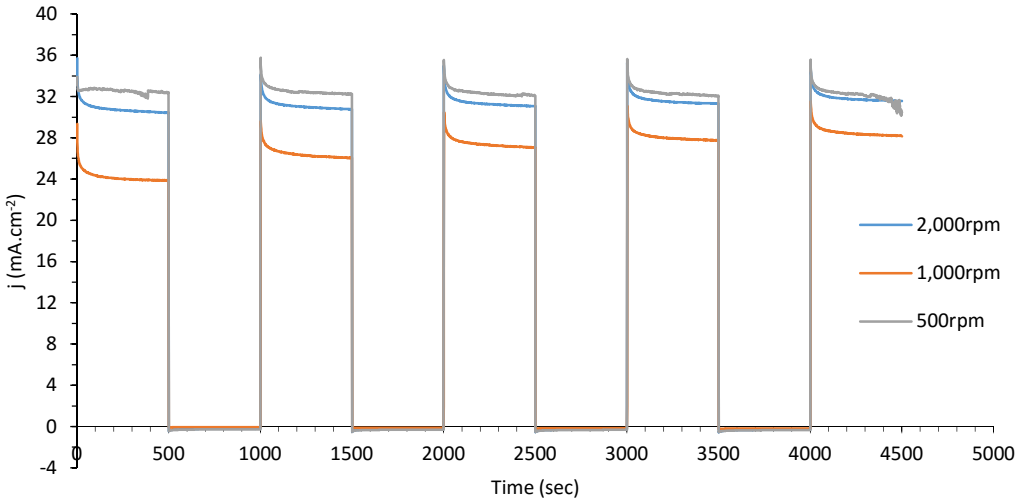

Figure 3.14 - Chronoamperometry of Ni (HN) in 1 M $NaBH_4$/3 M $KOH_{(aq.)}$ at variable rotation rates. The potential was switched between *OCP* and -0.8 V vs SCE continuously.

It appears that there was an unidentified layer, possibly nickel oxide, on the surface of the electrode. Applying a voltage generated a large current density peak (Figure 3.14) which deteriorated with progressive scans.

The results of this experiment showed that there was a difference between the different Ni electrocatalysts, which was suspected to be due to the different manufacturing methods used by the suppliers. In addition, the HN Ni showed layer being formed on the surface, as shown by the increase in current density generated after returning to the *OCP* in the chronoamperometry. This would indicate that the little current density being generated from the electrocatalyst was not due to the BOR, but the removal of the formed layer, making it unsuitable for the use as a DBAFC.

3.3.3 Platinum, Pt

As previously stated, Pt has long been known for its electrocatalytic activity towards oxidation of various fuels, due to its fast kinetics and increased current density production. Therefore, various electrochemical analyses were conducted on Pt in order to establish a "gold standard" with respect to current density generation under the conditions used in this work.

3.3.3.1 *Performance of 10 % Pt/C_a*

The performance of 10 % Pt/C_a was evaluated for the BOR using CV in 1 M $NaBH_4$/3M $KOH_{(aq.)}$ shown in Figure 3.15, whereby the potential was cycled four times, with each cycle being labelled as a scan. The 10 % Pt loading was used as a more commercially viable, from a cost perspective, electrocatalyst compared to the 50 % Pt. Other electrocatalysts evaluated in subsequent sections, including Ru and Pd, were not available from the same supplier on carbon black. As such, the Pt on activated carbon was evaluated to easily compare the effect of different precious metals (this is discussed in more detail in Section 3.3.3.4). The electrocatalyst was assessed for its kinetics and current generation properties in 1 M $NaBH_4$ as the large concentration of borohydride, and the fast 2,000 rpm rotation rate, would prevent the electrocatalyst from being starved of reductant, thus giving a true representation of the electrocatalytic activity.

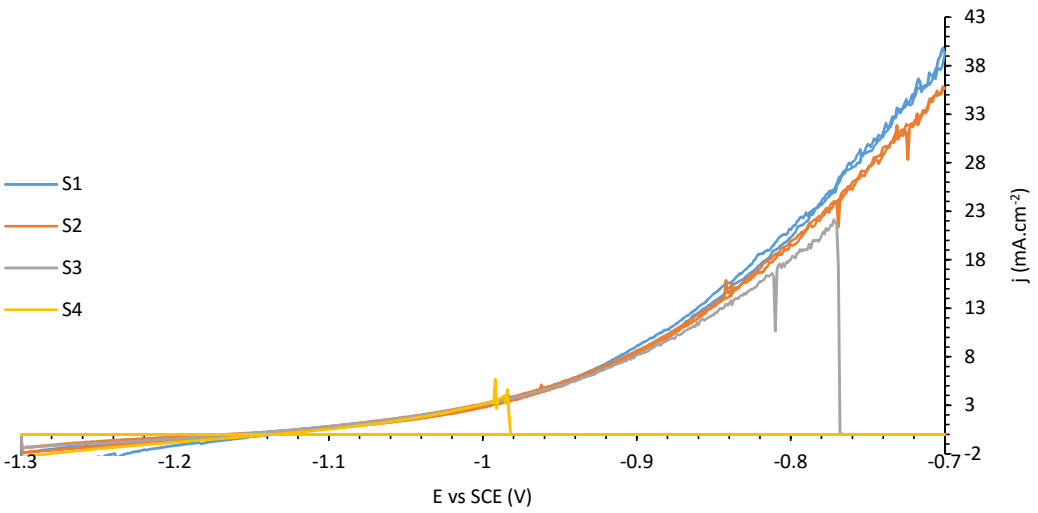

Figure 3.15 – Scans 1-4 of 10 % Pt/C_a in 1 M $NaBH_4$/3 M $KOH_{(aq.)}$ at 5 $mV.s^{-1}$ and 2,000 rpm (run 1).

The results from the first CV run (Figure 3.15) of the 10 % Pt/C_a shows significant levels of noise. Each run included four scans, for a given electrode. The high electrocatalytic activity of the 10 % Pt/C_a produced large amounts of hydrogen gas which was observed during the experiment. This may account for the noise shown in the CV plots. Furthermore, the generation of hydrogen bubbles could have potentially blocked the electrode surface, causing the current density dropping to zero. The experiment was repeated using the same electrode shown in Figure 3.16.

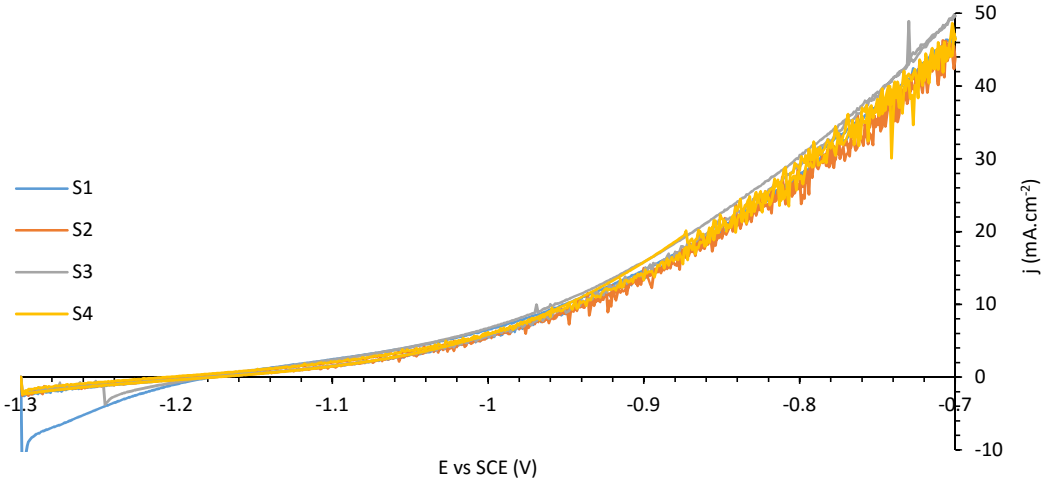

Figure 3.16 – Scans 1 – 4 of 10 % Pt/C_a in 1 M $NaBH_4$/3 M $KOH_{(aq.)}$ at 5 $mV.s^{-1}$ and 2,000 rpm (run 2).

The results of the second experiment (Figure 3.16) show similar peak currents but with slight noise reduction, as evident by the removal of parts of the CV plots generating zero current, such as that of scan 4. This could indicate that the surface was altered during the first run, producing a Pt layer which was slightly more electrocatalytically active. Comparing the results with the literature, Martins *et al.* [126], approximately 10 $mA.cm^{-2}$ at 0.7 V vs SCE was obtained in 39.68 mM $NaBH_4$/3 M $NaOH_{(aq.)}$ with a Pt rod. The work of Gyenge [125] shows that, at 0.7 V vs SCE in 30 mM $NaBH_4$/3 M $NaOH_{(aq.)}$ at 10 $mV.s^{-1}$, approximately no current density was produced using a Pt disc. Despite neither of the Pt-based electrocatalysts being on carbon, the plots produced in this work are more analogous to the work of Martins *et al.* as they show a similar trend to that produced in this work, with an increase in potential with no distinct anodic peaks. Other Pt-based electrodes have been researched in the form of fuel cell rig electrodes which have been summarised in Olu *et al.* with peak current densities of up to 890 $mA.cm^{-2}$ [73].

3.3.3.2 *Material Loading of Pt on Carbon*

Identifying the optimum material loading can lead to improved electron transfer kinetics while retaining cost effectiveness. This can be achieved by depositing small quantities of precious metal electrocatalyst on carbons, reducing the amount of precious metal (and therefore cost) whilst sustaining a high electrocatalytically active surface area.

Carbon is electrocatalytically inactive, with the activity arising from the metal deposited, in this case, Pt. The effect of Pt loading on peak currents was determined by investigating two percent weights; 10 and 50 wt. % (Alfa Aesar) in 1 M $NaBH_4$/3 M $KOH_{(aq.)}$ (Figure 3.17).

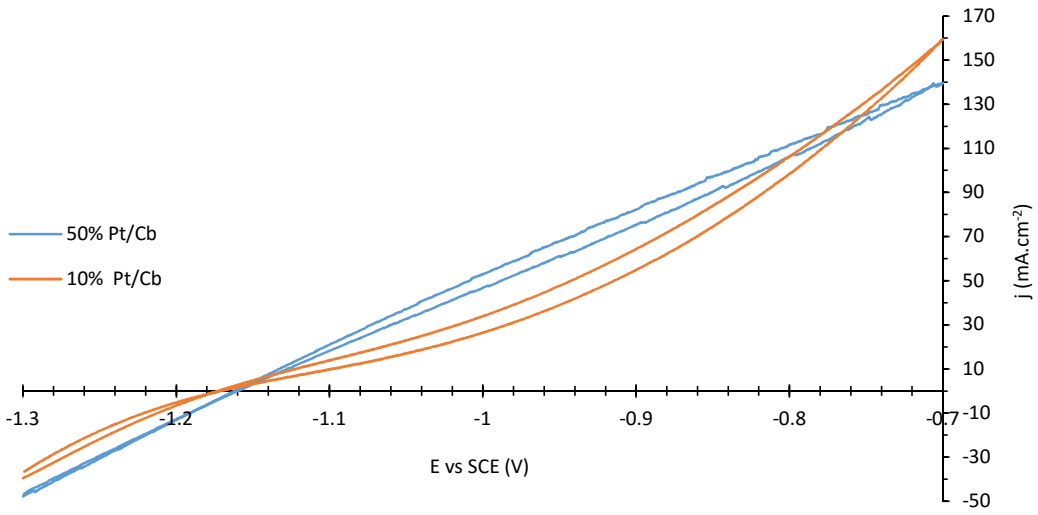

Figure 3.17 - Effect of Pt loading on current density in 1 M $NaBH_4$/$_3$ M $KOH_{(aq.)}$ at 5 $mV.s^{-1}$ and 2,000 rpm.

The results show that despite the five times increase in the amount of Pt, 50 % Pt/C_b performed only marginally better than 10 % Pt/C_b. The BOR initiates at approximately the same potential (-1.16 V vs SCE), the slope of the CV up to potentials of ca. -0.95 V shows improved kinetics for 50 % Pt/C_b while 10 % Pt/C_b generated a larger current density than that observed for 50 % Pt/C_b at larger overpotentials (> ca. -0.78 V).

Based on these observations and commercial availability of only two materials loadings, 50% Pt/C_b offers little performance enhancement for a large additional cost over 10% Pt/C_b. The latter was, therefore, the preferred electrocatalyst.

3.3.3.3 *Effect of Mass Transport on Electrocatalytic Activity of Pt*

Measuring the current density produced by electrocatalysts in 1 M $NaBH_4$ via CV allows for the broad evaluation of the electrocatalyst at conditions which may be more analogous to that used in a fuel cell. However, this is a very high concentration compared to the amount of electrocatalyst deposited on the RRDE and the effects of mass transport cannot be observed. Therefore, by repeating the experiment using a lower concentration and altering the rotation rate, one can control the flow of borohydride to the electrode's surface and thus determine the effect of mass transport. The experiment was performed using the potentiostat with a scan rate of 10 $mV.s^{-1}$ and -1.2 to -0.3 V vs SCE. A large potential range was used to identify any material behaviour that may occur and a fast scan rate was used as this to avoid any electrode degradation across the experiment.

At the higher potentials, > -0.7 V vs. SCE, one peak was observed indicating that only one significant process occurs. Having investigated the background behaviour of the support electrode, the same methodology was applied to 50 % Pt/C_b (Figure 3.18).

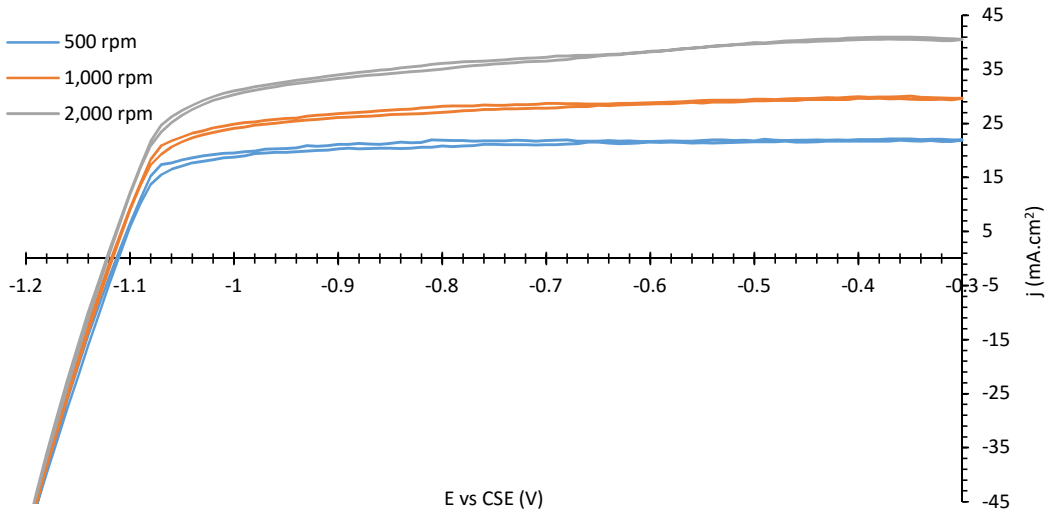

Figure 3.18 - Effect of mass transport 50 % Pt/C_b in 10 mM $NaBH_4$/3 M $KOH_{(aq.)}$ using a wide potential range.

The low observed overpotential and high associated slope for all rotation speeds shown in Figure 3.18 compared to the results presented in Figure 3.17 suggest that 50 % Pt/C_b, somewhat predictably, possesses significantly enhanced A_{act} and electrode kinetics. The plateau observed above -1.05 V vs SCE indicates that the mass transport limit was reached at low overpotentials.

50 % Pt/C_b shows high peak currents and fast kinetics under transport limited conditions. The high cost associated with such high loading electrocatalyst is a barrier to their adoption for energy generation applications. Furthermore, the overpotential observed in a fuel cell would be lower and no additional electrochemical processes of interest occur at higher overpotentials. 10 % Pt/C_a was evaluated using the same method for a lower potential window of -1.3 to -0.7 V vs SCE, as the overpotential would be more representative of typical fuel cell use and increasing the potential pass this range could potentially alter the electrocatalyst, skewing the results. The resulting voltammogram is shown in Figure 3.19.

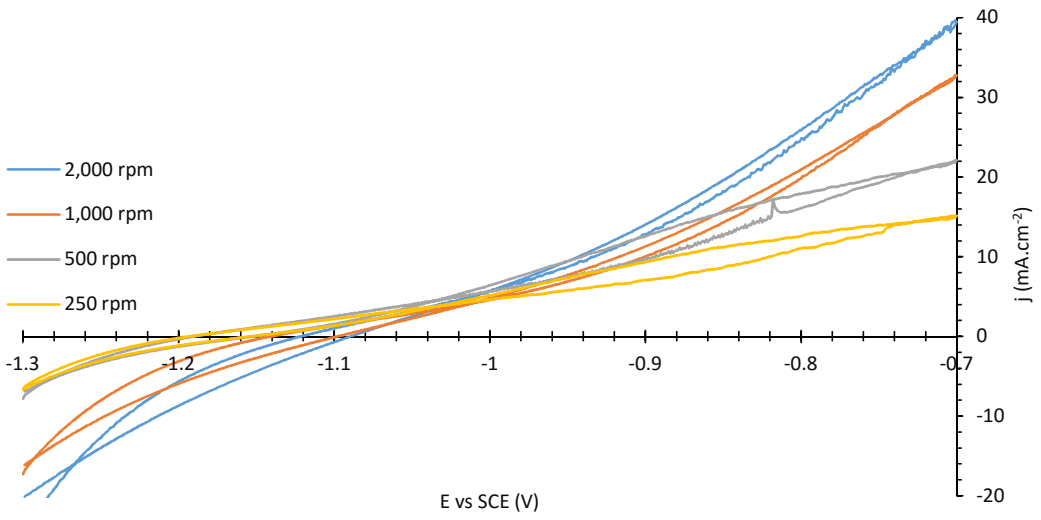

Figure 3.19 - Effect of mass transport on 10 % Pt/C_a in 10 mM $NaBH_4$/3 M $KOH_{(aq.)}$ at 5 mV.s^{-1} and 2,000 rpm.

10 % Pt/Cannot does not reach mass transport, which is required to use the Levich equation, rendering the calculation of the theoretical peak current density impossible.

Furthermore, both Pt/C electrocatalysts show a clear correlation between rotation rate suggesting both electrocatalysts capture the same number of electrons. In both cases, the electrocatalyst kinetics were fast and the current density was mass transport limited, further supporting the quality of Pt as an electrocatalyst.

These results indicate that using 10 mM borohydride at 500, 1,000 and 2,000 rpm, provides sufficient information to evaluate the effects of mass transport on electrocatalysts. It was found that increasing A_{act}, improves electron transfer kinetics and increases the observed current. Increasing electrocatalyst loading from 10 to 50 % Pt led to a modest increase in kinetics and no increase in peak current density at the highest potential measured, suggesting 10 % Pt loading was adequate for the use in DBAFC.

3.3.3.4 *Comparison of Pt on Carbon Black and Activated Carbon*

Carbon black and activated carbon can both be used as electrocatalyst supports. Carbon black has high electrical conductivity, larger particle size and surface area compared to activated carbon, leading to it being generally preferred as an electrocatalyst support. Nevertheless, electrocatalysts are often commercially available on an activated carbon support. It was, therefore, necessary to assess the performance of electrocatalysts manufactured using the same techniques on carbon black and activated carbon supports. A 10 % Pt/C loading was selected for both supports. Cyclic voltammograms were recorded in 1 M $NaBH_4$/3 M $KOH_{(aq.)}$ at 2,000 rpm and 5 $mV.s^{-1}$ (Figure 3.20).

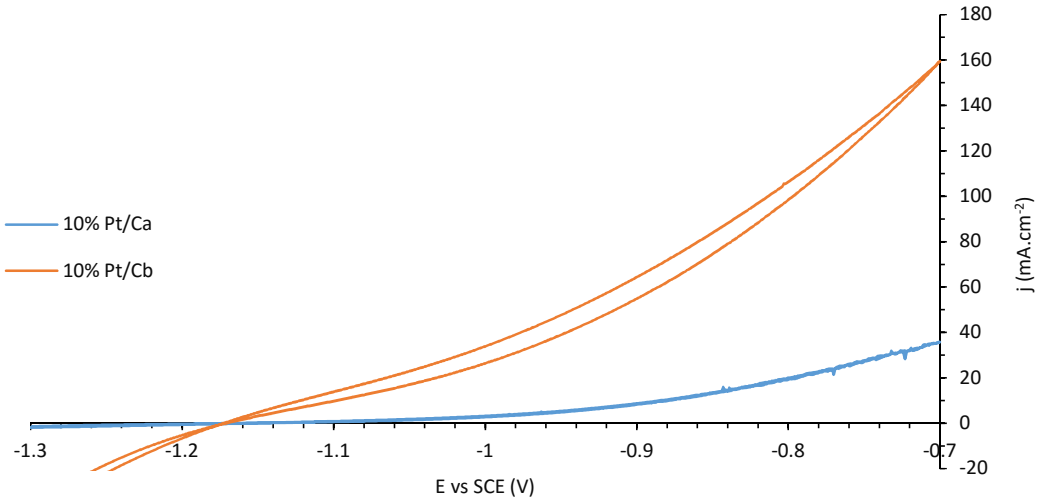

Figure 3.20 - Comparison of Pt on activated carbon and carbon black both supplied by Alfa Aesar in 1 M $NaBH_4$/3 M $KOH_{(aq.)}$ at 5 $mV.s^{-1}$ and 2,000 rpm.

From Figure 3.20, carbon black support offers enhanced electron transfer properties compared to activated carbon. This substantial increase may be attributed to the process method used to produce the electrocatalysts and suggest that manufacturing methods must be carefully considered when selecting an electrocatalyst. Unfortunately, the manufacturing methods for the electrocatalysts is not in the public domain so this cannot be confirmed.

3.3.4 Palladium, Pd

Pd is known to have some electrocatalytic activity towards HOR and is a lower cost precious metal alternative to Pt, presenting a potential cost saving in fuel cell manufacture.

3.3.4.1 *Performance of 10 % Pd/C_a*

The performance of 10 % Pd/C_a was evaluated for the BOR using CV in 1 M $NaBH_4$/3M $KOH_{(aq.)}$ shown in Figure 3.21 and Figure 3.22 (repeated twice).

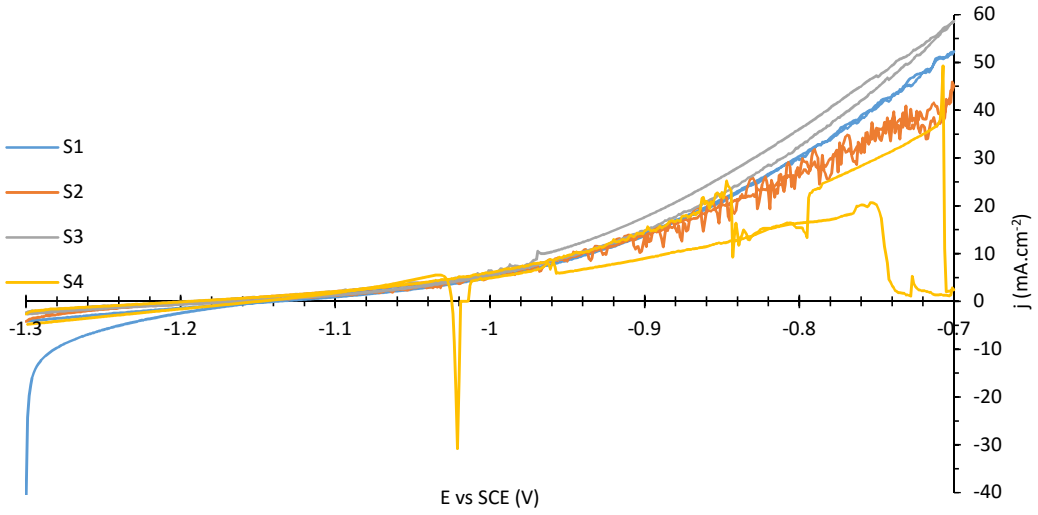

Figure 3.21 - 10 % Pd/C_a in 1 M $NaBH_4$/3 M $KOH_{(aq.)}$ at 5 $mV.s^{-1}$ and 2,000 rpm (run 1).

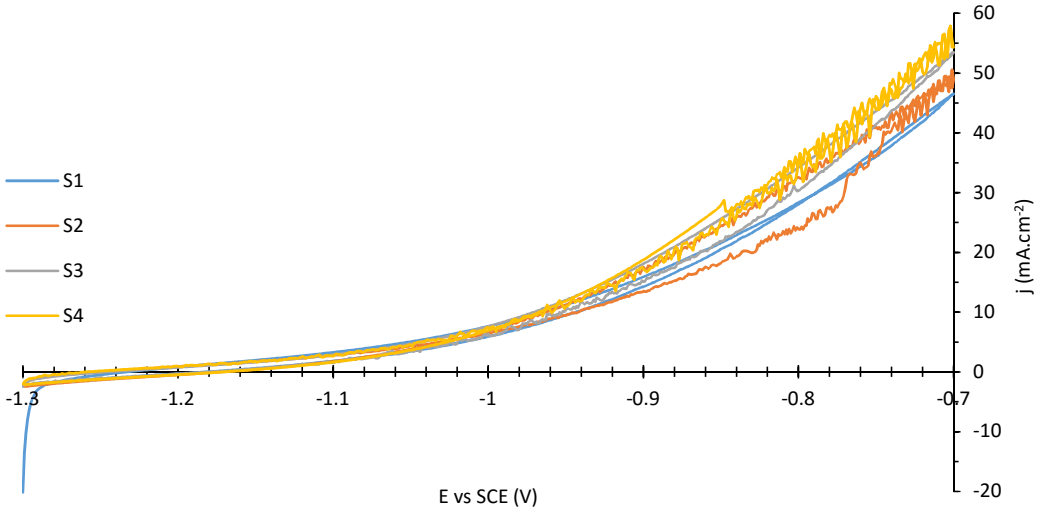

Figure 3.22 - 10 % Pd/C_a in 1 M $NaBH_4$/3 M $KOH_{(aq.)}$ at 5 $mV.s^{-1}$ and 2,000 rpm (run 2).

As with the 10 % Pt/C_a, the 10 % Pd/C_a shows a reduction in CV plot noise. This could also be due to the surface of the Pd being altered during the potential sweep or the adsorption of BOR by-products to the electrocatalyst surface. Scans 1 and 3 in the second run show smoother CV plots compared to scans 2 and 4. The generation of noise on the scan proceeding a smooth scan could indicate that surface modification of the electrocatalyst continues to happen due to the experimentation. The current also increases with the number of scans, which could indicate that the surface was becoming more electrocatalytically active. Alternatively, it could

show the oxidation of the surface; however, sodium borohydride is a strong reducing agent and it would be unlikely that surface could be oxidised whilst in its presence.

3.3.4.2 *Material Loading of Pd on Activated Carbon*

To compare material loadings and avoid using materials manufactured using different methods, materials available from a single supplier were selected; 1 and 10 % Pd/C_a (Alfa Aesar) were purchased. Electrocatalyst suspensions were produced using the method described in Section 3.3.1 and deposited on the RRDE. CVs were then recorded in 1 M $NaBH_4$/3 M $KOH_{(aq.)}$ (Figure 3.23).

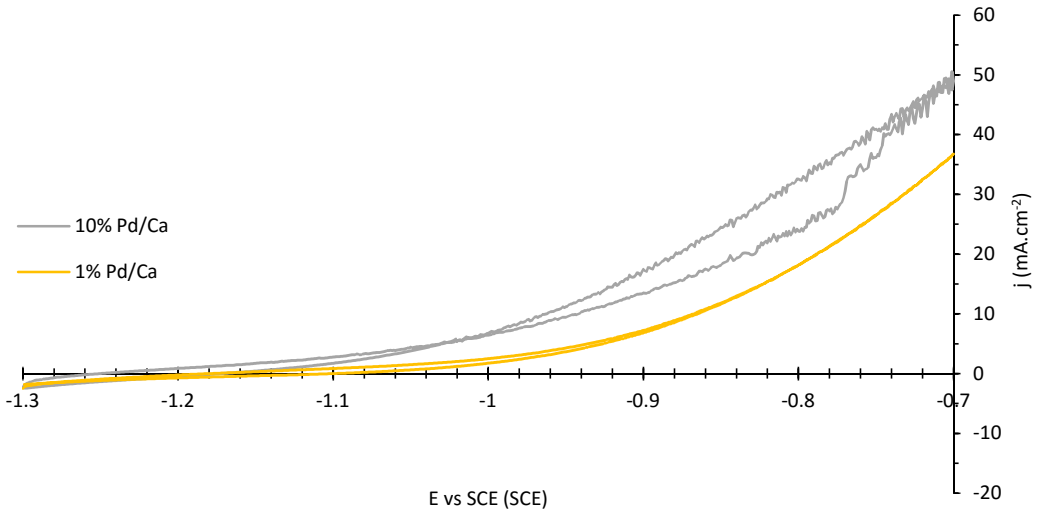

Figure 3.23 - The effect of Pd material loading on current density in 1 M $NaBH_4$/3 M $KOH_{(aq.)}$ at 5 $mV.s^{-1}$ and 2,000 rpm.

Table 3.3 - Peak current densities of 1 and 10 % Pd/C_a in 1 M $NaBH_4$/3 M $KOH_{(aq.)}$ at 5 $mV.s^{-1}$ and electrons transferred calculated based on the Levich equation.

Electrocatalyst	Measured Peak j ($mA.cm^{-2}$)	Electrons Transferred
10 % Pd/C_a	49.0	0.03
1 % Pd/C_a	36.8	0.02

The CV produced from the two Pd/C_a electrodes show that the kinetics and peak current densities produced increased with increased Pd loading. Furthermore, the 10 % Pd/C_a CV shows significant noise in comparison to the 1 % Pd/C_a. This could be due to the evolution of

hydrogen, as a by-product from the hydrolysis of borohydride. This is supported by the observation of significant amounts of hydrogen gas being generated, especially at high potentials. The peak currents generated at -0.7 V vs SCE produced 36.8 and 49.0 $mA.cm^{-2}$ for the 1 and 10 % Pd/C_a electrocatalysts respectively, representing an increase of over 37 %. This suggests that 10 % precious metal on carbon electrocatalyst appear to be a commercially viable electrocatalyst for a DBAFC.

3.3.4.3 *Effect of Mass Transport on Electrocatalytic Activity of Pd*

Mass transport studies were conducted on 10 % Pd/C_a due to its superior performance, following the methodology used for Pt based electrocatalysts, in 10 mM $NaBH_4$/3 M $KOH_{(aq.)}$. This produced the voltammogram shown in Figure 3.24.

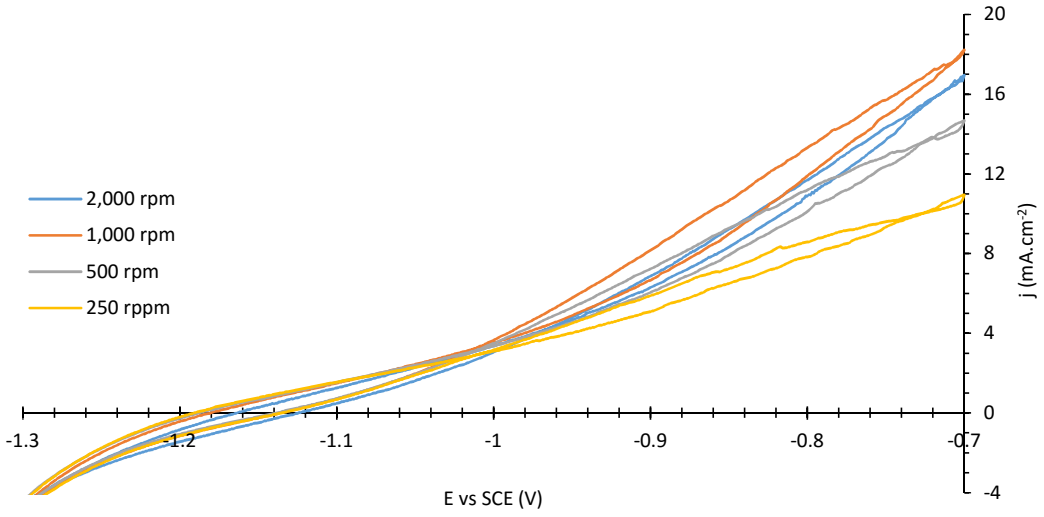

Figure 3.24 - Effect of mass transport on 10 % Pd/C_a in 10 mM $NaBH_4$/3 M $KOH_{(aq.)}$ at 5 $mV.s^{-1}$ and 2,000 rpm.

From Figure 3.24, the response of the electrocatalyst appears to be dependent on the rate of mass transport; however, the current density at -0.7 V does not satisfy the Levich equation (i.e. the current densities are not separated by √2). This is highlighted in Table 3.4 as, if the electrocatalyst was mass transport limited, the number of electrons would be the same and independent of the number of electrons transferred.

Table 3.4 - Peak current densities of 10 % Pd/C_a in 10 mM $NaBH_4$/3 M $KOH_{(aq.)}$ at 5 $mV.s^{-1}$ and electrons transferred calculated based on the Levich equation.

Rotation Rate (rpm)	Measured Peak j ($mA.cm^{-2}$)	Electrons Transferred
2000	17.0	1.1
1000	18.2	1.6
500	14.7	1.8
250	10.9	1.9

This could be due to two reasons; either the overpotential applied was not sufficient to separate the voltammograms or the reaction has slow kinetics [127].

3.3.4.4 *Pd on Carbon Black Production and Activated Carbon Comparison*

Carbon black-supported Pd electrocatalysts were prepared in house (see Section 3.2.3) and evaluated against commercially available activated carbon catalysts. Pd loadings of 1, 3 and 5 % were produced (see Section 3.2.3 for the method) were assessed using CV in 10 mM $NaBH_4$/3 M $KOH_{(aq.)}$, shown in Table 3.5 and Figure 3.25.

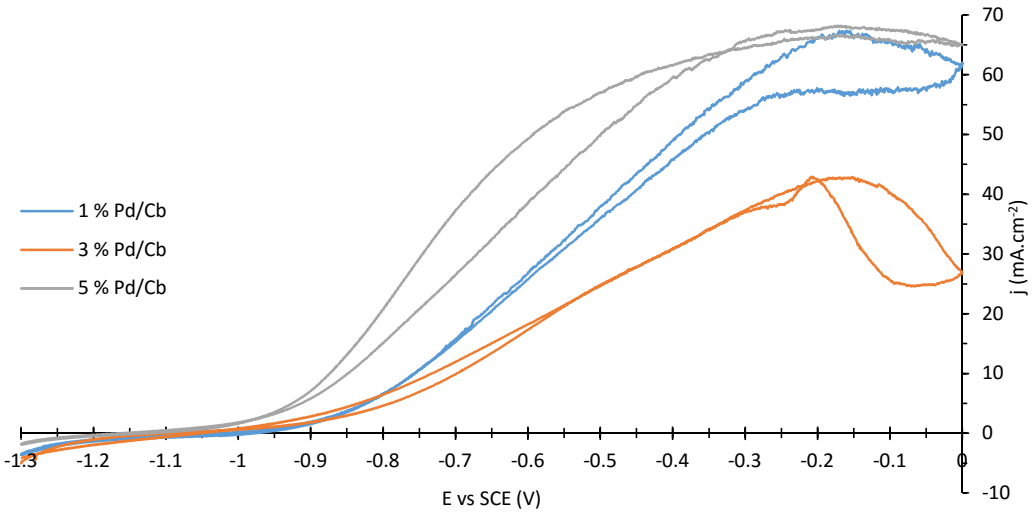

Figure 3.25 - Different Pd loadings on carbon black in 10 mM $NaBH_4$/3 M $KOH_{(aq.)}$ at 5 $mV.s^{-1}$ and 2,000 rpm.

Table 3.5 - Peak current densities (at -0.161 V vs SCE) of different Pd loadings in 10 mM $NaBH_4$/3 M $KOH_{(aq.)}$ at 5 $mV.s^{-1}$ and electrons transferred calculated based on the Levich equation.

Pd Loading (%)	Measured Peak j ($mA.cm^{-2}$)	Electrons Transferred
1	67.2	4.21
3	42.7	2.68
5	67.9	4.3

In Figure 3.25, 3 % Pd loading electrocatalyst showing both a lower current density and slower kinetics than the 1 % loading. This does not support the hypothesis of increasing the material loading would increase the current density being generated. This could be due variations in experimentation, either in the electrocatalyst manufacture or evaluation. It is suspected that the 1 % Pd should have had a lower performance compared to the 3 %. In the literature, using cyclic voltammetry, low Pd loadings have not been investigated (however, a wider range of Pd loadings have been investigated using fuel cell rigs [73]). Work conducted by Martins *et al.*[128] had a measured current density of approximately 0.01 $mA.cm^{-2}$ at 0 V vs SCE using a 25 % Pd/C_b in 30 mM BH_4/2 M $NaOH_{(aq.)}$ at 1000 rpm and 5 $mV.s^{-1}$, with the electrocatalyst being prepared using oleylamine (OAm)-mediated synthesis. Other work conducted by Grimmer *et al.* [129] obtained a current density of approximately 1.5 $mA.cm^{-2}$ at 0 V vs SCE using a 40 % Pd/C_b in 5 mM BH_4/1 M $NaOH_{(aq.)}$ at 1600 rpm and 10 $mV.s^{-1}$, using an instant reduction method. Although these loadings in the literature were much larger compared to the 1 - 5 % Pd/C_b shown in Figure 3.25, the current densities produced were much lower. This could be a result of the manufacturing process used as each electrocatalyst was produced using a different method. Comparing the shapes of the voltammograms produced from both Martins *et al.* and Grimmer *et al.* with the plots produced in Figure 3.25. Despite the lower current density, Martins *et al.* voltammogram profile was more analogous to the ones produced in this work. However, the much larger overpotential of Martins *et al.* makes it difficult to accurately compare the voltammograms. Despite this, some comparisons can be made. Both have no characteristic peaks with a lower current density on the return sweep.

The A_{act} of Pd electrocatalyst cannot be measured using the same method used for Pt, as hydrogen absorbs into the bulk of the electrocatalyst [130]. The direct comparison of the results obtained on Pd/C_b prepared with those on commercially available Pd/C_a is complicated

by the uncertainty over the manufacturing process. Table 3.6 shows the CVs recorded with 1% loading Pd on C_a and C_b in 10 mM $NaBH_4$/3 M $KOH_{(aq.)}$ for comparison.

Table 3.6 - Peak current densities (at -0.16 V vs SCE) of 1 % Pd on different carbons in 10 mM $NaBH_4$/3 M $KOH_{(aq.)}$ at 5 $mV.s^{-1}$ and electrons transferred calculated based on the Levich equation.

Electrocatalyst	Measured Peak j ($mA.cm^{-2}$)	Electrons Transferred
1 % Pd/C_a	51.6	3.2
1 % Pd/C_b	67.3	4.2

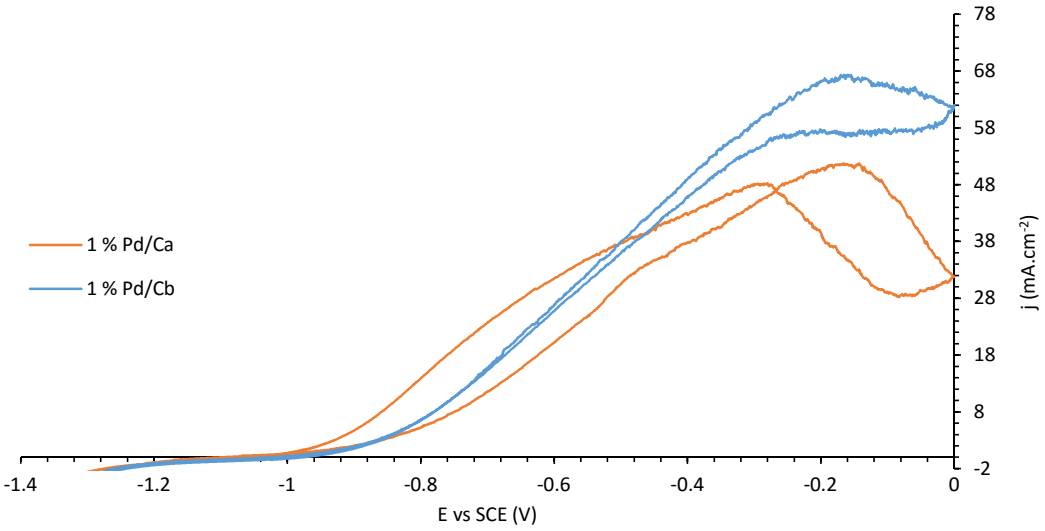

Figure 3.26 - Comparison of Pd on activated carbon and carbon black in 10 mM $NaBH_4$/3 M $KOH_{(aq.)}$ at 5 $mV.s^{-1}$ and 2,000 rpm.

Figure 3.26 shows that assuming the electrocatalyst had the same A_{rea} and electrocatalytic activity, carbon black is more electrically conductive than activated carbon, producing a higher peak current. The trace for 1 % Pd/C_a displays a crossover at E = -0.3 V vs SCE which is not observed with the 1 % Pd/C_b. This is a common feature for all Pd/C_b loadings and could indicate the presence of a surface process during the experiment, further supporting that the method of manufacturing Pd/C_b was analogous as the Pd/C_a used by the supplier as the electrocatalysts show similar CV characteristics.

Table 3.7 - Peak current densities (at -0.161 V vs SCE) of different Pd loadings in 10 mM NaBH4/3 M $KOH_{(aq.)}$ at 5 $mV.s^{-1}$ and electrons transferred calculated based on the Levich equation.

Pd Loading (%)	Measured Peak j ($mA.cm^{-2}$)	Electrons Transferred
1	67.2	4.21
3	42.7	2.68
5	67.9	4.3

These results highlight the importance of materials selection on overall electrocatalysts performance. The modest increase in the current density measured on carbon black support compared to activated carbon may lead to significant increases in current density (lower ohmic losses) when individual cells are assembled into stacks. The manufacturing method can significantly alter the performance of the electrocatalyst. The 10 % Pt/C_a vs. 10 % Pt/C_b indicates that changing the type of carbon has a large effect on electrocatalyst performance though manufacturing method could also lead to such a change. The 10 % Pt/C_a supplied and 10 % Pt/C_b manufactured (Figure 3.20), using suspected similar manufacturing methods, produced similar electrocatalytic activity. This supports the conclusion that the difference in the performance between 10 % Pt/C_a vs 10 % Pt/C_b was due to their different manufacturing process and highlights how crucial it is to optimise the electrocatalyst manufacturing method to produce an effective electrocatalyst.

There is little effect of material loading between 1 to 5 % Pd/C_b. Manufacturing Pd/C_b allowed for the effect of different materials loadings to be evaluated which could not have otherwise been supplied. The material loading results were inconclusive due to the 3 % Pd/C_b showing a lower current density compared to 1 % Pd/C_b. Potentially one of two conclusions could be drawn; either the 1 % Pd/C_b was incorrect and there was indeed an increase in the electrocatalyst performance as indicated by the 3 and 5 % Pd/C_b, or the 3 % Pd/C_b was incorrect and there was little difference in the performance of the electrocatalysts in this material range. To determine which of these conclusions are correct, the experiments would have to be repeated with a larger material loading range would have to be investigated.

3.3.5 Ruthenium, Ru

Ru has been shown to be electrocatalytically active in many low temperature fuel cells, including DBAFC [131]. Unfortunately, Ru electrocatalyst could only be sourced at 10 % Ru/C_a making a material loading study impossible.

3.3.5.1 *Performance of 10 % Ru/C_a*

10 % Ru/C_a electrocatalyst was evaluated in 1 M $NaBH_4$/3 M $KOH_{(aq.)}$ to determine its electrocatalytic behaviour towards the BOR (Figure 3.27 and Figure 3.28).

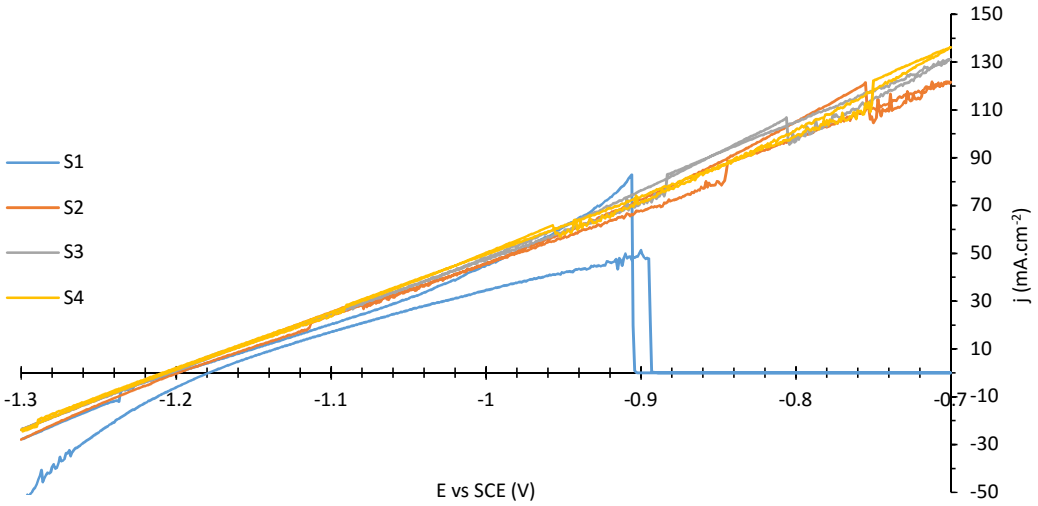

Figure 3.27 - 10 % Ru/C_a in 1 M $NaBH_4$/3 M $KOH_{(aq.)}$ at 5mV.s^{-1} and 2,000 rpm (run 1).

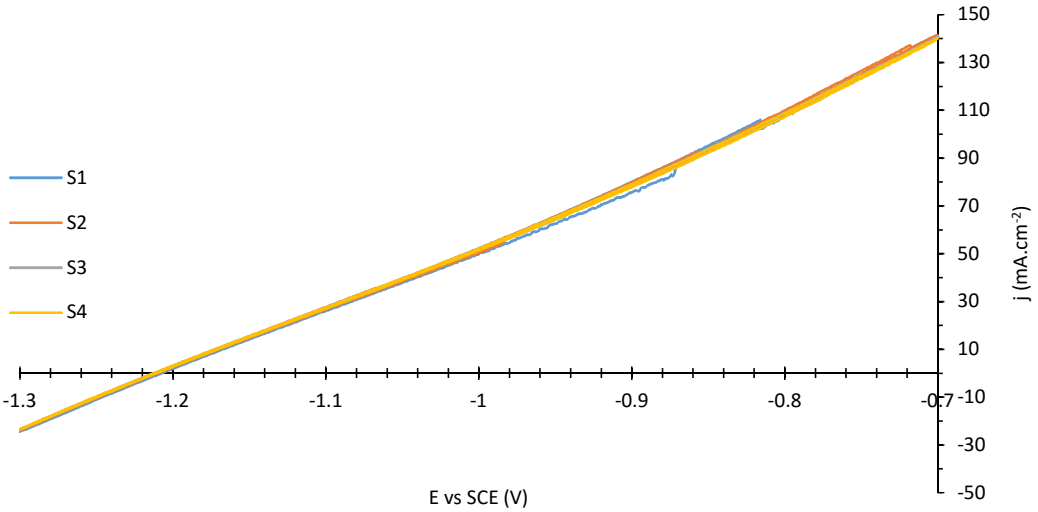

Figure 3.28 - 10 % Ru/C_a in 1 M $NaBH_4$/3 M $KOH_{(aq.)}$ at 5mV.s^{-1} and 2,000 rpm (run 2).

As with the other electrocatalysts, there was a reduction in the amount of noise between the first and second run of an electrode, with 10 % Ru/C_a showing the most reduction of the three. In addition, the current density dropped to zero during the experiment. Both the current density noise and the reduction could again be potentially accredited to the generation of hydrogen bubbles, blocking the electrode surface. Furthermore, the 10 % Ru/C_a generated high current densities with good kinetics.

3.3.5.2 *Effect of Mass Transport on Electrocatalytic Activity of Ru*

The mass transport of 10 % Ru/C_a was evaluated using 10 mM $NaBH_4$/3 M $KOH_{(aq.)}$ and is shown in Figure 3.29. The CV recorded at different rotation speeds show a relationship with the mass transport, which agrees with the Levich equation, i.e. the current density generated increases by approximately √2 when the rotation rate is doubled whilst producing the same number of electrons shown in Table 3.7. Comparing with the literature, the work of Grimmer *et al.* [132] show similar mass transport trends using 40 % Ru/C_b in 5 mM $NaBH_4$/1 M $NaOH_{(aq.)}$ at 2000 rpm and 10 $mV.s^{-1}$, with a current density of approximately 38 $mA.cm^{-2}$ at 0 V vs SCE. Although the peak current densities and profiles are very similar, the potential at which they occurred was very different. The results presented show peak current densities at approximately -0.92 V vs SCE whilst Grimmer *et al.* was at approximately 0 V vs SCE. The literature states that the BOR occurs at a low potential of -0.05 V vs RHE (-0.294 V vs SCE) and the higher potential range used in the experiment was due to the avoid hydrogen evolution; however, the source of this minimum potential isn't specified and can't be confirmed.

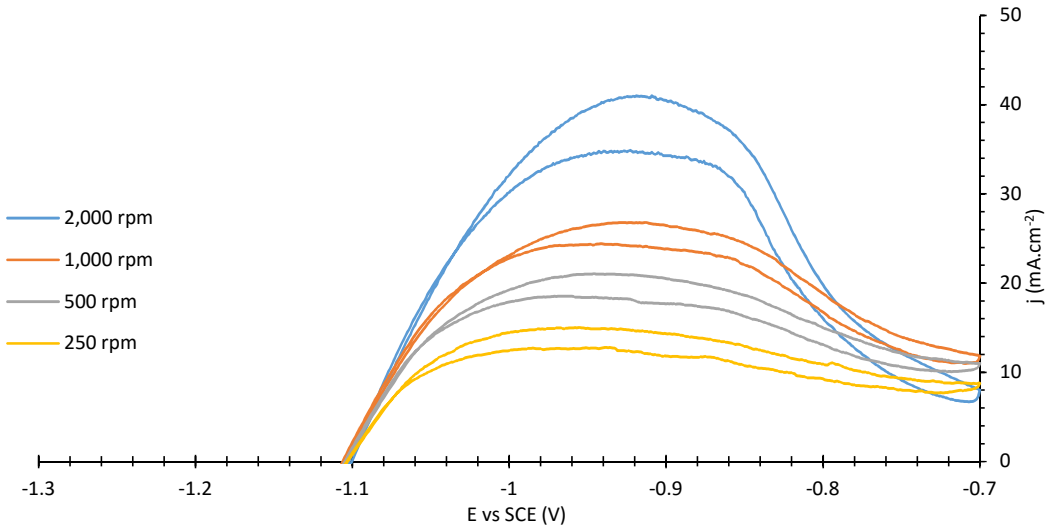

Figure 3.29 - Effect of mass transport on 10 % Ru/C_a in 10 mM $NaBH_4$/3 M $KOH_{(aq.)}$ at 5 $mV.s^{-1}$ and 2,000 rpm.

Table 3.8 - Peak current densities of 10 % Pd/C_a in 10 mM $NaBH_4$/3 M $KOH_{(aq.)}$ at 5 $mV.s^{-1}$ and electrons transferred calculated based on the Levich equation at -0.92 V vs SCE.

Rotation Rate (rpm)	Measured Peak j ($mA.cm^{-2}$)	Electrons Transferred
2000	40.8	2.6
1000	26.7	2.4
500	17.8	2.5
250	12.1	2.1

The results for the 10 % Ru/C_a show good electrocatalytic activity towards the BOR with high current densities being produced and a correlation between mass transport and the current densities generated. As with the other 10 % precious metal/C_a electrocatalysts evaluated, noise observed in the first run was less significant in the second run of the electrode, which could be attributed to the removal of an oxide layer, improving the electrode performance.

3.3.6 Electrocatalyst Comparison

Electrocatalysts may be compared according to performance or cost. Figure 3.30 shows CVs recorded in 1 M $NaBH_4$/3 M $KOH_{(aq.)}$ and the corresponding Koutechy-Levich plot in Figure 3.31 at a range of electrocatalysts under identical loading conditions. The peak currents and current densities are collected in Table 3.8.

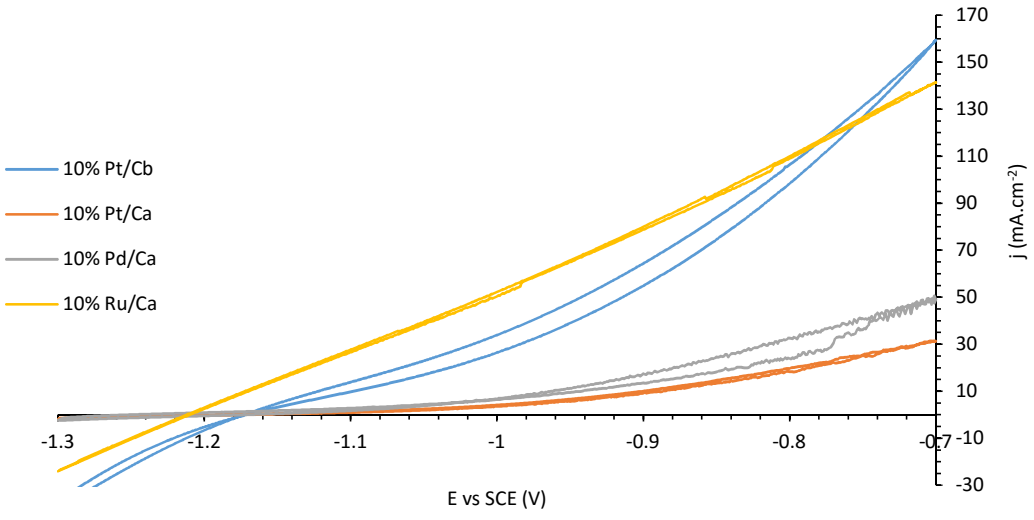

Figure 3.30 - Comparison CV of candidate electrocatalysts in 1 M $NaBH_4$/3 M $KOH_{(aq.)}$ at 5 $mV.s^{-1}$ and 2,000 rpm.

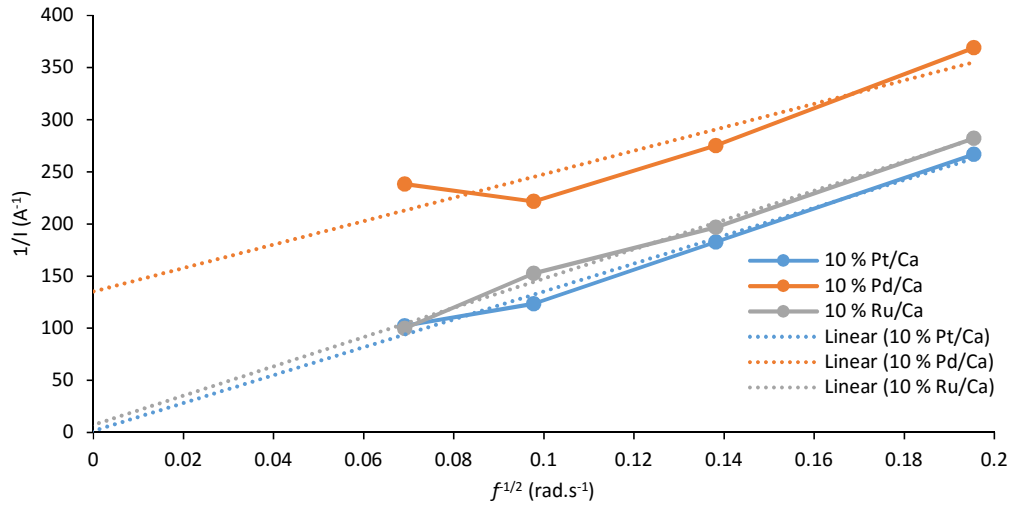

Figure 3.31 - Koutechy-Levich plot of different electrocatalysts in 1 M $NaBH_4$/3 M $KOH_{(aq.)}$ at 5 $mV.s^{-1}$.

The Pt/C_a, Pt/C_b and Pd/C_a electrocatalysts show poor kinetics at low overpotentials which gradually increase as the overpotential increases, with Pt/C_b showing faster kinetics. However, Ru/C_a shows a relatively linear CV plot, indicating that the kinetics were consistent over the potential range. All plots cross the x-axis at approximately the same potential, between -1.22 to -1.18 V vs SCE, which suggests that they all initiate the BOR at a similar overpotential. Furthermore, despite the Pt/C_b being of a higher specification (dictated by the supplier) and using a more electronically conductive carbon, the Ru/C_a arguably performs better with increased kinetics, leading to increased currents being generated. The Koutechy-Levich plot shows that Pt and Ru based electrocatalysts show near mass transport only dependence as presented by the extrapolation near to zero. The non-zero extrapolation of Pd indicates that the electrocatalyst is dependent on both mass transport and kinetic effects. Although the reciprocal current of Pd at 0.07 $rad.s^{-1}$ doesn't correspond to the linearity of the other points if it were to be removed the y-intercept of the extrapolation would be 75 A^{-1}, still non-zero. Fuel cell output is improved and electrode degradation minimised when lower overpotential are required to operate them. Therefore, faster kinetics at low overpotentials are highly desirable. It may, therefore, be concluded that Ru/C_a has performed better than the other electrocatalysts.

Table 3.9 - Comparison of candidate electrocatalyst's peak current and current density (at -0.7 V vs SCE in 1 M $NaBH_4$/3 M $KOH_{(aq.)}$ at 5 $mV.s^{-1}$ and 2,000 rpm).

Material	Peak I (mA)	j ($mA.cm^{-2}$)
10 % Pt/C_b	39.46	159.4
10 % Pt/C_a	7.73	31.2
10 % Pd/C_a	12.12	49.0
10 % Ru/C_a	35.00	141.4

Fuel cell efficiency may also be determined by measuring their cost-performance property. This is done by calculating the amount of current produced per unit cost of the produced electrocatalyst. The costs used to perform this calculation were the R&D cost of the material, (Pt/C_b = £17.10, Pt/C_a = £7.77, Pd/C_a = £5.65 and Ru/C_a = £2.55 per gram correct as of 14 Dec 2016 from Alfa Aesar) while the labour cost to assemble the electrodes was assumed to be constant across all materials. Figure 3.32 shows the current economy (A $£^{-1}$ values) for the four electrocatalysts considered in Table 3.8. The current at both -0.7 (the peak current) and -1.0 V vs SCE (an overpotential analogous to the anode in a fuel cell) were converted into cost-performance values. Although the costs of purchase of R&D material is much higher compared to bulk buying for industrial applications, it is assumed these values are representative and allow for adequate comparison. It should be noted that although current density is used to normalise and compare electrocatalysts, this would make the current economy value needlessly more complex to calculate. Since the electrocatalysts all had the same A_{geo}, only the current was used to calculate the cost economy.

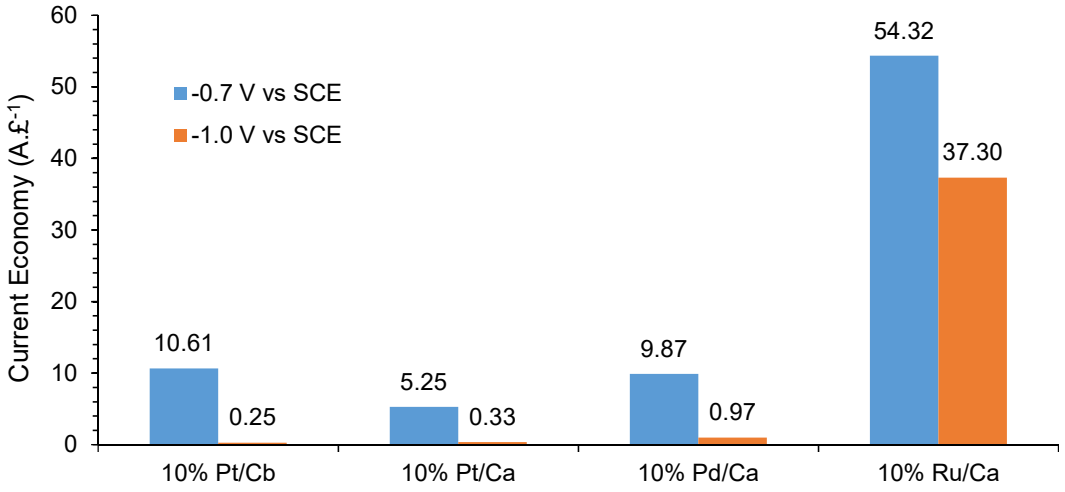

Figure 3.32 - The current economy versus performance comparison for candidate electrocatalysts at -0.7 and -1.0 V vs SCE.

As with the performance comparison, Ru/C_a outperformed the other precious metal on activated carbon electrocatalysts. Comparing the cost-performance of Ru/C_a to Pt/C_b indicated that the Ru/C_a outperformed the Pt/C_b considerably, especially at low overpotential. This reinforces the conclusion that, of the candidate, electrocatalysts evaluated, Ru/C_a had the highest overall performance with high current densities and cost-performance values. Although Pt/C_b performed well by generating high current densities, these were at high overpotentials which would be undesirable for most applications and the high cost of the Pt/C_b makes it considerably more expensive to use over the Ru/C_a.

3.4 Conclusions and Discussion

Four electrocatalysts were evaluated for their electrocatalytic activity towards BOR. Due to the poor performance of the Ni electrocatalysts, it was not put forward for further investigation with the Pt, Pd and Ru. The effect of mass transport, material loading and the type of carbon the precious metal was immobilised on was studied. Furthermore, their results were evaluated not just on their performance, but on their cost-performance, a method for taking their cost into consideration which, for real world applications, is of great importance.

It is important to understand the effects of experimentation on the materials being evaluated. Although the use of CV did impact the performance of candidate electrocatalysts, as shown by the decrease in A_{oct}, this was taken into consideration when interpreting the results. Furthermore, it highlighted the "shelf life" of the electrode, indicating that the electrode had to be replaced frequently between experiments.

The method of electrocatalyst manufacture was also found to have a significant impact on its performance. This was highlighted by the different Ni suppliers as well as the difference in performance between Pt/C_b and Pt/C_a. This increases the complexity of selecting a suitable electrocatalyst as the same material composition could have different performances depending on their manufacture.

The effect of material loading on Pd/C_b was determined, between 1 and 5 % Pd on activated carbon. Although the loading range was small, it would have identified any effect of material loading on current generation. Unfortunately, the material loading results were inconclusive and a wider range would have to be used. However, the results generated showed relatively low current densities being generated for these material loadings and hence may not be used for fuel cell applications. It may be interesting to investigate the effect of higher material loadings, such as between 10 – 30 %, as these would be more likely to be used.

The use of carbon black in electrocatalyst formulation may increase the current density generated due to the increased electrical conductivity of the carbon black. This would suggest that where possible, carbon black based electrocatalysts should be used an alternative to activated carbon. Although this may not be commercially available to the required specifications, the method outlined in this chapter to produce a Pd/C_b electrocatalyst was comparable with industrial practices could be used with a variety of metal salts for a range of metal loadings.

Finally, Ru/C_a was found to have the highest performance compared to the other candidate electrocatalysts studied. Its ability to generate high current densities in the presence of sodium borohydride, coupled with the lower cost compared to the other electrocatalysts, show it to be a potentially effective electrocatalyst to be used for DBAFCs, which performed better than Pt and Pd. This could be due to the Pt and Pd favouring the indirect oxidation, reducing the current density being generated. Another possibility could be that the Ru more readily oxidises any hydrogen gas being produced on the surface. Identification of the mechanism for the BOR on Ru could provide a pathway for the development of a Ru based DBAFC electrode.

3.5 Future Work

Several aspects of this work would benefit from further development. 10 % Ru/C_a performed well, so a wider material loading range should be investigated, between approximately 10 – 30 % Ru. This would build further on the cost-performance of Ru and identify if a specific material loading outperforms 10 %. For example, 20 % may perform significantly better, warranting the extra financial cost for its use in the anode. Conversely, the 20 % performance may be comparable to the 10 %, indicating that this was the ideal amount.

Another area of development would be to produce and evaluate Ru/C_b. Although the results from this work indicate that there would be an increase in the current generated, the measured amount of current would need to be determined. Furthermore, should Ru/C_b not be available for commercial uses, i.e. large quantities available, the increase in current density would have to be evaluated on cost-benefit basis with the set-up costs of the desired electrocatalyst mass production.

Finally, understanding the BOR on Ru would be a valuable insight. This could lead to further Ru development, producing a more effective electrocatalyst. However, although this would be useful in identifying an optimised electrocatalysts for the BOR, as with the Ru/C_b, the use of the electrocatalyst would depend on its cost, supply availability and its performance. The highest performing electrocatalyst may not be the best electrocatalyst for the application.

4 Electrode Manufacture and Evaluation

The main driving force for power generation in fuel cells are arguably the electrocatalysts, as these are responsible for the kinetic properties of the redox reaction. However, a good electrocatalyst can be inhibited when made into a poorly designed electrode. Therefore, this chapter focuses on the development, manufacture and analysis of the DBAFC anode and cathode.

4.1 Background

There are several factors which contribute to a well designed electrode, such as a suitable formulation and manufacturing method to obtain an electrode with the required properties. This section focuses on what the desired electrode properties are and methods to achieve them.

4.1.1 Electrode Structure

Due to the wide range of types and uses of fuel cells with varying temperatures, pressures and fuels, there is no standard electrode structure. Most low temperature fuel cells have electrodes consisting of current collecting plates, a metal/carbon plate which gives the electrode support and conducts the electrons generated, the GDL, a layer which promotes gas diffusion whilst rejecting aqueous media, and the electrode, which contains the electrocatalyst with other materials to help it bind to the adjacent GDL. The specific roles and materials used in a fuel cell are discussed in detail in the stack design chapter 5.

Many electrode physical characteristics can affect the performance of an electrode, not just those associated with the electrocatalyst being used. These characteristics are not only associated with the materials that are used to make the electrode, but also the way in which it is made. A summary of some essential characteristics will be discussed here.

4.1.1.1 *Adhesion, particle network strength and durability*

The durability of an electrode is the duration at which the electrode can continue to perform before it starts to decay and a loss of performance is observed. The electrode starts to degrade as a result of the electrochemical operation of the fuel cell, due to effects such as loss of active surface area and dissolution, carbon oxidation and the evolution of oxygen [133]. These can have complex mechanisms and are dependent on the electrocatalyst and fuel cell operating conditions being used. However, there are properties which are important to all fuel cells. Increasing the adhesion between the electrode and the GDL or substrate can help prevent the electrode from degrading during operation. Furthermore, the mechanical strength of the electrode, which is influenced by the particle network strength, can aid in the prevention of electrode dissociation and degradation [134].

4.1.1.2 *Conductivity*

Electrodes must have two major functions; to be electrocatalytically active (which is associated with the electrocatalyst) and must be electrically conductive to transfer the electrons and complete the circuit. There are a variety of electrocatalysts, all of which require them to have some electrical conductivity to remove the electrons during the redox reaction. If an effective electrocatalyst does not have a high electrical conductivity, it must be intimately associated with another material which does, such as carbon black. It is commonplace for metals to be supported either on a carbon, ceramic or even on an inexpensive metal. Metals have high electric conductivity and consequently, in the case of shell-core electrocatalysts, there is little electrical resistance. However, in the case of ceramics and carbons there is an electrical resistance challenge and so highly conductive support materials must be chosen. Furthermore, it's not just the electrocatalyst which dictates the electrical conductivity. Additional materials used in the electrode manufacture can reduce electrical conductivity. Polytetrafluoroethylene (PTFE or Teflon®) is a binder which is used in electrode manufacturing to increase the adhesion properties and, in some cases, control water management. Nafion®, a small cation conductor, is more commonly used due to its high electrical conductivity compared to PTFE; however, it is considerably more expensive and has durability challenges. Therefore, in the DBAFC developed here, PTFE is used. During the manufacturing process, the electrode is heated in a furnace to sinter the PTFE, adhering the electrode to the substrate, whilst burning off any surfactant or solvent. Although PTFE is a good binding material, it has a low electrical conductivity. Therefore, increasing the amount of PTFE on the electrode to increase the adhesion properties of the electrode will result in increased electrical resistance.

Furthermore, the use of a binder also coats the surface of the electrode, which results in the consequent inhibition. By using increased binder concentration, more of the electrode's surface becomes coated which will eventually lead to the inhibition of fuel to the surface of the electrode. Therefore, a balance between the binder concentration and adhesion properties must be obtained to obtain an appropriate electrode.

Another conductivity which is important for an electrode is its thermal conductivity. Heat is produced due to inefficiencies in the reaction causing the stack's temperature to increase. Although in some fuel cells and applications this is not an issue and can even be considered desirable, in other situations the temperature of the stack must be kept at a specific temperature and usually requires a cooling system. Having an electrode which can quickly distribute the heat generated can aid with the cooling of the cell, making it easier to stay at the required temperature.

4.1.1.3 *Permeability*

Another electrode characteristic is its permeability. Different electrodes have different permeability requirements due to the type of fuel cell they're used in. For a DBAFC, the anode requires a high electrolyte permeability so that a large concentration of borohydride can penetrate the electrode, increasing the length of the double phase boundaries. Conversely, the cathode needs moderate electrolyte permeability, to increase the number of triple phase boundaries. However, the electrolyte permeability, also known as the electrode's wettability, must decrease towards the GDL so not to induce electrode weeping. This is typically achieved by the addition of a hydrophobic material, i.e. PTFE, within certain parts of the GDL. Furthermore, the GDL must have a high gas permeability so that the oxidant can diffuse from one side to the other. Gas permeability through the GDL is influenced by the alignment of the fibres and pore size distribution [135].

4.1.1.4 *Surface Area and Porosity*

One major characteristic of an electrode is its surface area. The larger the surface area, the increase in the amount of double/triple phase boundaries. The main material which contributes to the surface area of the electrode is the electrocatalyst and more specifically the support it's on. This is not only related to the particle size of the electrocatalyst but also the

porosity of the material. These factors relate the different properties of the pores of the electrode.

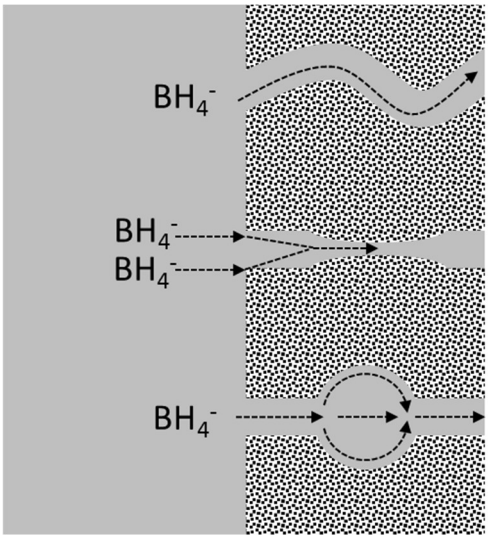

Figure 4.1 - Diagram indicating tortuosity (top) and constriction factor (middle path had a high constriction factor whilst the bottom had a low contraction factor).

An increase in the porosity, or the number of pores in the electrode, can increase the performance of the electrode. Different pore sizes affect different electrochemical properties of the electrode with the smaller micro-pores (< 2 nm) being responsible for the kinetics of the reaction whilst macro-pores (> 50 nm) affect the mass transport, ohmic resistance and potentially increase the constriction factor (the narrowing of pores) and tortuosity (the curvature or straightness of the pore) of the pores (Figure 4.1) [136]. Depending on the pore size distribution, different performances can be achieved as both micro and macro pores have an effect on different properties [137].

4.1.1.5 *Density and Uniformity*

The amount of electrode material deposited on the substrate is important as this effects the weight of the cell. However, if designed effectively, more of the electrocatalyst can be utilised to increase performance. An electrode that has a high bulk density or is thick would weigh more and could cause logistic issues, especially if the fuel cell is designed for portable applications. Therefore, a thin, low density electrode is desired with a high surface area to keep the cell weight low without compromising on performance.

Most electrodes are not a uniform layer of electrocatalyst but are a complex structure which varies with the way it's manufactured and the materials within it. They can be porous and have numerous channels going through the electrode from one surface to another. With the introduction of porous and channels comes the additional properties of tortuosity and convection factor. The uniformity of the electrode can not only be affected its formulation, but also by its manufacture.

There are many desirable physical properties for electrodes in a fuel cell and it is important to understand how these physical properties affect the final electrode's performance to develop one that is suitable for the specific fuel cell.

4.1.2 Electrode Materials

There are several components that are used in the production of an electrode, all of which contribute to its electrochemical performance. Some common electrode components used for low temperature fuel cells are:

- Binder – adheres the electrocatalyst to the substrate and gives the electrode its structural properties. Nafion® is the most common, although it is expensive with other low cost alternatives including PTFE [138] and chitosan polymers [74, 139, 140].
- Electrocatalyst – responsible for the electrochemical activity and vary considerably between electrodes and fuel cell types.
- Green binder – used as an intermediate binder before the curing process. Green binders can include derivatives of cellulose [134, 141-145]
- Pore former – used to control the porosity of the electrode. Such pore formers include carbon black, starch and various spherical polymers [146].
- Solvent – suspends the materials in a liquid and allows it to be deposited on a surface. The solvent is removed during the curing process so only the solids remain on the GDL or substrate. The type of solvent depends on the manufacturing process and the solvent-solid interactions. Some solvents include terpineol, texanol [134, 141, 142], water [147] and ethyl glycerol [148-150].

- Suspension aid – used to keep the solids suspended in the solvent. Various surfactants can be used, depending on the surface characteristics.

Although the list is relatively short, the number of different materials that can be used for each component can be considerable. Changing one of the materials can have a significant effect on the electrochemical and physical properties of the electrode. Therefore, it is imperative to choose a suitable material to produce an electrode with the desired characteristics.

4.1.3 Electrode Manufacturing Methods

Depending on the fuel cell operating conditions and the type of electrode being produced, there are a multitude of different manufacturing methods that could be used. Due to the vastly different processes, this section focuses on DBAFC and other low temperature fuel cells, such as AFC, PEMFC and DMFC electrode manufacture. DBAFCs are not researched as much as other fuel cells. However, other low temperature fuel cells have been developed extensively, which are similar to DBAFC and share various materials and techniques, are more widely researched and the work conducted on them reapplied to DBAFC. The main methods for the manufacture of different electrodes are discussed along with several alternatives.

4.1.3.1 *Low Temperature Electrode Manufacture*

Due to the similarities between AFCs and DBAFCs, AFC electrode manufacture of would be most suited to the DBAFC application. However, due to PEMFC and DMFC having similar electrode properties to DBAFC, these will also be discussed as their manufacturing processes could potentially be reapplied.

There are several methods used to manufacture electrodes for low temperature fuel cells with the most popular being rolling, electrospraying, doctor blade coating and screen printing [70] (which is discussed in more detail as this was the chosen electrode manufacturing method). Out of these methods, electrode rolling is arguably the most commonly used [16, 33].

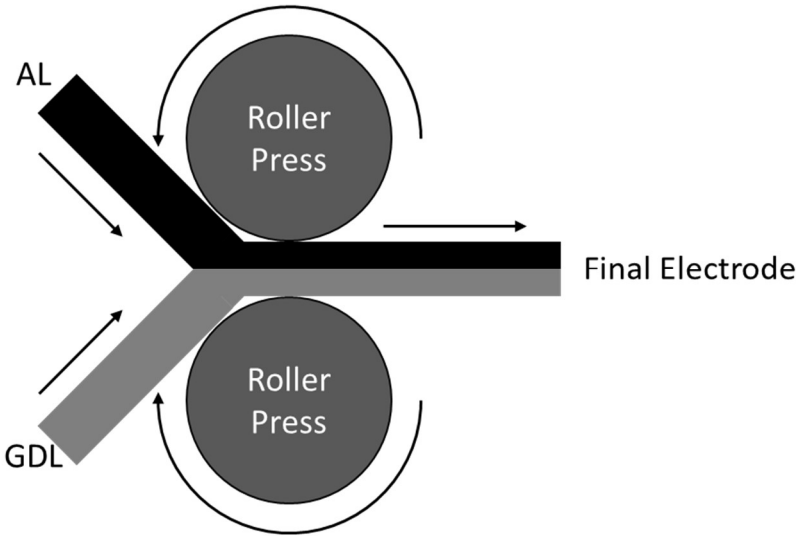

Figure 4.2 - Rolling electrode deposition manufacture using two counter-rotating presses compressing a GDL and active layer (AL).

In this method, the active layer and GDL are prepared separately and rolled into one sheet. The active layer, which consists of the electrocatalyst, carbon black and PTFE, are dry rolled to cross-link the particles to produce a self-supporting layer. Similarly, the GDL would be prepared by dry rolling porous organic materials to cross-link the particles [33, 151, 152]. Once the two layers are produced, they are laminated together to form a sheet of electrode with an active layer and GDL side (Figure 4.2). The electrode sheet would then be compressed onto a metal substrate and cured to sinter the PTFE, forming the final electrode. This method offers a low cost and flexible method for the production of electrodes[153].

Electrospraying, also known as spray electrode deposition, is a method whereby the electrocatalyst is prepared as an electrode ink suspension which is then atomised by a spraying nozzle and deposited onto each side of the membrane (MEM) (Figure 4.3). Once a thin layer of electrocatalyst had been deposited, a GDL is placed over it, compressed to make good electrical contact and put into a cell [154]. This method helps overcome various issues regarding the production of a homogenous electrocatalyst layer [155].

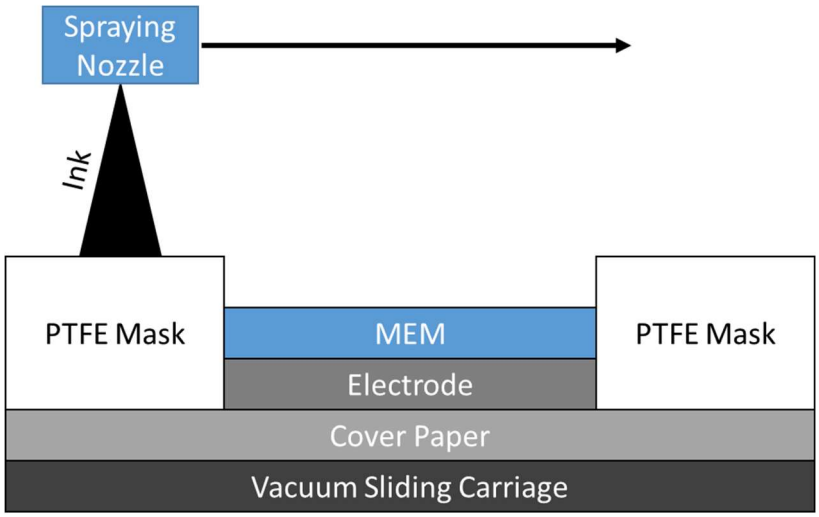

Figure 4.3 - Spray electrode deposition manufacture [154].

This method is not only used for electrocatalyst but can also be used to spray MEMs. In this case, the ink is prepared using a suspension of electrocatalyst, water, alcohol and PTFE [156]. Although the amount of material deposited can be easily controlled to produced thin layers, the electrode structure, including micro, meso and macro structural properties, are not so easily controlled and effect the electrode's overall performance [157]. An example of the different pore sizes in relation the electrode structure is illustrated in Figure 4.4.

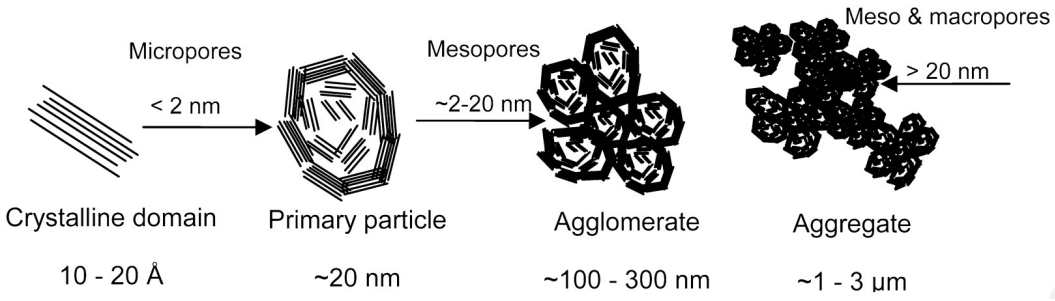

Figure 4.4 - Example of different pore sizes in relation to different particle states [158].

Another method is the doctor blade electrode manufacture. Unlike screen printing, which spreads a small amount of electrode ink over the desired geometry mesh, the doctor blade can be considered a levelling/metering tool. The electrode ink is deposited and the doctor blade brushes across the surface, creating a uniform electrode layer (Figure 4.5).

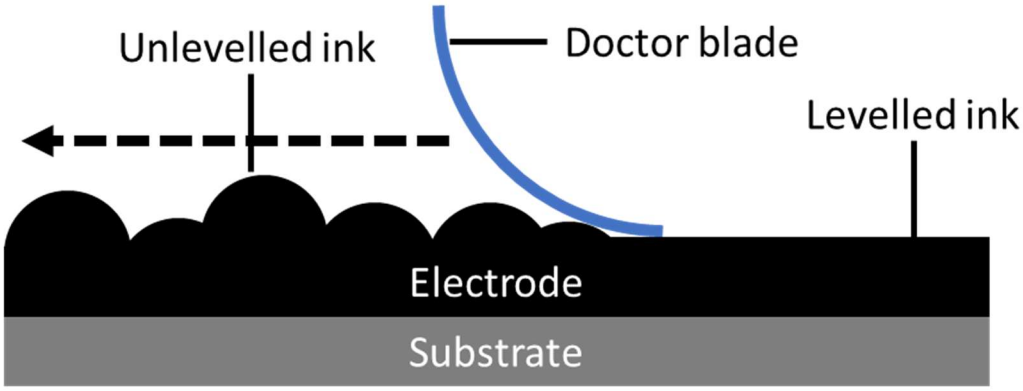

Figure 4.5 - Doctor blade electrode manufacture.

The doctor blade manufacturing process allows for a precise and reproducible amount of electrocatalyst to be deposited on the substrate/MEM/GDL [159]. However, this method is not only used for the deposition of electrode ink/slurries, as GDLs can also be produced. The GDL can be considered to have two components, a gas diffusion backing which is responsible for the oxidant diffusion, and a microporous layer which controls the transport of electrolyte or water which is governed by its wettability [160, 161]. As with screen printing, a non-Newtonian (shear thinning) liquid with a high viscosity is required to produce a uniform layer [162-164]. This requires the development of slurries with specific physical and rheological properties.

4.1.3.2 *Screen Printed Electrode Manufacture*

A popular method for the manufacture of fuel cell electrodes is by screen printing. Although these are occasionally used for low temperature fuel cells, they are more commonly used for SOFC. As such, many of the references are associated with SOFC manufacture; however, the theory and desired rheological properties of inks are the same as for low temperature fuel cells though there are differences between the materials used in the screen printing ink. Although there are many advantages, such as its convenience and adaptability [165], there are also some drawbacks to using screen printing manufacture. One of which is the thickness of the electrode which is approximately 10 – 100 µm thick [142]. Although this thickness may be suitable for fuel cells such as SOFC, this could be considered too thick for smaller fuel cells and

fuel cell applications. However, this could potentially be reduced by altering the manufacturing parameters and the ink used.

In the screen printed electrode method, electrocatalysts are made into an ink; however, the consistencies of the inks are much more viscous compared to that of spray electrode manufacture. Screen printed inks contain several different components which are highlighted in Table 4.1. Although the inks have key components such as electrocatalysts, solvents and permanent binder, many do not use all of the components discussed. Screen printed electrodes are not just for printing electrocatalyst layer, screen printable GDLs [148, 166, 167] have also been developed.

Table 4.1 – Common chemical components used in an electrode ink manufacture.

Component	Description
Electrocatalysts	The kinetic factor behind the reaction. Large amounts of the formulation dedicated to the electrocatalyst are desired to maximise the material loading and current density.
Green Binder	This is an interim binder which helps keep the shape of the printed electrode after printing but before entering the furnace where it's burnt off. The green binder had also been linked to overall porosity of the electrode [143, 145]. It's beneficial for the electrode to be highly porous; however, increasing the green binder can affect the overall ink printability [141].
Permanent Binder	The permanent binder is used to give the electrode structure. Without it, the electrocatalyst would not be able to stay adhered to the substrate. Depending on the electrode application, should a ceramic electrocatalyst be used it can be sintered and act as both the electrocatalyst and permanent binder.
Solvent	The solvent must suspend the solids sufficiently to allow for printing. It must also be volatile enough to be removed whilst the electrode is drying the furnace. Furthermore, the solvent must have a low cost as it could potentially be a large percentage of the final ink formulation.
Suspension aid	The suspension aid is a surfactant used to suspend the particles enabling the ink to flow during the printing process. Minimal amounts of

	suspension aid are desired to keep formulation costs low and to prevent any undesired foam formation.

Depending on the type of fuel cell and its operating temperature, the materials used for each component differ. The comparison of some components used in low and high temperature electrode inks for screen printing are summarised in Table 4.2.

Table 4.2 - Examples of materials used in screen printed electrode inks for low temperature (including AFC, PEM and DMFC) and SOFCs.

Component	**Low Temperature FC** [147-150, 167]	**SOFC** [134, 141, 142, 144, 168, 169]
Electrocatalysts	Precious metal/metal alloys on carbons with the most common being Pt.	Ceramics such as NiO/ScCeSz, lanthanum manganites, SmCeO, NiO and NiO-YSZ.
Suspension Aid	Due to the electrocatalysts being easily suspended in the solvent, suspension aids are not always required.	Various surfactants can be used which are specific for ceramic suspension aids.
Green Binder	Although not used as a binder, pore formers can be used to generate the same increased porosity green binders can produce.	Long hydrocarbons such as methyl and ethyl cellulose.
Permanent Binder	The ionomer Nafion is often used due to its binding properties and ionic conductivity.	The electrocatalysts are sintered and therefore do not require a specific binder.
Solvent	Polar solvents such water, IPA, glycol (glycerine), ethyl glycol and butyl-acetate.	Typically terpineol and texanol.

The screen used to print the electrodes were a thin woven stainless steel/polymer mesh sheets with a ridged steel border to keep the screen taut. In the centre of the screens, an image is produced with the desired geometry for the electrode as a negative using a photo-emulsion process which blanks the areas not part of the image. During the printing process, ink is forced through the open area of the mesh in the region of the image to produce the print on the substrate. The mesh size varies depending on the ink being used. An ink with larger particles of agglomerates would require a larger mesh size and vice versa. The mesh helps to prevent

the ink from being removed from the squeegee during the printing process. Another property of the screen is the overall thickness which is the sum of the mesh and the emulsion thickness. This gives an indication as to the final electrode thickness after printing.

Once the screens were selected, they are placed in a screen printer, which can either be manual or, more suitabley, an automated screen printer. For an automated process, the various parameters of the screen printer are entered, such as force, print speed, squeegee angle and screen height. The electrode substrate is positioned under the mesh geometry and secured to prevent it from moving. The screen lowers and ink is deposited from one side of the screen to another, covering the mesh geometry to ensure that an even layer of ink is deposited across the substrate surface. A squeegee spreads the ink from one side of the mesh geometry, over the substrate underneath and to the other side (Figure 4.16). The mesh geometry would then be filled with electrode ink. Finally, the screen is removed away from the substrate leaving the final wet electrode on the substrate. The electrode would then be cured in a furnace to sinter the binder present. This method is suitable for both printing on electrode substrates and MEMs; however, in the latter, the MEM would have had to be prepared first by the addition of Na^+ ions to prevent the MEM from swelling [147, 165].

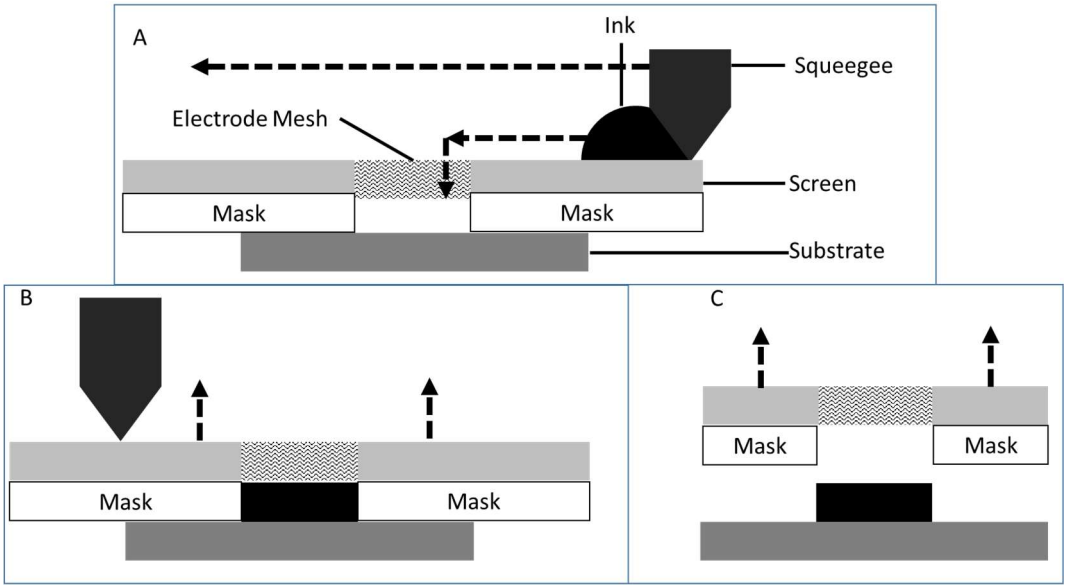

Figure 4.6 - Diagram showing screen printing process with "A" being the initial setup, "B" showing the ink the screen and "C" the removal of the screen to show the printed electrode.

Although different manufacturing methods have their various advantages and challenges, the use of screen printed electrodes offers a method to produces electrodes on an industrial scale with a variety of electrocatalysts. Furthermore, the relatively little literature for its use in AFC and novelty for DBAFC, it is chosen as the method for electrode manufacture in this chapter.

4.1.4 Rheology of Screen Printed Inks

Rheology is the study of material deformation to an applied force and is an important ink property for electrode spray deposition and, more importantly, screen printing manufacture. Since screen printing is the chosen manufacturing process to produce DBAFC electrodes in this work, examples of ink properties and how they relate to the manufacturing process are the focus of this section.

Important rheological properties can be studied using a rheometer, which consists of a torque spring attached to a rotating shaft. The bottom of the shaft is connected to, in the experiments presented in this work, a cone submerged in the ink (Figure 4.7). As the shaft rotates, controlling the shear rate, the resistance experienced by the fluid is measured by the torque spring. Using this method, different operating procedures were used to evaluate various fluid properties.

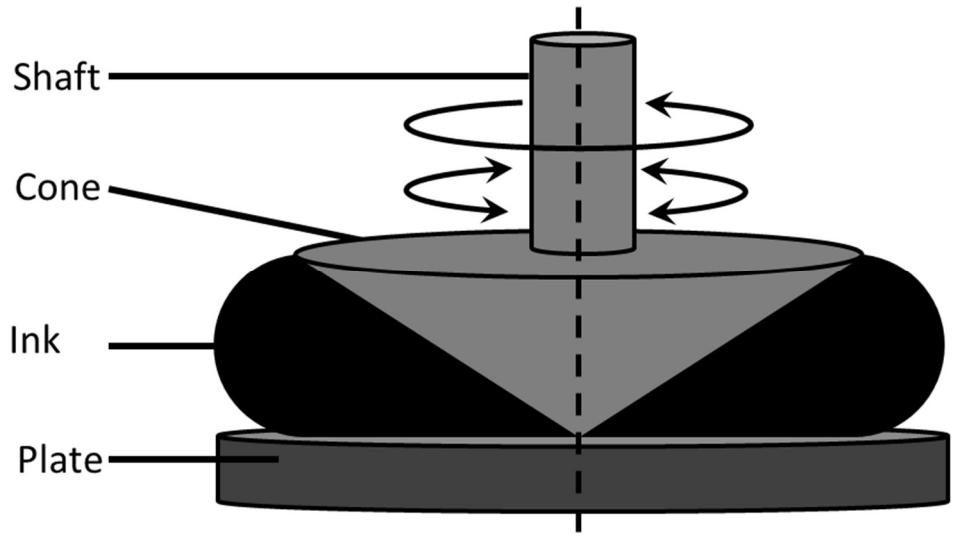

Figure 4.7 - Diagram of ink in a cone and plate rheometer setup.

The torque of the shaft is measured when the cone experiences resistance from the ink which is then converted to shear stress (τ) or the force applied to a given area. Once the shear stress is known for a given shear rate ($\dot{\gamma}$), the viscosity (v) can be calculated using Equation 4.1.

$$\tau = \dot{\gamma}.v$$

Equation 4.1 – Calculation of shear stress from shear rate and viscosity.

Many different material properties can be determined using this equation, depending on the type of experiment conducted. In this work, three rheological analysis techniques were used to assess the ink fluid properties. The first was the effect of shear stress on ink viscosity. Two different ink properties were identified using this method, whether the ink was shear thinning/thickening and if it was thixotropic. Shear thinning and thickening occurs when the material either reduces or increases viscosity non-linearly, unlike a Newtonian fluid which has a linear relationship. In screen printing inks, shear thinning properties are desired as when the ink is under shear stress, such as being spread by the squeegee, the ink viscosity decreases allowing it flow more easily across the screen into and through the mesh. Once the shear stress had stopped, after the ink was been printed, the ink viscosity would increase, allowing for the wet electrode to hold its structure. A shear thickening ink would make it difficult to print, solidifying during the printing process. The effect of shear rate on shear stress and viscosity for different fluids are shown in Figure 4.8.

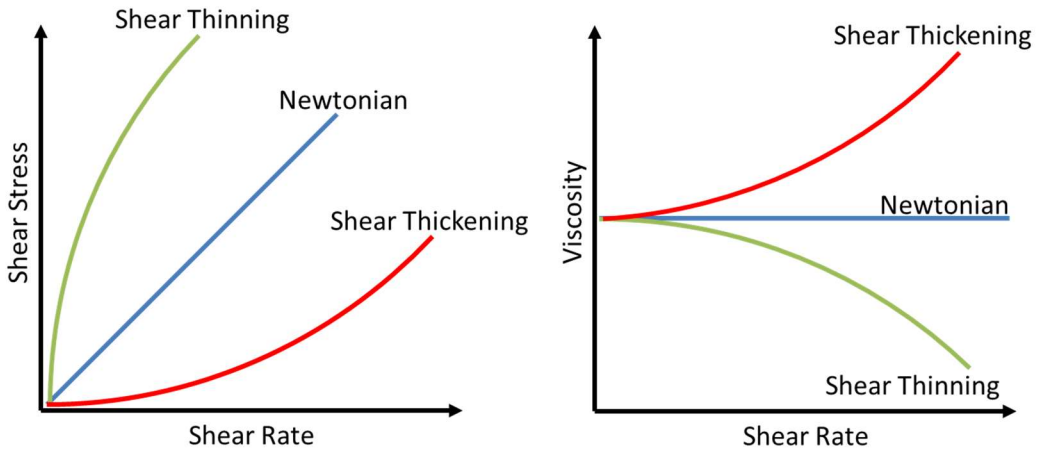

Figure 4.8 - Effect of shear rate on shear thinning, thickening and Newtonian fluids.

Another rheological property that can be observed from this type of plot is whether the material is thixotropic. Thixotropy is the material property which relates to whether the deformation of a material is reversible within a given time under content shear rate. For example, the particles in the material may require time to rearrange under the applied shear rate. In rheological data, this can be displayed in the form of a decrease in viscosity over time, followed by an increase in viscosity once shearing had stopped as the particles settle in a new position. This can result in a thixotropic loop whereby the decreasing shear rate profile had a higher viscosity compared the increasing shear rate as shown in Figure 4.9. Conversely, an anti-thixotropic material would have a shear thickening followed by a shear thinning response.

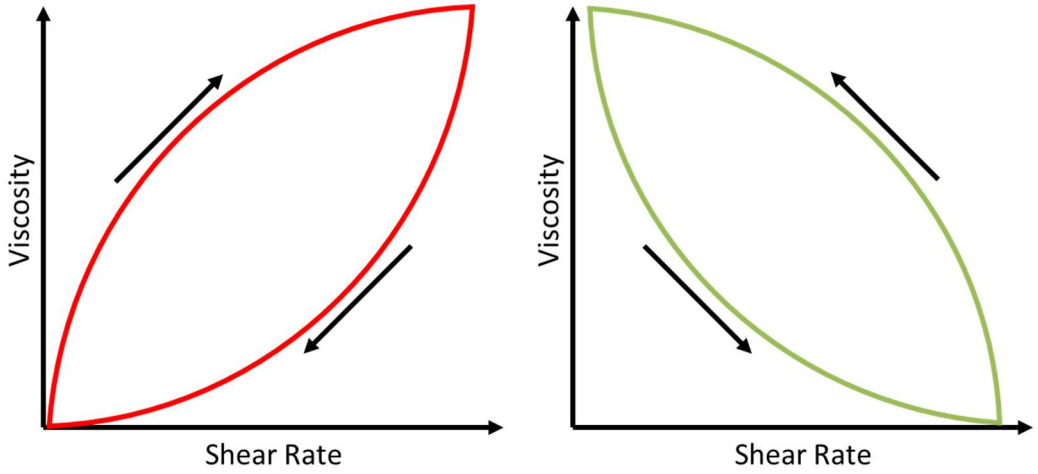

Figure 4.9 - Anti-thixotropic (left) and thixotropic (right) loops.

Determining if the ink was thixotropic was important as it can indicate the effects of screen printing on the ink. Once the ink had been printed, i.e. exposed to shear stress, most of the ink is in the mesh and starts to increase in viscosity. However, it is unlikely that the exact amount of ink will be used to make an electrode at one time. It is more likely that the ink will be in excess, which would be topped up periodically as the electrode substrates move through the screen printer. Determining if the material is thixotropic would indicate if the ink left of the screen or squeegee would have different rheological properties compared to fresh ink. If the ink does show thixotropic behaviour, the printing between fresh and reused ink may vary, resulting in different electrode qualities.

The second rheological analysis conducted is the effect of shear rate on shear stress as seen in Figure 4.8. However, by taking the $\log_{10}$ of both the shear stress and shear rate can identify materials that look Newtonian but may, in fact, be shear thinning (Figure 4.10). A Newtonian liquid would still show a linear response; however, if the material is shear thinning two different plots are produced; a plastic (which requires a specific yield stress to be reached before the viscosity increases) and a pseudoplastic which increase the shear stress non-linearly with shear rate. By plotting the inks in this way, the material can be further classified as a shear thinning fluid where it may have appeared to be a Newtonian fluid.

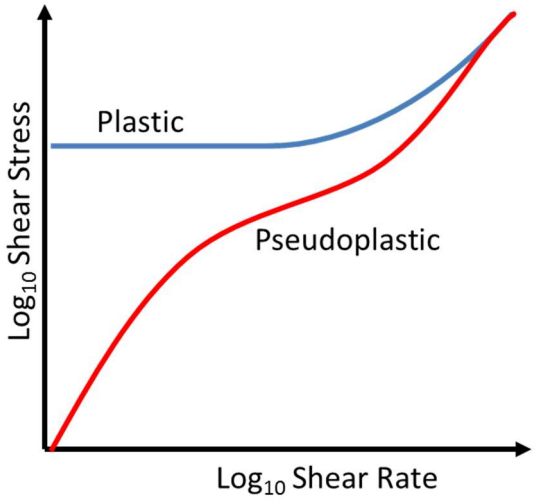

Figure 4.10 - Plastic and pseudoplastic behaviour.

Another rheological measurement is oscillatory rheometry, unlike the effect of shear rate on viscosity and shear stress plots above, which are forms of rotational rheometry. In rotational rheometry, the cone continually rotates in one direction during the experiment. However, in oscillatory rheometry, the cone rotates in one direction and then another. As it oscillates between the directions, well-defined small oscillation distances, it can measure different properties of the material. One such property is the storage (G') and loss (G") moduli. A high storage modulus is associated with materials that show elastic properties whereby the applied energy is stored in the material. Conversely a high loss modulus is associated with materials that show viscous properties, whereby the applied energy is dissipated in the material. The rheometer increases the angular frequency (radian.s^{-1}) and calculates both the storage and

loss moduli (Pa). Depending on the material many different plots can be observed in the rheogram generated and therefore an example copy cannot be shown but will be discussed further in the results. The benefit of understanding an inks loss and storage moduli allows for the quantification of the material's visco-elastic properties, i.e. whether it behaves more as a viscous liquid-like or an elastic solid-like material [142]. If the ink is highly viscous then should an adequate amount of shear stress be applied the ink should be able to print relatively easily with little disruption. However, if the ink shows high elastic properties then the ink may start to stick to the screen, deforming the electrode, decreasing the electrode quality and potentially increasing the amount of material wastage and manufacturing costs.

There are many insights that can be gained from understanding the rheological properties of an ink and how it directly affects both the screen printing process and the quality of the final electrode. As such, knowing the effects of materials on the final ink rheology as well as the desired rheological properties required to obtain an effective electrode could be key to screen printed electrode development.

4.1.5 Evaluation of Candidate Electrodes

The performance of a fuel cell is measured by determining its electrochemical properties. Electrocatalysts can be evaluated using voltammetric methods, as shown in Chapter 3; however, a fuel cell and its electrodes are measured via different methods. This section describes the various methods employed in determining the performance of the DBAFC developed.

4.1.5.1 *Fuel Molar Flow Rate*

It is important to know how much reactant is being supplied to the electrode during the experiment. Therefore, the molar flow rates ($\dot{\eta}$) of both the reductant and oxidant had to be calculated. This is done using Faraday's law which uses the current density (j), electron transfer number (n), superficial surface area (A) and Faraday's constant (F) to calculate the molar flow rate (Equation 4.2).

$$\dot{\eta} = \frac{jA}{nF}$$

Equation 4.2 - Faraday's equation for calculating the consumption molar flow rate of a reactant based on a specific current.

Faraday's law can be used to calculate the consumption of oxidant or reductant at a given volumetric flow rate and concentration. Although it is important to understand how much is consumed during the reaction, it is also good practice to use an excess to prevent any transport issues.

4.1.5.2 *Polarisation and Power Curves*

There are two types of electrode polarisation curves. One is the application of a potential and the measurement of current and the other is the inverse, drawing current and measuring the potential, with the latter being the most common in comparing fuel cell performance. The polarisation curves generated are used to assess the losses and power generation of either an electrode or the fuel cell. Furthermore, the polarisation curve can be converted into a power curve, which is the power (P) generated with the change in current (I) over a range of cell voltages (V_{cell}) using Equation 4.3.

$$P = I.V_{cell}$$

Equation 4.3 - Power as a function of current and potential.

The polarisation curve is significantly different to the power curve as, unlike the power curve which typically increases to a peak then decrease, declines with higher currents. The produced polarisation curve has three regions (Figure 4.11) which include the activation losses, ohmic losses and mass transport losses. For a given redox reaction, there is an associated theoretical *OCP* (OCP_{theo}) which is calculated based on the Gibbs free energy of formation ($\Delta\overline{g}_f$), number of electrons (n) and Faraday's constant (F) shown in Equation 4.4. This is what the *OCP* of the system would be at equilibrium if it experienced no losses. However, all fuel cells have initial losses, due to fuel crossover and internal currents to one extent or another. Furthermore, the OCP_{theo} is calculated under standard conditions, 1 bar oxygen and 25 °C. Hence, the fuel cell typically sits at a lower *OCP* known as the real or measured *OCP* (OCP_{real}). The ideal electrode

would have a OCP_{real} equal to the OCP_{theo} as the fuel cell would sit at a higher potential, allowing for greater currents to be drawn at higher potentials.

$$OCP_{theo} = -\frac{\Delta \overline{g}_f}{nF}$$

Equation 4.4 - Theoretical *OCP* calculation using Gibbs free energy of formation.

The curve starts at the OCP_{real} and as an applied potential increases, the current changes. Initially, the fuel cell experiences an activation loss which is associated which is related to the kinetics of the redox reaction. Electrocatalysts which have poor kinetics take longer to start the redox reaction and as such is shown as a steep decline in the polarisation curve. Conversely, electrocatalysts with fast kinetics show little or no activation losses and so do not appear on the polarisation curve. Typically, due to the 21 % oxygen in the air, the cathode reaches mass transport limits before the anode. Furthermore, due to the slower kinetics of the cathode ORR, the activation losses on the cathode plot is classically more dominant compared to the anode.

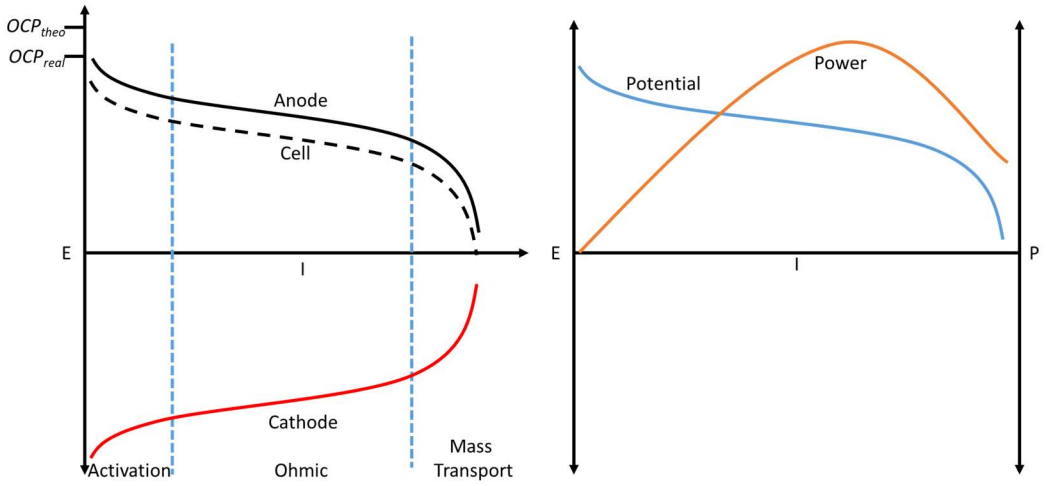

Figure 4.11 - Polarisation (left) and power (right) curves.

The next and largest region on the polarisation curve is the ohmic region. The losses experienced by the cell at this point of the polarisation curve is due to the increase in ohmic

resistance (R_Ω), such as connectors and electrolyte, and charge transfer resistance and as a result of the increase in potential (E) and current (I). Losses are typically linear over the measured range (as shown in Equation 4.5). Generally, the operation of a fuel cell in real world applications would lay within this region.

$$R_\Omega = \frac{E}{I}$$

Equation 4.5 - Resistance as a function of potential and current.

The final region on a polarisation curve is associated with the mass transport. At high current densities, the fuel cell starts to be deprived of reactants (either fuel or oxidant) or being inhibited by by-products leading to a dramatic reduction in performance. Fuel cells are not operated in this region as the electrodes would start to significantly degrade.

Although power curves do not describe the fuel cell in the same amount of detail as the polarisation curves, with the different loss regions, it is still an important tool for determining the performance of a fuel cell. The power curve shows when and if the fuel cell had reached its mass transport if it cannot be seen on the polarisation curve. Furthermore, and more importantly, it can be used to determine at what operating conditions the candidate fuel cell can achieve its maximum power. This is shown by the peak of the power curve generated and its associated current and potential. This can be used to compare the optimum operating conditions for different fuel cells. For example, if two fuel cells were to have the same peak power but one is at a lower current density, that fuel cell may have performed better than the other as the same amount of power is generated but at a lower overpotential. Another method often used to describe a fuel cell's performance is using area specific resistance (*ASR*), which is the ohmic loss as a function of the fuel cell's A_{geo}.

4.1.5.3 *Electrochemical Impedance Spectroscopy, EIS*

Potentio- or galvano- electrochemical impedance spectroscopy (PEIS and GEIS respectively) is an electroanalytical technique used to measure the resistance experienced throughout the cell. Impedance (Z_ω /Ω) is the relationship between frequency-dependent potential (E_ω) and

frequency dependent current (I_ω) due to the combination of resistance and reactance of a circuit and is analogous to electrical resistance experienced by DC circuits (seen in Equation 4.5 where Z_ω = R, E_ω = E and I_ω). A simple equivalent circuit, known as a Randles circuit, can be produced to describe the different electrical properties of the DL using resistors and capacitors shown in Figure 4.12. For a Randles circuit, the two resistors represent the series resistance (R_S, which is typically from the electrolyte) and the charge transfer resistance (R_{CT}, the resistance experienced by the electron migration from the anion through to the electrode). Due to the charge build up on the surface of the electrode, a double layer capacitance is produced (C_{DL}). The Randles circuit in Figure 4.12 is an idealised electrode, as depicted by the perfect semi-circle Nyquist curve. In practice, the electrode does not perform ideally and often the C_{DL} is replaced with the constant phase element. Furthermore, other components can be added to the circuit to represent other phenomena the electrode experiences such as the Warburg element which represents diffusion through the electrode. Two circuits can also be combined to represent the fuel cell connected by R_S and with the addition of two other resistors representing the resistance due to electrical connections.

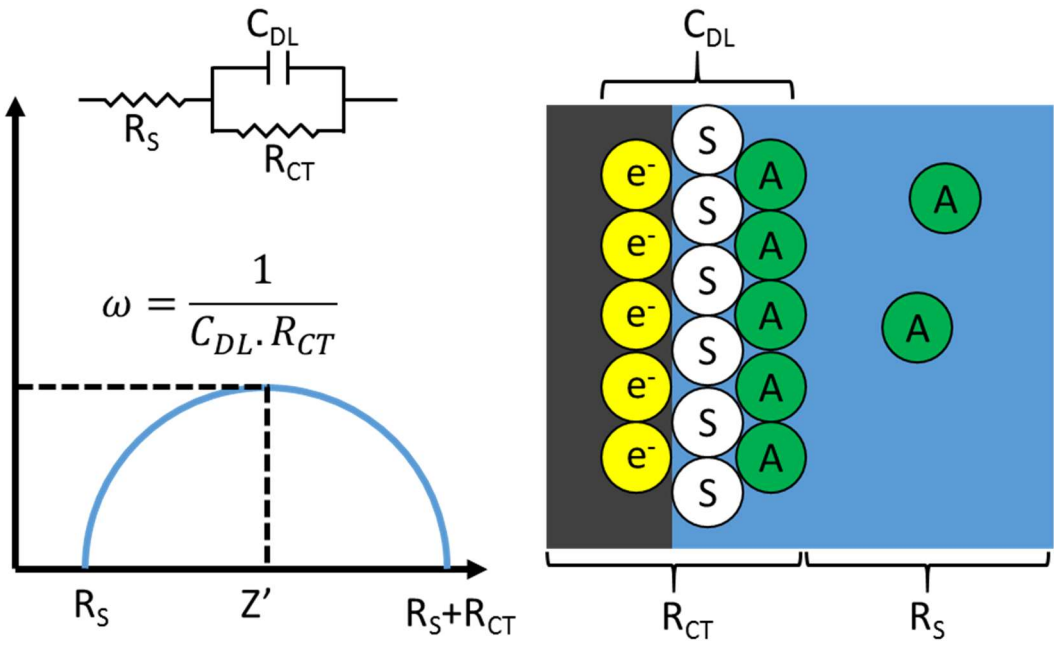

Figure 4.12 – Left figure shows a simple EIS Nyquist curve and its equivalent circuit showing the series resistor (R_S), charge transfer resistor (R_{CT}) and double layer capacitance (C_{DL}). The right figure shows the equivalent circuit on the DL formed on the electrode (grey), charge (e^-), solvent (S) and anions (A) in the electrolyte (blue).

There are several system characteristics which can be identified, and in some cases quantify, using EIS. Applying an impedance at a specific potential (PEIS) or current (GEIS) will result in curves on a resistance vs imaginary resistance, due to reactive components (capacitors and inductors) expressed as Z (Ω) vs Z' (Ω). Each curve represents an electrochemical process within the system (either a single electrode or the entire cell depending on the experimental setup). The smaller the curve, the less resistance is experienced when a frequency is applied. The initial resistance at which the first curve starts is the series resistance of the system. This is the total resistance of everything including the interfaces, bulk resistance and the electrolyte. Typically, most of the series resistance measured is due to the electrolyte between the electrodes with the electrodes also greatly contributing. This is due to resistance being the conductivity of the material divided by the distance the electron must travel. Hence, a large electrode gap can quickly increase the resistance of relatively conductive electrolyte.

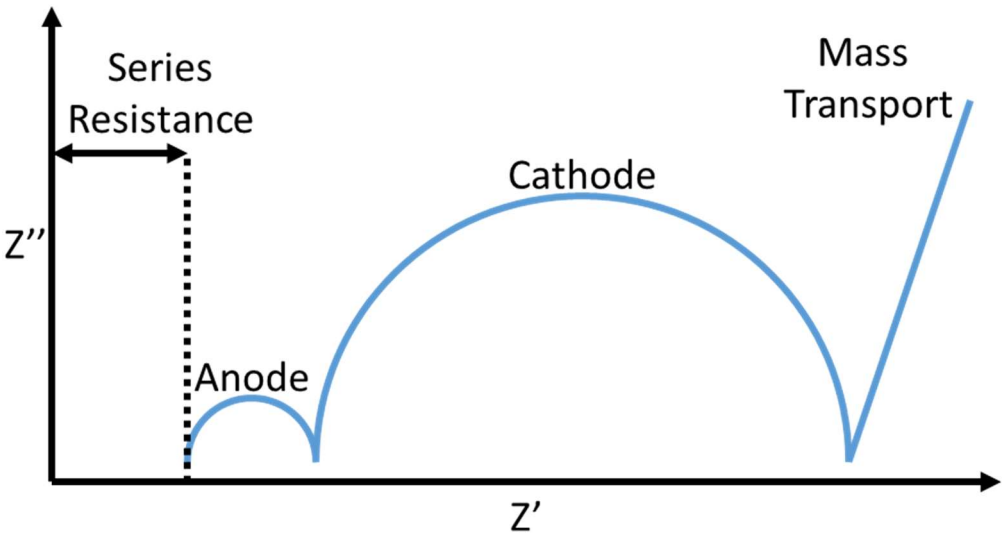

Figure 4.13 - A typical fuel cell EIS plot.

The size of the curve is an indication of the resistance experienced due to a specific process. For example, a lot of fuel cell EIS plots have two curves; one small curve followed by a larger one (Figure 4.13). These two curves represent the two different redox reactions at the different electrodes whereby the small curve is associated with the anode (HOR) and the larger curve with the cathode (ORR which is known to have slower kinetics than the HOR and therefore experiences a higher resistance). However, this assumes that there are only two

processes and each is associated with one electrode. It is possible for more than one chemical process to occur at the electrode which would result into multiple curves. Finally, there is a tail at the end of the resistance curve which is associated with mass transport/diffusion effects through the electrode (Warburg).

Although polarisation and power curves give the main performance results for the fuel cell, as it is closer to what the fuel cell may experience in real world applications, EIS can also be an important tool. The curves generated can highlight which of the two electrodes are responsible for the highest amount of resistance, which would indicate if a specific electrode is the bottleneck of the reaction and would benefit from further development. Therefore, it would be instrumental in the development of suitable electrodes for DBAFC. As such, EIS and polarisation/power curves were used as the electrochemical methods for determining the performance of the electrodes developed in this work. Using a reference electrode separates the polarisation and EIS curves, allowing for the evaluation of each electrode compared to the fuel cell as a whole.

4.1.5.4 *Direct Borohydride Alkaline Fuel Cell Performance*

DBAFCs have a variety of different parameters which can affect performance such as operating conditions, electrocatalysts, membraned or membraneless and if the former, the type of membrane being used. The work of more than 50 papers has been summarised by Pierre-Yves Olu *et al.* [73], highlighting the DBFC power and current densities generated from various electrocatalysts and operating conditions. The literature with the highest current densities and their associated system setups for membrane and membraneless DBAFCs have been highlighted in Table 4.3.

Table 4.3 - Highest literature current and power densities for DBAFC with and without membranes.

Anode	Cathode	Separator	Reductant	Oxidant	T (°C)	P (mW.cm^{-2})	j (mA.cm^{-2})
Membraned							
Ni + Pd/C + CCH	Pt/C	CS	5 wt. % $NaBH_4$ in 10 wt. % NaOH	O_2	70	810	1680
Ni + Pd/C + Nafion + CCH	Pt/C	CS	5 wt. % $NaBH_4$ in 10 wt. % NaOH	Humidified O_2	60	685	1400
CoO powder + PTFE on Ni	$LaNiO_3$ + CNT	PFM	0.8 M KBH_4 in 6 M KOH	O_2	65	663	1200
Membraneless							

MmNiCoMAl + C + CoO	$LaNiO_3$ + Carbon	None	0.8 M KBH_4 in 6 M KOH	Air	65	127	280
Ni powder + MmNiCoMnAlO	MnO_2 + Carbon	None	0.037 M KBH_4 in 6 M KOH	Air	25	70	180
MmNiCoMnAl + C + CoO	FePc + Carbon	None	0.8 M KBH_4 in 6 M KOH	Air	RT	92	175

Note: CCH = chitosan chemical hydrogel binder, PFM = polymer fibre membrane and CS = chitosan based binder [73-75, 84, 139, 170, 171].

The literature shows some interesting trends with the development of DBAFC. The highest performing setups were based on membraned DBAFC, pure oxygen as the oxidant and high operating temperatures. The use of a membrane allows for more flexibility when choosing an electrocatalyst due to the dramatic reduction, if not complete removal, of fuel crossover issues. The membranes used in the DBAFC, CS and PFM, and CCH binder are a low cost and more environmentally friendly alternative to the popular Nafion®. The power and current densities are good with the highest, 1680 $mA.cm^{-2}$, being significantly higher than the target 200 $mA.cm^{-2}$ (0.2 $A.cm^{-2}$) and are comparable to other more established low temperature fuel cell. Although the performance is high, these membraned fuel cells would still have the same undesirable characteristics of membraned fuel cells such as the requirement for an external cooling system and membrane durability challenges. Furthermore, the use of high temperatures and pure oxygen make it logistically difficult to utilise for certain applications such as transport or small electronic devices.

The highest performing membraneless DBAFCs in the literature were a much lower current compared to the membraned, with the highest being 280 $mA.cm^{-2}$. However, it should be noted that although the highest membraneless current density was achieved using 0.8 M $NaBH_4$. No flow rates are given in the literature; however, if they were assumed to be the same for all three membraneless DBAFC in Table 4.3, then the setup producing 180 $mA.cm^{-2}$ would show the most promise as it is run at a lower temperature and less than 5 % of the highest current density's borohydride concentration. However, for the comparison of the fuel cell developed in this work the results from Choudhury *et al.* [74] and Ma *et al.* [171], of 1680 $mA.cm^{-2}$ and 280 $mA.cm^{-2}$ respectively, were used as a benchmark for the DBAFC developed in this work.

4.2 Methods

Many different methods were used to evaluate the electrodes developed at different stages, from the ink and manufacturing process to the electrochemical physical electrode properties. These methods are described in this section.

4.2.1 Ink Preparation

There was little literature on screen printable electrode with respect to fuel cells and none specifically for AFCs. However, reapplying the work by Somalu *et al.* [134, 141] on their work with screen printable ceramic SOFC electrodes, it was possible to produce a base formulation.

The materials in Table 4.1 are not an exhaustive list and the materials vary depending on the type of electrode being produced. Furthermore, the manufacturing method depends on the materials used. As such, materials had to be chosen specifically for the use in DBAFC, a low temperature, flowing liquid alkali electrolyte fuel cell with the potential for increased electrode erosion (due to the evolution of hydrogen bubbles). Once the materials had been chosen, the method for both the ink and electrode preparation had to be developed to produce a high quality and effective DBAFC electrode.

The materials, quantities and order of material addition varied as the inks for the anode and cathode were developed. However, the method in which the materials are combined was kept constant. The EC green binders were dissolved in the terpineol and texanol at elevated temperatures (approximately 80 °C) whilst being stirred for approximately an hour (increasing the temperature can reduce the amount of time the EC took to dissolve; however, the solvent evaporation would increase). A stock solution of EC in the required solvent was typically prepared with additional solvent added when required as the quantities of EC were too small to be measured using balances available. Furthermore, high concentrations of EC in a solvent could not be prepared as the stock solution would solidify/gelatinate, making it difficult to disperse in the ink. The HEC was used as a green binder for the aqueous inks as a water soluble alternative to EC. Unlike EC, the HEC dissolved quickly in water (approximately 8 mins) whilst being ultra-sonicated at elevated slightly temperatures (JPL 8050 H Professional Ultrasonic Cleaner, Maplin). The inks were mixed using a Thinky mixer (ARE-250), a planetary centrifugal

mixer which was used to mix colloidal suspensions. This produced a homogenous ink suspension, provided the ink did not agglomerate forming a large mass of gelled ink.

4.2.1.1 *Ink Materials*

Varying the quantities and types of materials in each ink formulation influenced its physical properties. Therefore, the effect of increasing and changing the materials of the inks was prepared and assessed. Initially, the solid loading capacity of the solvent was determined followed by the slow addition of other materials

Table 4.4 - Materials used for DBAFC screen printable inks.

Material	Purpose	Reason for use
Norit	Electrocatalyst	Norit, an activated carbon, was used as an inexpensive alternative to activated carbon based electrocatalyst during the development of the anode ink due to its similar physical properties.
Pt/C_b, Pt/C_a, Pd/C_a, Ru/C_a, $Mn_{1.5}Co_{1.5}O_4$	Electrocatalyst	Varying electrocatalysts were used for the anode and cathode ink.
Tergitol TMN6	Suspension aid	A relatively inexpensive surfactant often used for similar colloidal suspensions.
Ethyl cellulose (EC)	Green binder	A binder previously used in the literature. Two different viscosities were chosen, 5 – 15 and 30 – 70 mPa.s for their effect on viscosity. The EC is soluble in the texanol and terpineol.
Hydroxyethyl cellulose (HEC)	Green binder	A water soluble form of EC suitable for aqueous based formulae.
60 wt. % $PTFE_{(aq.)}$	Permanent binder	Often PTFE was used as it was inexpensive, could be sintered to form a strong network of PTFE across the electrode, being chemically inert as well as control the wettability of the electrode due to being hydrophobic. However, PTFE had some challenges such as being having

		a high electrical resistance which can affect electrode performance and stability in different solvents.
Texanol and Terpineol	Solvent	A non-aqueous solvent used in the literature as a suitable solvent for screen printable inks.
Water	Solvent	A low cost alternative to texanol and terpineol; however, little to no literature on its use in screen printable inks.

Table 4.4 shows the materials that have been chosen to be used for the DBAFC. Although there are other electrode materials, they may not be compatible with the operating conditions of a DBAFC.

4.2.1.2 *Cathode Manufacture*

Unlike the anode in a DBAFC with the borohydride in the electrolyte, the cathode requires a GDL which had several functions including electrocatalyst support, controlling the diffusion of gas and liquids, aid with sealing and being electronically conductive to transport generated electrons. Therefore, the cathode was composed of two different layers; the cathode active layer (CAL) and the GDL, collectively called the cathode electrode which, when compressed onto the substrate, formed the cathode. A commercially used cathode electrode was originally used and was supplied as a thin, rubber-like, cathode sheet. The cathode electrode must be immobilised on a perforated nickel substrate so that it could be used in the fuel cell. This substrate gave the rubber-like cathode electrode structure whilst conducting the electrons generated and allowing the passage of air to be transported from one side of the cathode to the other. A high electrically conductive plate was used for the support as the charge collection over the back of the cells were low. The substrates were also chemically etched to roughen the surface to aid in adhesion. The substrate was first cleaned using an IPA wipe to remove any contaminants. Once dry, small quantities of PTFE was rubbed onto the clean side of the substrate and then polished back. This was to aid the adhesion between the cathode electrode and the substrate but not so much as to add additional electrical resistance. IPA was pipetted onto a piece of rectangle greaseproof paper with the CAL side of the cathode electrode being placed on top of the IPA. The PTFE side of the cathode electrode was then placed in the middle of the GDL side of the cathode electrode. The greaseproof paper was then folded in half so that both sides of the cathode were covered. The two layers were then compressed to 2.5 tonnes for 1 min using a hydraulic press (0.45 mm diameter ram, Clarke). It must be noted that

commercially manufactured cathode used in previous experiments consisted of two layers which were originally compressed to 1 tonne; however, the work conducted by a Lancaster University student (Samritha Parhar, MEng 2016) showed that there was an increase in fuel cell performance when the compression pressure was increased from 1 to 2.5 tonnes. Once the cathode electrode and substrate were compressed to form the cathode, it was placed in a furnace at 250 °C for 30 mins to allow the PTFE to sinter and burn off the PTFE dispersant, reverting the PTFE back to its hydrophobic state. Any excess cathode electrode was cut from around the edges which produced the final cathode.

Originally the cathode sheet came premade and only required immobilising onto the nickel substrate. However, the commercially used cathodes could no longer by supplied and so had to be prepared in-house. The GDL formulation was known and so the same formulation was used. Carbon black (C_b) (Cabot Vulcanised carbon black, 12.16 wt. %), Norit activated carbon (1.52 wt. %), multiwalled carbon nanotubes (MWCNT) (Nanocyl NC7,000, 1.52 wt. %) and IPA (Sigma Aldrich, 46.81 wt. %) were weighed into a Thinky pot and spun mixed for 1 min at 2,000 rpm. A PTFE suspension (60 wt. % in water, Sigma Aldrich, 37.99 wt. %) was added to the carbon paste and spun mixed for another minute at 2,000rpm until a putty was formed. This putty was then carefully roller pressed until it was approximately 1 mm thick sheet using manual calendering rollers. The GDL was allowed to dry slowly under scrunched greaseproof paper at room temperature overnight. The slower the drying process the reduced the number of drying cracks formed.

The CAL was based on a manganese cobaltite (MnCoO) ($Mn_{1.5}Co_{1.5}O_4$, Fuel Cell Materials), spinel electrocatalyst with a surface area of 18.2 $m^2.g^{-1}$ and a d50 particle size of 0.35 µm. It was decided to continue using this spinel as the MnCoO appeared to be selective for the ORR in the presence of borohydride and hydrogen. Due to the nature of the DBAFC, the cathode must be selective or else the cathode would cause the oxidation of the borohydride, causing a collapse in cell voltage and no useful power output.

The commercially used method for producing the CAL was to vibro-mill the MnCoO (15.11 wt. %) and IPA (45.34 wt. %) until a suspension was formed. To the suspension, carbon black (2.35 wt. %), MWCNT (5.47 wt. %) and additional IPA (24.58 wt. %) would then be added and mixed

using a Z-blade mixer. Finally, 60 wt. % $PTFE_{(aq.)}$ (7.15 wt. %) would be added and continued to be mixed until the CAL putty was formed. The putty would then be roller pressed using the same method as the GDL until a thin sheet was formed. The CAL and GDL, before drying and still both saturated in IPA, would be laminated together by carefully laying one sheet over another. The two sheets would be roller pressed together (such as in Figure 4.2) until a single thin sheet was formed, with the CAL on one side and the GDL on the other to form a cathode sheet. The wet cathode sheet would then allowed to dry slowly until the final cathode sheet was formed. This would then be compressed onto the cathode substrate as mentioned above.

Although the CAL was the same formulation as that supplied by the company, it was manufactured using a different method as there was no vibro-mill or Z-blade mixer available. This is discussed further in Section 4.3.2 during the development of the CAL and GDL.

4.2.2 Electrode Printing and Manufacture

Initially, the electrodes were to be printed using an automated screen printer (DEK 248). However, due to resource reallocation, a manual screen printer was used as a replacement. Although the use of an automated screen printer allows of the same printing parameters to be used each time, including screen height, printing force and speed, reasonable control can be achieved using a manual screen printer.

The screen tautness was routinely measured to confirm the screen had not changed during repeated use (an average of approximately 25 $N.cm^{-1}$ taken at the four corners and centre of the screen). In the centre of the screen was the desired electrode geometry, a 34 × 34 mm square image. Two different overall thicknesses were used, a 160 and 300 µm screen which allowed for thin and thick electrodes to be produced. The various properties of the two screens are summarised in Table 4.5.

Table 4.5 - DEK screen properties.

Overall Thickness (µm)	Thread count ($P.cm^{-1}$)	Mesh opening %	Thread diameter (µm)	Theoretical ink volume* ($cm^3.m^{-2}$)	Average fabric thickness (µm)	Specified tension ($N.cm^{-1}$)
160	32	245	65	87	140	20-25

300	77	90	40	43	90	30-35

Once the screens were selected, they were placed in the manual screen printer (FLAT-DX) shown in Figure 4.14. One end of the screen was screwed into the screen printer clamp once aligned with the substrate underneath. Next to the clamp were two adjustable screws which allowed for the height of the screen to be varied. The height of the screen was also controlled by screen height regulators, sheets of nickel with a known thickness of 300µm which were placed on the edges of the screen and opposite side of the vice to ensure that the screen was level. The screen height was then moved up in multiples of 300 µm depending on the manufacturing parameters.

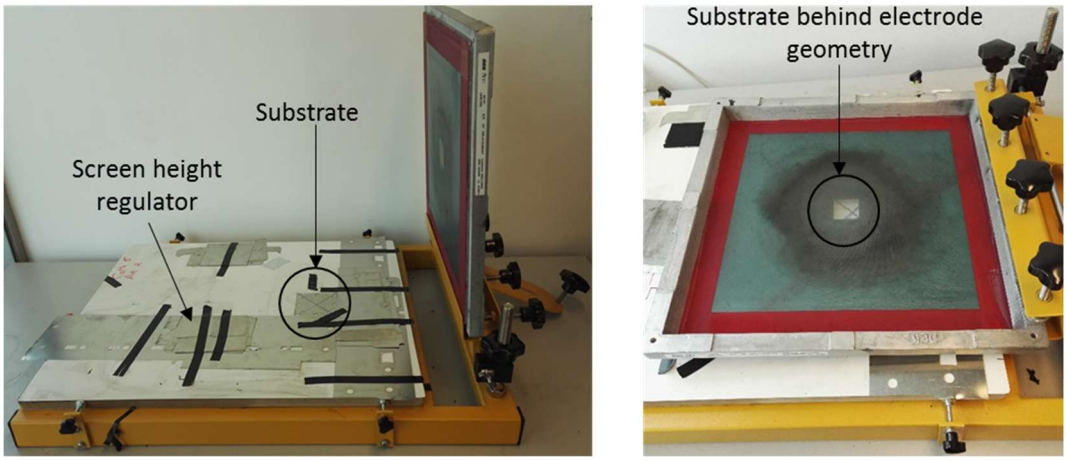

Figure 4.14 - Manual screen printer.

The substrate was positioned under the mesh geometry. A dummy substrate with an “X” was placed under the screen to align the screen with the substrate position. The dummy substrate was then replaced with an actual substrate which was secured to prevent it from moving during the printing process and getting stuck to the screen after.

The print was made using a consistent force and speed applied to the squeegee which was wiped across the image on the screen. Finally, the screen was removed away from the substrate leaving the final wet electrode on the substrate. Care had to be taken when lifting the screen away from the substrate. Although the screen was taut, the surface tension of the

ink would cause the screen to become slightly adhered to the electrode on the substrate. As the screen was pulled away from the substrate, a “screen snap” would occur. This was the point at which the screen had detached from the electrode completely. Should the peeling away of the screen from the wet printed electrode be too fast, the screen snap could have potentially led to the electrode becoming deformed and with surface defects. Furthermore, depending on the surfactant content of the ink, this could lead to foaming, causing large defects and potentially being detrimental to the wet electrode.

4.2.3 Physical Ink and Electrode Analysis

The physical properties of the ink and electrode are of great importance in determining the suitability of a formulation for the use in a DBAFC. Therefore, several methods were used to evaluate the ink and electrode which include surface observation and electrochemical analysis.

4.2.3.1 *Identification of Surface Defects*

To determine if the electrode produced was of a suitable quality, several visual assessments were conducted. Although ultimately the electrochemical and adhesion properties of the electrode would have had the biggest impact on the electrode suitability, visual observations of the electrode give an indication of the electrode’s quality. Certain electrode surface defects could be detrimental to its performance. The different observations are described in Table 4.6.

Table 4.6 - Visual assessments of screen printed electrode defects.

Defect	Description	Effect on Electrode
Cracking	Large cracks (> 150 µm wide).	These large cracks or craters can go through the entire thickness electrode, potentially causing electrode weeping.
Defined geometry	How well the ink had kept the desired geometry of the screen.	Poorly defined electrodes may have less electrode than required, leading to a reduction in current density. Furthermore, if the desired geometry is not achieved the electrode may not align

		with other parts of the fuel cell, potentially causing leaking issues.
Fissuring	Long and narrow cracks (< 150 µm wide).	Less likely to go through the electrode compared to cracks, although still possible, they may increase electrode degradation by reducing electrode adhesion to the substrate.
Pitting	Small pits formed by the surfactant in the ink.	Although small pits may slightly increase the electrode performance, by increasing the surface area, they can potentially go straight through the electrode to either the GDL or substrate underneath. This could then lead to electrode weeping.
Solvent leakage	The extent of the solvent leaking from the electrode to the surrounding substrate. This was usually seen as a shaded border around the edge of the black electrode.	Solvent leakage can lead to ink components being spread out further than required, leading to material potentially being transported away from the reaction site. Furthermore, this can also affect the sealing around the electrode.

The various electrode surface defects, which are identified using light microscopy, can be a result of the ink formulation, manufacturing process or both. Therefore, to obtain the ideal electrode with no surface defects, care must be taken both in the formulation design and the manufacturing process development.

4.2.3.2 *Rheology Testing*

Rheology is a complex discipline, with much of the topic out of scope for this work. However, some basic rheological analysis on formulae was carried out to gain insights into the interactions of material and their effect on screen printing. Small amounts of the theory are discussed in the background (Section 4.1.4), enough to understand and interpret the results obtained.

The rheological analysis conducted on the different formulae were carried out on a Rheolyst AR 1,000-N rheometer (kindly provided by Prof. Rob Poole, Liverpool University, Centre of Engineering Dynamics Department). Small amounts of ink were deposited on the bottom plate of the cone and plate setup (cone 6 cm, 2.2 °, 61 µm, stress factor 0.0177 and rate factor 28.0). As the cone was lowered, the ink spread to coat the plate. The experiments were run, generating the rheological data, and converted into the appropriate plots.

4.2.3.3 *Electrode Height Measurement using SEM 3D Image Construction*

Depending on the screen printing process, the quality of the final electrode could vary considerably with the same ink. Therefore, it was important to identify the effect of different printing conditions on the final electrode.

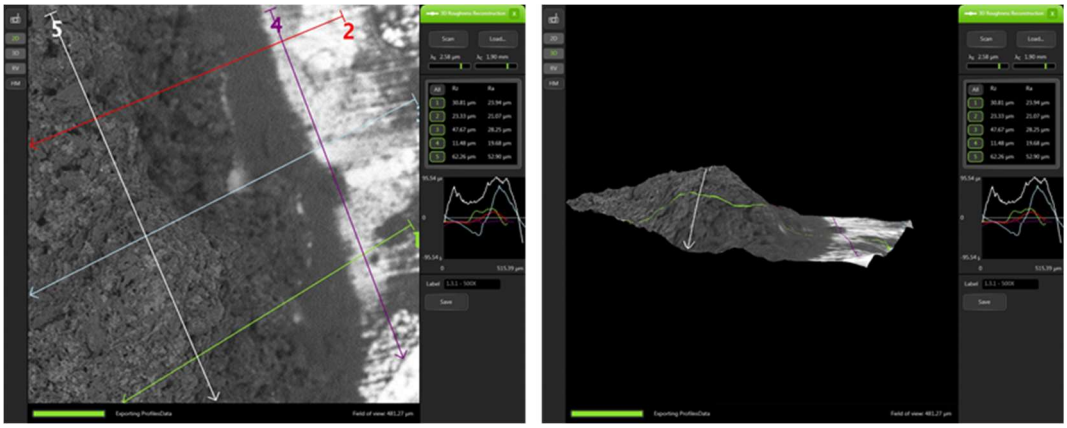

Figure 4.15 - 3D roughness reconstruction of an electrode surface with surface profile paths.

There were several parameters during the screen printing process which were taken into consideration (described in Section 4.2.2). Therefore, a method to determine the effect of different printing parameters on the electrode was developed using 3D SEM roughness reconstruction software. In this method, several SEM images (Phenom) were taken at different angles of the same area of the electrode. The 3D roughness reconstruction software then converted the 2D images into a 3D representation of the electrode's surface (Figure 4.15). Paths were then drawn across the surface of the 3D electrode surface image which generated a path profile. A total of five paths were drawn along the surface of the electrode with the path's height being measured. Three paths were drawn perpendicular to the electrode's edge (known as the step profiles) and two in parallel (one on the substrate known as the baseline

and one on top of the electrode known as the edge profile). The averages were taken of the sample lines to give an average edge, step and baseline profiles with the idealised profiles shown in Figure 4.16.

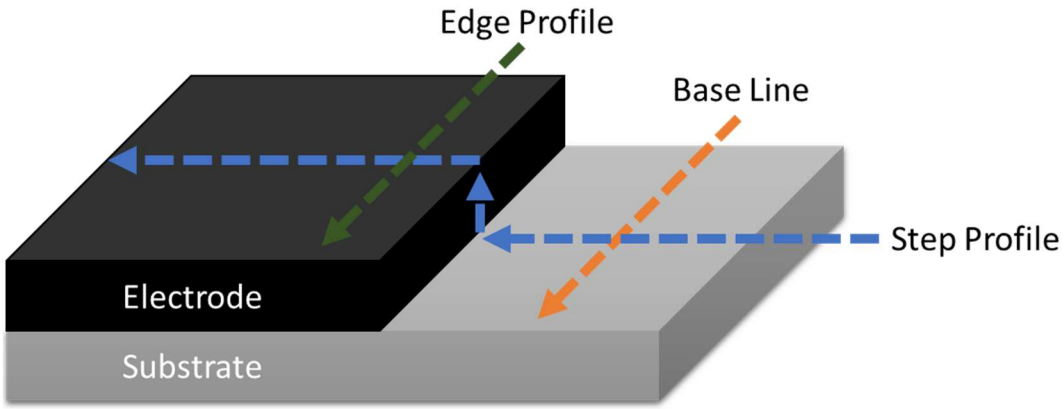

Figure 4.16 - Different profiles measured during 3D roughness reconstruction.

Most of the baseline histogram paths produced had a negative profile and so the peak height had to be offset by this value. In this way, the effect of screen printing method on the electrode's height was evaluated. Due to the heights of the electrodes, approximately 5 µm, the electrode height was difficult to be measured by any other means. The use of atomic force microscopy (AFM) would give high surface profile resolution but the height of the electrode would be out of range. Furthermore, the use of a micrometre would not have been accurate as it may have compressed the electrode and would not be measuring the correct electrode height. Therefore, this method was used as a suitable alternative.

4.2.4 Electrochemical Testing and Operating Conditions

Although the physical properties of the electrode are important, it was ultimately the electrochemical properties which dictate whether the electrode was effective for the use in a DBAFC. Therefore, several electrochemical analysis techniques must be employed such as determining the *OCP*, fuel cell polarisation and GEIS.

The borohydride molar flow rate ($\dot{\eta}_{BH_4^-}$) was calculated based on the stoichiometry of the reaction for a fuel cell with A_{geo} = 12.22 cm^2 (A) and a current density (j) of 0.2 A.cm^{-2} using

Faraday's equation (Equation 4.2). This produced a molar flow rate of 3.166×10^{-6} mol.s^{-1} and using a specific volumetric flow rate, for a single pass system, of 5 cm^3.min^{-1} required the borohydride concentration to be 38 mM. The borohydride volumetric flow rate was based on literature stating that 5 cm^3.min^{-1} produced the largest current density at a similar temperature (80 °C) and setup (a cell with a A_{geo} = 25 cm^2) [127, 172]. The concentration differed from the literature (0.5 M $NaBH_4$ equating to a molar flow rate of 4.17×10^{-5} mol.s^{-1}) as the molar flow rate used in this work was calculated based on an acceptable current density of 0.2 A.cm^{-2}. Furthermore, the molar flow rate required for the DBAFC designed would be lower than the literature due to having approximately half the geometric surface area.

The oxidant, using 21 % oxygen in air, molar flow rate ($\dot{\eta}_{O_2}$) was calculated using Faraday's equation and the molar volume of an ideal gas. This produced a molar and volumetric flow rate of 3.166×10^{-5} mol.s^{-1} and 0.7379 cm^3.min^{-1} respectively. As with the theoretical borohydride calculation, this value assumes the reaction was 100 % efficient, which will not be the case due to various losses. Therefore, an oxidant 542 × excess based on the 0.2 A.cm^{-3} stoichiometry of 0.4 L.min^{-1}. This large excess was due to requiring a large volumetric flow rate of air at the back of the cathode compared to requiring a specific molar flow rate. The 0.4 L.min^{-1} flow rate was based on a similarly sized industrial AFC used to benchmark the designed DBAFC performance.

Measuring the *OCP*, polarisation and GEIS was a relatively simple procedure as once the electrode had been made into a fuel cell rig, see Figure 4.17 for the fuel cell rig setup, it was attached to the potentiostat (Biologic SP-240). The potentiostat would then actively monitor the *OCP* across the fuel cell using the system software (EC-Labs), although chronoamperometry can be used to measure the change in *OCP* over time. A GEIS was then performed on the fuel cell followed by polarisation with specific experimental parameters. A three cell system was used with a reference electrode, Ag/AgCl, being used to separate the polarisation curve into two, one for each electrode.

During the experiments, the various operating conditions, such as fuel molar flow (see Section 4.1.5.1) and temperature, had to be kept constant to obtain accurate and comparable results. The degradation of borohydride on the surface of the electrode, which was spontaneous due

to borohydride hydrolysis, slowly decreases the concentration of the borohydride fuel. Therefore, for the concentration of fuel to be kept constant on the surface of the electrode, the volumetric and molar flow rate of borohydride must have also been kept constant. The experimental setup was based on system 8 (see 6.3.8) but only for the use at room temperature (Figure 4.17). This made the setup simple but adequate for the evaluation of different electrodes.

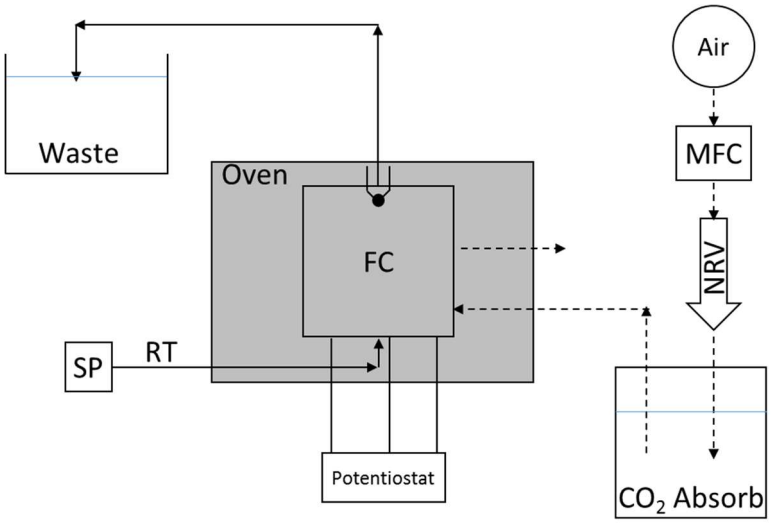

Figure 4.17 - Simple fuel cell testing setup based on system 8.

4.2.5 Quantification of Electrode Degradation

As previously discussed in the electrode manufacturing chapter, degradation in electrodes cause a reduction in the power output. Therefore, a test was developed to quantify the amount of degradation experienced by an electrode using image analysis in MatLab. In this method, an initial background calibration of the electrode was used to count the number of pixels in an image which had the same geometry of the printed electrode. This gave the number of pixels for a complete electrode with no degradation. When a prepared electrode was to be evaluated, it was scanned using a photocopier to produce a grey scale image (Figure 4.18). This image was then imported into MatLab and using a specifically designed image analysis code, the image was converted into a black and white representation. To do this, the contrast of the image had to manually controlled to obtain the correct dimension of the electrode. The electrode from the image was then identified and the number of black pixels was counted. Finally, the number of black pixels were then compared to the reference

geometry and the decrease in the number of black pixels (as white pixels represent the substrate underneath) would give the degradation of the electrode as a percentage of the reference. The MatLab code was compared to ImageJ, software which was used specifically to measure particle and object sizes in images, with similar results.

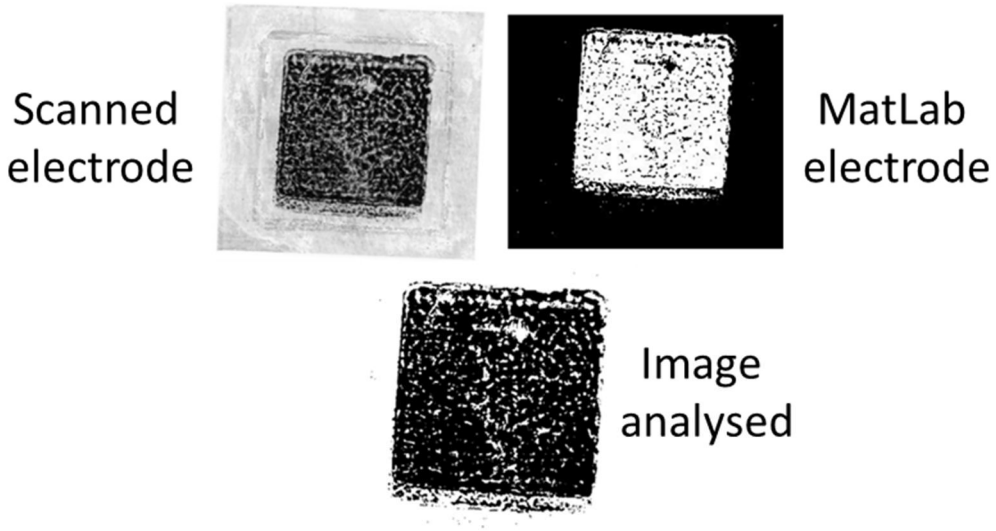

Figure 4.18 - Electrode degradation image analysis.

This method of measuring the effects of electrode degradation was relatively quick and simple compared to other surface analysis such as SEM or AFM. However, the amount of information generated from this method was low compared to others. The method relies on a 2D representation of the electrode whereby the degradation of the electrode could occur in the Z plane. As such, this would result in the method only picking up on the degradation when it had occurred sufficiently enough as to expose the substrate underneath. For thicker electrodes, this may not produce an accurate quantification of degradation. However, for the purposes of this work, this method was deemed acceptable. It would be recommended to find an alternative method for the effects long term fuel cell usage of the degradation of electrodes.

4.3 Results

Initially, the development of the anode ink was required for the candidate electrocatalysts highlighted in the previous chapter. The anode ink developed was then compared to commercially used electrodes for their performance in a DBAFC. Due to the intended cathode for the DBAFC no longer being available from the supplier, the cathode which was not originally going to be investigated had to be developed and reformulated. Once the cathode process was developed, it was compared to a commercially used manufactured cathode, both using the same electrocatalyst. Finally, the effect of different printing processes on the final electrode was investigated.

Another notation used was electrode and wastage weight percentage. These values indicate the amount of material in the ink which was associated with the final electrode, which included the electrocatalyst and the solid PTFE (electrode weight percentage), and the materials which were removed during the curing process, which included the solvent, green binder, suspension aid and the liquids from the PTFE suspension (wastage weight percentage). Ideally, from a cost perspective, the wastage material would be kept to a minimum.

4.3.1 Development of Anode Ink Formulation

A variety of methods were employed to assess the various anode ink formulations. Formulae were based on carbon black (Vulcan XC72R) in place of an electrocatalyst. This allowed for anode ink development using a much lower costing material to be used before adding an expensive precious metal electrocatalyst. Since the precious metal electrocatalysts were on activated carbon, using only activated carbon was originally deemed as a suitable substitute. An anode ink formulation was developed based on 10 % Pt/C_b electrocatalyst shown in Table 4.7. The ink printed well with no agglomerates or surface defects.

Table 4.7 - Final non-aqueous anode ink formulation.

Material	Quantity (wt. %)	Manufacturing Process
EC70	1.71	Dissolve EC70 at 80 °C whilst mixing
Texanol	80.09	
Tergitol	1.60	
$PTFE_{(aq.)}$	1.60	Mix at 2,000 rpm for 1 min

10% Pt/C_b	15.0	Mix at 2,000 rpm for 1 min
Electrode	16.0	
Wastage	84.0	

4.3.1.1 *Anode Ink Observations*

During the development of the ink, several interesting material interactions affecting the ink and electrode properties were identified. One of these was the substitution of the surrogate carbon black for 10 % Pt/C_b which caused the ink viscosity to decrease significantly. As a result, the 10 % Pt/C_b loading was increased by 2.4 times with increased PTFE and Tergitol to sufficiently adhere and stabilise it respectively. This was not only the case for the texanol based anode ink. An aqueous anode ink (described further below) was developed. A surrogate electrocatalyst of Norit was used (during the aqueous ink development the candidate electrocatalyst was changed from a precious metal on carbon black to activated carbon and the developed ink reflected this). Substituting in the candidate electrocatalysts changed the viscosity significantly with 10 % Ru/C_a ink having a very low viscosity and 10 % Pd/C_a having enough solvent to completely wet the surface. This was most likely due to different particle size distributions and surface areas of the surrogate carbons and electrocatalyst. This suggests that carbons cannot be used as surrogates for carbon based ink development and that one formulation cannot be used for a variety of electrocatalysts as their physical properties have a significant effect on the viscosity of the final ink.

Terpineol has been identified as a suitable solvent for screen printed electrode inks [141]. As such, the anode ink was originally designed using terpineol to obtain a higher performing electrode. Another solvent described was texanol; however, it did not perform as well as terpineol in the literature. Despite the lower performance, texanol was evaluated in place of terpineol due to being approximately seven times lower in cost (correct as of November 2016, Sigma Aldrich). The results showed that there was no observable difference in ink viscosity between the two solvents. Due to the lower cost, texanol was used as the primary solvent for the anode ink.

Another solvent investigated was water due to its low cost and boiling point, which would allow the electrode to dry at a lower temperature and potentially reducing any electrocatalyst degradation. Several different formulae were developed to stabiles the ink; however, it would often form an unspreadable gel. This occurred after mixing the PTFE into the slurry and it was speculated that the PTFE was not stable in aqueous inks without the use of significant amounts of Tergitol surfactant. Furthermore, the gelation occurred more so when the ink was warm, which was a result of dissolving the water soluble green binder HEC at increased temperatures. Norit based aqueous inks were developed shown in Table 4.8.

Table 4.8 - Norit based anode ink formulae.

Material	Quantity (wt. %)
HEC	3
Water	65
Tergitol	5
$PTFE_{(aq.)}$	9
Norit	18
Electrode	24
Wastage	76

During the manufacture of the Norit based aqueous electrodes, the smaller mesh size screen was used, as with the texanol based anode inks. However, this produced an electrode with most of the solids caught in the mesh and small particles and solvent being pushed onto the substrate underneath. A screen with a larger mesh was available, with a different geometry, and was used to investigate the effect of mesh size. The result was an electrode which was much more uniform and most ink deposited on the substrate. This indicated that the solids were poorly suspended in the aqueous ink, although it could have potentially been used in conjunction with a larger mesh size screen. Due to the large changes in ink consistency when the electrocatalyst was substituted in, the aqueous ink formula was not continued.

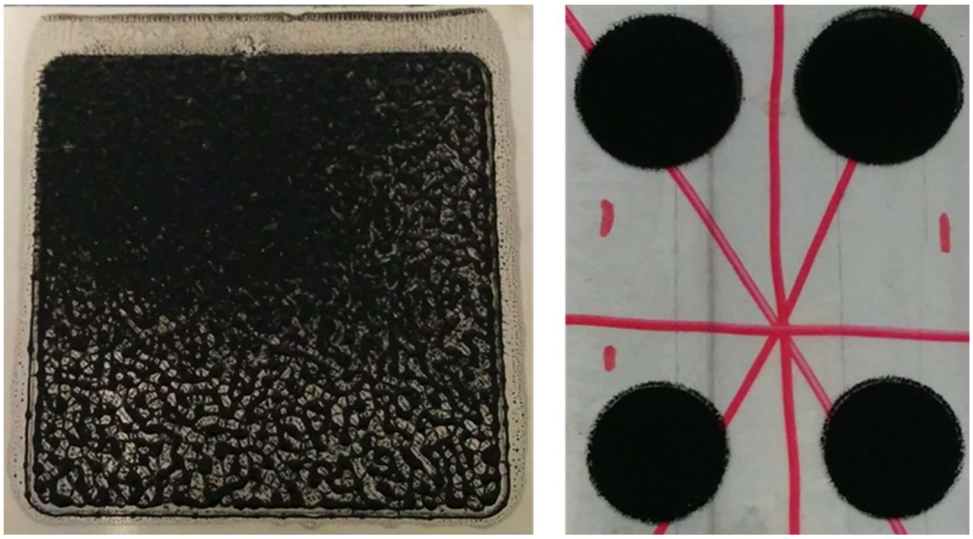

Figure 4.19 - Printed aqueous anode ink electrodes using small (left) and large (right) mesh screens.

Two different PTFE types were evaluated in the ink, a powdered $PTFE_{(s)}$ (particle size approximately 1 µm) and suspended $PTFE_{(aq.)}$ (particle size approximately 50 - 500 nm). Initially, the powdered PTFE was used in the ink formulation as it served two purposes, to increase the adhesion and viscosity properties of the ink. Increasing the electrocatalyst alone to increase the viscosity would cause the volume percentage ratio between the electrocatalyst and PTFE to increase, reducing the adhesion of the electrode. However, when the powdered PTFE ink was produced into an electrode and evaluated using an SEM, the PTFE stayed in discrete spherical particles on the electrode's surface after being sintered at 250 °C. This indicated that a sintered PTFE network did not form across the electrode's surface, causing a reducing in electrode strength and adhesion. The powdered PTFE was then substituted for the PTFE suspension with the resulting electrode adhering better to the substrate. It was suspected that the PTFE formed a fibrous network across the surface, as the smaller PTFE particles could sinter easier due to the increase in surface area. It should also be noted that the PTFE agglomeration and ink gelation observed only occurred whilst using the suspended PTFE. This could be due to the PTFE chains in the small particles unwrapping and interconnecting easier compared to the larger PTFE particles. Due to the increase in adhesion properties of the electrode, the suspended PTFE was used in place of the solid PTFE powder.

4.3.1.2 *Effect of Green Binder on Ink Viscosity*

Other components are required in an ink other than the electrocatalyst and the solvent, one of which is the green binder. Ethyl cellulose (EC) had been identified as a suitable green binder

in other electrode inks and was reapplied to the anode ink presented in this work [134, 141, 145, 163, 173]. Two different EC materials were evaluated, one with a viscosity of 5 - 15 (EC15) and another 30 - 70 (EC70) mPa.s.

The green binder had an important function in keeping the structure of the electrode after printing and before the curing phase. As such, understanding its effect on the rheology of the ink was important. Although the other materials may have an effect on the ink's rheological properties, EC was a thickening agent and so would have arguably more of an effect than the others. As such, two slurries were prepared, one containing 5 wt. % carbon black in terpineol, which was used as the baseline, and another with the addition of 0.25 wt. % EC70 (5 % of the carbon black).

Three rheological properties of the slurries were measured which included steady state viscosity, the effect of shear stress on shear rate and small amplitude oscillatory shear (described in Section 4.2.3.2). The steady state viscosity (Figure 4.20) showed several interesting properties of the slurries. Both plots have a forward and backward measurement for each sample. The forward plot represents the effect of increasing the shear stress on the viscosity and shear rate. Once the peak shear stress had been reached, it started to decrease whilst still measuring the effect, creating the backward plots. As such, each measurement was shown to have two plots to show the increase and decrease of shear stress.

The shear stress vs viscosity plot in Figure 4.20 shows two distinct plots with each sample measured as the forward and back measurement sweeps. The forward measurements show a decrease in the viscosity with applied stress which characterises the slurries as shear thinning. This was advantageous for screen printable inks as during the screen printing process, the slurries would act more as a fluid making it easier to spread and fill the screen mesh. Once the shear stress had been reduced, as the slurries would be removed from the squeegee pathway whilst it's in the electrode mesh geometry, the ink would slowly start to thicken which would help keep the desired electrode shape.

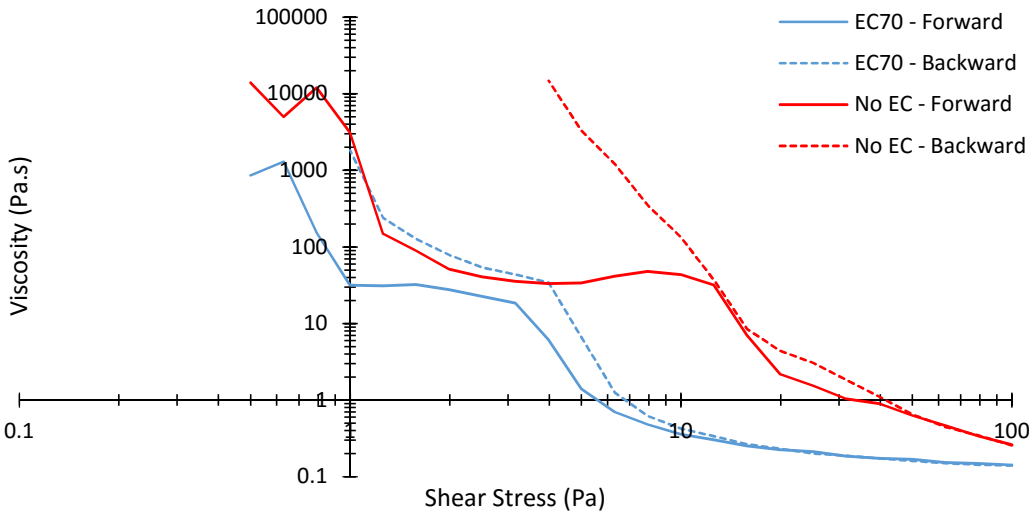

Figure 4.20 - Effect of shear stress on the viscosities of carbon and EC70 slurries.

Another characteristic that was observed was that the backward plot was different from the forward. This indicated that the slurries were irreversibly altered during the increase in shear stress, making it a thixotropic ink. Although the results show that the slurries were thixotropic, this may only be the case during the duration of the experiment. If the experiment run times were longer, the slurries may have had more time to revert to its original state. Being thixotropic affects the manufacturing process in that once the slurries had been printed, any residual ink left on the squeegee would have different rheological properties compared to when it was initially applied. This would have to be taken into consideration when designing the electrode manufacturing process as the quality of the electrode could differ from the production of one electrode to another.

Finally, comparing the different slurries show that the addition of EC70 decreased the viscosity. This was unexpected as EC70 was a thickening agent and its addition should increase the overall viscosity. It could be that at low quantities EC70 could reduce the viscosity, potentially lubricating the interactions between angular particles. To determine this effect, several samples with increasing amounts of EC70 and its effect on their viscosity would have to be evaluated. Furthermore, due to evaporation around the edge of the plate, the ink could have started to solidify, showing an apparent increase in the viscosity. The EC70 may have helped prevent the solvent evaporating showing a lower viscosity to just the solvent and carbon slurry.

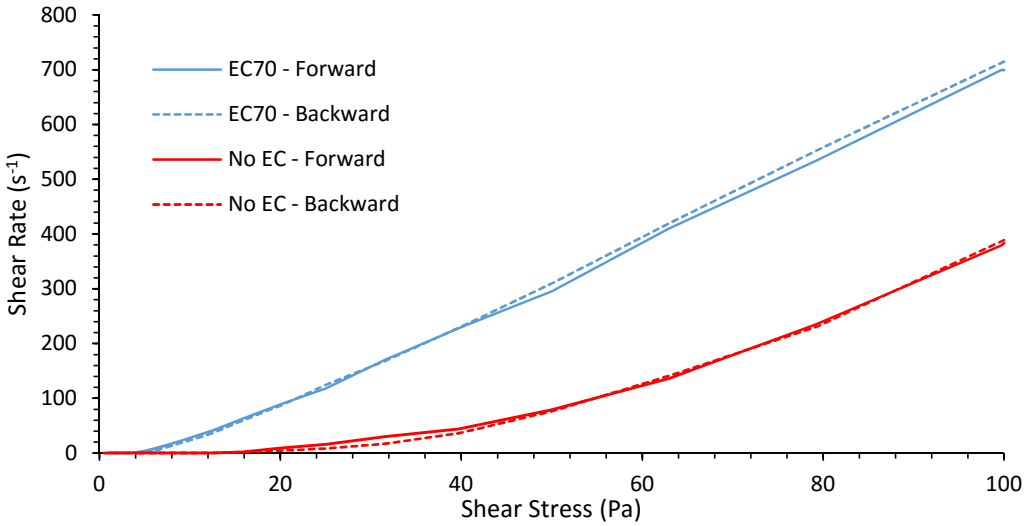

Figure 4.21 - Effect of shear stress on the shear rates of carbon and EC70 slurries.

The shear stress vs shear rate results in Figure 4.21 shows that the shear rate increases with increased shear stress. Furthermore, the slurry without the EC70 shows shear thinning characteristics as signified by the non-linear increase in shear rate with shear stress. To determine what type of shear thinning, the results were plotted on a logarithmic scale and with the axis swapped as shown in Figure 4.22.

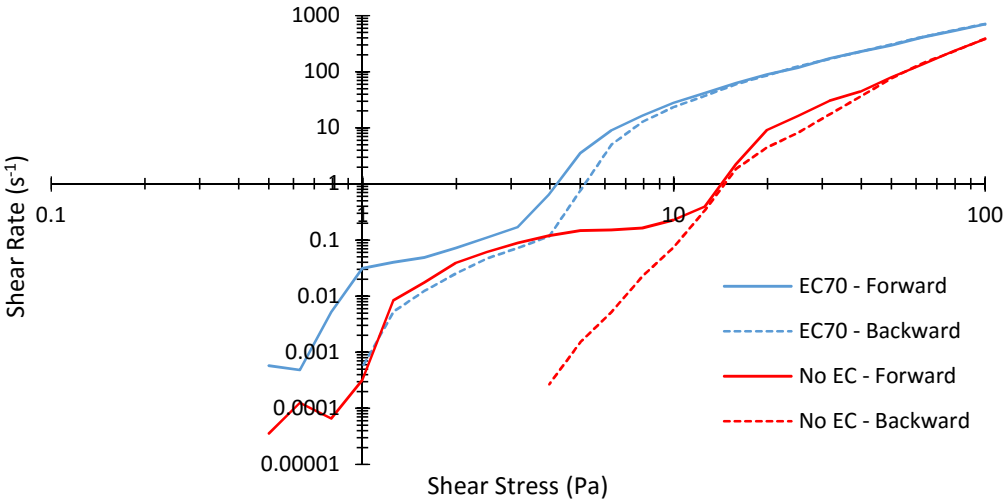

Figure 4.22 - Plasticity of carbon and EC70 slurries.

Using a logarithmic scale shows that although the slurry without EC70 shows shear thinning properties, so does the EC70 containing slurry. Unlike a Newtonian liquid, which would be linear, the shear thinning properties of the slurries have non-linear plots. The results indicate that both slurries were consistently shear thinning

The final rheological results generated were the effect of angle frequency on the storage and loss moduli. Unfortunately, due to time constraints, the slurry only containing carbon (no EC) could be analysed. The results show that carbon slurry displays visco-elastic properties, as indicated by the storage modulus being higher than the loss modulus. Furthermore, both moduli were slightly parallel which was an indication that the slurry shows gel-like properties. By altering the quantity of the materials in the ink, the visco-elastic properties could be altered so the ink behaves more like a liquid, making it easier to print.

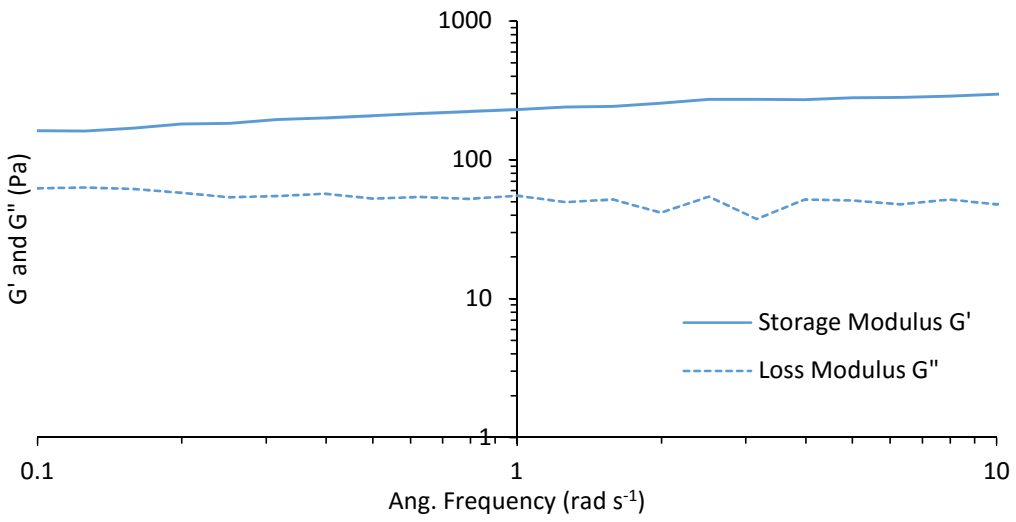

Figure 4.23 - Small amplitude oscillatory shear of carbon slurry.

This work was to initially establish the effect of EC70 on the rheological properties of a terpineol-carbon slurry. As the anode ink was developed further, they diverged away from using terpineol, as texanol was a low cost alternative, and using smaller amounts of EC70, due to the very little change in apparent viscosity. Furthermore, the work with PTFE (discussed later in this chapter) shows that altering the material quantities can have a very significant effect on the final ink printing properties and electrode layer produced. Although the slurries

were not representative of the final anode ink, due to the addition and alteration of materials, this work was still relevant. It highlights how the rheological properties of the final electrode ink can affect the quality of the printed electrode. Furthermore, it shows that different ink properties were achieved with relatively small additions of ink components, indicating that the interactions between the materials in the final formulation would be complex.

4.3.1.3 *Electrochemical Analysis of Screen Printed Anode*

To determine whether the anode developed was suitable, a cell was constructed using the developed candidate anode with a commercially used cathode and evaluated electrochemically by polarising the cell. Due to ink suspension and consistency issues regarding the substitution of Norit to an electrocatalyst, the non-aqueous ink formulation was evaluated using 10 % Pt/C_b. The screen printed anode fuel cell was used with 1 M $NaBH_4$/3 M $KOH_{(aq.)}$ at room temperature and were submitted to current hold (Figure 4.24) polarisation (Figure 4.25) and GEIS (Figure 4.26) analysis. The fuel/electrolyte was recirculated through the fuel cell at a volumetric flow rate of approximately 250 $cm^3.min^{-1}$.

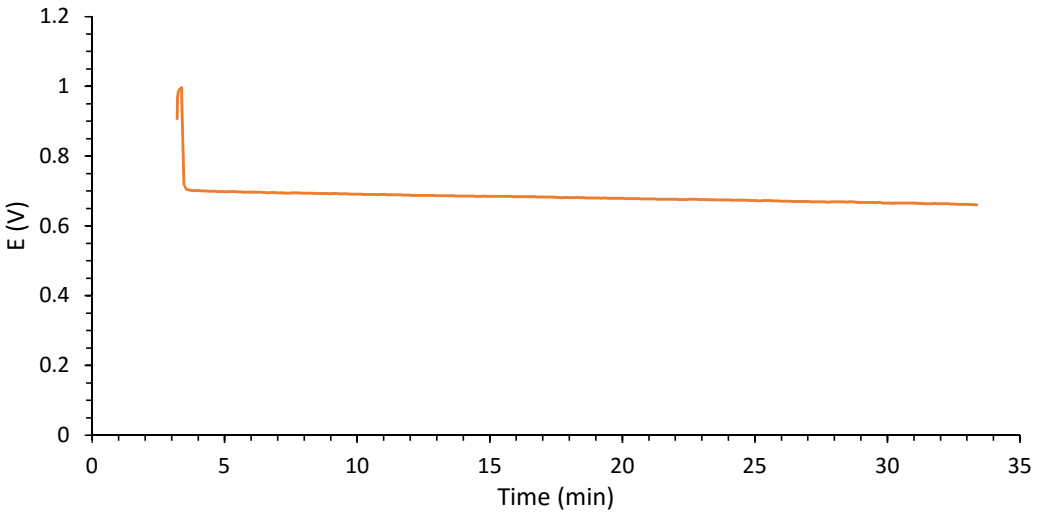

Figure 4.24 – Current hold of screen printed anode fuel cell at 0.1 A (81.83 $mA.cm^{-2}$) at room temperature, using 1M $NaBH_4$/3 M $KOH_{(aq.)}$ at approximately 250 $cm^3.min^{-1}$ flow rate.

The current hold results show that initially, the screen printed anode fuel cell reached an *OCP* of 1.00 V, which was lower than the theoretical *OCP* of 1.64 V for borohydride. Once the current was applied, 0.1 A (81.83 $mA.cm^{-2}$), the potential dropped to 0.70 V and declined over

the 30 mins to 0.66 V. Although the decrease in potential appeared to be low, fuel cells are expected to run for several thousand hours and so the rate of potential decline experienced implies that the electrode would degrade substantially over the expected duration of an operating fuel cell.

The polarisation curve of the screen printed anode fuel cell didn't show the stereotypical curve observed for fuel cells, one which contains activation/kinetic, ohmic and mass transport regions (such as that in Figure 4.11), within the potential range evaluated. The curve indicates that the rate of reaction was relatively fast, due to no observable kinetic region. Most of the curve appears to be due to ohmic losses due to the steady gradient with no mass transport region and therefore the fuel cell was not limited by the amount of borohydride or oxidant present. The current reached before the potential limit was low, with a hydrogen fuel cell having a respectable 0.2 $A.cm^{-2}$ this electrode should be generating approximately 2.4 A. The results of both the relatively linear potential and low currents are observed in the power curve which had no peak power within the current range and having a relatively low value.

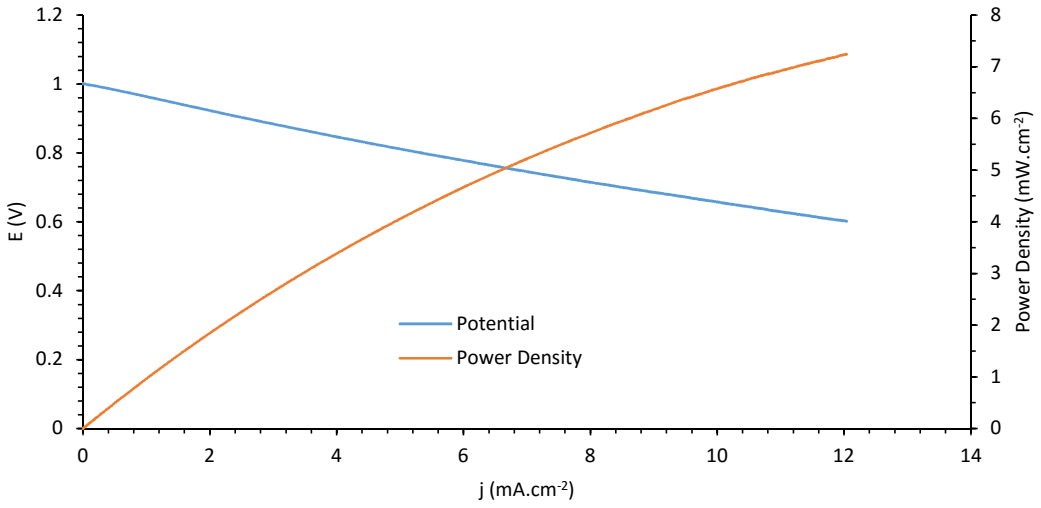

Figure 4.25 - Polarisation of screen printed anode fuel at room temperature, using 1M $NaBH_4$/3 M $KOH_{(aq.)}$ at approximately 250 $cm^3.min^{-1}$ flow rate and an A_{geo} = 12.22 cm^2.

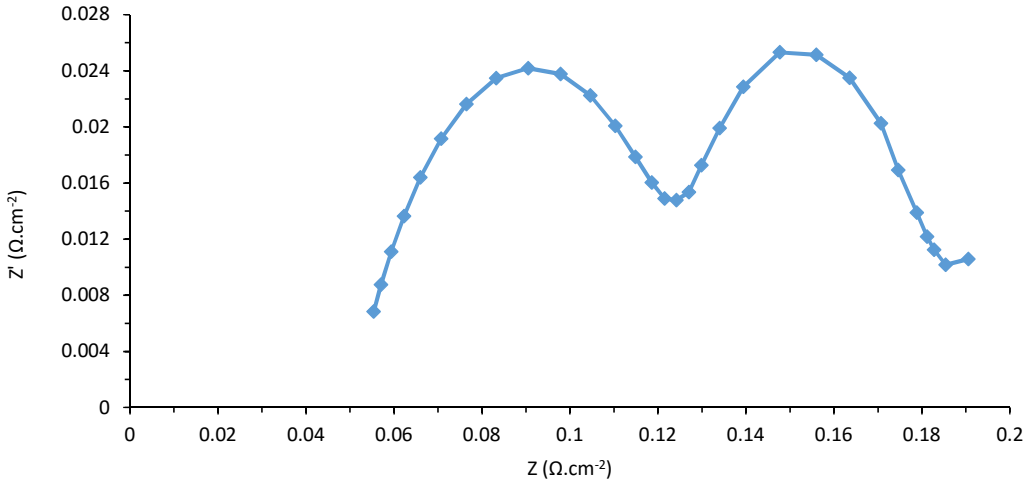

Figure 4.26 - GEIS of screen printed anode at -0.1 A, 10 kHz – 0.1 Hz at 6 points per decade, room temperature, using 1 M $NaBH_4$/3 M $KOH_{(aq.)}$ at approximately 250 $cm^3.min^{-1}$ flow rate.

The GEIS results show that the fuel cell had a total ohmic resistance 55.4 $m\Omega.cm^{-2}$ and two electrochemical processes occurred, as indicated by the two arcs. The final point of the GEIS plot may also indicate the effect of diffusion/mass transport of the borohydride/oxidant. Typically for hydrogen AFCs, the first arcs are much smaller followed by a larger second arc. This would show that the relatively fast HOR on the anode, generating a small peak, was followed by the slower more resistant ORR, generating a large arc. The two arcs are equally large, which may be due to the screen printed anode being more resistive and kinetically slower than desired, making it as slow as the cathode. The electrocatalyst could have performed well but the wettability or surface area of the electrode may have lowered the performance of the printed layer.

To determine if the screen printed anode's relatively low performance was due to the anode or the fuel cell system setup, it needed to be compared to another. However, due to DBAFC not being a commercially used product, it was not possible to supply a DBAFC specific anode. Therefore, commercially used hydrogen AFC electrodes were sourced. The commercially used anode was based on a Pt on activated carbon electrocatalyst; however, the material loading and manufacturing process was not known. The hydrogen AFC anode was constructed of two layers, an AL and a GDL. The commercially used electrodes were made into a fuel cell and polarised under the same conditions as the screen printed anode. These results were then compared to those generated for the screen printed anode (Figure 4.27).

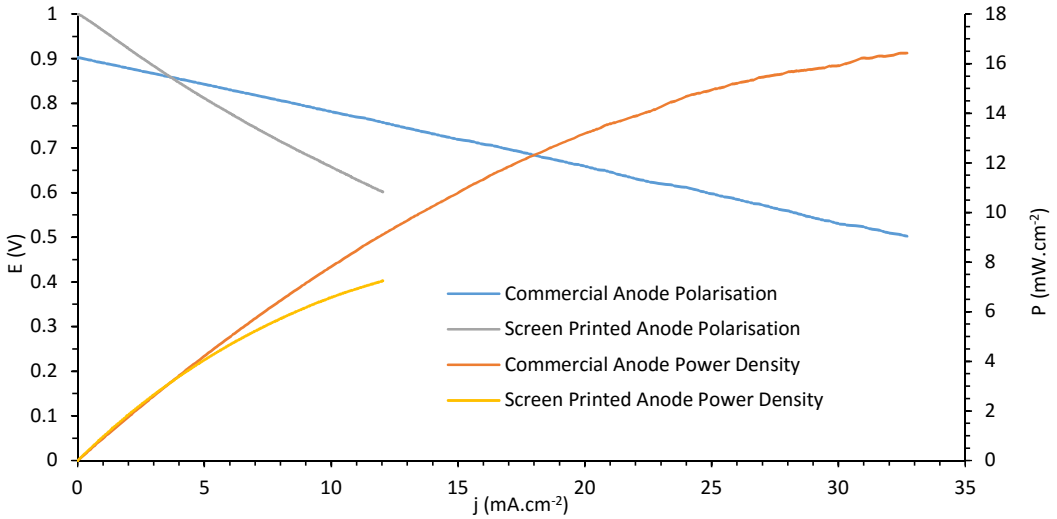

Figure 4.27 - Polarisation and power curve comparison of the screen printed and commercially used available anodes.

The polarisation curves (Figure 4.27) show that the screen printed anode fuel cell managed to achieve a higher *OCP* compared to the commercially used anode fuel cell. However, the screen printed anode fuel cell experienced increased ohmic losses, making the polarisation curve gradient steeper, reducing the current that can be drawn, hence reducing the power output. Both polarisation plots show a similar polarisation trend with the potential curve being relatively linear, though the screen printed anode fuel cell shows slight non-linearity towards the end of the curve. This indicates that potentially both anodes have relatively quick activation rates and do not experience any mass transport limitations within the potential range.

The GEIS of the different fuel cell configurations (Figure 4.28) shows that the commercially used anode fuel cell shows that the screen printed anode has a slightly higher series resistance of 55.6 $m\Omega.cm^{-2}$ compared to the commercial anode with 54.0 $m\Omega.cm^{-2}$. The GEIS plot of the commercially used anode fuel cell in Figure 4.28 appears to show no distinct semi-circular arcs related to electrochemical processes. This could be due to being very conductive or any processes occurring at a higher frequency outside of the experimental range. The series resistance of the electrodes were relatively large. This could be due to the fuel cell rig design as the electrolyte chamber is wide leading to a 20 mm gap between the electrodes. Since the

electrolyte generates most of the series resistance, the large volume of electrolyte between the electrodes would significantly contribute to the series resistance.

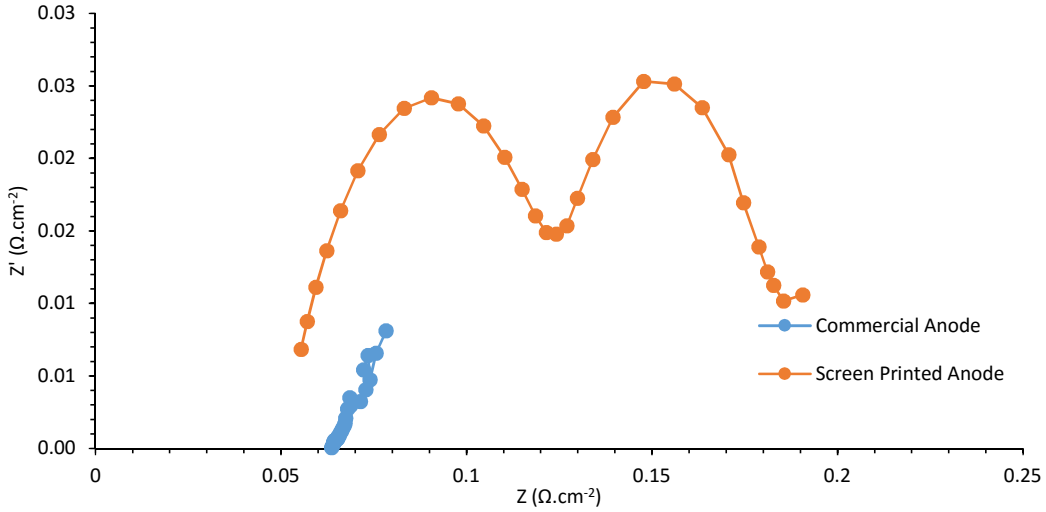

Figure 4.28 - GEIS comparison of the screen printed and commercially used anodes at -0.1 A, 10 kHz – 0.1 Hz at 6 points per decade, room temperature, using 1 M $NaBH_4$/3 M $KOH_{(aq.)}$ at approximately 250 $cm^3.min^{-1}$ flow rate.

One method to increase the current that can be drawn from a fuel cell was to increase the amount of electrocatalyst. Rather than changing the electrocatalyst loading in the formulation, causing a reformulation which could take time to develop, a thicker electrode could achieve the same effect. Therefore, an electrode with double the thickness was manufactured using the same anode ink previously developed. However, after the initial layer was printed, a second layer was printed on top, doubling the thickness of the final anode. The new double layer (2L) screen printed anode was evaluated under the same conditions as the single layer and the commercial. The comparison of the single and double layer screen printed and commercially used anode fuel cells are shown in the GEIS (Figure 4.29), potential polarisation (Figure 4.30) and power curve (Figure 4.31).

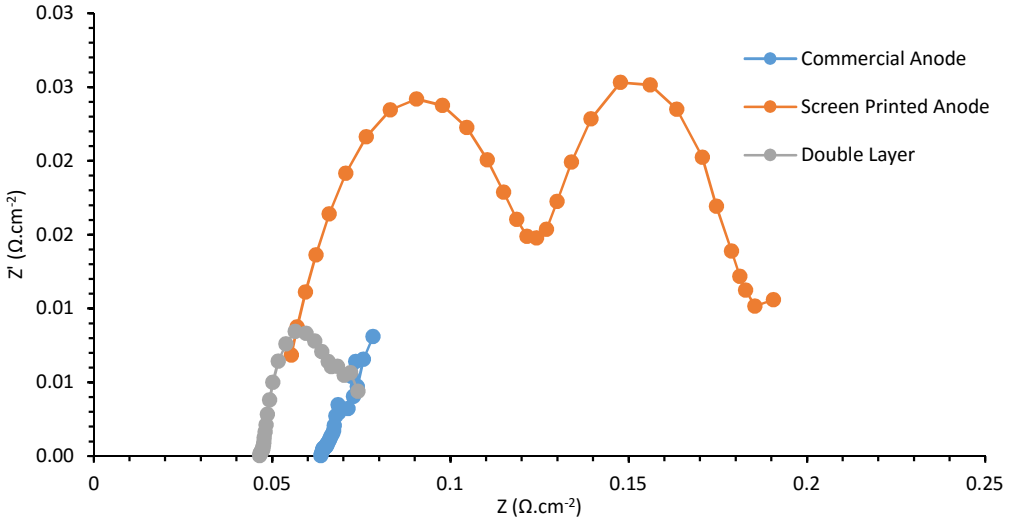

Figure 4.29 - GEIS of a single layer, double layer screen printed and commercially used anodes in borohydride.

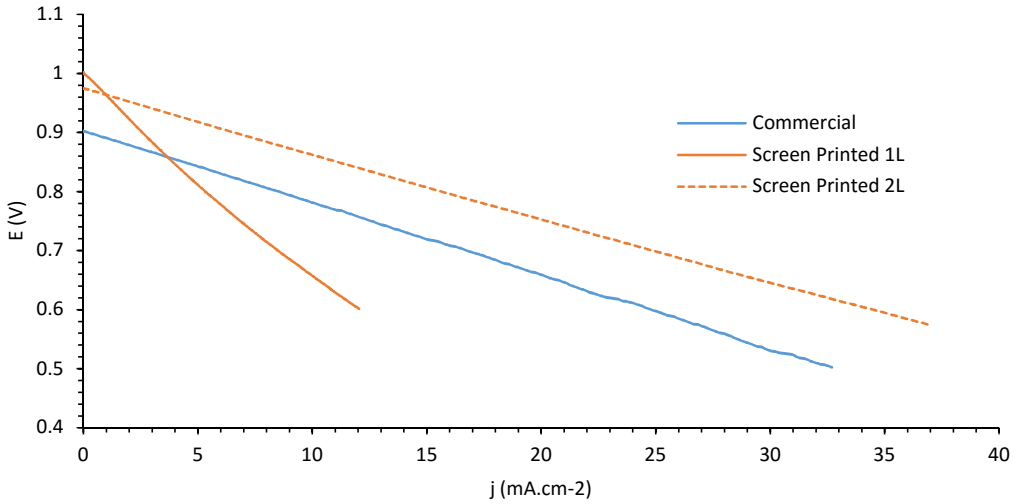

Figure 4.30 - Comparison of potential polarisation of commercial, single layer and double layer screen printed anode fuel cells.

The double layer screen printed anode fuel cell shows a significantly improved performance compared to the single layer. Although the *OCP* was slightly less compared to the single layer, at 0.97 V and 1.0 V respectively, the double layer anode experienced far less ohmic losses. Despite the commercially used and double layer screen printed anode fuel cell experiencing approximately the same amount of ohmic loses, due to the double layer anode starting at a higher *OCP*, the power was improved significantly as shown in Figure 4.31.

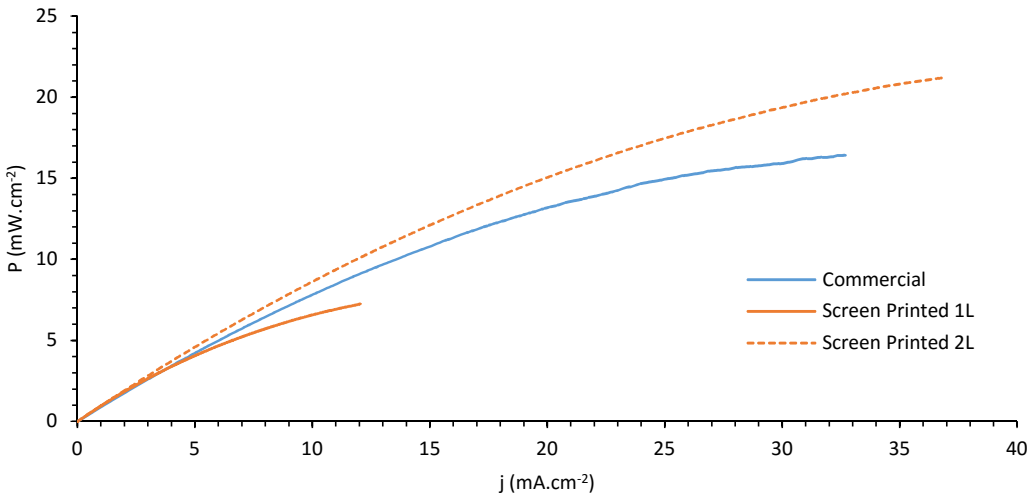

Figure 4.31 - Comparison of power curves of commercial, single layer and double layer screen printed anode fuel cells.

Printing a double layered anode improved the performance compared to the single layer, to the extent whereby it outperformed the commercially used electrode with the electrochemical properties summarised in Table 4.9.

Table 4.9 - Electrochemical properties of commercially used and screen printed single layer and double layer anode fuel cells using borohydride.

Anode	*OCP* (V)	Peak P		I at Peak P		E at Peak P	
		W	$mW.cm^{-2}$	A	$mA.cm^{-2}$	V	$mV.cm^{-2}$
Commercial	0.90	0.201	16.4	0.400	32.7	0.502	41.1
1L	1.00	0.088	7.2	0.147	12.0	0.602	49.2
2L	0.97	0.259	21.2	0.451	36.9	0.575	47.0

Several observations were made during the operation of the fuel cell. The first was that the generation of hydrogen caused foam to appear. This indicates that the Tergitol was not removed from the electrode whilst in the furnace. Therefore, to remove the Tergitol the anode was rinsed with water prior to being used in the fuel cell.

By printing another layer on the anode, the performance had significantly improved using the same ink formulation. This highlights the importance of the manufacturing process and

although an optimal electrode formulation can be produced, if the correct manufacturing process is not used it will produce a poor electrode. Furthermore, the results from this research have developed an anode ink formulation which was not only suitable for screen printing but can produce an anode which can be used as a base formulation for a DBAFC anode. Although the power generated was low, compared to hydrogen AFCs, this may not be solely due to the electrode but could also be an effect of the fuel cell operating conditions, including the evolution of hydrogen gas potentially blocking active electrode sites.

4.3.2 Development of Cathode Ink Formulation

Originally a commercially used electrode was used in the fuel cell when evaluating a candidate anode. However, the cathode supplier stopped production of the cathode. As such an in-house manufactured cathode had to be designed and developed.

4.3.2.1 *Reproducing Commercially used Cathode*

The cathode active layer ink (CALI) was based on a commercially used cathode, which ceased to produce a MnCoO specific formulation. The new formulation was based on a Pt which, although would have been suitable as an electrocatalyst for the cathode, was not specific to the ORR and lead to BOR occurring. Although the MnCoO is not as electrocatalytic active towards the ORR as Pt, it still had sufficient electrocatalytic activity to be used. Furthermore, it was selective towards ORR which was desirable due to the exposure to the borohydride fuel. As such, the MnCoO was used as the electrocatalysts for this DBAFC. Both the formulation and the manufacturing process was known and the cathode was reproduced in-house (Table 4.10). Unfortunately, the same equipment used to manufacture the commercially used CALI, namely a Z-blade mixer which was used to mix highly viscous fluids and an ultrasonic probe which used high energy ultrasonic waves to break up large solid particles, were not available. In place of these pieces of equipment, a Thinky mixer and an ultrasonic bath were used in place of the Z-blade mixer and ultrasonic probe respectively.

Table 4.10 - Formulation and manufacture of commercially used CALI.

Material	Quantity (wt. %)	Commercially used Manufacturing Process	In-house Manufacturing Process
IPA	75.00		

MnCoO	25.00	Sonicated using an ultrasonic probe for 20 mins.	Sonicated in an ultrasonic bath for 20 mins.
IPA+ MnCoO Pre-mix	60.41	Mix with a Z-blade mixer until homogenous.	Mix in Thinky for 1 min at 2,000 rpm.
Carbon Black	2.35		
MWCNT	5.48		
IPA	24.57		
60 wt. % $PTFE_{(aq.)}$	7.20		Mix in Thinky for 1 min at 2,000 rpm.

This method was used to replicate the cathode in the lab, with the alteration of sonicating the MnCoO and IPA and spin mixing the carbons and PTFE compared to vibro-milling and using a Z-blade respectively. However, the resulting CAL was physically very different from one that was commercially manufactured, which crumbled easily and was very difficult to roll. A cathode managed to be manufactured and compared to the commercially used cathode by measuring the open circuit (Figure 4.32) and polarisation (Figure 4.33) under the same conditions (38 mM $NaBH_4$/30 wt. % KOH, room temperature, 5 $cm^3.min^{-1}$ electrolyte flow, 0.4 $L.min^{-1}$ and 2 bar air flow and pressure).

The time taken to reach *OCP* of two in-house manufactured cathodes were evaluated against a commercially used cathode. The results in Figure 4.32 show that while the fuel cell using the commercially used cathode took less than 5 mins to obtain an *OCP* of approximately 0.95 V, the two fuel cells using the in-house cathodes took longer with the first taking approximately 10 mins and the second approximately 25 mins. Furthermore, the *OCP* of the in-house manufactured cathodes was much lower, approximately 0.65 V. The long duration taken for the cell to reach *OCP* increases the amount of time before power can be drawn. This would restrict the fuel cell from applications where power would be required almost instantaneously. Low resistance associated with screen printed electrode could be due to a low porosity, particle connectivity and a reduction in the number of triple boundaries [123, 174].

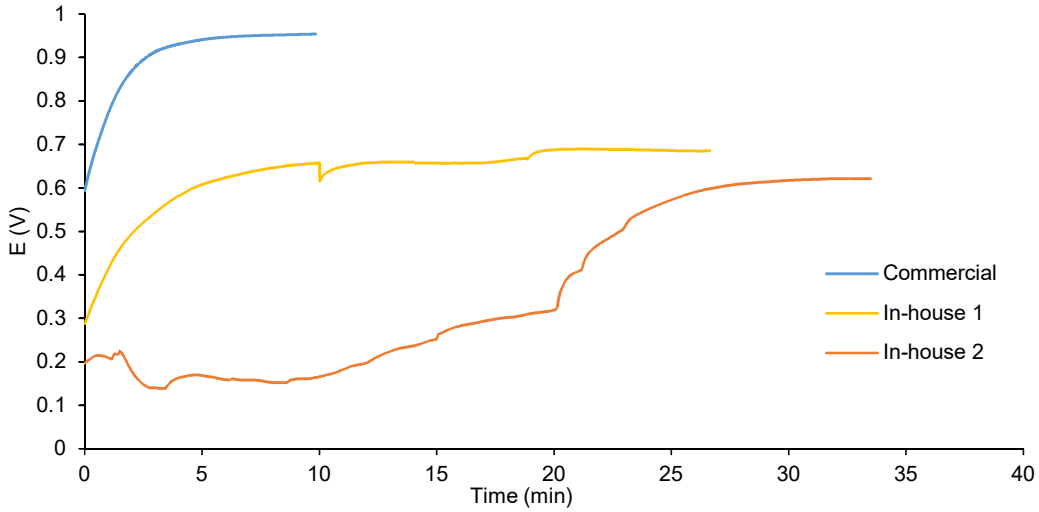

Figure 4.32 - Commercially used and in-house cathode *OCP* over time using 38 mM $NaBH_4$/30 wt.% $KOH_{(aq.)}$.

The polarisation of the commercially used and in-house cathodes are shown in Figure 4.33. The commercially used cathode fuel cell reached higher current densities compared to the in-house cathode fuel cell. The low *OCP* of the in-house cathode fuel cell reduces the peak current density that can be drawn as the potential range had been reduced (the potential limit was 0.65 V). Furthermore, the ohmic loss of the in-house cathode fuel cell was significantly more compared to the commercial, which was shown by the in-house cathode fuel cell gradient being considerably steeper.

The fuel cell using the in-house cathode didn't reach the OCP_{theo} (which for borohydride was 1.64 V) and therefore only produces low current densities by the 0.65 V limit. As only the method of manufacture had changed, not the formulation, the *OCP* and polarisation results show that the in-house method does not produce the same cathodes as the commercially used cathode. Therefore, a new in-house method was developed to produce a suitable cathode which uses the MnCoO. Since extensive work was done developing an anode screen printable ink, insights gained were used to develop a screen printable cathode active layer ink. As the in-house GDL had the same consistency and appearance as the commercially used GDL, it was decided to focus solely on the CAL. Therefore, a CALI was developed to be screen printed onto the GDL.

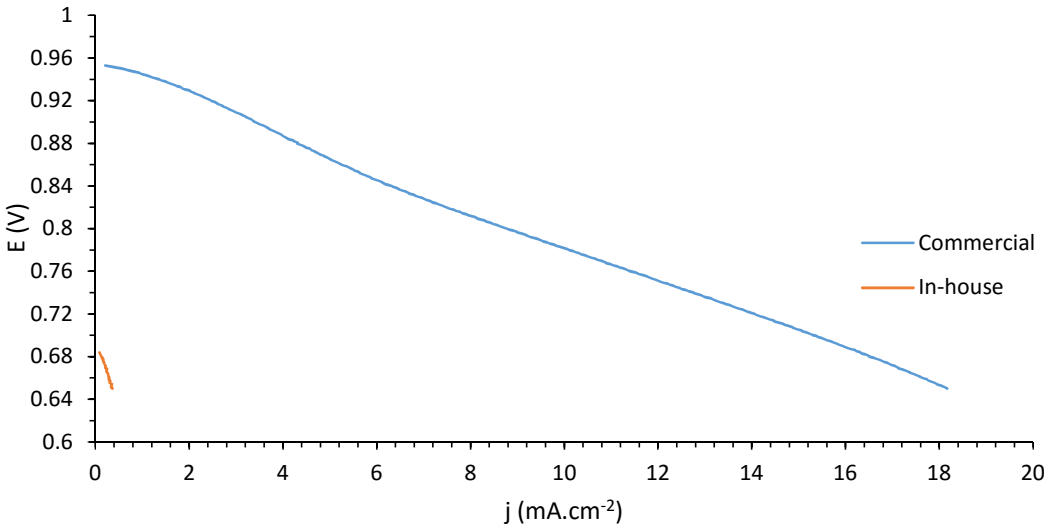

Figure 4.33 - Commercially used and in-house cathode polarisation curve comparison in 38 mM $NaBH_4$/30 wt.% $KOH_{(aq.)}$.

4.3.2.2 *Cathode Ink Formulation*

The MnCoO electrocatalyst, unlike the other electrocatalysts used previously in this work, was not electrically conductive, which was a necessity of an electrocatalyst. However, the electrode would conduct electricity if it were to be mixed with an electrically conductive carbon. As such the MnCoO and carbon, in this case, carbon black, formed the basis for the CALI. As with the anode ink, additional materials were required to make it into a suitable screen printable ink. Water was used as the solvent to suspend the material, Tergitol TMN6 to aid suspension, $PTFE_{(aq.)}$ for the permanent and HEC for the green binders. Furthermore, the order of addition was similar to anode manufacture and all the CALI discussed used the same manufacturing method. This led to the formulation in Table 4.11.

Table 4.11 – CALI formulation. And manufacturing process.

Material	Quantity (wt. %)	Manufacturing Process
HEC	1.16	Sonicate 8 mins 65 °C
Water	48.49	
Tergitol	6.93	mix 30 s
MnCoO	27.71	Sonicate 16 mins @ RT + 1 min mix
$PTFE_{(aq.)}$	11.84	mix 30 s

Carbon black	3.86	mix 30 s
Electrode	39	
Waste	61	

The resulting ink suspended well and, although had a slightly lower viscosity, was acceptable for printing. The ink was then printed on a nickel substrate using the large mesh screen twice to create a double layered electrode. During printing, bubbles formed after the screen snap off which would indicate that there was an excess of Tergitol. The printed cathode was then put in an oven for 30 mins at 40 °C to allow the water to evaporate. Although the electrode did not go into the furnace as the final cathode would have done, to sinter the PTFE, it was sufficient to evaporate the water, leaving a dry cathode. This cathode was then placed under a light microscope (0.65 × and 5 × magnification) to observe the surface characteristics (Figure 4.34).

The images show pitting, where the electrode was either thin or absent and exposes the substrate underneath. This was undesirable as a uniform, homogenous layer was required and as pitting would, in a full cathode, expose the GDL underneath which could lead to electrode weeping. These pits were most likely due to the bubbles formed during the printing stage due to an excess of Tergitol and so had to be reduced.

Several different CALIs were developed, altering the amount of Tergitol, solvent/solvent type and green binder. None of the CALI formulae developed produced a cathode without surface defects; however, out of the formulation in Table 4.11 showed the least and hence was the CALI used.

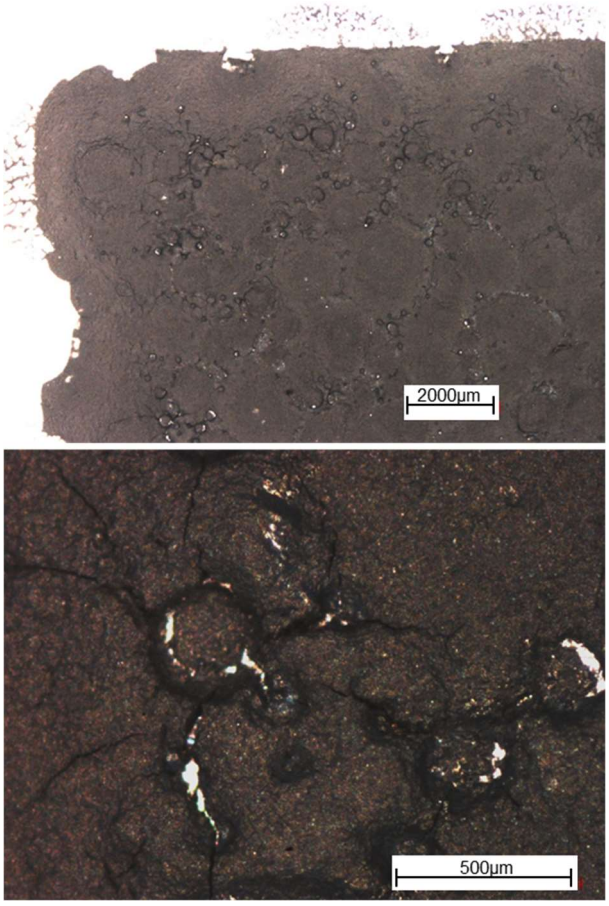

Figure 4.34 – Initial CALI formulation light microscope images.

4.3.2.3 *Cathode Ink Observations*

Several interactions between the materials and manufacturing process with the ink were observed. One of which was the use of texanol and water as solvents. Initially the cathode ink was produced using water; however, texanol was investigated as an alternative to determine if changing the solvent could reduce the surface defects. Both solvents showed PTFE agglomeration and readability issues. Most of the ink developed used water as a solvent and showed defects on the electrode surface. Replacing the solvent with texanol, and consequently, the green binder to EC70 did not improve the ink printability and resulted in an electrode which had no uniformity (Figure 4.35). Different screens and texanol based formulae were developed but showed many of the same surface defects, many of which to a greater extent.

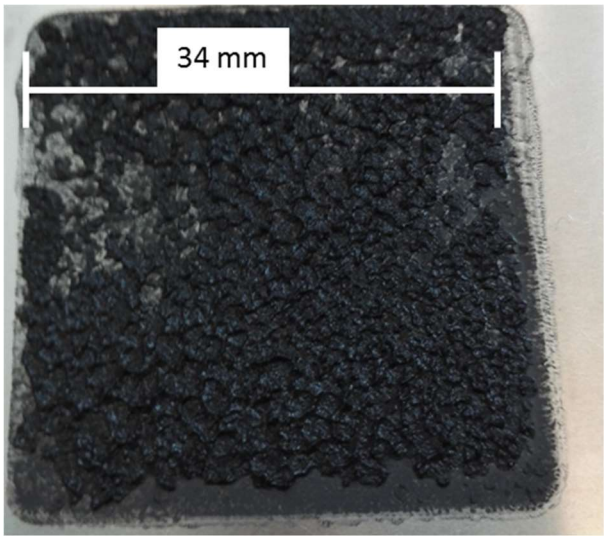

Figure 4.35 - Texanol CALI image (print was a 34 × 34 mm square) showing no uniformity of ink.

An interesting observation was the effect of the manufacturing process. Due to the spectacled effect of heat on PTFE agglomeration, the manufacturing process was altered to reduce the amount of heat produced as much as possible. This led to a change in manufacturing process highlighted in Table 4.12.

Table 4.12 - Comparison of cathode texanol based ink manufacturing process.

Material	Original Process	New Texanol Process
EC70	Pre-mix by dissolving the EC70 in texanol and Tergitol at high heat and stirring. Allow to cool.	Pre-mix by dissolving the EC70 in texanol at high heat and stirring.
Texanol		
Tergitol		Thinky mix for 30 secs at 2,000 rpm.
MnCoO	Thinky mix for 1 min at 2,000 rpm.	Thinky mix for 2 mins at 2,000 rpm. Allow to cool.
Carbon black	Thinky mix for 30 secs at 2,000 rpm.	
$PTFE_{(aq.)}$	Thinky mix for 30 secs at 2,000 rpm.	Thinky mix for 2.5 mins at 500 rpm.

The main difference between the new and old manufacturing methods was the dispersion of materials, apart from the $PTFE_{(aq.)}$, whilst the solvent was warm. This should have increased the mobility of the materials and aided in the mixing. The suspension was then allowed to cool

to room temperature for a prolonged period, followed by the $PTFE_{(aq.)}$ addition. The $PTFE_{(aq.)}$ was then mixed at a lower rotation rate and for a longer period. The decrease in mixing speed was to ensure that less heat was generated by the friction of materials on the pot walls and the Thinky mixer itself. This new manufacturing process was used to produce the cathode inks.

The literature stated that the green binder content could affect the number of cracks on the surface of the electrode [134, 141]. As such, during the aqueous ink development, the HEC was increased (Figure 4.36) and decreased (Figure 4.37) in the formulation to determine its effect on surface defects.

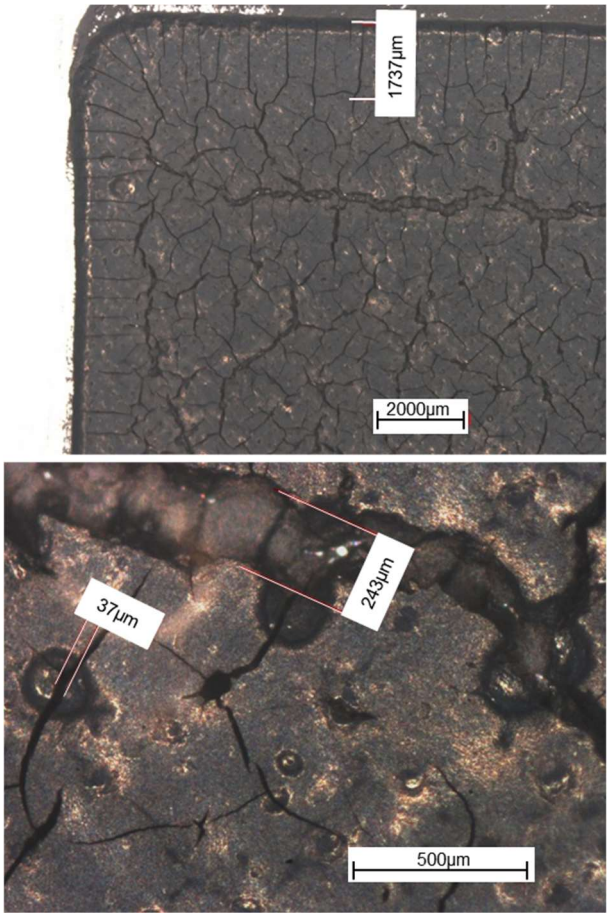

Figure 4.36 - Increase in green binder content CALI microscope images.

This ink shows the formation of large cracks, approximately 5 × more than the fissures. Although the width of the cracks was significantly larger, they do not seem to penetrate

through the electrode. This could indicate that the increased green binder content may increase the surface tension on the surface of the electrode, leading to larger cracks to form. However, in the bulk of the electrode, the green binder may have increased the particle network strength, keeping the structure of the electrode underneath the surface.

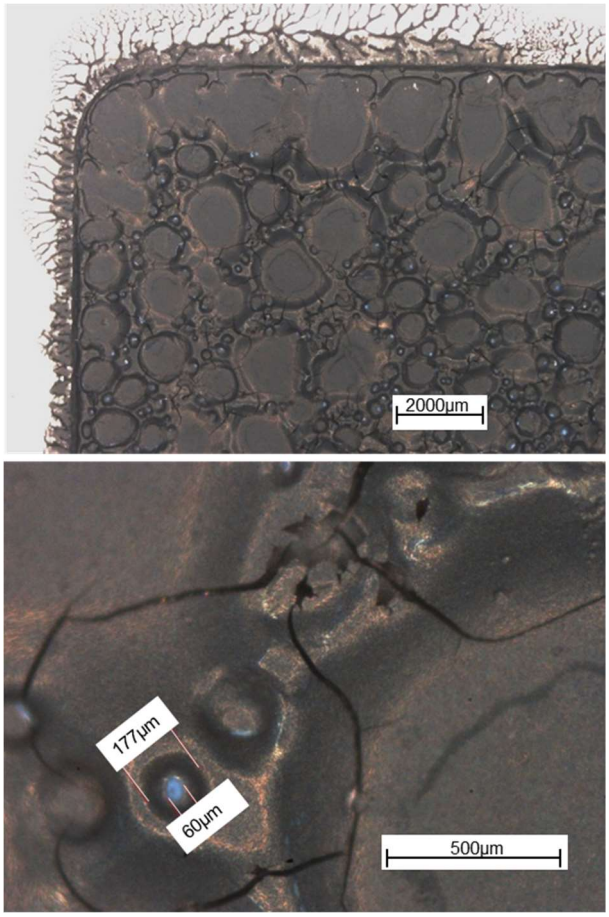

Figure 4.37 – Removal of green binder CALI microscope image.

Conversely, the HEC was completely removed from the formulation. During printing, there were a considerable amount of bubbles being produced during the screen snap stage. This supports the theory that the HEC and Tergitol interact, with increased HEC reducing the amount of Tergitol available to form bubbles. After the electrode was put in the oven, light microscopy images were used to evaluate the electrode's structure (Figure 4.37). Although still present, the number of fissures decreased considerably and there was a complete removal of the large cracks seen in the previous ink electrode. Furthermore, the fissure border around the edge of the electrode had significantly reduced. Although there was an acceptable

geometry definition, there was severe solvent leakage, as seen by the branching away from the bulk of the electrode. One of the main observations of this electrode was the very particular characteristics of the surface. The other inks produced an electrode surface which was planar with defects, such as pitting and cracks, which occurred at sharp angles. However, the defects in the electrode's surface seem to have occurred at a less steep angle (Figure 4.38). This could be due to interactions of the ink with the screen during printing. Removal of the HEC would have decreased the particle network strength. Furthermore, the increase in Tergitol activity, due to the removal of HEC, would have caused more Tergitol to stay on the screen during printing. Removing the HEC may have removed the small pitting, such as that observed in the reduced Tergitol ink, but increased the pit size significantly as to change the profile of the electrode surface.

Figure 4.38 - Defects in increased HEC electrode's surfaces (left) compared to no HEC binder(right) not to scale.

In some of the pits, a white material was observed which was most likely the PTFE. This shows that the HEC was not only responsible for several electrode structural properties, but it aids the dispersion of PTFE in the ink suspension. Removal of HEC had localised the PTFE. Should the electrode be put into a furnace, the PTFE would only sinter in these localised PTFE pockets, reducing the amount of PTFE around other areas of the electrode. This would consequently reduce the electrode's structural rigidity and would make the electrode more susceptible to degradation. Furthermore, the PTFE was responsible for the electrode wettability. Should the PTFE not be evenly dispersed this would lead to areas of high and low hydrophobicity, which could lead to areas of electrode weeping and simultaneously electrode starvation. Conversely, the smaller PTFE particles could be held within the suspension whilst the larger PTFE particles drop out of suspension, collecting on the top of the electrode which eventually dries. The HEC in this instance would aid in suspending the carbon and small PTFE particles. Due to the several different functions of the green binder, it was vital in the ink and must be present to help disperse the PTFE.

Tergitol was required to prevent the ink from forming a gel but not so much as to cause bubbles during the screen snap which was thought to cause the pitting on the electrode. Therefore, half the amount of Tergitol was added to the reduced water CALI. This would have produced a 43 wt. % electrode. The resulting ink did not agglomerate during manufacture and was printed on a nickel substrate. The electrode was then heated in an oven for 30 mins at 40 °C to remove the water and observed under a light microscope (Figure 4.39).

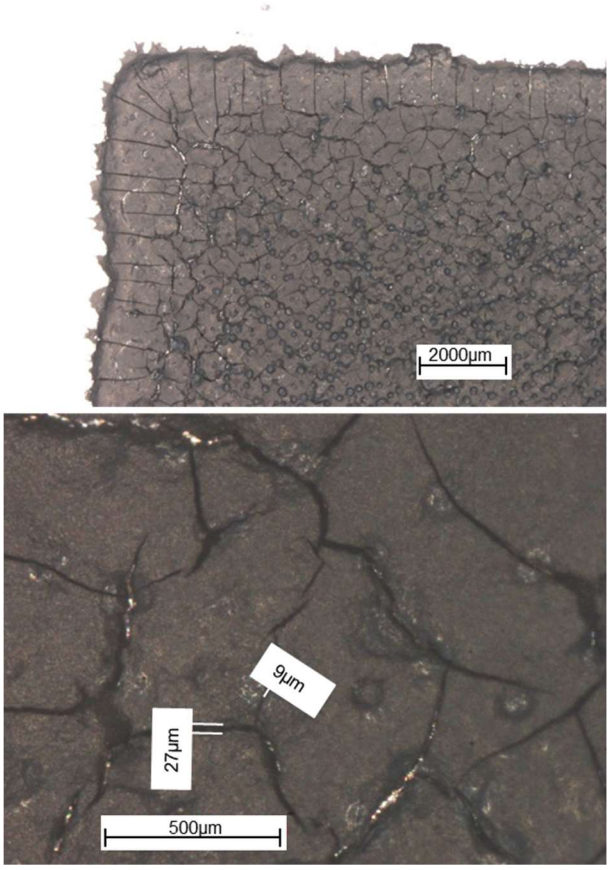

Figure 4.39 – Small Tergitol quantity CALI microscope images.

The electrode printed shows a relatively good geometry definition. The perimeter of the electrode had a border of cracks radiating from the outer edge of the electrode inwards. Furthermore, there were small fissures across the entire surface of the electrode. This was not seen in the initial CALI formulation, or at least not to the same extent. However, though there were far more pits in this formulation compared to the initial CALI, they do not go down through to the nickel substrate underneath. This was more favourable as it would be less likely

to experience electrode weeping. Furthermore, these pits would also slightly increase the surface area of the electrode which could aid kinetics.

Although a large number of pits may not have been detrimental to the electrode, the fissures would be as they go through the electrode completely (which was highlighted in the microscope image as the bright areas in the fissures). Therefore, the formulation was developed further to reduce the cracking on the surface, or at least the removal of cracks which penetrate the electrode's surface.

4.3.3 Summary of Material Interactions

Several different inks were developed in this works with various results. There have also been some key observations in material interactions which are highlighted in Table 4.13.

Table 4.13 - Material interactions in cathode inks.

	HEC	**Water**	**Tergitol**
Water	Increasing the amount of HEC increases the viscosity of the ink.		
Tergitol	HEC interacts with the Tergitol, reducing bubble and pit formation.	Too much Tergitol causes bubbles and pitting during screen snap.	
$PTFE_{(aq.)}$	HEC aids the dispersion of the PTFE in the ink. Increasing the amount of HEC increases PTFE dispersion.	The suspended PTFE can easily agglomerate too much water was present.	Tergitol was key to preventing the agglomeration of PTFE. Increasing Tergitol increases PTFE stability.

Altering a single material affected multiple ink properties. For example, increasing the Tergitol would stabilise the PTFE and prevent agglomeration whilst increasing pitting defects on the electrode's surface. There was a synergetic effect between the materials which makes the development of a suitable ink more complex as changing one aspect would have multiple consequences. This highlighted that it was essential to understand the effects of materials not only have on each other but the physical printing and final electrode properties.

4.3.4 Cathode Surface Repair

Several different cathode inks were produced to decrease the number of defects on the electrode surface; however, altering one aspect of the formulation affected several different properties and therefore a formulation which would produce an electrode with no surface defects was not identified. However, there are several methods to produce an electrode without surface defects. One of which was to print an electrode and then repair any pitting, fissures and cracks present, which was the focus of this section.

Out of the various formulae developed, the ink with the least amount of surface defects was used for the effect of surface repair. First, the electrode was prepared by adhering the GDL to the cathode substrate (as discussed in Section 4.2.1.2). After the GDL had been sintered to the substrate in the furnace, a double layered CALI1 ink electrode was printed in the centre. The electrode was then placed in an oven for 30 mins at 40 °C to remove the water. As with the initial CALI ink seen printed previously (Figure 4.34) fissures were observed on the surface of the electrode which was printed on the GDL (Figure 4.40).

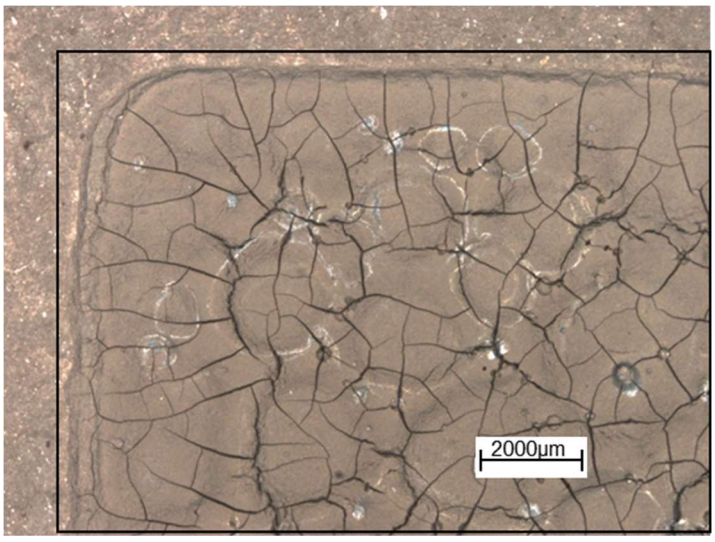

Figure 4.40 – Initial CALI printed onto a GDL with the black border indicating the edge of the electrode.

The CALIs developed in Section 4.3.2 were originally printed directly onto the electrode substrate and not onto a GDL as it would have been done for a functioning electrode. This was

to increase the ease at which the electrodes were produced and reduce material wastage during the ink development. Although printing the electrode onto a GDL at this point was acceptable for the development of the inks, it was not wholly representative of the final electrode. After the ink had been printed onto a GDL, the solvent diffused away from the electrode through the GDL. This would cause the electrode to dry out prematurely and could potentially cause an increase in surface defects. If the inks all printed directly onto a nickel sheet, the solvent would not be able to diffuse through and would evaporate at the desired rate in the oven which could reduce the number of surface defects formed. Therefore, should an ink prototype develop any surface defects on a nickel sheet, it would be more suitable to even more defects developing on a GDL. Hence, any CALIs develop which had few surface defects could possibly be used on a GDL.

After the electrode had been dried in the oven, it was compressed at 2.5 tonnes for 1 min using the same method for the GDL adhesion. Compressing the printed electrode under a high load changed the surface of the electrode, filling in the pits, fissures and cracks, and levelling out the electrode, making it flatter (Figure 4.41).

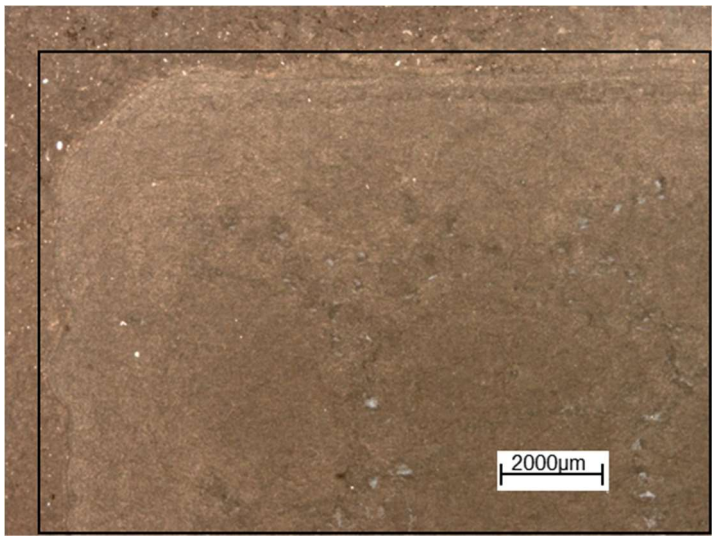

Figure 4.41 - Repeated CALI1 cathode with the black border indicating the edge of the electrode.

It was important to compress the electrode prior to the PTFE sintering stage. After the oven, most of the electrode's structure was a green binder scaffold as the PTFE was dispersed

particles. Once the electrode had been compressed and distorted compared to the printed electrode, although disrupted, the green binder kept a lot of the original electrode structural properties. Curing the electrode at this stage sintered the PTFE in the final desired electrode structure, potentially reducing electrode degradation during operation. Should the PTFE be sintered prior to the compression, the high load would deform the electrode, potentially reducing the porosity, although these would be much larger than the suspended PTFE particles used in the ink formulation. Without the PTFE framework, the electrode could have experienced severe degradation and would eventually fail. Therefore, the electrode was compressed and then put in an oven at 250 °C for 30 mins to allow the PTFE to sinter and the final electrode to form (Figure 4.42).

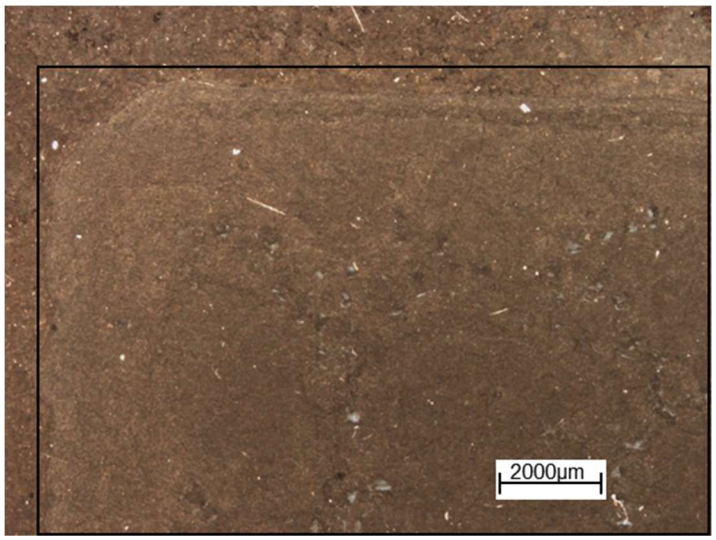

Figure 4.42 - Final CALI electrode after sintering with the black border indicating the edge of the electrode.

The final electrode had a dramatic reduction of visual surface defects compared to the original electrode (for a comparison see Figure 4.43). However, there were some areas which appeared to still be slightly uneven. The small white areas observed on the electrode's surface could be small amounts of PTFE on the surface.

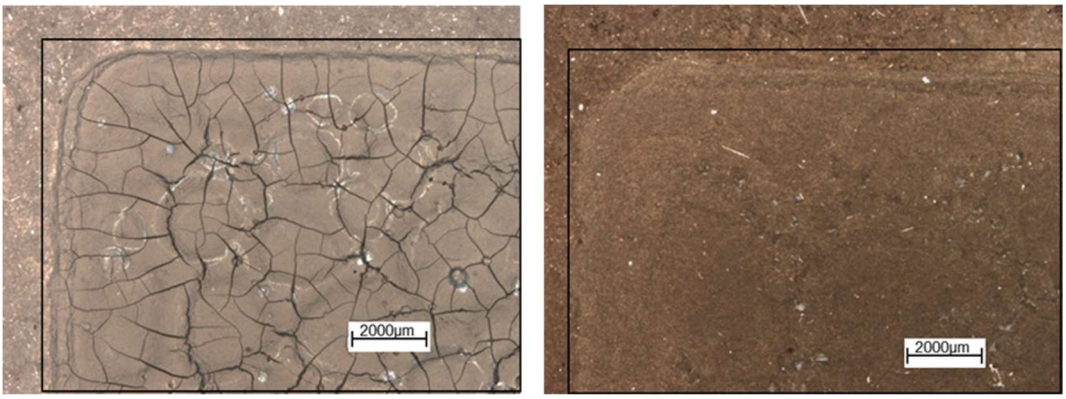

Figure 4.43 - Comparison of a pre-compressed (left) and final repaired (right) electrode with the black border indicating the edge of the electrode.

Although this method had removed most of the visible surface defects, the act of compressing the electrode may have altered the physical properties within the bulk of the electrode. An important characteristic of an electrode is its porosity and the ability for fluids to transport between one side and another of the electrode. A high porosity allows for the fluid to transport easily through the electrode and increases the 3D surface area, increasing the number of triple phase boundaries. The act of compressing the electrode may collapse the electrode's structure, reducing the overall porosity. Furthermore, as the printed electrode was being compressed, the GDL underneath gets displaced to accommodate the electrode. As such, the GDL directly under the electrode may have become compressed, potentially reducing the porosity which could restrict the oxidant diffusion and eventually reduce the rate of reduction on the cathode and overall power generation. This would support the compression of the electrode prior to being sintered.

4.3.5 Comparison of Screen Printed and Commercially used Cathode

To determine whether the repaired cathode was suitable, it was first compared to a commercially used and manufactured cathode. Both the cathodes used the same electrocatalyst, but had different manufacturing methods with the commercially used cathode produced from a kneading and laminating process (see Section 4.2.1.2) compared to the screen printed cathode developed in this work. The cathodes were used in a DBAFC and polarised against a Pd containing, commercially used anode, of the same composition the screen printed anode was compared to, testing rig using 38 mM $NaBH_4$ / 30 wt. % $KOH_{(aq.)}$ at a flow rate of 5 $cm^3.min^{-1}$, at room temperature and an air flow rate of 0.4 $L.min^{-1}$ to produce

the potential (Figure 4.44) and power (Figure 4.45) polarisation plots. The electrodes with compared using the fuel cell testing rig, with an electrode gap of 20 mm.

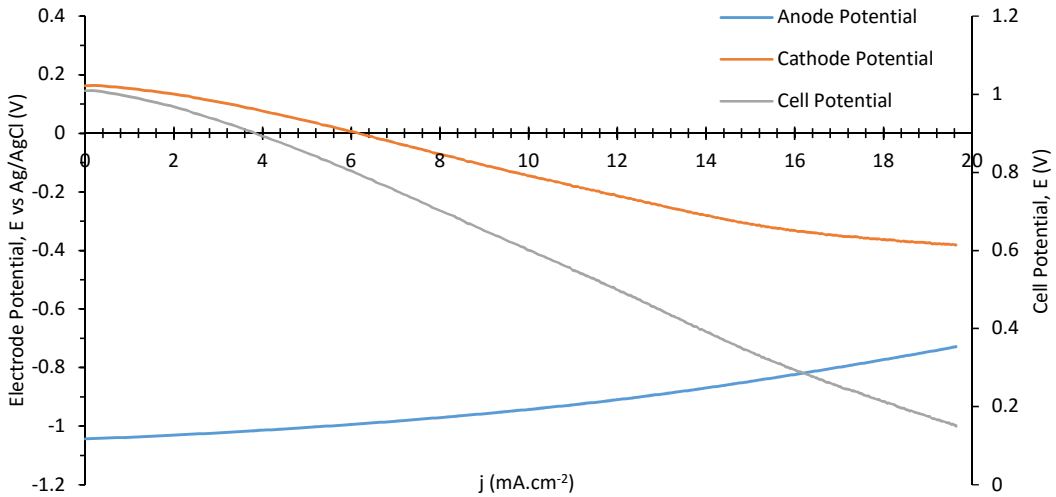

Figure 4.44 - Potential polarisation curves of screen printed cathode and commercially used anode (vs Ag/AgCl) and cell in 38 mM $NaBH_4$ / 30 wt. % $KOH_{(aq.)}$.

The curves in Figure 4.44 show the effect of polarisation on the individual electrodes. Both electrodes performed well with the fuel cell, their half-cell potentials described in Table 4.14. The cathode appeared to be closer to the theoretical *OCP*, which had a difference of 0.04 V, compared to the anode, which had a difference of approximately 0.4 V which is significantly different. This shows that, for DBAFC, the anode could potentially be improved more so compared to the anode.

The cathode polarisation curve in Figure 4.44 doesn't show the typical activation loss and mass transport trend at lower and higher overpotentials respectively. Instead of showing a relatively sharp decrease, the polarisation curve starts to plateau. This could be attributed to a change in the experimental conditions which could have resulted from (or a combination of):

- Hydrogen evolution due to borohydride hydrolysis
- Electrode degradation due to an unsuitable formulation
- Electrode removal from substrate due to poor binding

If the polarisation curve had a different reverse scan, this would have confirmed it. Unfortunately, only a single forward scan was conducted. As such, more work should be conducted evaluating the reason for the unusual polarisation trend.

Table 4.14 - *OCP* of screen printed electrodes using borohydride.

Electrode	Observed *OCP* vs Ag/AgCl (V)	Observed *OCP* vs SHE (V)	Theoretical *OCP* vs SHE (V)
Cathode	0.163	0.360	0.4
Anode	-1.043	-0.846	-1.24

Although the individual electrode half-potentials give an indication of the electrode efficiency towards the reaction of interest, it was the cell potential (E_{cell}) which was the most important and was used to compare different fuel cells. Furthermore, this was converted into a power curve which was calculated using Equation 4.3. The peak of the generated power curve shows the maximum power that the fuel cell can generate over the potential and current density range. The power curve was calculated for the screen printed electrode using borohydride and shown in Figure 4.45.

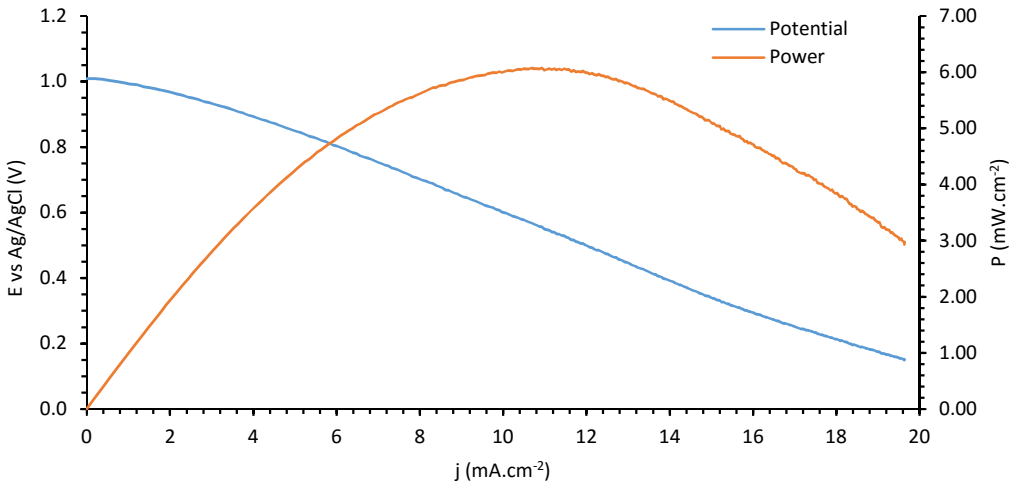

Figure 4.45 - Potential and power curve curves of screen printed cathode and commercially used anode using 38 mM $NaBH_4$ / 30 wt. % $KOH_{(aq.)}$.

The polarisation plots show the cell had a lower than expected *OCP* at 1.01 V and peak power of 6.076 $mW.cm^{-2}$ at 10.93 $mA.cm^{-2}$. The power generated from the cell polarisation was relatively low compared to the expected 200 $mA.cm^{-2}$ for this sized geometry. However, this was in borohydride and the lower power generation could be attributed to the low operating temperature, borohydride concentration, electrode design or a combination of all three.

To determine whether the poor power generation was due to the cathode or other parts of the system, it was compared to the commercially used electrode under the same conditions to produce the polarisation plot below (Figure 4.46).

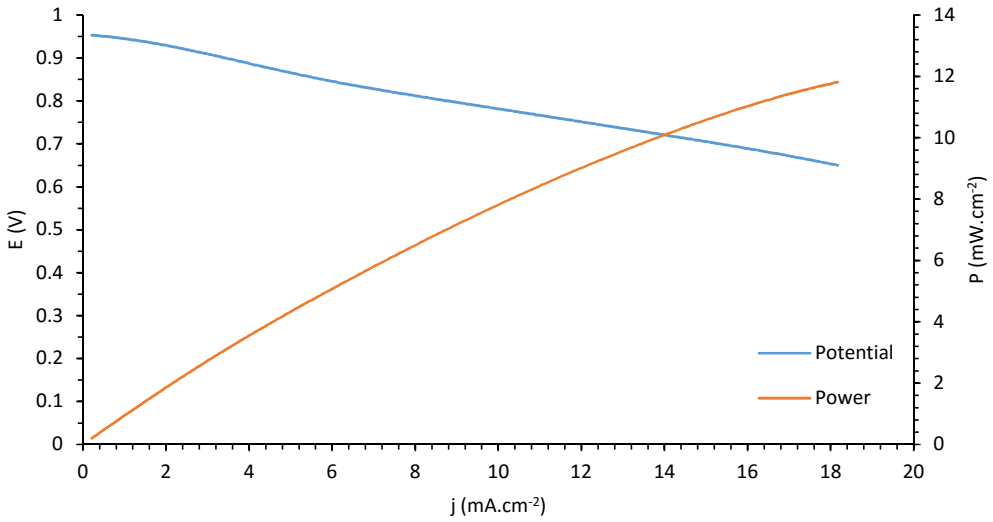

Figure 4.46 - Potential and power curve for commercially used electrodes using 38 mM $NaBH_4$/ 30 wt. % $KOH_{(aq.)}$.

Although the commercially used cathode was designed to allow for using hydrogen gas as a reductant and to allow it to diffuse through the electrode, it performed relatively well with a high *OCP* of 0.953 V, peak power of 11.8 $mW.cm^{-2}$ at 18.2 $mA.cm^{-2}$.

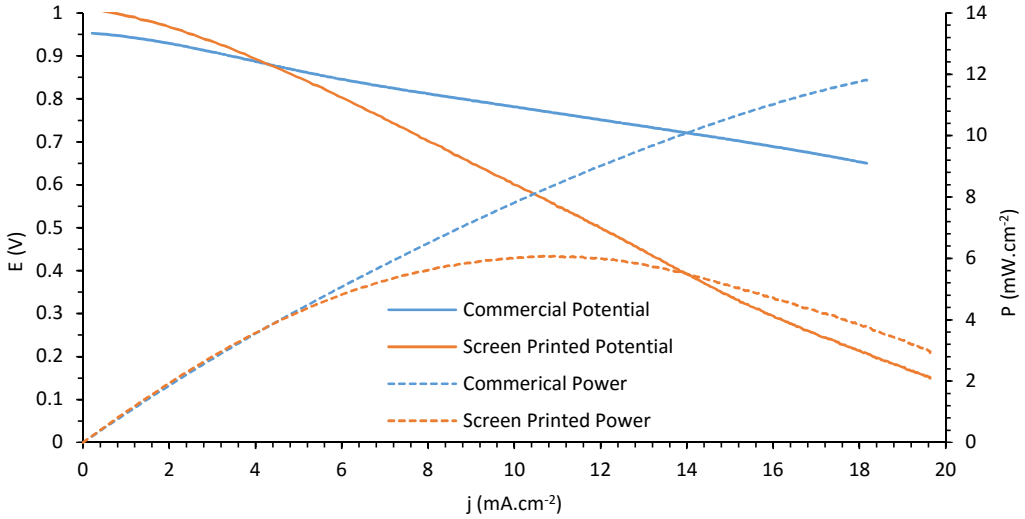

Figure 4.47 - Comparison of screen printed and commercially used cathodes in 38 mM $NaBH_4$/ 30 wt. % $KOH_{(aq.)}$.

Comparing the screen printed and commercially used cathodes (Figure 4.47) there were several differences observed between the two electrodes. The first was that the screen printed cathode didn't produce as much power as the commercially used cathode at higher currents, despite the higher starting *OCP*. Furthermore, the screen printed electrode had a low peak power whereas the commercially used electrode continued to increase, with the actual power outside of the current range measured. This indicates that the commercially used electrode could be polarised much further compared to the screen printed electrode to generate higher currents. However, under standard conditions, a fuel cell would not be polarised to this extent due to increased electrode degradation and the fuel cell was typically polarised only by a few hundred millivolts. Another observation from the polarisation curves for both the commercially used and screen printed cathodes was the power range that was being generated. The highest current at peak power was only approximately 16.34 $mA.cm^{-2}$ compared to the 200 $mA.cm^{-2}$ desired for the A_{geo} of the cathodes. This can most likely be attributed to the low operating temperature and high ohmic resistance.

The screen printed cathode was also evaluated against an anode using hydrogen as the reductant. The cathode was prepared using the same method as above but with 30 wt. % $KOH_{(aq.)}$ and 0.4 $L.min^{-1}$ hydrogen and air. The screen printed electrode was polarised at room temperature in a fuel cell testing rig, with a commercially used anode, to generate the polarisation curve in Figure 4.48 and Figure 4.49. The hydrogen gas rig used was different to

the borohydride rig with a much smaller electrode gap of 3 mm and measured using a Scribner fuel cell testing station. It must be noted that the Scribner is unable to measure below approximately 200 mA (which equates to approximately 12.5 mA.cm^{-2} with A_{geo} = 16 cm^2). As a result, the polarisation plots appear to have a plateau at low current densities. The polarisation curve shows a high starting potential at 1.01 V with a peak power of 32.32 mW.cm^{-2} at 71.60 mA.cm^{-2}. This shows that the cathode worked well at getting to the correct *OCP* and an acceptable current and power density.

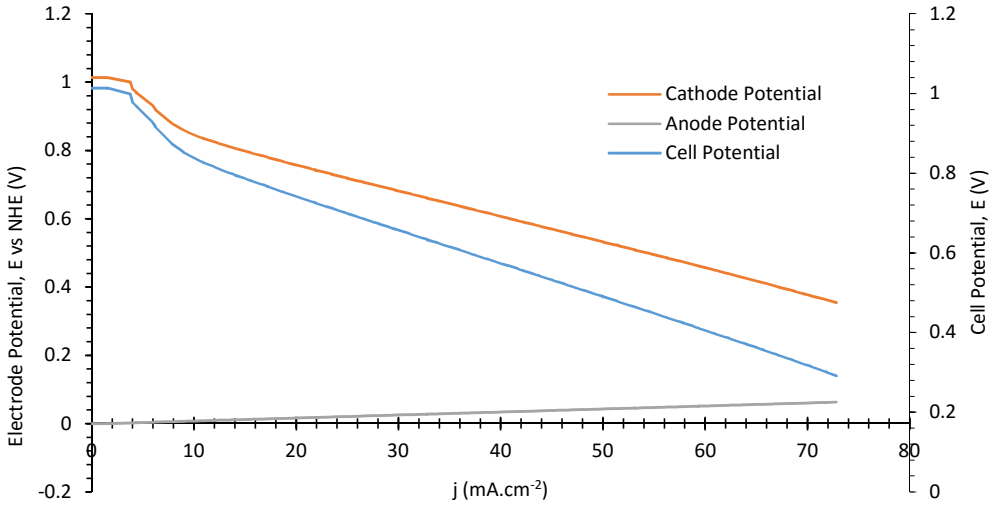

Figure 4.48 - Potential polarisation curves of screen printed cathode and commercially used anode (vs NHE) and cell in hydrogen at 100 mL.min^{-1} hydrogen and 399 mL.min^{-1} air.

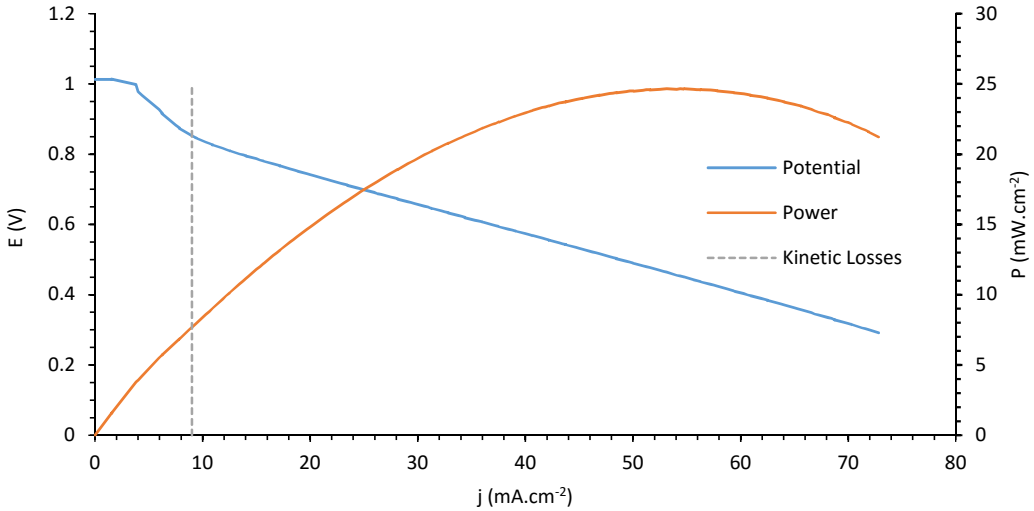

Figure 4.49 - Polarisation of a screen printed cathode using hydrogen gas as the reductant at 399 mL.min^{-1}.

Due to the commercially used cathode no longer being available, no new experiments could be conducted. Therefore, the screen printed cathode using hydrogen gas was compared to historical commercially used data (Figure 4.50).

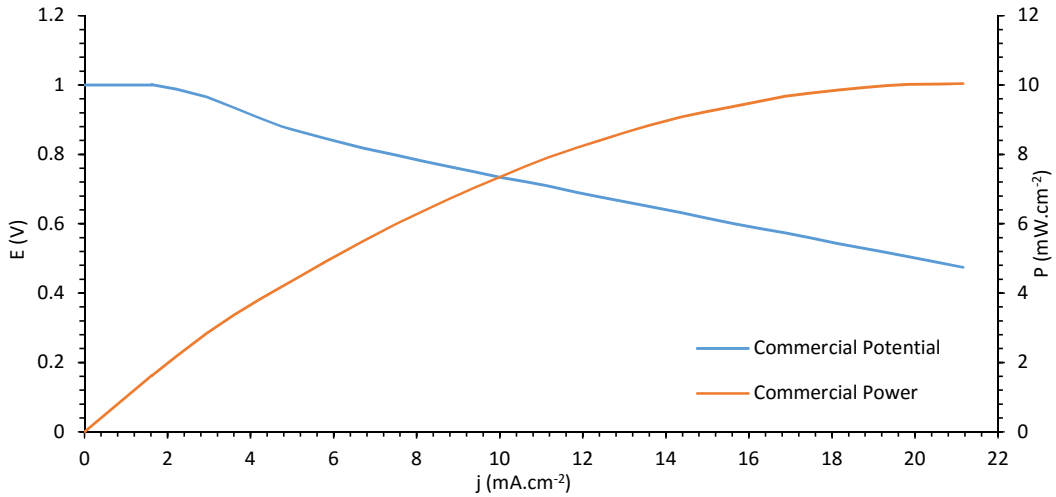

Figure 4.50 - Historical polarisation data for the commercially used cathode using hydrogen gas at 100 mL.min^{-1} and air at 498 mL.min^{-1}.

The polarisation of the commercially used cathode using hydrogen at 70 °C shows high *OCP* at 0.976 V. It should be noted that unlike a DBAFC which had a theoretical *OCP* of approximately 1.64 V, a hydrogen-based AFC had a theoretical *OCP* of 1 V. As with the commercially used cathode using borohydride, the peak power continues past the current range in the experiment; however, can be 67.92 mW.cm^{-2} at 122.7 mA.cm^{-2}. This was a large increase from the current density generated using borohydride. The screen printed and commercially used cathode fuel cell polarisations using hydrogen were then compared in Figure 4.51. The fuel cell rig for the commercially used cathode evaluation was based on historical data.

Both fuel cells show a similar starting *OCP*. The gradient of the potential polarisation curves, after the kinetics losses region, relates to the ohmic losses associated with the electrode. This indicated that the ohmic resistance of the commercially used cathode was greater than the screen printed, producing a steeper gradient. The large kinetics and ohmic losses of the

commercially used cathode indicated that the screen printed cathode used was more suitable when used with hydrogen gas, which was to be expected as the commercially used electrode was specifically designed for the use of hydrogen.

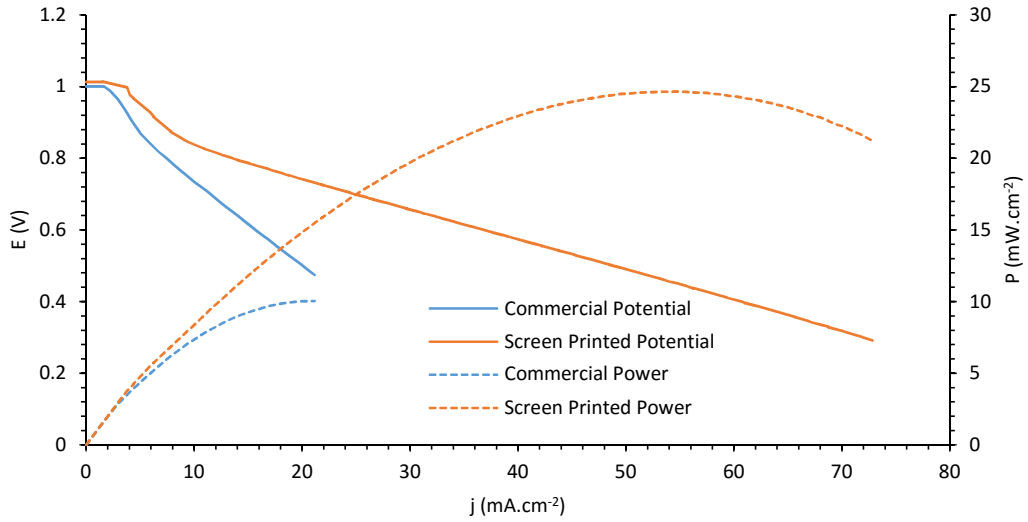

Figure 4.51 - Comparison of screen printed and commercially used electrodes using hydrogen gas (commercial hydrogen = 100 mL.min^{-1}, air = 498 mL.min^{-1} and screen printed hydrogen = 100 mL.min^{-1}, air = 399 mL.min^{-1}, 30 wt.% $KOH_{(aq.)}$).

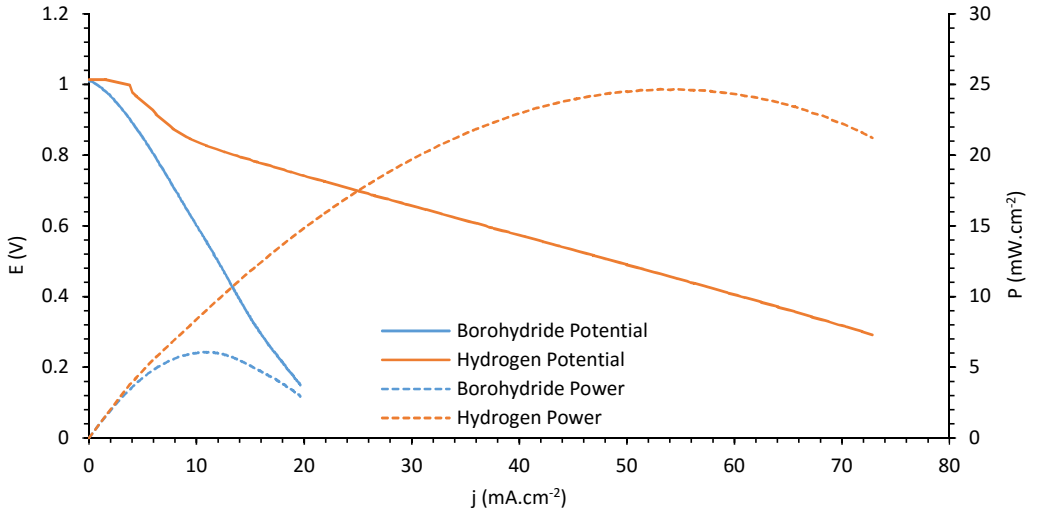

Figure 4.52 - Comparison of screen printed cathode using both borohydride (38 mM $NaBH_4$/30 wt.% $KOH_{(aq.)}$ and hydrogen gas (399 mL.min^{-1} hydrogen, 30 wt.% $KOH_{(aq.)}$).

Another comparison that can be made from the generated polarisation plots was the performance of the screen printed cathode using borohydride and hydrogen as shown in

Figure 4.52. The performance of the screen printed cathode was significantly increased when used in an AFC compared to a DBAFC. The similar *OCP*'s indicated that the anode was evolving and subsequently reducing hydrogen. The ohmic loss experienced by the cathode increased greatly, causing a dramatic decrease in the peak power density. Unfortunately, the system used to generate the hydrogen polarisation data didn't have the functionality of being a three celled system, allowing for the use of a reference electrode and measuring the potential on both electrodes compared to the entire cell. Therefore, it was difficult to determine whether the poor power generated using borohydride was attributed to a single electrode. The amount of hydrogen used was significantly more with the borohydride used had a molar flow rate of 0.190 $mmol.min^{-1}$ compared to the hydrogen which was a molar flow rate of 17.85 $mmol.min^{-1}$. This does not seem to have affected the fuel cell performance as there were no issues observed in the mass transport region. The electrode gap was larger in the DBAFC which would have contributed to the increase in electrical resistance experienced by the cell. If the electrodes were the cause of the high ohmic loss, as indicated by the polarisation curve, there would be a large voltage drop experienced in the hydrogen AFC. Therefore, these results indicate that the fuel cell rig may need redesigning to reduce ohmic losses.

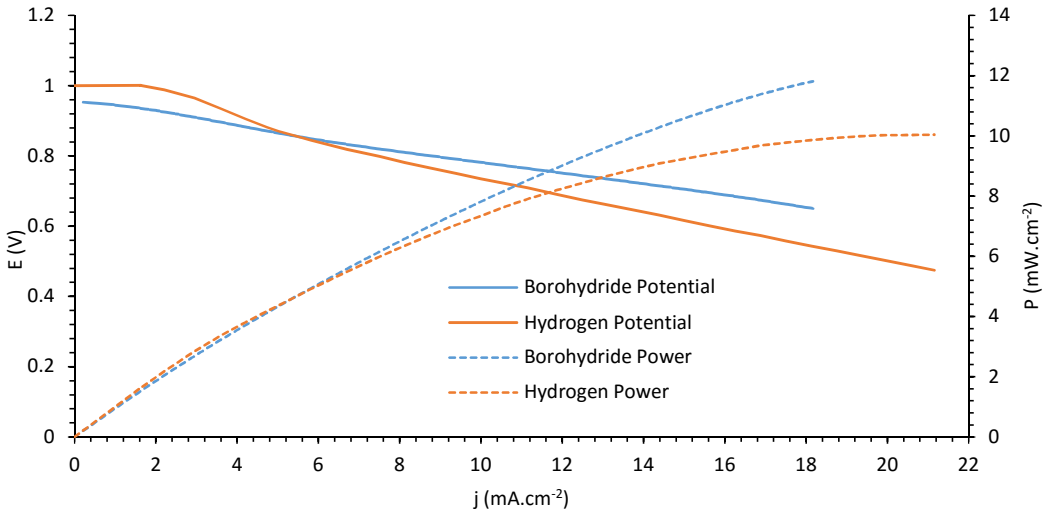

Figure 4.53 - Comparison of the commercially used cathode using both borohydride (38 mM $NaBH_4$/30 wt.% $KOH_{(aq.)}$ and hydrogen gas (399 $mL.min^{-1}$ hydrogen, 30 wt.% $KOH_{(aq.)}$).

The comparison of the commercially used electrode using borohydride and hydrogen reductants in Figure 4.53 show a similar trend as the screen printed electrode in Figure 4.52. There was a significant difference between the polarisation plots with an increased ohmic loss

in borohydride, reducing the peak power density. As with the screen printed electrode, these losses could be attributed to the difference in the design of the DBAFC testing rig compared to the AFC. However, the commercially used electrode had a similar polarisation profile with both reductants showing that the reaction processes may be similar between the two reductants.

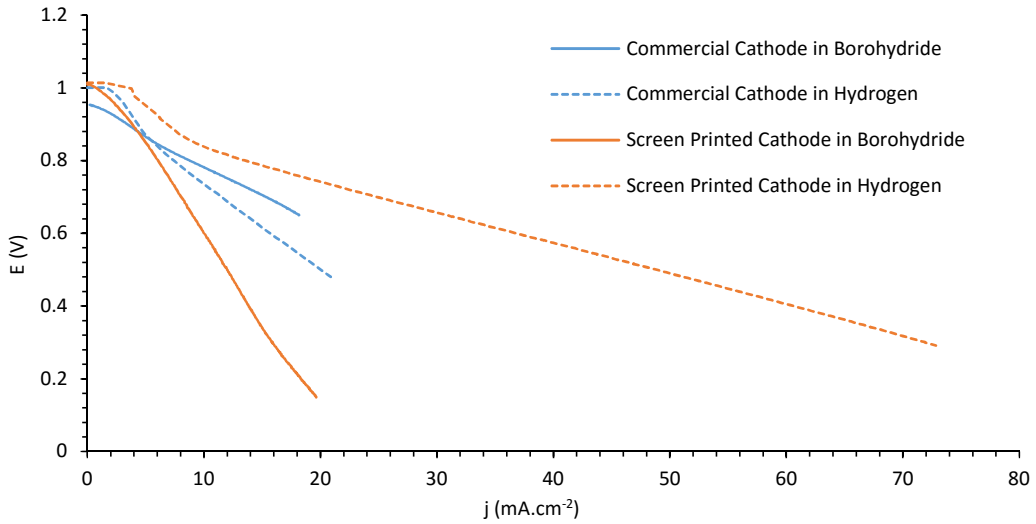

Figure 4.54 - Commercially used and screen printed cathode polarisation comparison using both borohydride (38 mM $NaBH_4$/30 wt.% $KOH_{(aq.)}$ and hydrogen gas (399 mL.min^{-1} hydrogen, 30 wt.% $KOH_{(aq.)}$).

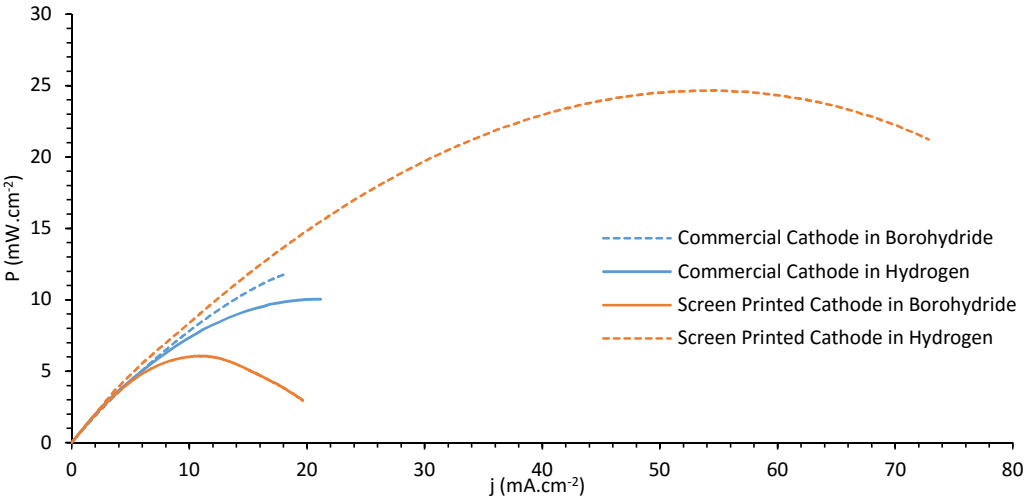

Figure 4.55 - Commercially used and screen printed cathode power curves comparison using both borohydride (38 mM $NaBH_4$/30 wt.% $KOH_{(aq.)}$ and hydrogen gas (399 mL.min^{-1} hydrogen, 30 wt.% $KOH_{(aq.)}$).

Figure 4.54 and Figure 4.55 compare the commercially used and screen printed cathodes polarisation and power curves in borohydride and hydrogen gas fuels. The polarisation curves show that the *OCP* of both cathode fuel cells were similar, regardless of the reductant used which was unexpected due to borohydride's higher theoretical *OCP*. This could indicate that the anode predominantly follows an indirect oxidation mechanism when used in borohydride. Both the electrodes show a power density reduction of approximately 50 % when used in borohydride compared to hydrogen. This could be due to the different testing rigs used. Furthermore, the *OCP* could be lower than the theoretical *OCP* due to the large electrode gap, evolution of hydrogen gas and subsequent decrease in electrolyte conductivity and inhibition of the active surface area. The anode may be hydrolysing the borohydride and reducing the generated hydrogen which may have a slower reaction rate compared to that of hydrogen.

The screen printed cathode developed performed reasonably well using hydrogen gas; however, showed a decrease in performance in borohydride. The screen printed cathode was developed to continue to use of MnCoO as the cathode electrocatalyst. Furthermore, the production of the cathode was novel, with it being specifically designed for a DBAFC and using a screen printing process. This screen printing process may potentially decrease manufacturing costs and times in the production of cathodes and although not fully optimised, the cathode presented, based on the initial CALI formulation, provided a basis in which to further develop a more effective cathode.

4.3.6 Effect of Printing Method on Electrode Structure

The printing method can have a great impact on the electrode being produced. Therefore, it's important to determine how the printing process dictates the final structure of the electrode. To accomplish this several different printing methods, highlighted in Table 4.15, were evaluated using 3D roughness reconstruction from SEM images (discussed in Section 4.2.2).

Table 4.15 - Electrode printing conditions.

Method	Layers	Print Height (µm)	Time at 90 °C (min)	Notes
1	1	0	15	Base/control

2	1	30	15	Effect of increasing screen distance from the substrate.
3	2	30	15	Effect of printing a double layer.
4	2	30	30	Effect of doubling heating duration.
5	1	0	15	Change in morphology using low PTFE content.
6	2	30	15 × 2	Effect of heating each layer individually.
7	1	0	15	Different ink manufacturing method.

The first electrode was manufactured as the most basic printing method, which involved depositing a single layer of the electrode, the height of which was dictated by the screen emulsion thickness. The electrode was then placed in an oven for 15 mins at 90 °C. Images were then taken, at different angles, using an SEM to generate the 3D image, from which the surface profiles were generated. From this, the base printing method was used and the effect of varying this method on the electrode structure was determined. The effect of altering the manufacturing process on the total electrode, average layer and weight was described in Table 4.16.

Table 4.16 – Effect of printing method on electrode weight.

Method	Electrode Weight (mg)	Average Electrode Layer (mg)
1	88	88
2	77	77
3	144	72
4	90	45
5	73	73
6	134	67
7	62	62
Average (mg)		69
Relative Standard Deviation (%)		18

The electrode weight results show that altering the printing method didn't have a large effect on the weight of the final electrode as the average electrode layer weights were approximately the same. However, method 4, which involved doubling the heat duration, had a lower weight at 45 mg. It could be speculated that the extra duration of heat may have dried the electrode out more than the others, removing the solvent and leaving a drier, lighter electrode. However, if this was the case then method 6, which involved increased heat duration but for each layer, would have mirrored this decrease in weight, if not more so. The lower weight of method 4 may possibly due to weight measurements being less accurate than required (the average substrate weight was approximately 8 g with the electrodes being two orders of magnitude lighter). The weight generated are only used as an indication but the results show a relatively good correlation between each other. Although important, the electrode weight does not fully explain the effects of printing of the electrode structure. Therefore, 3D roughness reconstruction was used to determine the electrode surface profile. These profiles were then averaged to give an electrode height, which was then converted into the height of each layer (Table 4.17).

Table 4.17 - Effect of printing method on electrode height based on the edge profiles.

Method	Average Height (µm)	No. Layers	Average Height per Layer (µm)
1	68	1	68
2	83	1	83
3	84	2	42
4	32	2	16
5	126	1	126
6	31	2	16
7	37	1	37

The average electrode height results vary considerably ranging from 16 – 126 µm per layer. There are two possible explanations for the wide electrode height range; either the method of printing had a large impact on the electrode structure produced or the 3D roughness reconstruction software methodology was inadequate for the application. Although the printing method would have influenced the electrode, the results generated by the 3D roughness reconstruction may not be very accurate. Although care was taken to ensure that the baseline, i.e. the substrate the electrode was printed on, was flat so that an accurate

electrode height could be generated, the 3D roughness reconstruction software was not suitable for the electrodes used. In many cases the baseline dipped significantly, apparently warping the image generated and potentially generating inaccurate results (as shown in Figure 4.56, which had a common trench in the substrate next to the electrode's edge).

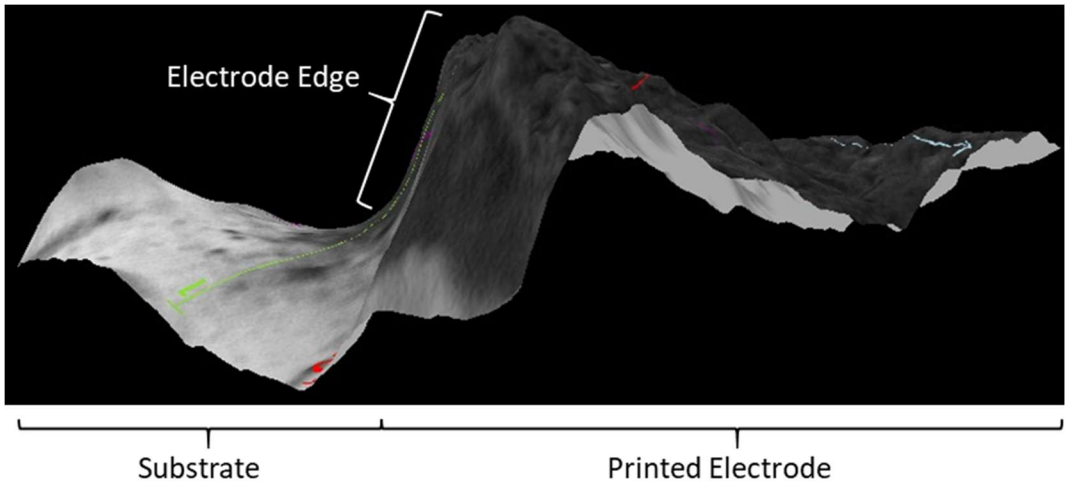

Figure 4.56 - Annotated 3D roughness reconstruction showing uneven substrate, poor electrode edge definition and the uneven electrode surface.

Furthermore, there were discrepancies between the different profile pathways, as shown in the plot in Figure 4.57. The baseline measurements show the instability with the surface dipping in places due to the 3D reconstruction. The step profile, which was taken perpendicular to the electrode's edge from the substrate to the electrode, shows the electrode's edge to only gradually increase when this was not the case as confirmed by the microscopy images. Therefore, the edge electrode profile was used to determine the average electrode height as it was deemed more accurate than determining it at the step profile the electrode began.

It was speculated that the low accuracy of this methodology, coupled with the poor correlation between the 3D roughness reconstruction and the electrode weight data, was the source of the sporadic electrode height values observed. However, the methods 1 and 2 showed similar electrode heights and weights which signifies that there may be little difference in the effect

on the electrode between these two methods. As previously shown, using two layers was more advantageous compared to the single layer, so this method was chosen as the optimum printing process for this ink.

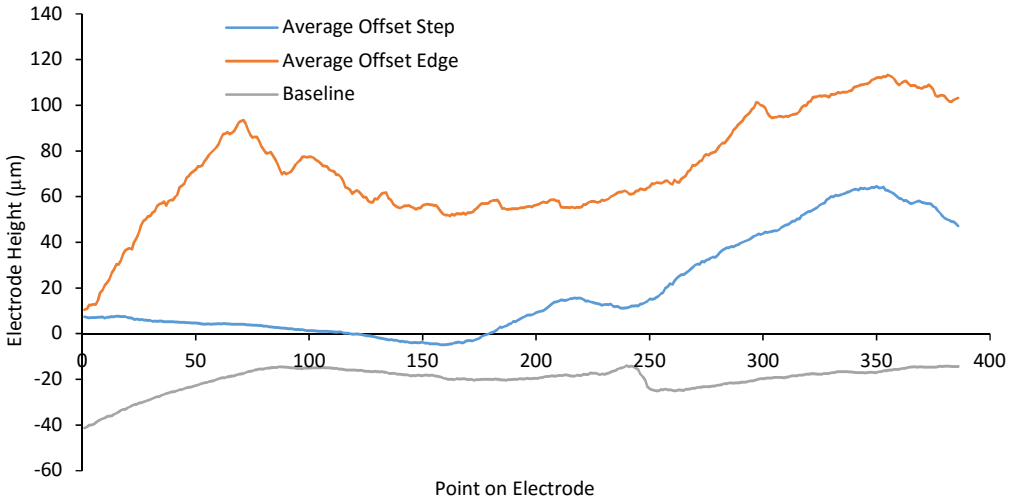

Figure 4.57 - The step, peak and baseline measurements from an electrode using the 3D roughness reconstruction software.

Due to the electrode's height, in the mid micrometre range, it made it difficult to use various pieces of equipment. White light interferometry would be an acceptable method but the black electrode would have made it difficult to detect electrode surface characteristics whilst atomic force microscopy has a resolution of nanometres which would have made the electrode too large to be used. Although the data used to determine the effect of the printing process on the electrode was not as accurate as other methods, it gave an indication as to which process was most suitable for the current formulation. However, more evidence needs to be generated regarding the effect of printing on the electrode, using much more accurate and reliable methods.

4.3.7 Electrode Adhesion on Substrate

An important characteristic of electrodes is their adhesion properties to the substrate. The electrode had to be sufficiently adhered to the substrate to prevent it from degrading during fuel cell operation. Several different factors cause the electrode to either detach or peel away from the substrate. The liquid electrolyte flow across the surface of the electrode, the passage

of air at the back of the cathode substrate, the hydrogen generation due to indirect oxidation and electrode weeping can all cause the electrode to detach from the substrate which would be detrimental to fuel cell performance. However, the electrode was primarily adhered using the PTFE within the electrode or between the electrode and substrate. Increasing the PTFE content increases electrical resistance and, in the electrode specifically, affects the wettability.

To ensure that the electrode sufficiently adhered to the substrate, several different methods were used. To determine the effect of these different methods on the electrode adhesion properties, a method involving a MatLab program (explained in Section 4.2.5) to quantify the amount of electrode removal during operation was used. One of these methods was to roughen the surface of the substrate prior to printing or GDL compression. Fine grade sandpaper was used to scrape the surface of the substrate. This increased the surface area of the substrate and create microscopic substrate ridges on the surface, producing more points at which the PTFE in the GDL or electrode can adhere to. Although adhesion increased, the electrode didn't fully adhere to the substrate when it was exposed to the electrolyte. After the surface roughening, a small amount of PTFE was rubbed onto the surface of the substrate. Once rubbed on, the PTFE was then buffered back until it was not visible. This process left a small layer of PTFE on the ridges of the roughened surface. Although only small amounts of PTFE were added, this increased the adhesion significantly. However, care was taken not to add so much PTFE as to increase the electrical resistance.

During the operation of the fuel cell, the electrode degradation did not proceed as expected. Rather than small amounts of electrode detaching from the substrate, the electrode started to peel away as a single piece (Figure 4.58). This suggested that the binding in the electrode ink was sufficient to keep the electrode's structure; however, the adhesion needs to be improved. Furthermore, due to the electrode peeling off in a single piece rather than in small quantities, the method for quantifying electrode degradation was not suitable and a different method should be used.

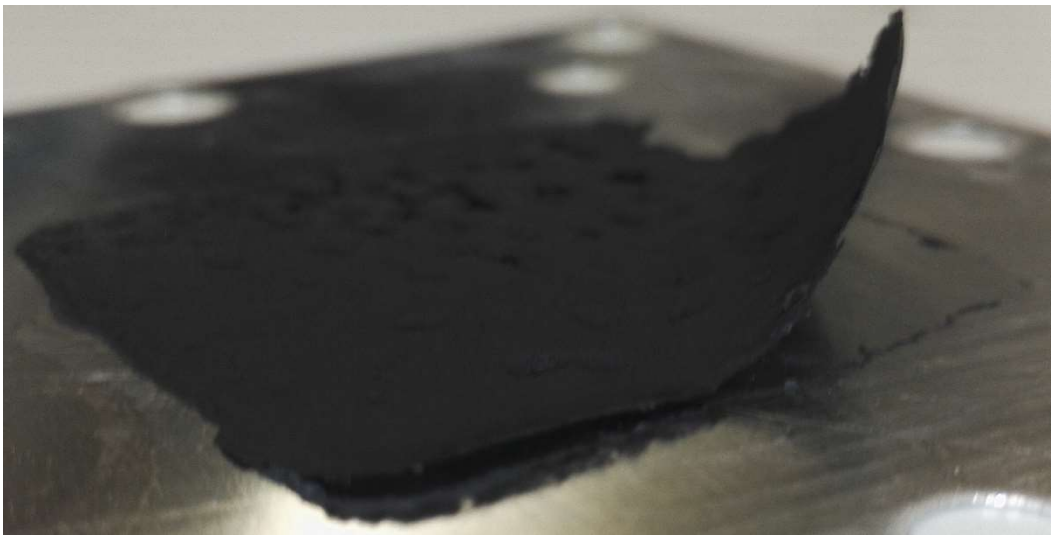

Figure 4.58 - Electrode peeling from the substrate during fuel cell operation.

4.4 Conclusions and Discussion

Three anode inks were originally developed, two aqueous using Norit and a non-aqueous using 10 % Pt/C_b. However, substituting the Norit for an electrocatalyst caused a significant change to the viscosity and consistency of the ink, depending on the specific electrocatalyst. The results from the substitution of Norit for electrocatalysts showed that the Norit cannot be used as an inexpensive alternative in place of similar electrocatalysts for electrode development. Although the Norit had to be replaced for an electrocatalyst, as Norit is only carbon and was considered to have had no electrocatalytic activity, it would have been useful to use it as a substitute for electrocatalysts, reducing the cost of formulation development. Furthermore, one base ink formulae cannot be used for similar electrocatalysts as each has a different effect on the final ink's physical properties. This further supports that the interaction between materials was complex and had a major effect on the final ink. This also makes the development of future inks expensive as specific ink formulae would have to be developed for a specific electrocatalyst.

In many fuel cells, the cathode is the most researched out of the two electrodes due to its slow reaction kinetics compared to the anode. Although initially out of scope, the work presented shows a formulation and method a screen printable DBAFC cathode. The screen printed cathode performed better compared to the commercially used cathode in the presence of hydrogen gas though not in borohydride. This could be due to either the CALI formulation not

being suitable for a DBAFC, as it may have a low wettability preventing the electrolyte diffusing through, or it could be due to the manufacturing method being inconsistent with different electrode weights being deposited. Furthermore, the act of screen printing had a potential cost reduction over the traditional method for preparing the commercially used cathode. Finally, the performance could potentially be increased by increasing the amount of cathode printed, as shown by the single and double layer anode results.

Both the chosen non-aqueous and Norit based aqueous inks printed well, but there was an unexpected difference between them which may be another factor when choosing a suitable solvent. The aqueous ink dried quickly during the printing process, more so compared to the non-aqueous inks. This meant that the aqueous printing process had to be much quicker when printing various layers as the ink would dry in the mesh, clogging the channels and would have inhibited the next print. Furthermore, this led to more cleaning between printing different electrodes as much of the ink used could not be reclaimed. Although the low boiling point of water compared to texanol made it a desirable solvent, due to its ease in being removed during the curing process, it's this property which caused the increased difficulty in printing the electrodes. In this regard, a cost-benefit analysis would have to be conducted as to whether the reduction in material costs would be worth the potential increase in manufacturing difficulties.

Defects on the surface of an electrode could lead to degradation and poor electrode performance. Although the ideal ink and manufacturing process would produce and ink with no surface defects, the work in this chapter highlighted a method to repair the surface of a cathode. This would increase the flexibility in formulation design, whether that be to decrease material or manufacturing costs. Furthermore, this method was not isolated to the cathode and could be applied to the anode if required.

Many of the results in this chapter have highlighted the complex interactions between materials in the ink. From the addition of EC70 and its effect on rheology to a sensitive relationship between a stable PTFE with Tergitol and preventing its agglomeration. Some important interactions have been highlighted in Section 4.3.3; however, these are not the only interactions that occurred. Understanding the effects of these interactions on the many

properties of an ink and electrode was imperative to develop an optimum electrode. However, it's speculated that understanding these interactions could have the potential to be a vast undertaking due to the number of materials, the quantity ranges, manufacturing conditions and the desired final ink physical and electrochemical properties.

The screen printing process for producing large amounts of quality electrodes was possible; however, it must be tailored to the specific electrode being printed. Out of the different methods evaluated in this chapter for the screen printing an electrode, there were no effects on the electrode thickness. This was convenient as this allows for more flexibility during full-scale manufacturing. Furthermore, a thicker electrode can perform significantly better compared to a thinner layer, as shown by the single and double layer anode polarisation which can be attributed to the increase in electrocatalyst present. Once an ink had been developed, it was important to select a screen with an appropriate mesh size to accommodate the particles. The Tergitol used in the ink to aid with the PTFE stabilisation was not removed during the curing process. Although this was not detrimental to the electrode, it should be removed by washing the electrode prior to use. It was unlikely that an electrode could be produced using PTFE but without the use of a surfactant to help stabilise the PTFE in suspension.

Comparing the electrochemical results generated in this chapter, summarised in Table 4.9, with the literature data, highlighted in Table 4.3, showed that the anode developed did not perform as well as other DBAFC setups. The anode developed showed a considerably lower power density, 21 $mW.cm^{-2}$ for the double layer, compared to the overall highest literature data, 810 $mW.cm^{-2}$, as well as the highest comparable DBAFC, 127 $mW.cm^{-2}$, setup. Although the power density generated by the anode developed was low compared to others, the screen printing manufacturing presents a method to produce the electrodes on a larger scale. The anode and cathode inks developed here are suitable to be a base formulation, as they are printable and produce active electrodes for a DBAFC, from which more optimised electrodes could be produced.

4.5 Future Work

There are two major focuses for future work regarding the electrode manufacture, one of which was the optimisation of an anode ink with a specific electrocatalyst. Although some

electrochemical results were generated using 10 % Pt/C_b in a texanol based ink, it was difficult to compare the electrocatalyst with others as there are no other similar electrocatalysts, i.e. 10 % metals on carbon black, that were manufactured using a similar procedure. Therefore, if an aim were to determine the electrocatalytic activity of various electrocatalysts in a fuel cell, it would be best to evaluate electrocatalysts which have been prepared using a similar manufacturing process. However, comparing similar electrocatalyst may not be simple as they would each require their own unique ink formulation to be printable.

The other major focus should be to determine the effect of different materials, and material quantities, on the electrode and ink properties. Although developing and building on previous formulae may obtain a suitable anode, it may not produce an optimal one. By doing a full design of experiment with the materials used in this chapter, followed by rheological, surface area and electrochemical analysis, including polarisation, power curves and more comprehensive EIS, on the final electrode would allow for smart formulation development. This could potentially produce an electrode which was inexpensive, reproducible and effective.

There are other minor investigations which could potentially aid in the development of an optimal anode. One such investigation would be determining the effect of compression on the porosity. During the electrode repair and electrode adhesion, the electrode was compressed. This could potentially crush the electrode and reduce its porosity which may affect its performance. Another would be to determine the best method to adhere an electrode to the substrate. In this chapter, PTFE was deposited on a roughened substrate surface with the electrode being compressed and cured. It was possible to decrease the amount of PTFE used by sintering the substrate to the electrode. This would remove the additional PTFE, which would increase the electrical resistance, but would help decrease contact resistance between the substrate and the electrode.

5 Fuel Cell Stack Design and Architecture

5.1 Background

Although optimisation of the electrocatalyst and electrode, and the associated electrochemistry, are vital to the operation of a fuel cell, focusing research solely on them would not lead to the development of a useful and practical fuel cell and stack. To produce a stack for real world applications, the components used need to be designed with specific features to give high performance and long life. This includes the flow of fluids across the electrodes, transport of fluid through the stack, ohmic resistance and the weight of the stack which is important for portable applications. This chapter describes the different components, their role, the effect of design and materials on the fuel cell stack.

5.1.1 Common Rig and Stack Components

Different types of fuel cells require different components to operate, depending on their electrolyte, oxidants and reductants. However, there are some common components shown below in Figure 5.1.

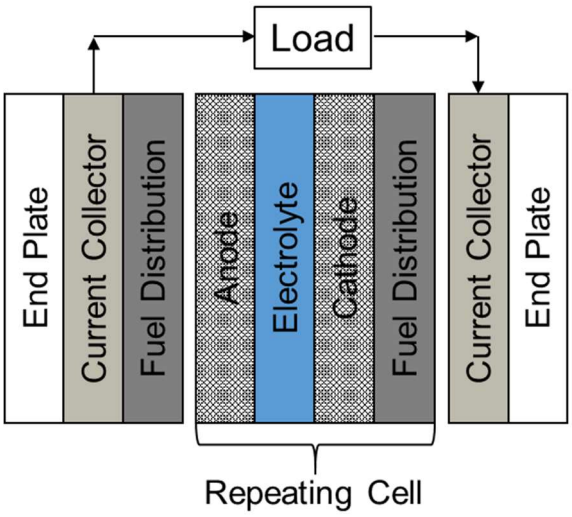

Figure 5.1 - The common components in most fuel cell types.

In a generic fuel cell, the reductant and oxidant, which is usually supplied as a gas, is supplied to the anode and cathode respectively. The gases then diffuse through the electrodes, which are comprised of various layers/parts, to the electrode surface where they react at the triple

phase boundary in the electrolyte plate where gas, electrolyte and electrocatalyst meet. The electrons generated from the redox reaction then travel through the anode to the adjacent current collectors, which are connected to an external electronic load. The electrons then travel to the cathode via the other current collector where it is used to complete the redox reaction.

Although all the components are important for the function of the stack, the development of some components affect the performance of the cell and stack more than others and have therefore been the focus of more research. The following sections describe the components most researched.

5.1.2 Fluid Transport and Distribution Plate

Fuel cells require at least two fluids, the oxidant and reductant, with additional fluids including coolant and electrolyte, to be distributed through the fuel cell stack. In low temperature fuel cells, this is most commonly achieved by using components known as the bipolar plate (BPP).

Bipolar plates (also referred to as flow field plates) in fuel cells have several major functions which include the distribution and separation of fluids and electrical contact in a fuel cell [175]. They also provide increased mechanical strength in a fuel cell stack, aid water management and in some cases coolant [176]. Primarily used in PEMFC, the basic properties of a BPP are a sheet of metal, carbon loaded polymer graphite with a series of channels or grooves cut into the surface. These channels allow for the transportation of the reductant or oxidant across the surface of an electrode. A simple PEMFC using bipolar plates diagram is shown in Figure 5.2.

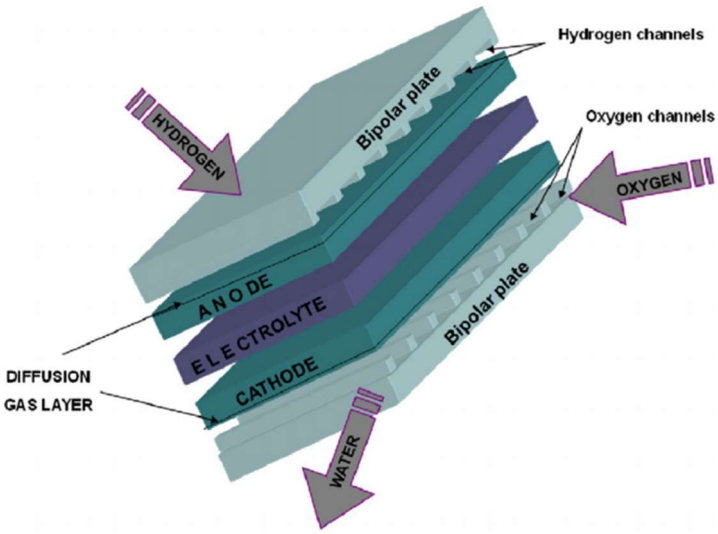

Figure 5.2 - Single cell using bipolar plates to distribute fluid [177].

Due to the transportation of fuels, the channels would benefit from being large, enabling large quantities of fuel to be distributed, reducing losses due to pressure drop. However, increasing the size of the BPP increases the cost of the plate manufacture, its electrical resistance and pressure drops can aid in flow distributions. The oxidants and reductants flow rate can be increased to accommodate for the reduction in BPP thickness, which is advantageous as the BPP can represent a significant weight within the fuel cell stack (Figure 5.3).

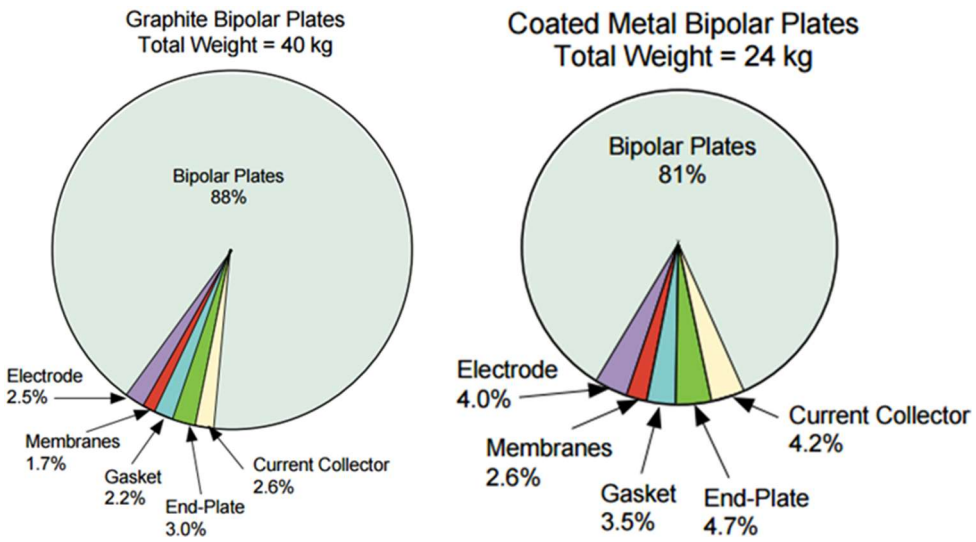

Figure 5.3 - Mass Distribution in a 33 kW PEMFC [178].

There are four common types of BPP flow fields which include pin, parallel, serpentine and interdigitated (Figure 5.4) [179-181]. The flow of gas through pin and parallel designs flow around the pins and walls through the outlet. The flow through the serpentine; however, is a straight path between the inlet and outlet. Conversely, in the interdigitated design the gas flows into dead-end fingers in the plate where it diffuses through the porous electrode at the end of the terminals. The gas then leaves the plate through the other side of the fingers to the outlet.

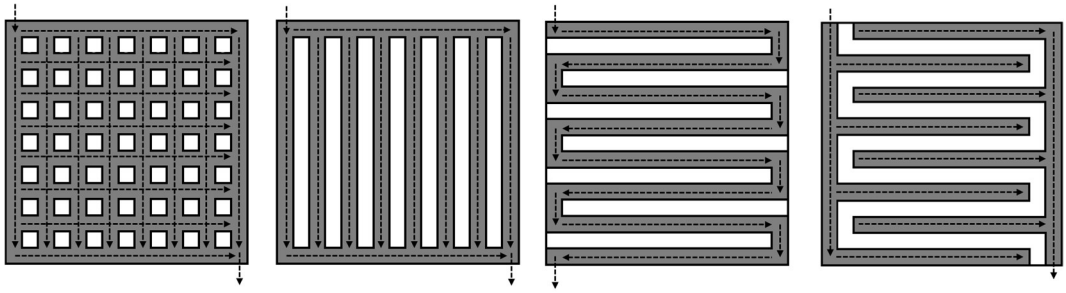

Figure 5.4 - Simple pin (far left), parallel (middle left), serpentine (middle right) and interdigitated (far right) bipolar plates.

The types of bipolar flow plates are not restricted only to the ones mentioned above. Many different designs, materials and manufacturing processes have been developed which have been extensively reviewed [175, 182, 183]. Most of the research has been focused on PEMFCs, although BPP can be used in borohydride fuel cells [184-186]. However, the BPP described in DBAFC used are membraned and in some cases, use peroxide as the oxidant. Although BPP is an integral part of many fuel cells, they may not be required for a membraneless DBAFCs. In place of the BPP is an air plate which distributes the air through the stack. The borohydride/liquid electrolyte and the air are separated by the various electrodes without the requirement of a bipolar plate.

Although the bipolar plate is not required for a membraneless DBAFC, it can be used to aid in heat management throughout the stack. One of the benefits of using a flowing electrolyte is the ability to change the stack temperature by controlling the temperature of the liquid electrolyte whereby the electrolyte can also be used as a coolant. Should this be either insufficient or reduces the stack's efficiency, a liquid specifically used as a coolant can be used

in a bipolar plate. This would give two benefits; the possibility for increased stack efficiency and the separation of electrolyte flow rate from stack cooling. In this way, the flow rate of the electrolyte could be optimised and controlled based on fuel cell performance whilst the coolant could have a separate flow rate to focus on maintaining stack temperature. Furthermore, the use of a specific coolant would give the option of using a liquid with the desired physical properties to optimise stack cooling. The BBP would replace the air plate, controlling the distribution of air across the back of the cathode and the coolant at the back of the anode. Due to the exothermic hydrolysis of borohydride at the anode (see borohydride electrooxidation reaction in Section 2.3.4), it is suspected that the anode would be the largest contributor to the heat being generated in the stack.

5.1.3 Electrolyte

There is a wide range of different electrolyte materials used for fuel cells. Due to the large variation, this section will only focus on alkaline electrolytes used in AFCs and DBAFC.

5.1.3.1 *Solid Anion Exchange Membrane*

A large proportion of low temperature fuel cells use a solid electrolyte known as a solid polymer electrolyte (SPE) or solid polymer membranes. These are polymer matrixes saturated in the electrolyte, causing the electrolyte to be immobilised within a rigid gel structure. The use of SPE gives some benefits over using a liquid electrolyte for low temperature fuel cells, including AFC and PEMFC. The benefit associated with using a SPE is mainly due to the reduction, immobilisation or complete removal of the liquid electrolyte. In AFCs, the formation of solid carbonates, produced by the presence of carbon dioxide in alkaline electrolyte, is detrimental to the life of the fuel cell. Having the electrolyte immobilised in the polymer matrix reduces the amount of carbonate formed due to the electrolyte having low mobility. The removal of liquid electrolyte also prevents any potential leakage due to poor sealing, electrode weeping, no ionic leakage (discussed later) and a dramatic reduction in the weight of the stack [36, 187]. Although there are many benefits, there are still some considerable challenges. Generally, SPEs have low ionic conductivity, chemical stability and require the use of expensive solvents for their synthesis [187]. The use of a flowing electrolyte in AFCs are less researched compared to ones that use an SPE. Furthermore, the use of combined liquid electrolyte with borohydride for DBAFC has been even less researched. The development of a DBAFC with a liquid electrolyte is one of the main novelties of this research.

There are two different types of SPE depending on the pH of the electrolyte; the proton exchange membrane (PEM), used to transport protons in PEMFCs, and the anion exchange membrane (AEM), used to transport hydroxyl ions, OH^-, in AFCs. The hydroxyl ion in an AFC migrates from the cathode to the anode through the AEM whilst inversely the proton in a PEMFC migrates from the anode to the cathode through the PEM Figure 5.5.

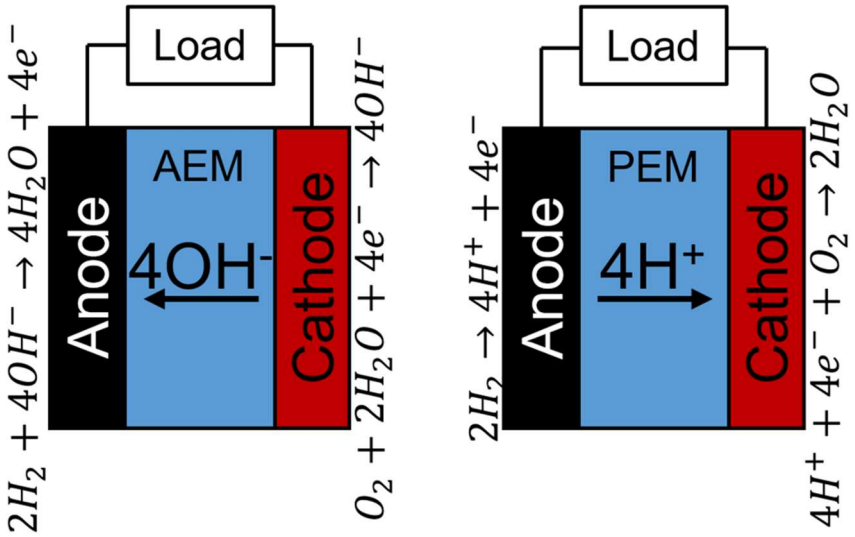

Figure 5.5 - Flow of hydroxyl ion through AEM in an AFC (left) and a proton through a PEM in a PEMFC (right).

The AEM is a long chain polymer with cationic groups covalently bound throughout, either on alkyl branches or on the polymer backbone itself. These cationic groups conduct the hydroxyl, anions and allow them to diffuse from the cathode to the anode [188]. There are two different types of AEM materials; ion-solvating/polymer-salt complexes and polyelectrolyte. Polymer-salt AEMs use electronegative heteroatoms, including sulphur, nitrogen and oxygen, to transport the anion. This type of AEM was used mostly in batteries. The more recent AEMs use polyelectrolyte which are polymers containing either quaternary ammonium ions or sulphur groups to transport the anions [36, 37, 188, 189]. The transport mechanism of hydroxyl ions through the AEM, due to the development of novel AEMs being in its infancy, is still unknown. It is thought that the transport is a combination of Grotthus, convection, diffusion and migration of hydroxyl ions through the AEM [36]. Although not an AEM and cannot be used for DBAFC, a noteworthy SPE is Nafion® (Figure 5.6), a cation exchange

membrane composed of perfluorsulfonic acid polymer developed by DuPont, which is used extensively in PEMFC [190].

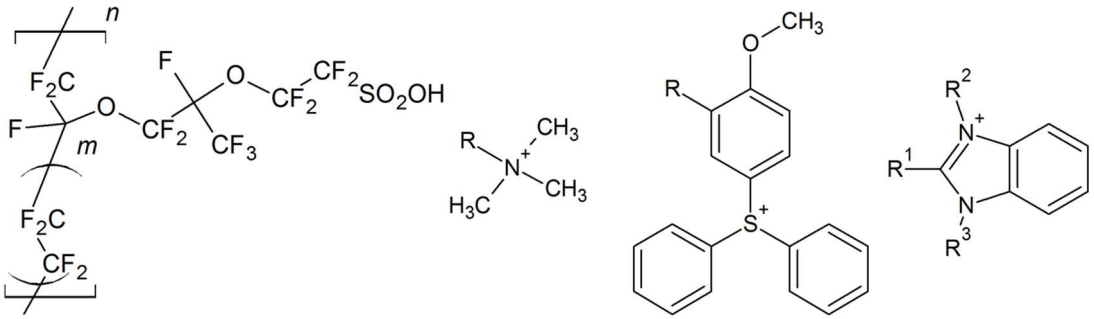

Figure 5.6 - Chemical structures of PEM Nafion® (left) and quaternized ammonium (middle left), tertiary sulfonium (middle right) and benzimidazolium (right) AEM functional groups [191].

AEMs are less developed as the PEM due to the high research activity of PEMFCs. As such, unlike with Nafion® for PEMFC, there is not a single functional group which is considered the lead material for AEM. Many different AEM materials have been developed over the years with the quaternized ammonium, tertiary sulfonium and benzimidazolium functional groups being some of them and shown in Figure 5.6. The different functional groups have their individual benefits and challenges. For example, the quaternized ammonium functional group, which is well established in AEMs, has low anionic conductivity and stability at high pH's; however, it has a simple synthetic route compared to other functional groups making it a relatively low cost material to us as an AEM [191].

The use of AEMs in AFCs are common due to their many benefits. However, using borohydride allows for the fuel to be dissolved in a liquid electrolyte, only if an AEM is not used. This is where one of the research novelties developed in this work.

5.1.3.2 *Liquid Electrolyte and Ionic Leakage*

The alternative to using an SPE in low temperature fuel cells is to use a liquid electrolyte. There are two types of liquid electrolyte setups which are static, self-contained liquid electrolyte held between the electrodes in each cell, and flowing, a single electrolyte which flows between all cells (Figure 5.7). Another popular membraneless fuel cell is the laminar flow fuel cell, also known as the microfluidic fuel cell, which is a subcategory of the flowing electrolyte fuel cells,

whereby the oxidant and reductant flow in parallel between the electrodes (Figure 5.7) [34, 192, 193]. Laminar flow fuel cells have received a lot of attention and are the most popular flowing liquid electrolyte fuel cells; however, have low energy density prevent them from commercial use [193, 194]. This section will focus on non-laminar flowing electrolyte fuel cells as they are more comparable to the flowing DBAFC developed in this work.

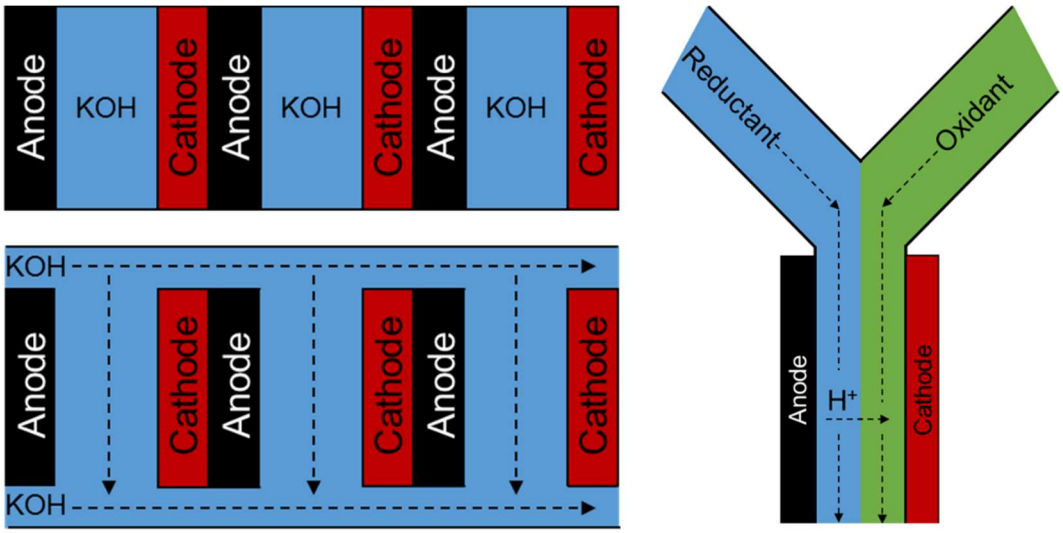

Figure 5.7 - Static (top), flowing (bottom) and laminar (right) liquid AFC.

There are several advantages of having a liquid flowing electrolyte over an AEM. One of these includes the ability to control the stack temperature using the electrolyte as a coolant. The temperature of the electrolyte is altered before it enters the stack to control its temperature. Another is that should the electrolyte become contaminated, either by carbonates or reaction by-products, it can be easily replaced by exchanging the electrolyte. Despite the benefits of using a flowing electrolyte, there are some disadvantages which have led to many AFC and DFAFC research using an AEM. The main disadvantages are the carbon dioxide sensitivity due to the electrolyte (explained in detail in Section 2.3.2). Another drawback is the introduction of ionic leakage (also known as shunt currents). This is due to ionic currents flowing between anodes at a high potential to cathodes leading to a reduction in the stack efficiency. Reducing the ionic leakage can only be reduced by increasing the electrical resistance between the adjacent cells through the electrolyte. Another disadvantage is the increase in the weight of the stack due to the large amounts of liquid required. This liquid electrolyte also requires excellent sealing to prevent leakage of caustic liquid which would present a chemical hazard

and potential corrosion of components within the fuel cell system. The use of a liquid electrolyte in a DBAFC, specifically with the borohydride dissolved in the electrolyte compared to being separated outside of the anode, is one of the novelties of this research.

5.1.4 Electrode Substrate

The electrode substrate is an electrically conductive plate which is used as a structural support for the electrode. In an AFC, the electrode can be relatively brittle and would not be able to form a plate on its own. Furthermore, if it were possible to develop an electrode without the requirement for a substrate, due to the use of precious metals it would not be cost-effective to do so. As such, a low cost support is used to provide an electrically conductive scaffold and give the electrode structural integrity when compressed between the adjacent plates.

Nickel is often used as the electrode substrate for AFCs due to being resistant to chemical corrosion from alkaline media and having a high electrical conductivity. The nickel is often in the form of a nickel mesh with the electrocatalyst deposited on the surface. This gives the electrode two properties, increased electrode surface area and the electrode becomes three-dimensional, which is required for a gas diffusion electrode (GDE). Recent research has opted for a nickel foam over the mesh (Figure 5.8) as it has the potential for a reduction in both cost and density compared to the mesh, which is advantageous for fuel cell stacks [195].

Though the nickel foam has been extensively used for AFCs, it has also been investigated for the use in DBPFC. The work conducted by Cao *et al.* [196] showed increased electrooxidation of Au/Ni foam compared to Ni foam alone. This piece of work is, to the author's knowledge, the only published work focused on using nickel foam as a substrate for any type of direct borohydride fuel cells (DBFC, all types of fuel cells which oxidise borohydride directly which includes DBAFCs and DBPFCs). Although this is only one study, it shows that there is interest in using such substrates in DBFC.

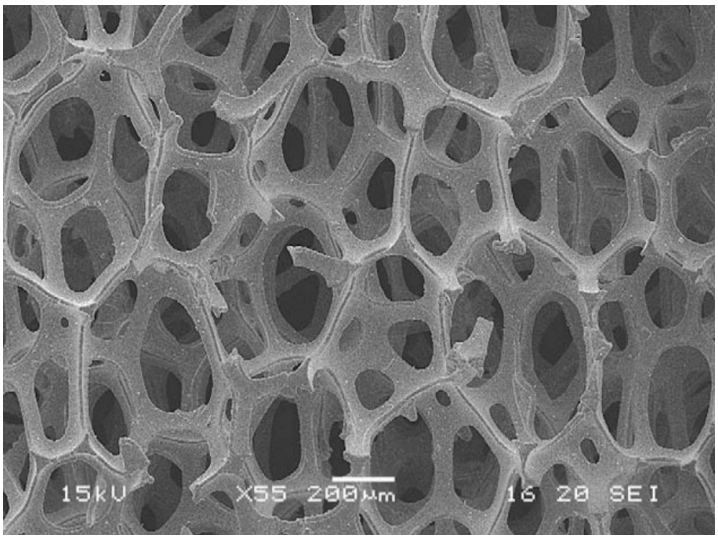

Figure 5.8 - Nickel foam used as an electrode substrate [195].

Although using a 3D nickel foam or mesh has advantages, the cost of its preparation compared to a nickel sheet is expensive. Due to simplicity, low manufacturing cost and the anode in the DBAFC designed was not required to be a GDE, a nickel sheet was used as the substrate for that anode and a perforated nickel sheet for the cathode. The perforated cathode substrates were etched; however, other methods such as laser drilling and electroforming could also be used.

5.1.5 Current Collector

Electrons generated by the redox reaction at the anode's surface migrate to the adjacent current collector, an electrically conductive material also referred to as charge carriers, which is connected to the external electronic load. Once the electrons have been used they leave the load to return to the cathode via another current collector on the other side of the stack, completing the circuit. As such, the current collectors take no part in the redox reaction and act only as an electrical component within the fuel cell stack. This is highlighted in Figure 2.2.

Although the current collector has some desirable properties, which include low electrical resistance, cost, density and high chemical corrosion resistance, its design is something that is not typically researched. The current collectors commonly used in industrial fuel cells are simple metal frames adjacent to the electrode [197-201]. However, research into making the

current collectors lighter and low cost have led to the development to metal foams [202] and porous graphite [203] designs being developed.

5.1.6 Other Components

There are other components that are part of a fuel cell and stack which, although play an important role in its operation, are not researched as the component designs are relatively simple.

One such component is the end plate. The end plates are at the beginning and end of the stack and provide two important characteristics; structural integrity for the stack and connecting the fluid inlets and outlets. The end plates are manufactured out of a material which is resistant to chemical corrosion, in the event of fluid leakage, and must be able to withstand the compression applied when constructing the stack. The design itself can be relatively simple and would only require a method for compression, i.e. using bolts or a vice, and channels for fluid insertion and removal.

Another important component is the various seals used through the stack. Due to the use of liquid and gases and metallic plates, as metals provide poor sealing, rubber seals are often used to prevent leakage. The material must be compressible and resistant to chemical corrosion. Furthermore, the ideal material would be stable for prolonged periods of time under compression without fracturing.

5.2 Methods

The following describes the manufacture and assessment of the individual components within the fuel cell stack.

5.2.1 Definitions

In this section, various parts and components of a fuel cell stack and rig will be discussed. This can be complicated due to the number of different parts which make up an electrode. As such a clear definition of these parts and how they are constructed must be used.

The two electrodes, anode and cathode, were not single components, such as the current collectors, but were a collection of parts. The cathode component (Figure 5.9), used to describe all parts of the component, was comprised of three parts which included the cathode electrode, the GDL and the cathode substrate. The cathode electrode, which contained the electrocatalyst, was screen printed onto the GDL, the layer which allowed the passage of air but prevents the liquid flow. These layers were compressed onto the cathode substrate, the metal plate used to give the cathode electrode and GDL structure but allow the GDL to be exposed to the air.

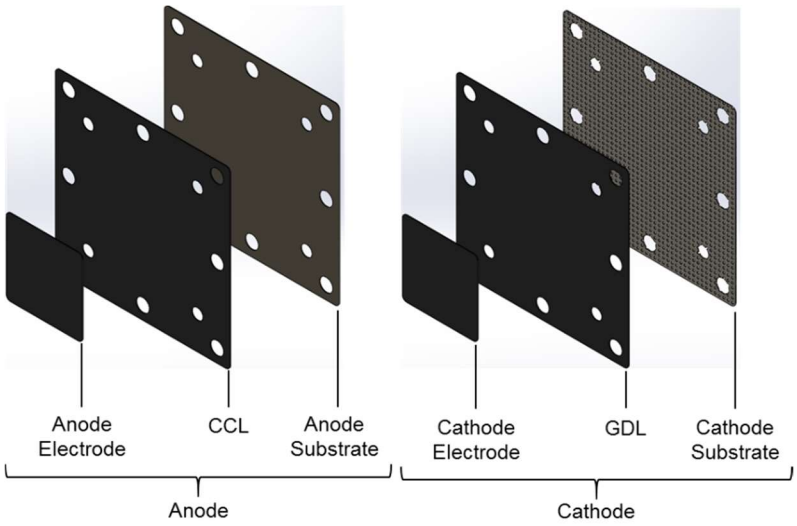

Figure 5.9 - The anode and cathode components and their constituent parts.

The anode component (Figure 5.9) was either comprised of two or three parts depending on its construction. The anode electrode, which contained the electrocatalyst, was either screen printed on the carbon contact layer (CCL), a carbon based material which aided adhesion or printed directly onto the anode substrate, a metal plate used to give the anode electrode structure. Although the materials or design of the parts changed, the anode and cathode components still served the same function.

5.2.2 Effects of Component Material and Design

All component materials were required to be resistant to alkaline corrosion, due to the presence of the electrolyte, but they also required other properties. The effect of their material and the geometry were important for the running of the stack and these are described below.

5.2.2.1 *End Plates*

The end plates needed to be strong and ridged to keep the structure of the fuel cell and incorporate the electrolyte and air inlet/outlet connectors. The material also needed to be chemically and electrically resistant. The material used in this work was Perspex due to its low cost and its chemical and physical properties. The geometry of the end plate was relatively simple and only required holes for the bolts and fuel/oxidant inlets and outlets.

5.2.2.2 *Current Collectors*

The current collector material needed to have a high electrical conductivity, leading to the use of high purity nickel. Much like the end plates, the geometry spanned the whole fuel cell face and only required holes for the bolts and fuel/oxidant. The more contact the current collector had with the adjacent plate, the more efficient it was at removing electrons from the adjacent electrodes. It also had two clips to connect to the electronic load.

5.2.2.3 *Anode Substrate*

As with the current collector, the support needed to have a high electrical conductivity. The anode electrocatalyst support had the same geometry as the current collectors, without the electronic load connects, for the same reasons.

5.2.2.4 *Electrolyte Flow Plate*

The electrolyte flow plate needed to be a good electrical insulator. This was to prevent the fuel cell from short-circuiting between the anode and cathode. It also needed to be hard so that the geometry could be sustained during electrolyte flow. PTFE has was used for the electrolyte flow plate as it fulfilled most the material characteristics requirements which included high chemical and electrical resistance and its flexibly aided with sealing against adjacent metallic plates.

The distance between the electrodes in a cell had to be low to reduce the electrical resistance of the cell when would have accumulated when put into a stack. Therefore, the thickness of the electrolyte plate had to be thin enough to have a low electrical resistance but not so thin that it could affect the structural integrity of the design. To determine the effect of electrolyte plate thickness, three different PTFE thickness were assessed, 1, 1.5 and 2 mm.

The geometry of the electrolyte flow plate was very important as the fuel cell performance was directly related to the flow of electrolyte between the electrodes. One phenomena related to the geometry is ionic leakage as described in Section 5.1.3.2. Therefore, to reduce the effect of ionic leakage, a high electrical resistance electrolyte path was designed. To maximise the resistance, the flow path was designed to be as long as possible. The introduction of a serpentine flow path increased the distance the electrons would have had to travel through the electrolyte, increasing the electrical resistance and therefore lowing ionic leakage losses. However, using a plate that only contained a serpentine would have restricted the amount of exposed electrocatalyst and therefore decreased the amount of borohydride oxidised and increased the pressure drop across the cell. This led to the design of a plate which contained a full serpentine (FS), designed for maximum reduction of ionic leakage, and a partial serpentine (PS), designed for a reduction in ionic leakage but maximum electrocatalyst exposure.

5.2.2.5 *Cathode Electrocatalyst Support*

As with the current collector, the support needed to have a high electrical conductivity. The cathode electrocatalyst support had the same geometry as the anode support but with the addition of air channels in the middle of the plate. This was to allow the passage of the air oxidant from the air flow plate through to the GDL where it was reduced. Increasing the channel diameter increased the amount of air that could be passed through to the GDL. However, increasing the channel diameter too much would have resulted in a reduction in the available substrate surface area for the electrode to be adhered to. The cathode substrate used in this work was commercially available and so the number and size of the channels were predetermined. However, the design of the cathode substrate was designed specifically to work with the stack developed in this work.

5.2.2.6 *Air Flow Plate*

High purity nickel was also used for the air flow plate due to the high electrical conductivity requirement. The air flow does not experience the ionic leakage issues compared to the electrolyte and so the geometry only required the air to flow across the back of the GDL/cathode substrate. The influence of the air flow geometry was the amount of air that can get to the GDL. Unlike the liquid electrolyte, the gaseous air would naturally expand into the open plate domain design, reducing the number of starved areas. In this work, a simple air flow plate was designed, manufactured and used. Although it could have been optimised further, the stack performance would have benefited further by electrolyte flow plate optimisation compared to the air flow plate.

5.2.3 Development of Stack Components

It should be noted that the stack designed was compared extensively to the single cell fuel cell rig. The rig was initially designed by Hui Choy (BEng, 2014), a student from Lancaster University (with Dr Richard Dawson as primary supervisor) and is shown in Figure 5.10. The position of the bolts and fluid flow was based on this design, as experiments using this setup showed good fluid transport through the cell with no leakage. However, two additional bolts were added for the stack design around the perimeter to aid in the prevention of electrolyte leakage.

A fuel cell rig and a stack perform the same role, producing energy from the oxidant-reductant redox reaction, and so the components used were similar. The fuel cell rig was designed to assess various electrocatalyst materials and electrode designs, but it was not for optimal power generation. As such, the components of the single cell rig had to be altered for scale-up application. This work describes the manufacture and design of stack specific fuel cell components, focused on scale up.

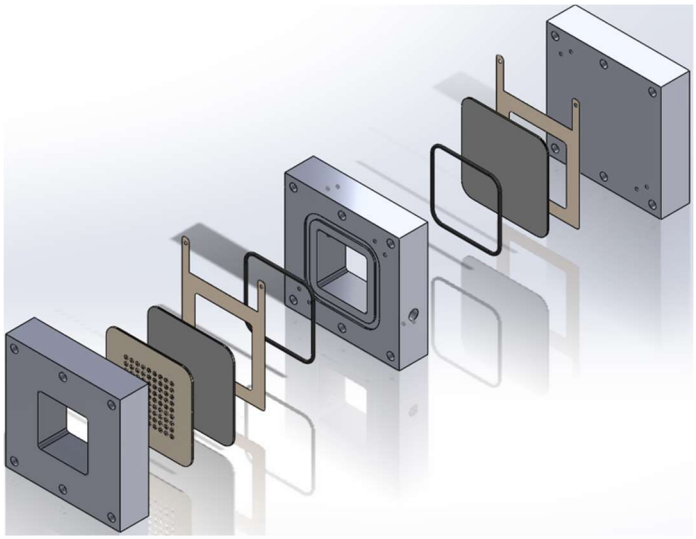

Figure 5.10 - Fuel cell rig designed by Hui Choy.

It should also be noted that the term “rig” has been used to describe the fuel cell previously designed, which was used to evaluate electrode design. The term “stack” has been used for the design developed which, although may only contain a single cell, was suitable for scale up with multiple repeating cell units.

5.2.4 Assessing Component Design

The flow of electrolyte and air through the electrolyte plate was important as it controlled where the reaction occurred on the face of the electrode. The poor flow could have left areas of the electrode starved, reducing the power and potentially damaging the electrode. Therefore, it was important to understand how the fluid flows across their respective plates. One way to do this was to use COMSOL Multiphysics, software which computes the effects of different physics on a given geometry. Using the plate design, produced in SolidWorks CAD software, along with material properties and stack operating conductions, COMSOL calculated various properties depending on the physics used. The benefit of using multiphysics simulations over computational fluid dynamic (CFD) specific software was the ability to build on the model, adding new physics and interactions to generate a more detailed and in-depth understanding of the system. However, in this work COMSOL was only use for its CFD capabilities which included the velocity fields of various fluids in different plates were determined using fixed inlet volumetric flow rates.

Before the simulation was set up, the correct physics had to be identified. For testing the electrolyte plate, the flow of the liquid electrolyte had to be modelled and the physics used to simulate this was determined by the type of fluid used, i.e. either a laminar or turbulent flow model. To determine this, the Reynolds number (R_e) was calculated using Equation 5.1 whereby ρ is the density of the fluid (kg.m^{-3}), V is the velocity (m.s^{-1}), L is the length (m) of the path and μ is the viscosity (Pa.s or kg.m^{-1}.s^{-1}).

$$R_e = \frac{\rho V L}{\mu}$$

Equation 5.1 - Reynolds number calculation equation.

Since the fuel cell was to be operated at different temperatures, the density and viscosity of the electrolyte would have changed. These changes for 30 wt.% $KOH_{(aq.)}$ have been summarised in Table 5.1.

Table 5.1 - Potassium hydroxide (30 wt. %) density and dynamic viscosity at different temperatures [204].

Temperature (°C)	Density (kg.m^{-3})	Dynamic Viscosity (Pa.s)
20	1294	2.46×10^{-3}
50	1279	1.36×10^{-3}
70	1265	1.01×10^{-3}

It must be noted that the viscosities and densities used for the simulation were based on 30 wt.% $KOH_{(aq.)}$ and didn't take into consideration the borohydride dissolved in the electrolyte. It was assumed that the addition of borohydride had a negligible effect on the viscosity and density.

Calculating Reynolds number required the velocity, which is a function of the cross-sectional area and volumetric flow rate, of the electrolyte. The volumetric flow rate of the electrolyte was kept constant at 5 cm^3.min^{-1}; however, the cross-sectional area of the electrolyte path had to be calculated. This was relatively simple for the FS design; however, not for the PS. To calculate the Reynolds number, and therefore use the correct fluid model, the PS was split into

a serpentine and a chamber. The serpentine was taken from the inlet to the central chamber where the electrode would have sat and from the chamber to the outlet. The chamber length was measured as the distance between the inlet and outlet serpentine (Figure 5.11).

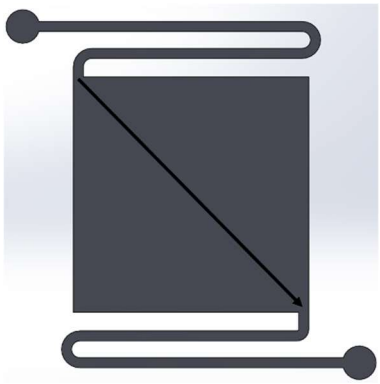

Figure 5.11 - Flow length calculation of PS chamber.

This led to the cross-sectional area calculations and the Reynolds number shown in Table 5.2 and Table 5.3 respectively.

Table 5.2 - Electrolyte plate lengths and cross sectional areas.

Design	Length (cm)	Cross Sectional Area (cm^2)
FS	51.75	0.02250
PS – Serpentine	8.16	0.02250
PS – Chamber	4.95	0.3713

Table 5.3 - Reynolds number calculations for different electrolyte plates.

Reynolds Number			
Temp. (°C)	FS	PS	
		Serpentine	Chamber
20	10083	1590	58
50	18027	2842	104
70	24008	3785	139

The Reynolds numbers calculated in Table 5.3 are highlighted in green, yellow and red depending on whether they were considered laminar ($R_e < 2300$), transitional ($2300 > R_e < 4{,}000$) or turbulent ($R_e > 4{,}000$) respectively. This showed that the flow through the FS was very turbulent and so a model which simulated turbulent flow was required. Therefore, to simulate the FS in COMSOL, turbulent κ-ε model was used, which is commonly used in industrial applications. The turbulent RANS type, κ-ε model equations used is shown in Equation 5.2, Equation 5.3, Equation 5.4, Equation 5.5 and Equation 5.6. However, the serpentine and chamber showed very laminar flows so only Equation 5.2 was used for the serpentine modelling.

$$\rho(V \cdot \nabla)V = \nabla \cdot [-\rho I_d + \mu(\nabla V + (\nabla V)^T)] + F$$

Equation 5.2 - Incompressible equation used to model turbulent and laminar flow whereby *F* = volume for vector ($N.m^2$), *V* = velocity ($m.s^{-1}$), *ρ* = density ($kg.m^{-3}$), *μ* = dynamic viscosity (Pa.s), *T* = temperature (K) and I_d = identity matrix.

$$\rho(V \cdot \nabla)k = \nabla \cdot \left[\left(\mu + \frac{\mu_T}{\sigma_k}\right)\nabla k\right] + P_k - \rho\varepsilon$$

Equation 5.3 – Turbulent transport equation for *k* whereby *k* = kinetic energy, *ε* = dissipation rate and *P* = pressure (Pa).

$$\rho(V \cdot \nabla)\varepsilon = \nabla \cdot \left[\left(\mu + \frac{\mu_T}{\sigma_\varepsilon}\right)\nabla\varepsilon\right] + C_{\varepsilon 1}\frac{\varepsilon}{k}P_k - C_{\varepsilon 2}\rho\frac{\varepsilon^2}{k}, \varepsilon = ep$$

Equation 5.4 - Transport equation for *ε* whereby $C_{\varepsilon 1}$= 1.44, $C_{\varepsilon 2}$= 1.92 and σ_ε= 1.3.

$$\mu_T = \rho C_\mu \frac{k^2}{\varepsilon}$$

Equation 5.5 - Equation used to calculate turbulent viscosity (μ_T) whereby C_μ= 0.09.

$$P_k = \mu_T[\nabla V : (\nabla V + (\nabla V)^T)]$$

Equation 5.6 - Equation used to calculate the production term.

The PS serpentine showed laminar flow at low temperatures; however, as the temperature increased the flow became more transitional. This made it difficult to simulate due to the flow showing traits of both turbulent and laminar flow. However, since the serpentine didn't contain the anode (as the anode was positioned in the chamber), the flow through the serpentine didn't need to be modelled. The flow through the chamber where both the electrodes were positioned had a low Reynolds number and was therefore simulated using a laminar model. To model this using COMSOL, a 3D model was produced which had the following boundary conditions:

- No slip on all walls
- Normal inflow velocity on the inlet
- Normal flow on the outlet

It should be noted that for all models, a fine physics defined mesh was used whereby the program automatically meshes the geometry. The number of total elements has been stated for each model.

The electrolyte plates were assessed under different temperatures (25, 50 and 70 °C). Due to time constraints, the temperature was investigated over other operational parameters, which included volumetric and molar flow rates. This was because out of the different operational parameters, the temperature was arguably the most important. Increasing the temperature reduces ohmic resistance and increases current densities. However, challenges included the requirements for heating and, in the case of DBAFCs, the evolution of hydrogen gas. Although investigating the effects of the other parameters were important, the temperature would have had the biggest effect on the DBAFC and was therefore chosen to be investigated further.

5.3 Results

The work presented in this Results section shows a simple diagram of the component described.

5.3.1 Parallel vs Series Fluid Flow

The flow of fluid through a stack, much like the flow of electricity through an electrical circuit, can be one of two different methods, the series (Figure 5.12) and parallel (Figure 5.13) flow.

In a series flow setup, the flow of fluid passes through each cell, one after another, alternating direction as it passes through each cell. The advantage to this is the ability to accurately control the volumetric flow rate throughout the entire stack. Furthermore, the amount of fuel utilisation increases as it flows past the surface of every electrode in the stack, increasing its chances of being oxidised. With the electrolyte path being very long in a series flow stack, and therefore increased electrical resistance between the cells, there would potentially be a decrease ionic leakage losses. Serpentine designs have been used in the majority of cases as a method to increase fluid distribution across the electrode [205], compared to reducing ionic leakage. In this instance, the serpentine was applied to the flow between the various plates in the stack, compared to the flow across the electrode surface. However, research into serpentine of electrolyte adjacent to the surface of the electrode could lead to a reducing in blockages compared to parallel flow [184, 206].

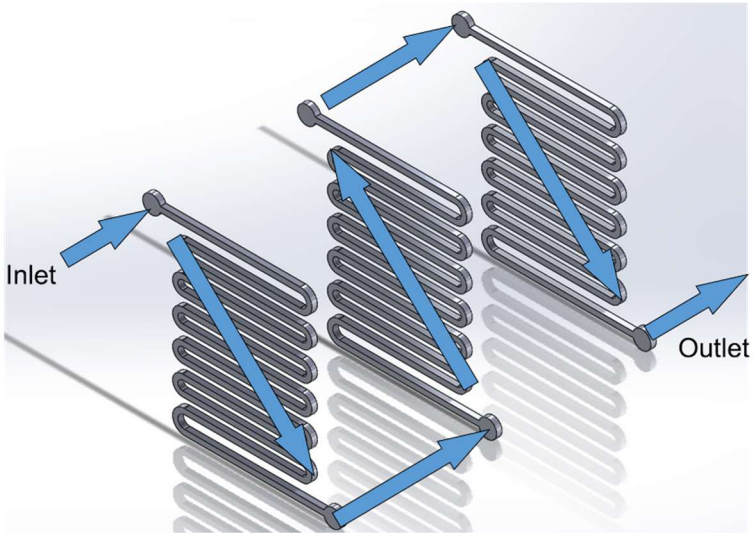

Figure 5.12 - the Series flow of electrolyte through a three cell stack.

There are some challenges with this configuration which include cell starvation. Unless the fuel is in a large excess, the cells towards the end of the stack will become starved, due to the concentration gradient, which could potentially damage the electrodes. Furthermore, having the fuel in such a large excess would not be beneficial for a DBAFC as having a high concentration of borohydride increases the amount of hydrolysis, which is an accelerated issue at increased temperatures. There would also be an increase in pressure drop which reduces the overall system efficiency [207]. In addition, the alternating direction of electrolyte in a DBAFC could potentially cause a build-up of hydrogen gas pockets within the cells where

the flow of electrolyte is down, causing a potentially explosive hazard. Furthermore, the hydrogen pocket would prevent electrolyte flow to the area, causing it to become inactive. Conversely, on the air side of the cell, any moisture which may accumulate is difficult to remove and may cause small blockages. Much like with the hydrogen generation, as the stack is run, there would be a generation of other by-products from the redox reaction, notably the metaborate. Due to the single flow configuration, the by-products would accumulate throughout the stack with the cells in the latter part of the stack having considerably higher concentrations of by-products. This would starve the electrodes of borohydride leading to inefficiencies and electrode degradation.

In a parallel system setup, the fluid flows through each cell in the stack simultaneously. This configuration allows for a more uniform fuel concentration between the first and final cell in the stack. This also allows for the electrolyte to flow in a single direction which for DBAFC is advantageous as it allows for any hydrogen gas as well as the removal of any moisture on the air side. Furthermore, the parallel flow does not suffer from the same pressure drops experienced with the series flow.

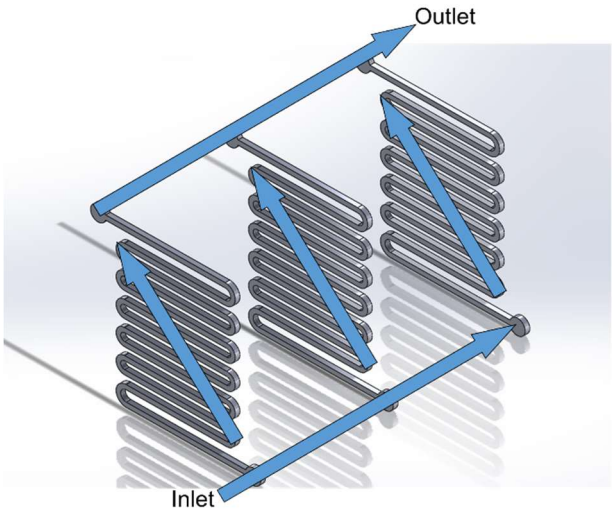

Figure 5.13 - the Parallel flow of electrolyte through a three cell stack.

The disadvantage to using a parallel flow is that it is difficult to accurately control the volumetric flow rate in each cell as they are governed by inlet flow rate and the design of the associated plate. This could lead to different volumetric flow rates depending on the position

of the cell in the stack. Different volumetric flow rates could potentially lead to two challenges in the stack; different molar flow rates and rate of by-product removal. A decrease in the volumetric flow rate would result in a decrease in the molar flow rate, and therefore the oxidant or reductant concentration, available for the redox reaction. Although there would be concentration difference between the cells, this would be far less compared to the first and last cells in a series configuration. The other effect of different volumetric flow rates would be the removal of reaction by-products which include metaborate and hydrogen. Cells in the stack with a low volumetric flow rate would accumulate by-products, which in the case of metaborate could lead to less unoxidised borohydride being available to the electrode. The accumulation of hydrogen would also reduce the mass transport of borohydride to the surface of the electrode but would also create an explosion risk. However, removal of by-products from a parallel flow configuration would allow the hydrogen to be removed easily, as it would rise away from the electrode, and the concentration of metaborate would be considerably less compared to the series flow configuration. Also, the inlet and outlet channels decrease the flow distance between the cell which can lead to an increase in ionic leakage. In this configuration, it is important to have low lost headers, i.e. large electrolyte inlets and outlets, to promote even flow.

Both flow configurations have advantages and challenges; however, for the purposes of DBAFC the direction ease of removal of by-product and moisture generated and the relatively uniform molar flow rate and low concentration gradient between the first and final stack make it a more suitable setup for this particular fuel cell.

5.3.2 End Plates

The stack and rig gain a large amount of its structure from the end plates and its construction. The end plates were constructed from acrylic (poly(methyl methacrylate) or PMMA from The Plastic People) blocks. Acrylic is a low cost material which is chemically stable in alkali media at low temperatures (under 100 °C). It is easily machined and hard enough to keep the rig and stack structure. Being electrically insulating, it provided a suitable material to use at the ends of the stack. Furthermore, the acrylic was transparent when polished. This gave the option of observing the fuel cell during operation to identify any hydrogen generation. There are two end plates which differ slightly between the fuel cell rig and stack.

The manufacture of the stack end plates was relatively simple. A large piece of acrylic, which had the same width and depth as the final design, was supplied and cut using a jigsaw into multiple end plate squares. The holes were then drilled around the perimeter and for the inlet and outlet.

For the rig, both end plates consisted of 6 holes around the edges for the bolts to hold the rig together. In addition, the cathode end plate had an open void allowing for air flow at atmospheric pressure. For the stack, the end plate had 8 holes around the outer perimeter for the bolts and an additional 2 holes for the fluid inlet and outlet. A connector fitting (SMC part LQ1H2A-M) was used to connect the system tubing with the stack end plates. Both the anode and cathode had the same end plate design, unlike the rig design as the transport of compress air had to be taken into consideration (Figure 5.14).

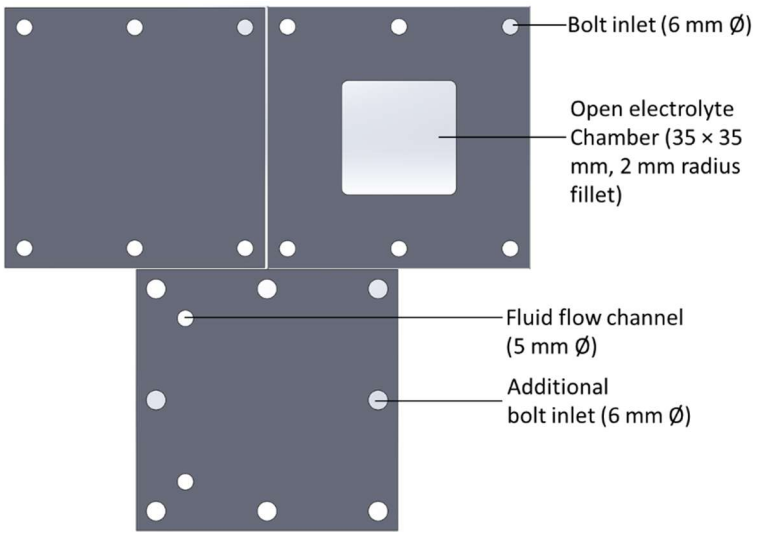

Figure 5.14 - Rig (top) and stack (bottom) end plates manufactured out of 80 × 80 × 20 mm acrylic.

The end plate design worked well. The additional two bolts of the stack compared to the rig end plates provided a more even compression across the surface of the plate. The inlet and outlets lined up correctly with the other component plates and the connectors worked well when the stack was connected to the rest of the system. When the stack was constructed, the end plate showed signs of flexing in the middle when tightened (each bolt was compressed to

2.5 N using a torque wrench). Although the acrylic was hard enough to give the stack structure, it suffered warping as a consequence.

5.3.3 Current Collectors

The function of current collectors was to collect electrons and provide a conduction path in the circuit. The material required a high electrical conductivity and chemical corrosion resistance. The design had to accommodate the bolts and transport of fluid through the cell and must also be able to connect to the potentiostat or electronic load. This led to the design in Figure 5.15 which was manufactured out of 0.3 mm thick high purity nickel sheet. The rig contained an open void in the middle to allow air to flow from the open side of the cathode at atmospheric pressure. Although the current collector performed well, it was not designed to allow the passage of multiple fluids separately through a stack. Furthermore, the current collector had to be to be carefully placed to match the air opening in the end plate and the void in the current collector. This often slipped, making rig construction difficult to align. This design was then adapted into the stack design (Figure 5.15) which had a full face design, i.e. no void, and featured 8 holes for bolts around the perimeter, 4 large fluid transport channels to allow air and electrolyte and two connectors that allow crocodile clips to be attached.

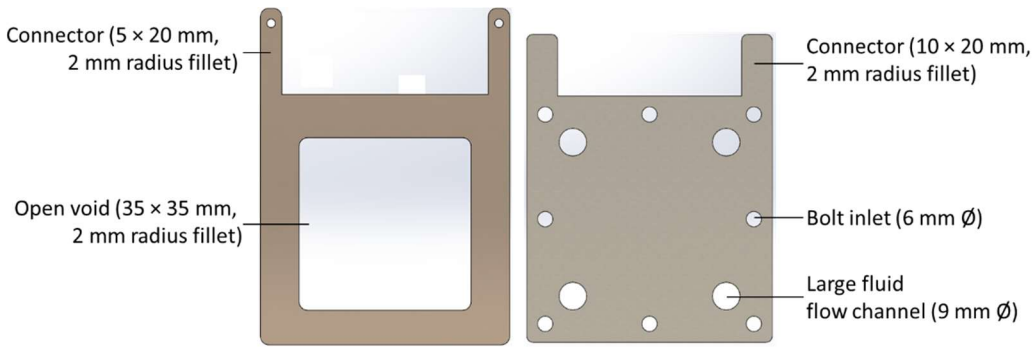

Figure 5.15 - Nickel current collector for a rig (left) and stack (right). The rig current collector body was 58 × 58 mm whilst the stack current collector was 80 × 80 mm.

The stack current collector performed well. The four large fluid transport channels in the plate used to transport fluid through the stack were wider than others in different plates. This was due to the poor sealing that would have occurred between the current collector and the adjacent metallic anode or air plate (see Section 5.3.4 and Section 5.3.7 respectively). To

prevent this, ethylene propylene diene monomer (EPDM, J-Flex) rubber seals in the form of an O-ring were placed in the voids of the current collector prevent fluid leakage. Furthermore, due to the aligned bolt holes, the placement of current collectors in the stack were simple and did not alter during construction, unlike the current collectors used in the rig.

5.3.4 Anode and Anode Substrate

The anode electrode was screen printed onto the anode substrate (see Figure 5.16). The design for the anode substrate was relatively simple and had a similar design to the current collector. The anode substrate was manufactured using a guillotine to cut large sheets of 0.3 mm thick high purity nickel followed by drilling holes for the bolts and fluid transport.

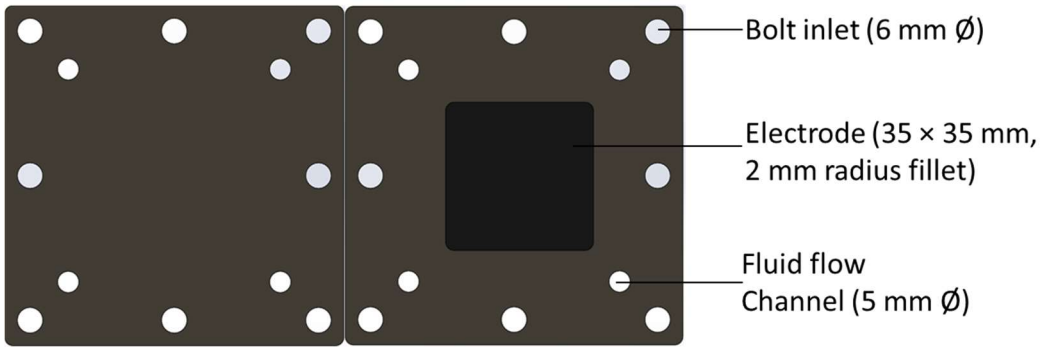

Figure 5.16 - Anode substrate (left) and anode electrode on anode substrate (right). Both substrates are 80 × 80 × 0.3 mm with 2 mm fillets.

Once the anode substrate was manufactured the surface was prepared, or a CCL added, and the anode electrode printed. The EPDB seals that sat in the voids of either the current collector or the air plate pressed against the anode substrate, sealing between the adjacent plates. The plate aligned with the other components and the transport of fluid in the stack.

5.3.5 Electrolyte Flow Plate

Two different electrolyte flow plates were designed for the stack; a full and partial serpentine. This section describes the theory behind and the effect of fluid flow on the different designs compared to the rig electrolyte plate design.

5.3.5.1 *Electrolyte Material and Design Properties*

The electrolyte plate is an important part of the fuel cell stack and its design, both its geometry and materials used, have a substantial effect on the efficiency of the stack. To produce an electrolyte plate which was suitable for a DBAFC stack the plate required several characteristics which include:

Table 5.4 - Effects of electrolyte properties on DBAFC stack.

Plate Property	Effect
Light weight	Due to a stack being an accumulation of many cells, the electrolyte plate needed to be light weight to reduce the overall stack weight. This was more important for portable applications.
High chemical corrosion resistance	Increased KOH concentrations are corrosive and therefore to prolong the life of the plate it had to possess high chemical corrosion resistance.
Thin	A thin electrolyte plate reduces the distance between the two electrodes exposed to the reductant and decreased the ohmic resistance of the cell.
High electrical resistance	Electrical contact between the two electrodes when not in the presence of fuel would have caused the cell to essentially short circuit. Having a plate with a high electrical resistance prevented this.
Low cost	The lower the cost of the plate, the lower the cost of the stack.
Easily manufactured	If the plate could be easily manufactured, it would have reduced the production cost and the overall cost of the stack.
Good sealing	Using a liquid electrolyte required good sealing between the electrodes to prevent the electrolyte flooding into different parts of the stack, leading to corrosion, short circuiting and make the stack hazardous. Although this could have been done using a dedicated seal, having a material which could be used as the plate and sealed well could have potentially reduced the cost and complexity of the stack.
Low ionic leakage	The plates needed to provide enough electrical resistance between the inlet and out to prevent ion leakage to increase efficiency.
High electrode exposure to fuel	Keeping as much of the electrode exposed to the fuel would have ensured high current densities.

A material which has many of these desired characteristics in Table 5.4 was PTFE. The soft plastic, which had good sealing properties, is known for its high chemical corrosion and electrical resistance. Furthermore, it's relatively light and low cost compared to other

materials. Another material which could have been suitable was EPDM. The rubber is resistant to chemical corrosion, light, would seal well against the adjacent electrodes and is relatively low cost. These properties make PTFE and EPDM ideal materials to use as an electrolyte plate. The geometry of the electrolyte must be so that there is a low ionic leakage, high electrode exposure, thickness and ease of manufacture, are related to the design. However, finding the best geometry was not simple and led to the development of different electrolyte plate designs.

5.3.5.2 *Open Chamber Electrolyte Flow Plate*

The electrolyte chamber had a simple design, with an inlet and outlet for the electrolyte and two open faces for the electrodes (see Figure 5.17). The plate was machined out of 80 × 80 × 20 mm acrylic and features six holes for bolts and a groove on the electrode faces for an O-ring to increase sealing.

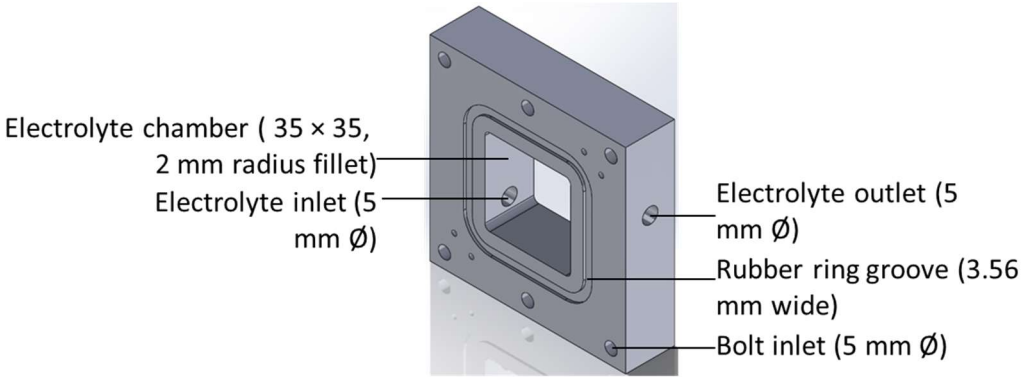

Figure 5.17 - Rig electrolyte chamber made from 80 × 80 × 20 mm acrylic.

The purpose of this design was to provide a simple electrolyte plate which could transport the fuel between the electrodes. Although this design was adequate for single cell testing, it didn't possess the desired characteristics of an electrolyte flow plate for a stack. The acrylic would have sealed poorly against the metallic electrodes and so an O-ring was required which was an additional expense. The large thickness (20 mm) of the plate caused increased ohmic resistance which would have accumulated in large stacks. Furthermore, the large thickness of the plate would make the stack bulky and heavy which is undesirable, especially for portable applications. Finally, the basic design of the electrolyte chamber would lead to a high ionic

leakage due to the low electrolyte electrical resistance. These reasons led to a stack specific electrolyte plate had to be designed.

5.3.5.3 *Stack Electrolyte Plate Design and Manufacture*

To reduce the amount of ionic leakage experienced by the stack, there had to be a significant electrical resistance between cells via the electrolyte flow. One of the ways to do this was to increase the electrolyte path length, such as the introduction of a serpentine into the electrolyte plate design. However, having only a serpentine connecting the inlet and outlet restricted the amount of exposed electrode surface area (EESA). Therefore, two different designs were produced; a full and partial serpentine (Figure 5.18 and Figure 5.19). In the partial serpentine (PS) design there was a small serpentine at the inlet and outlet but between them there was an open plane where the electrode resided, allowing for full electrode exposure (12.22 cm^2). However, having this open plane potentially increased the ionic leakage. In the full serpentine (FS) design the electrolyte flowed from the inlet and outlet solely through a serpentine. Doing so increased the path length, and the electrical resistance, reducing ionic leakage when in a stack. This FS design came at the expense of reducing the electrode exposure (4.741 cm^2) and could have potentially reduced the current density per cell.

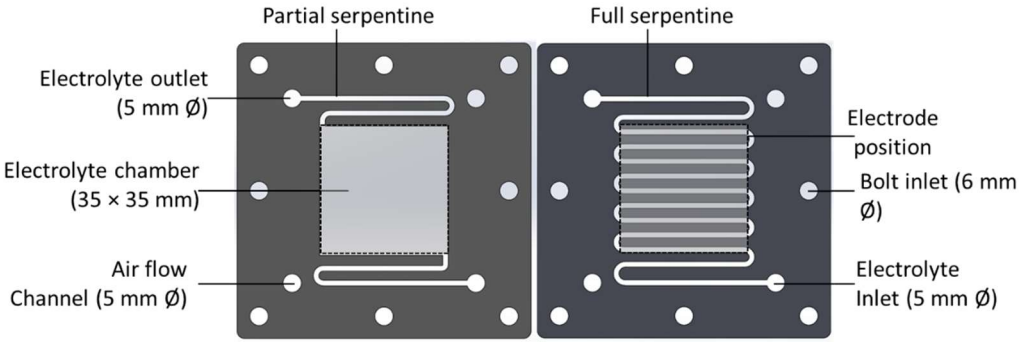

Figure 5.18 - PS (left) and FS (right). Both were 80 × 80 mm (various thicknesses) and had various serpentine dimensions.

The first material used to make an electrolyte plate was EPDM. The design was cut out of a 1 mm thick sheet of EPDM using a waterjet cutter (Figure 5.20). Due to the flexibility of the EPDM, the resolution of the design was low, leading to a rough cut along the wall.

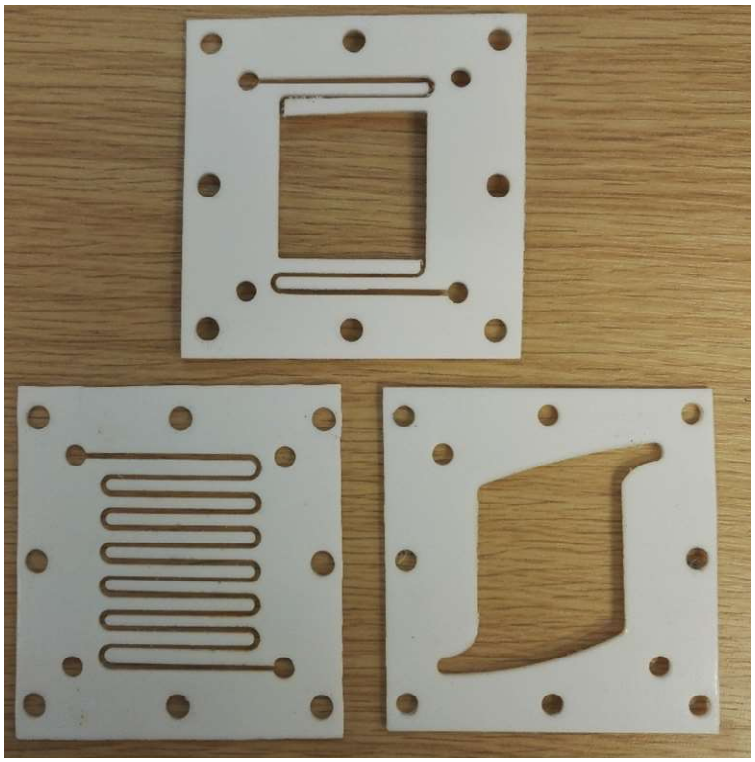

Figure 5.19 - Photo of PS (top), FS (bottom left) and air (bottom right) plates manufactured from PTFE sheet.

Not only did the flexibility of the EPDM cause difficulty in cutting the FS, it led to flexing in the EPDM fingers. Once the plate was manufactured it was tested for fluid flow to ensure that there were no complications once the electrolyte would be used. The plate was placed between two plates, one with an inlet and outlet, and water pumped through at approximately 250 cm^3. The results showed that the force of the water being pumped caused the fingers to bend and flex, closing the channels.

To prevent flexing, the plates were manufactured again but out of PTFE which was less flexible compared to the EPDM. Both plates were manufactured out of 1, 1.5 and 2 mm PTFE sheets (The Plastic People). To manufacture the different plates a variety of manufacturing methods were used. Although the designs were relatively simple the thin finger dimensions of the serpentine coupled with the soft plastic made the manufacture of the plates difficult. This was not so much of an issue for the PS design as the serpentine was short with relatively wide fingers.

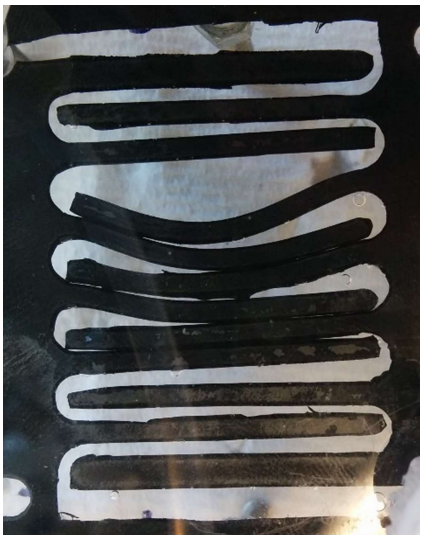

Figure 5.20 - Flex in full serpentine design in EPDM.

Initially, the FS was based on a narrow serpentine design (see Figure 5.22) to maximise the flow length between the inlet and outlet. The first plate was manufactured using a 1 mm thick PTFE sheet to reduce the ohmic resistance between the electrodes through the electrolyte. This was initially manufactured using a water jet cutter. However, the thin fingers, PTFE flexibility and the force of the water jet cutter tore the fingers off. A laser cutter was then used to manufacture the plate as there was no force during the manufacturing process. This lead to the fingers being burnt off due to the heat produced. Furthermore, laser cutting melts the PTFE which could potentially have released hazardous fluorinated gas. Finally, a jig was produced with the design and the plate sheet was machined using a 2 mm PTFE sheet. The method was successful with all the PTFE fingers staying intact and produced a plate with a higher resolution compared to EPDM. As with the EPDM, the PTFE plate was compressed between two end plates and water pumped through to evaluate the effect of liquid flow (see Figure 5.21). Flexing in the PTFE finger was also seen, showing that the thickness of the fingers, coupled with the flexibility of the material, was insufficient for the use of an electrolyte plate. This indicated that if this design were to be used, at a similar thickness, a much more rigid material would be required. However, the physical and chemical properties of PTFE, along with the low cost, still make it a viable material to be used as the electrolyte plate. As such two similar but different designs were assessed, the wide and extra wide FS (Figure 5.22 which had different path lengths, and therefore electrolyte electrical resistance, and EESAs).

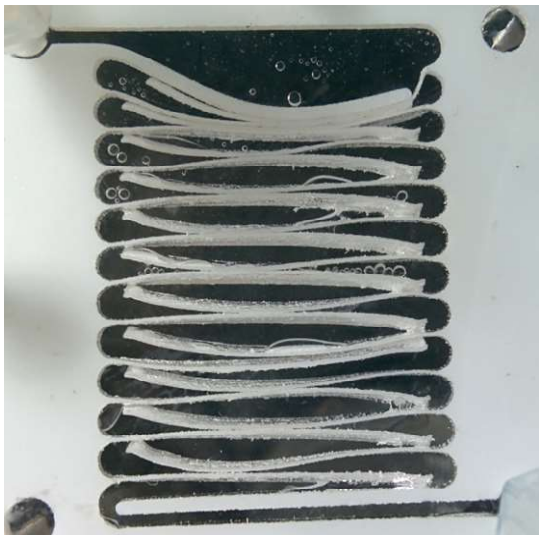

Figure 5.21 - Flex of PTFE fingers in FS narrow design.

Table 5.5 - Full serpentine designs and properties.

FS Design	Channel Width (mm)	Finger Width (mm)	Path Length (cm)	EESA (cm^2)
Narrow	1.5	0.5	91.85	13.60
Wide	1.5	2.5	52.25	4.741
Extra Wide	5	7.5	23.85	5.367

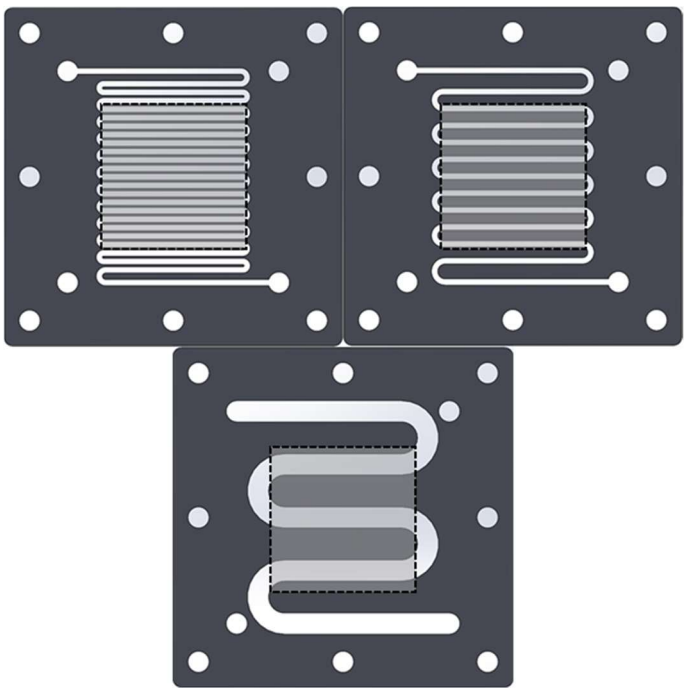

Figure 5.22 - Narrow (top left), wide (top right) and extra wide (bottom) full serpentine designs.

The aim of the wide and extra wide designs was to increase the finger width whilst still having a long flow path. Depending on the PTFE finger thickness, the electrode underneath may not be starved of fuel but being too thick or thin each has their own advantages and issues. During operation, the electrolyte would diffuse through the electrode, with the extent of diffusion prominently governed by the pressure of the electrolyte and the porosity of the electrode. Wide PTFE fingers would have concealed more of the electrode compared to thin PTFE fingers, potentially making much of the electrode inactive. Conversely, should the PTFE fingers be too thin, the electrolyte could diffuse behind the finger (Figure 5.23). If this were to occur across the whole of the electrode face, the electrical charge could bypass the serpentine as a lower path of electrical resistance would have been created, increasing ionic leakage significantly.

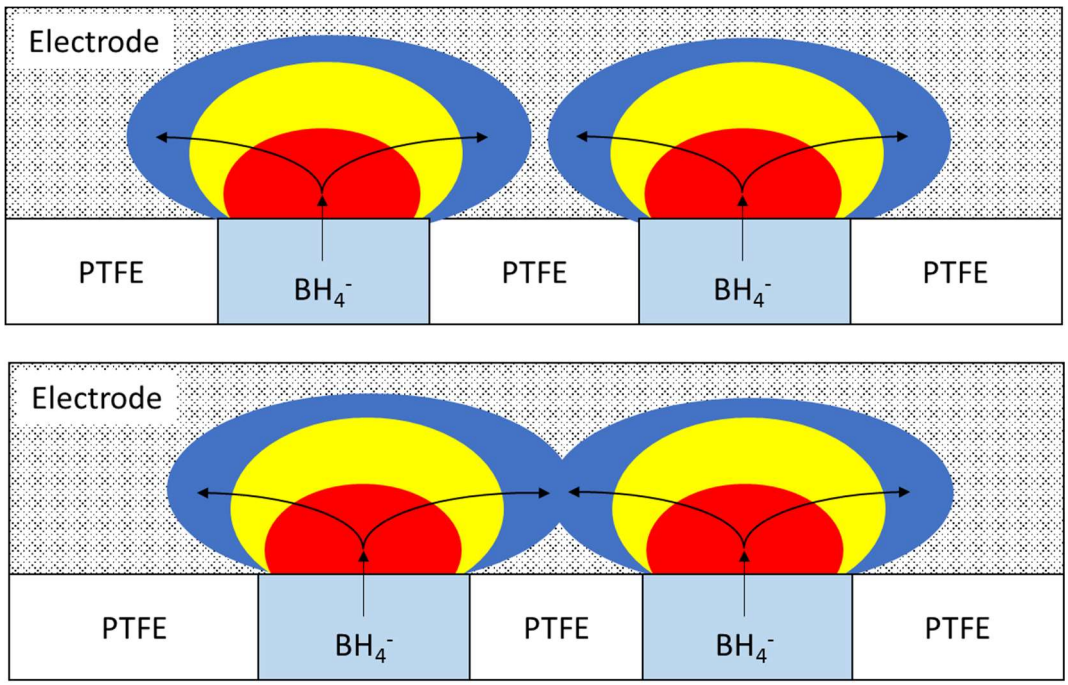

Figure 5.23 – Illustration of electrolyte diffusion (with high, medium and low field velocities as red, yellow and blue respectively) through the electrode with thick (top) and thin (bottom) PTFE fingers.

However, the PTFE finger width would not be the only factor in determining ionic leakage via diffusion through the electrode. The porosity of the electrode could be low or high when used with the thin or thick PTFE finger width respectively. This would counter the effects of finger width and in an ideal electrode, the electrolyte would diffuse behind the PTFE finger as much as possible, having a high active area, without the individual flow fields touching, preventing

increased ionic leakage. Computation simulation could be used to evaluate the extent of diffusion through the electrode, but electrode properties including porosity and density would be required, which were not available during this work.

The wide FS design was manufactured and the effect of liquid flow was assessed. The 2 mm thick sheet and 2.5 mm thick fingers combination was sufficient to prevent finger flexing during the fluid flow. Therefore, it was this design which was put forward as the FS design.

5.3.5.4 *Electrolyte Plate Electrical Resistance*

The difference in design between the FS and PS was to increase the electrical resistance between the electrolyte inlet and out for the cell to reduce the ionic leakage. Although the path length would increase the electrical resistance, it needed to be empirically measured to confirm that the designs have the desired electrical resistance. This was achieved by putting the plate between two plates (as with the effect of flow on PTFE fingers (Section 5.3.5.2)) and filling with 5 wt.% $NaCl_{(aq.)}$ to complete the circuit between the electrodes A Pt-wire electrode was placed in the inlet and outlet of rig and a potentio-electrochemical impedance spectroscopy (PEIS) was conducted to determine the electrical resistance of the electrolyte path.

Three plates were tested, the PS, FS and the stack air plate (Figure 5.35). The air plate was used as an example of a design which is completely open plane with no serpentine and theoretically high ionic leakage. The electrical resistance results are summarised in Table 5.6.

Table 5.6 - Electrolyte flow length and electrical resistance of different electrolyte plates.

Plate	Path Length (cm)	Electrical Resistance (Ω)
Air plate	0.8747	890
PS	13.11	4583
FS	51.75	8652

The high electrical resistance measured was desired as to reduce ionic leakage, without compromising the electrical resistance between the anode and cathode through the electrolyte plate. The electrical resistance results show that the addition of a serpentine, even a short one such as that of PS, compared to the air plate increases the electrical resistance significantly. Therefore, the plate designs are sufficiently different to determine the effect of serpentine length and EESA.

5.3.5.5 *Partial Serpentine Electrolyte Plate – Fluid Flow*

The flow of electrolyte and fuel through the electrolyte plate is important as it controls where the reaction occurs on the face of the electrode. Poor electrolyte flow can leave areas of the electrode starved, areas of the electrode with the restricted fluid flow, reducing the power and potentially damaging the electrode. Therefore, it is important to understand how the electrolyte flows across the surface of the plate. One way to do this is to simulate the flow of fluid through the plate using computational modelling such as COMSOL Multiphysics, software used to simulate and model the effects of different physics on a given geometry (see Section 5.2.4). The geometry was meshed with 1.65 million elements. The electrolyte path of three PS cells was joined via a connecting tube were designed using SolidWorks CAD software (Figure 5.24). The model was then simulated at temperatures 20, 50 and 70 °C using the appropriate densities and viscosities (Table 5.1) to observe the electrolyte movement through the stack.

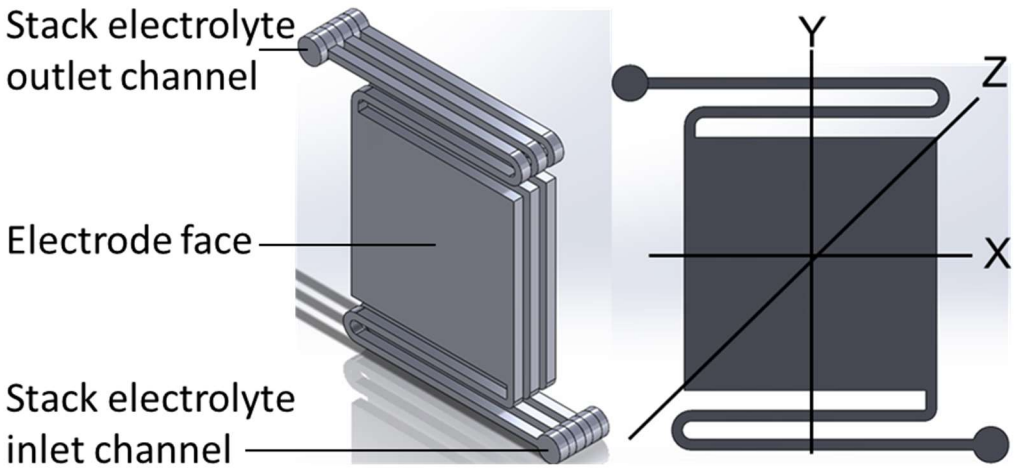

Figure 5.24 - Three cell PS geometry used for simulation modelling (left) and the planes used for simulation (right).

The results from the simulations are summarised in Figure 5.26. There was little difference in flow between the different electrolyte temperatures. Increasing the temperature slightly increased the flow direction between the inlet and outlet with higher volumetric flow rates in the centre of the electrode. Also, increasing the temperature of the stack changed the direction of the high velocity field, at the end of the inlet serpentine, slightly for 20, 50 and 70 °C by approximately 38, 32 and 30 °C respectively. Both the increased starved region and change in flow direction are highlighted in Figure 5.25.

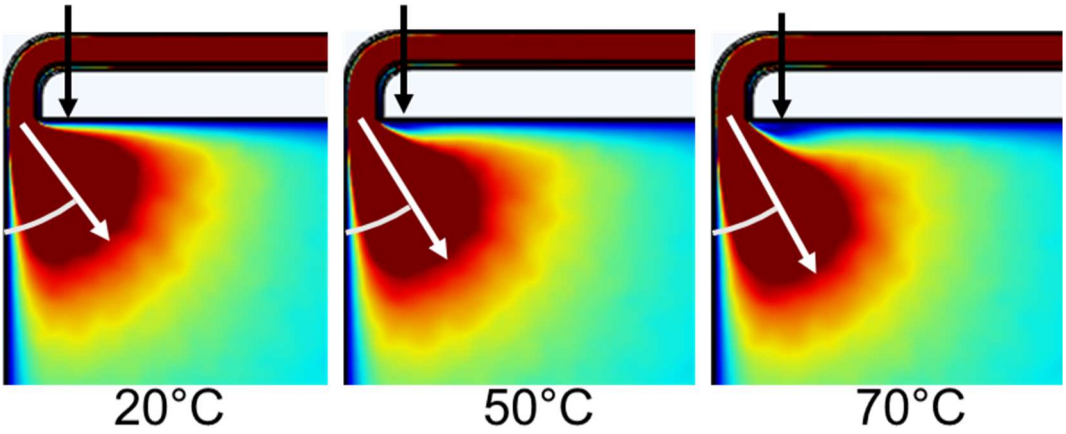

Figure 5.25 - Increased starved region (black arrow) and change in inlet flow direction (white arrow) at different temperatures for PS.

The development of a starved region at increased temperatures shown in Figure 5.26 could be an effect of a change in the flow direction (shown in Figure 5.26). The viscosity and density of the electrolyte decreased with increased temperature, thus allowing for the electrolyte to become more mobile. This increase in mobility led to the electrolyte to flow more towards the inlet direction, i.e. parallel to the wall. Conversely, at lower temperatures the electrolyte would be less mobile, making it less affected by the inlet direction and would cause it to fan out. This change in electrolyte flow direction reduced the amount of electrolyte available to flow and spread out from the inlet, causing the development of a starved region.

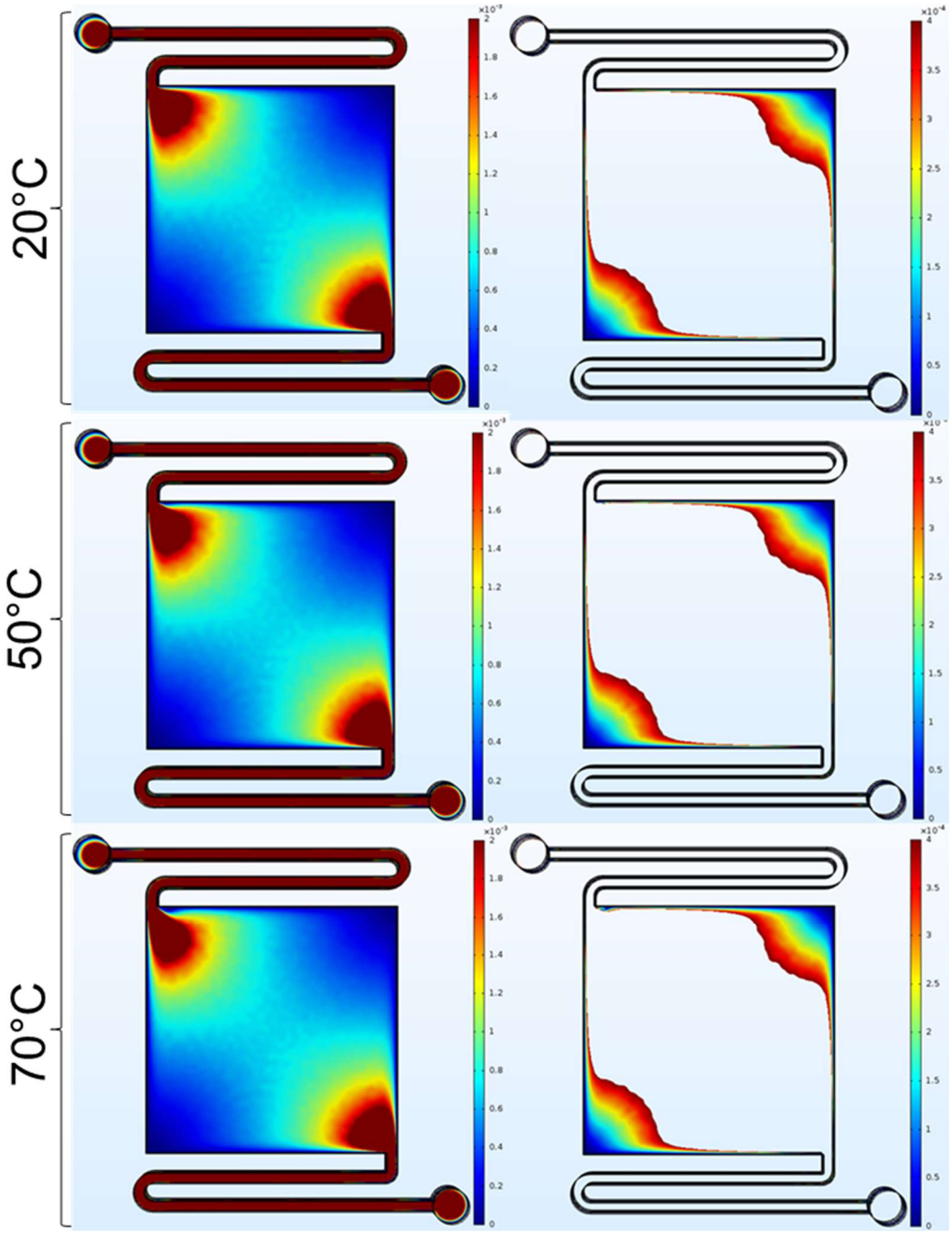

Figure 5.26 - Velocity (m.s^{-1}) flow of electrolyte through PS middle plate (XY plane) of entire (left) and starved (right) regions at various temperatures.

There were two regions of the electrolyte plate; the corners which do not contain the inlet and outlet, which have a significantly lower volumetric flow rate of electrolyte, and therefore fuel, compared to the rest of the electrode. These areas were considered starved and the decrease in the amount of fuel could have potentially led to a reduction in power and increased electrode degradation.

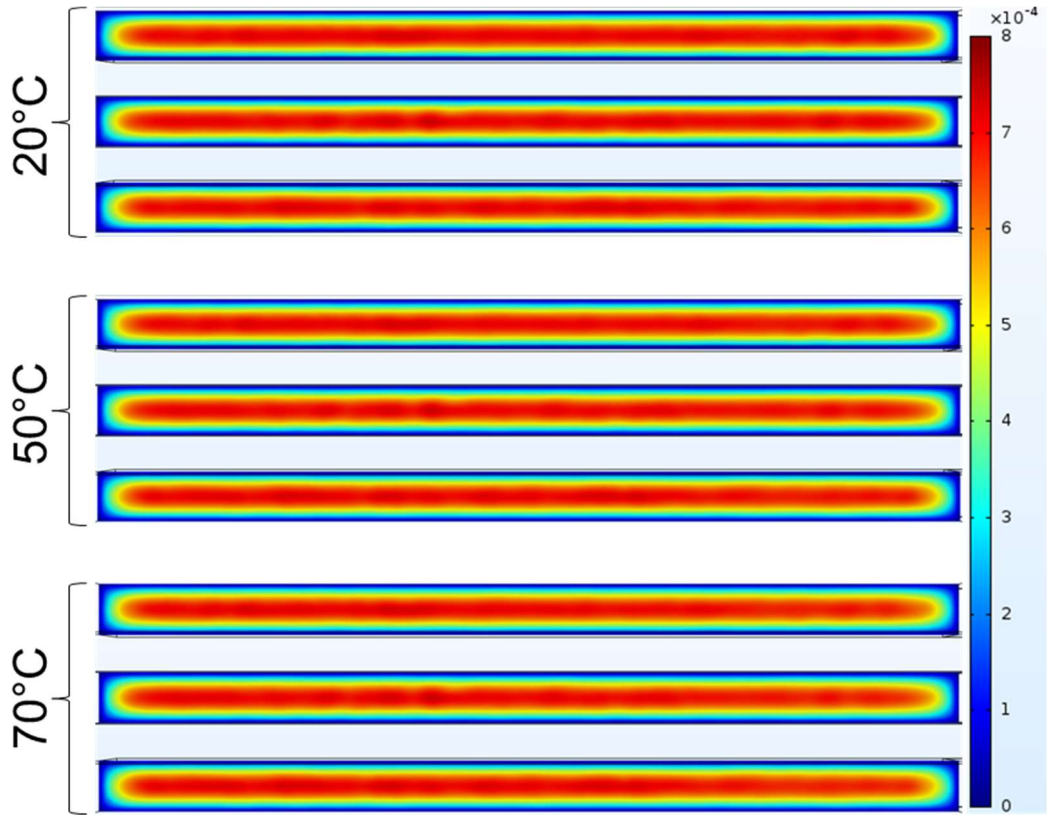

Figure 5.27 - Velocity (m.s^{-1}) flow of electrolyte through PS middle plate (YZ plane) at various temperatures.

The cross-section of the stack (Figure 5.27) shows the flow of electrolyte across the surface of the electrode (the bottom boundary of each cell). There were negligible differences in velocity between the top, middle and bottom cell. The flow of electrolyte through the cells show a laminar flow and therefore have a low velocity flow rate profile close to the electrode surface. This is undesirable as ideally there would be a high volumetric flow rate of fuel directly in contact with the electrode to prevent the electrodes from becoming starved and remove reaction by-products.

5.3.5.6 *Full Serpentine Electrolyte Plate – Fluid Flow*

The flow of electrolyte through the FS was simulated at different temperatures, under the same conditions as the PS above (Figure 5.29 and Figure 5.30), using the geometry and planes used for the FS simulation are highlighted in Figure 5.28. The FS geometry was meshed using 1.22 million elements.

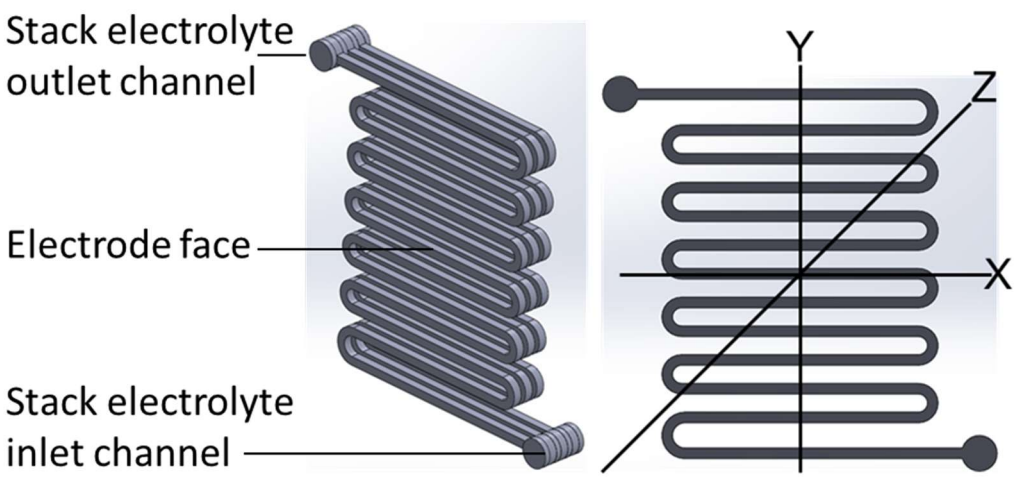

Figure 5.28 - Three cell FS geometry used for simulation modelling (left) and the planes used for simulation (right).

The flow of electrolyte through the serpentine showed a uniform velocity through the straight, approximately 1×10^{-2} m.s^{-1}, with an increase at the bends, approximately 1.8×10^{-2} m.s^{-1}, as expected. There were negligible differences in velocity between the different temperatures in the XY plane. There were; however, changes in velocities with respect to temperature in the YZ plane. Increasing the temperature increased the velocity in the centre of the serpentine but as a result decreased the velocity around the serpentine walls, which included the adjacent electrodes. This indicated that increasing the temperature would reduce the amount of fuel at the surface of the electrodes, potentially leading to the electrode becoming starved, decreasing power density and increasing electrode degradation. The cause of the change in velocities through the serpentine channels was most likely similar to the change in velocity profiles as seen in Figure 5.26, a decreased viscosity and density with increased electrolyte mobility.

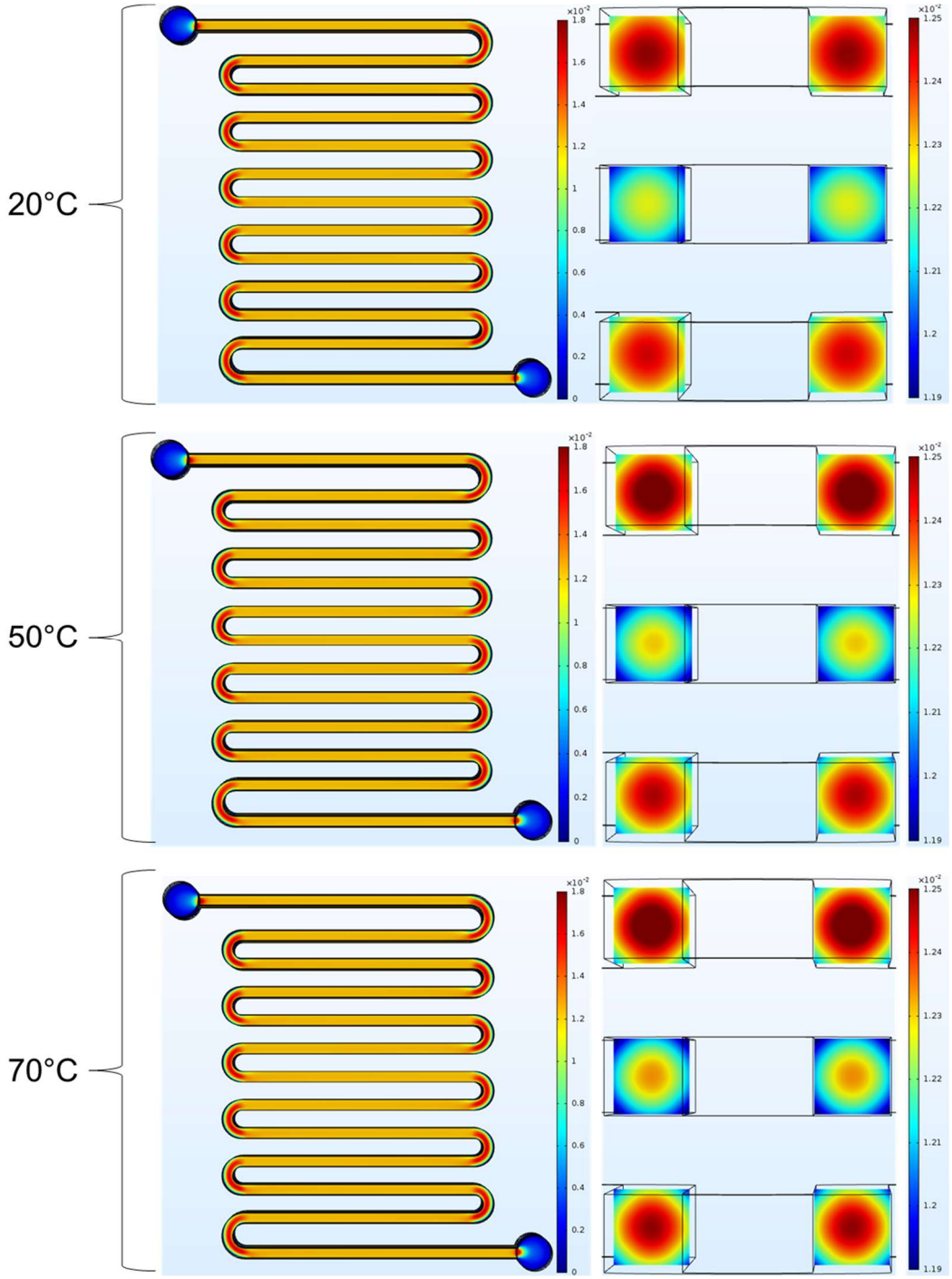

Figure 5.29 - Velocity (m.s^{-1}) flow of electrolyte through FS middle plate (XY plane left) and stack (YZ plane right) at various temperatures with the top cell containing the inlet and the last cell containing the outlet.

However, there was a significant difference between both the different cells within the stack and the temperatures. In Figure 5.29, regarding the YZ plane profiles, the electrolyte entered the first cell (with the inlet on the right) from the right hand side. The electrolyte then flowed through the cell and left the stack through the last (with the outlet on the left). There was a large velocity through the first cell which decreased in the middle cell and then finally

increases, though not so much as to match the velocity of the first cell. A 5-cell FS stack simulation was run at 20 °C to identify the effects of increased stack number with changes in velocity with cell number (Figure 5.30).

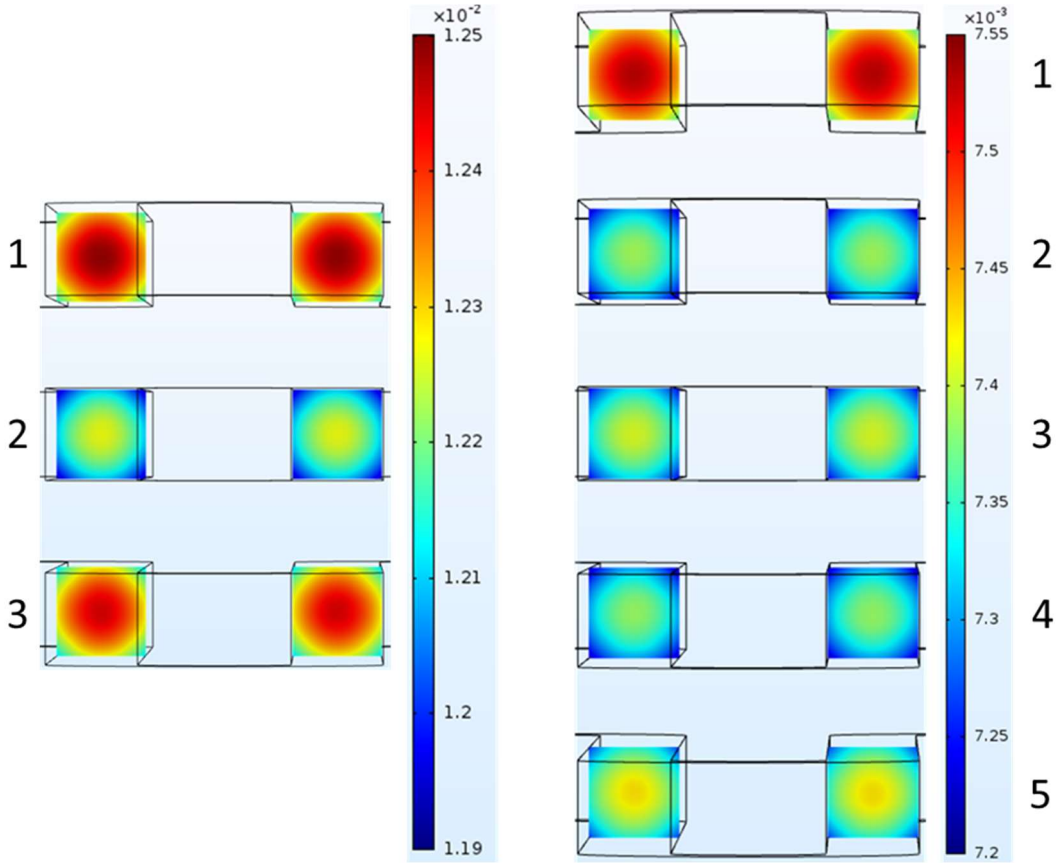

Figure 5.30 - Velocity (m.s^{-1}) flow of electrolyte through FS (YZ) plane for a 3 (left) and 5 (right) cell stack at 20 °C with cell 1 containing the inlet and cell 3 or 5 containing the outlet.

The large change in velocities between the cell numbers seen in the 3 cell stack could have been due the cell position, i.e. adjacent to the first cell, adjacent to the final cell or in the middle of the stack, rather than representative of all cells between the first and final cell. Although, as a percentage, the difference between the cell was not significant. The simulation results from the 5 cell stack, as a comparison, indicated that the middle cell of the 3 cell stack was representative of all cells between the first and final. The results also showed that there was a significant decrease in velocity between the 3 and 5 cell stacks with the highest velocity of the 5 cell stack being only 60 % of the highest 3 cell stack velocity. The inlet velocity of 0.3395 m.s^{-1} was the base variable for the simulation and kept constant throughout, with a suppressed backflow outlet and a U flow configuration. This was due to the increased number

of cell and the inlet velocity being kept constant. Comparing the relative flow velocities, i.e. comparing the colour distribution rather than their velocities, for each stack, the first cell and middle cells in both stacks were relatively constant. However, the final cell in each stack was significantly different with the final cell in the 3 cell stack having a higher relative velocity compared to the 5 cell stack. This indicated that the effect of increasing the number of cells in the stack affects the end cell more than the middle cells. This could be due to any excess electrolyte which does not flow through the first or middle cells being forced through the final cell.

5.3.6 Cathode, GDL and Cathode Substrate

For the fuel cell rig, a small semi-perforated cathode substrate (Figure 5.31 and Figure 5.32) was used to allow the passage of air behind the cathode. The design was based on a current commercial design based on AFCs.

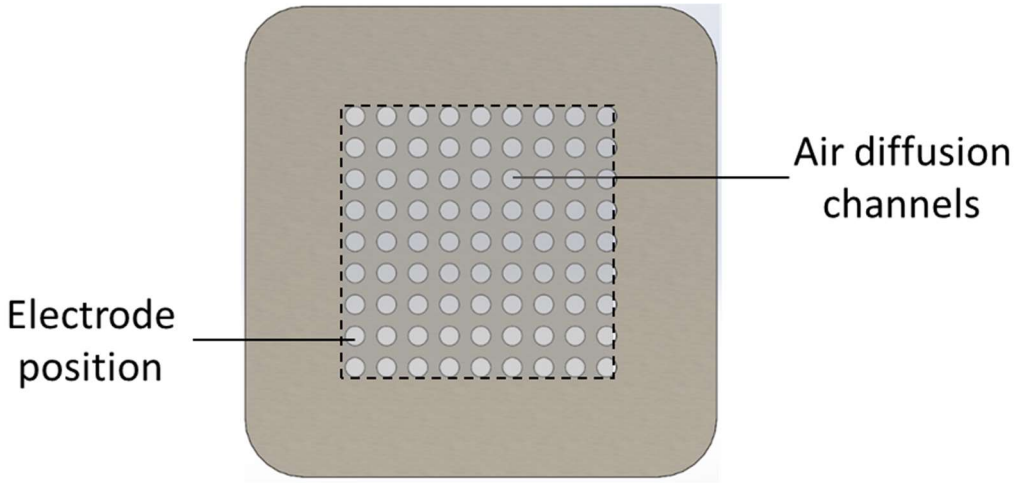

Figure 5.31 - Diagram of a perforated cathode substrate used in a rig. Manufactured from a nickel sheet (60 × 60 × 0.3 mm with a 7.5 mm radius fillet) with perforations through the centre equating to 35 × 35 mm.

The rig cathode substrate consisted of a front and back. The front, which was compressed against the GDL, was fully perforated, but only with the centre channels cut through to the other side. This gave a higher surface area and roughness which made it easier for the GDL to bind to the substrate. The back, which was exposed to the air plate, had a non-perforated outer border which allowed for more contact with the air plate for increased electrical conductivity.

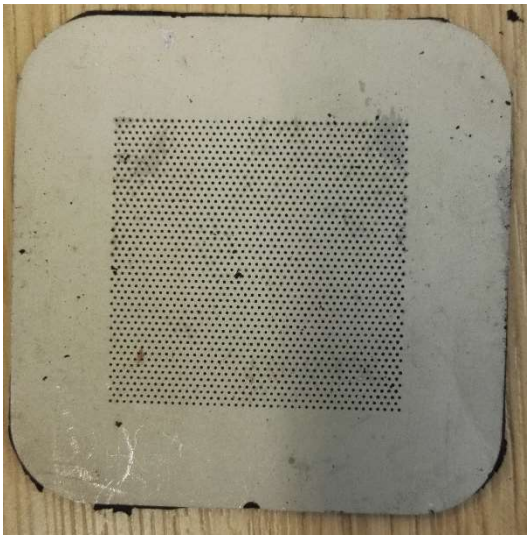

Figure 5.32 - Photo of a cathode rig substrate with an electrode on the reverse.

Although the cathode was suitable for the rig, it wasn't for a stack. There were no electrolyte or air flow channels for distribution through the stack. Furthermore, the cathode had to be carefully placed on the end plate as it was only enough to cover the electrolyte chamber and not the face of the entire rig. This led to a stack specific design in Figure 5.33 and Figure 5.9 which covered the full face and was fully perforated cathode capable of fluid transport. This allowed for good contact with the adjacent plate or current collector and increased ease of stack construction.

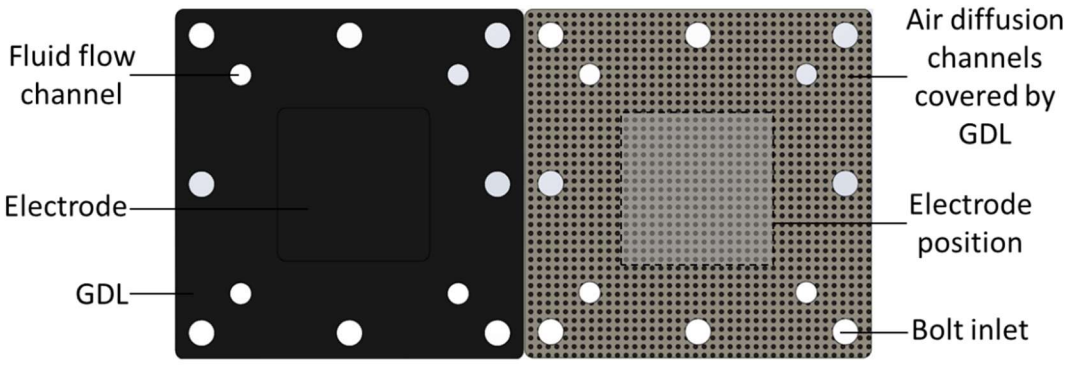

Figure 5.33 - The front (left) and back (right) of the full cathode containing the cathode electrode, GDL and cathode substrate. The dimensions are the same as the substrate (Figure 5.16).

For the purposes of the stack designed, the cathode electrode (the part which contains the electrocatalyst) was at the same size of the anode electrode, i.e. 35 × 35 mm for the electrode versus the size of the plate which is 80 × 80 mm of the substrate. Although was acceptable, the cathode could be printed bigger if necessary due to the lower cost compared to the anode electrode. This would be done to increase the amount of electrolyte/fuel exposed to the electrocatalyst (through diffusion of the surrounding border) or increase sealing with adjacent plates.

The stack cathode worked well at distributing fluids through the stack and holding the cathode in place. The increased number of channels through the plate allowed for increased air flow through the GDL as well as increased adhesion.

5.3.7 Air Plate

Initially, the air plate was also the end plate for the rig (Figure 5.34). As with the end plates, it was also manufactured out of acrylic. This very basic design of having an open void allowed the back of the GDL to be exposed to air whilst providing support for the rig. The design didn't allow for controlling the air flow rate through the cell and relied on the diffusion of air through the GDL alone. Since this air plate was part of a single cell rig, it was not required to be electrically conductive nor to allow for fluid distribution. The current collector was placed between the cathode substrate and the air plate.

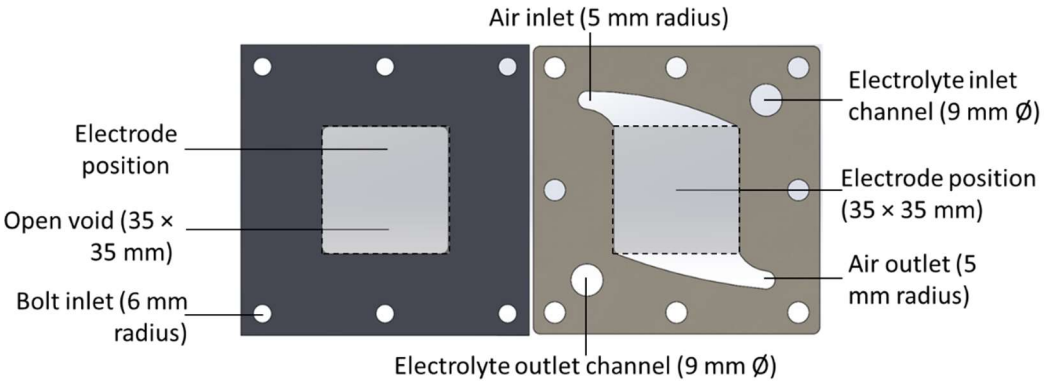

Figure 5.34 - Air plate for the rig (left) and stack (right). The rig air plate was manufactured from acrylic (20 mm thick) whilst the stack was from a nickel sheet (0.3 mm thick). The outer and inner radius of the air flow was 95.31 and 10 mm respectively.

The air plate was designed to maximise the cathode exposure to the air. Unlike the electrolyte, the air had no effect on the cell stack resistance with respect to ionic leakage. However, the air flow was responsible for temperature and water management in addition to being used in the redox reaction. Having the air plate open allowed for maximum exposure to the back of the cathode, unlike the serpentine designs, removing more water and potentially reducing electrode flooding. The curved inlet/outlet allowed for the reduction in the starved/low distribution electrode area. However, a disadvantage to this was the decrease in flow distribution compared to a serpentine design. Due to time constraints, multiple types of air plate wasn't evaluated and a simple open plate design was used. As such, to negate some of the flow distribution contains a much larger volumetric flow rate was used for air compared to borohydride. This was deemed acceptable as, unlike the borohydride/electrolyte, air is abundance source if the system used a blower from outside of the fuel cell system; hence, wastage was not a concern.

Although this was convenient for a single cell rig, this was not appropriate for a multi-cell stack. The air plate needed to be electrically conductive to complete the circuit between the adjacent cells and allow the passage of fluid. Although acrylic could be used with an outside connector to link all the cells in a series, this would have led to increased stack complexity. Although the acrylic was less dense than the nickel used, and would, therefore, weigh less with the same design, sheet nickel was used which could be manufactured more easily when the sheet was very thin. The addition of large fluid transport channels allowed for the nickel air plate to be used in a stack when used with an EPDM seal.

The central chamber of the stack air plate contained a specifically designed air flow path between the inlet and outlet to ensure optimum flow of air past the back of the GDL. As with the electrolyte plates, three air plates were put in parallel to simulate the effects of being in a stack configuration (Figure 5.35).

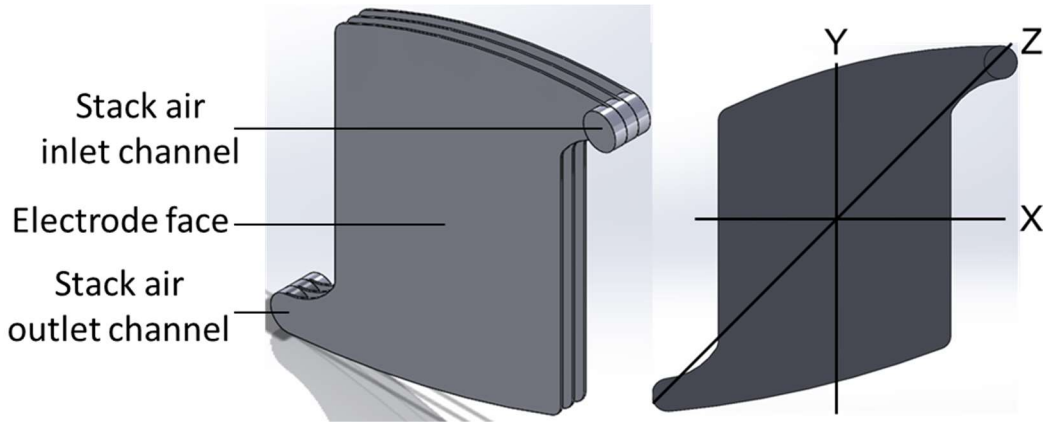

Figure 5.35 - Three cell stack air plates used to simulate air flow in COMSOL (left) and the planes used for simulation (right).

This was then modelled in COMSOL using a laminar flow, due to the open design, low air density and high volumetric flow rates, physics (1.83 million element mesh) with an inlet volumetric flow rate of 400 $cm^3.min^{-1}$ (with a measured velocity of 0.3395 $m.s^{-1}$). The air entering the stack at room temperature, the volumetric flow rate was relatively high and the relatively low heat transfer coefficient of air meant that it was unlikely that the air would increase in temperature as it went through the fuel cell. This was confirmed when the air was passed through the heating coil used to bring the electrolyte up to temperature. Therefore, the effect of different temperatures on air flow was not modelled.

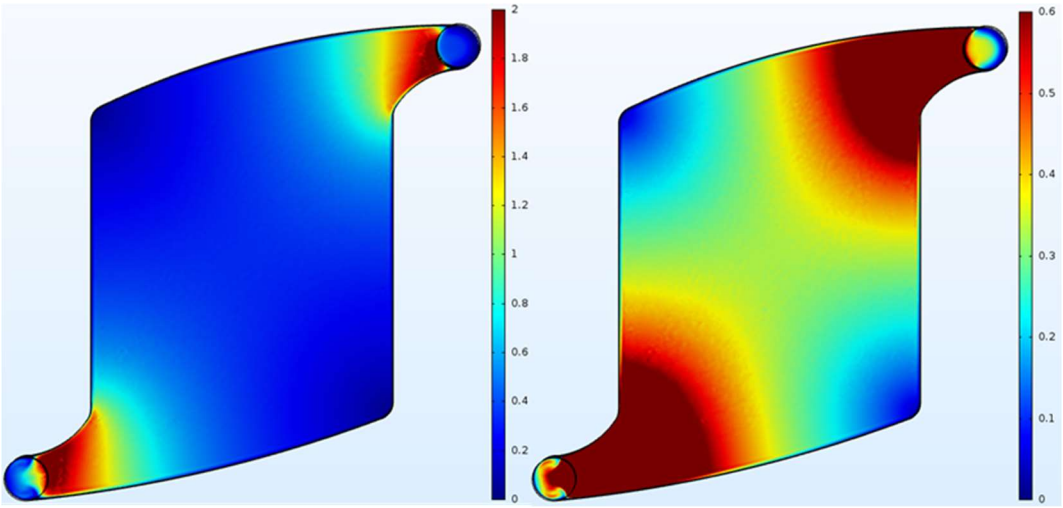

Figure 5.36 - XY velocity ($m.s^{-1}$) of air through the middle stack air plate (inlet top right, outlet bottom left).

The results from the XY plane simulation (Figure 5.36) showed a relatively good air distribution across the GDL. However, there were two regions whereby the GDL was slightly starved (Figure 5.37), opposite the inlet and outlet.

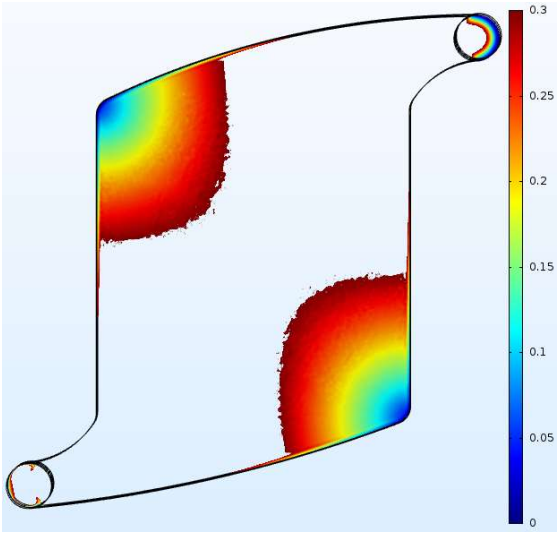

Figure 5.37 - Air velocity ($m.s^{-1}$) in starved regions of stack air plate.

Although the two starved regions in the air plate were starved, compared to the bulk electrode, the regions were still getting some air (between approximately 0.04 - 0.2 $m.s^{-1}$).

The ZY plane simulation (Figure 5.38) showed a classic laminar flow through a pipe with slower velocities at the walls. There was little variation between the different plates in the stack (top, middle and bottom) which indicated a uniform flow between the different plates. The lines observed at the bottom of the top plate and the top of the bottom plate (in the 0.2 $m.s^{-1}$ range) was not a result of the simulation but part of the design and should not be considered.

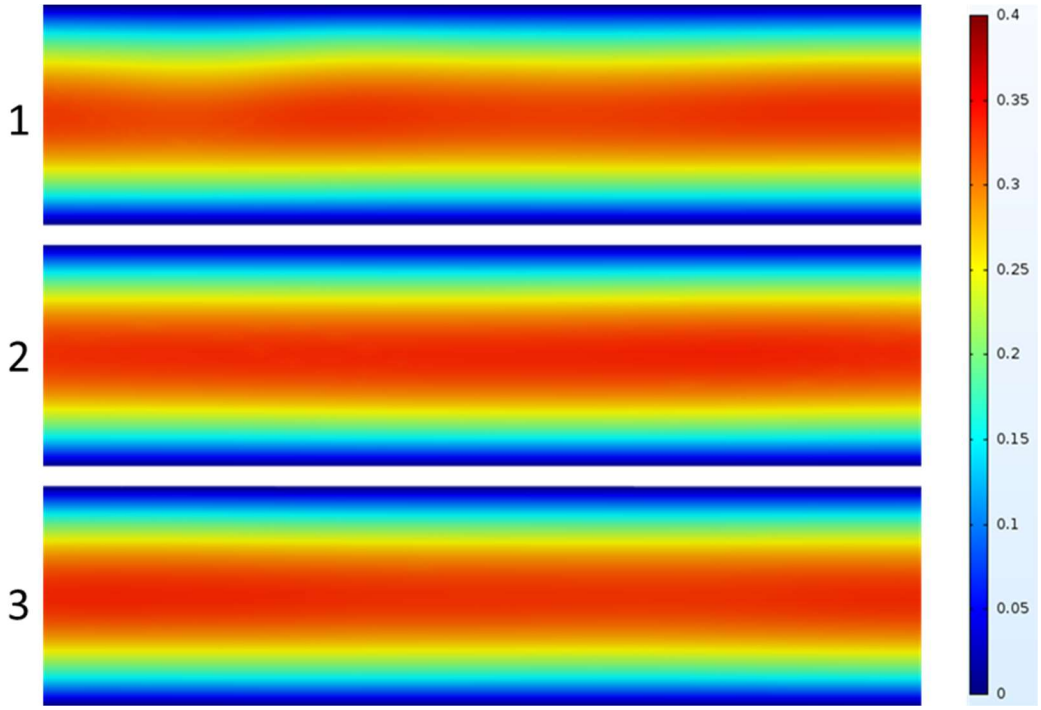

Figure 5.38 - ZY velocity (m.s^{-1}) of air through stack air plate cross section (inlet to the left of cell 1 and the outlet to the right of cell 3).

5.3.8 Other Components

There were some minor components used in the fuel cell construction that has not been mentioned but are still vital for the stack construction. This included the 8 × 5 mm bolts which were used to keep the stack together. These bolts, tightened to 2.5 N using a torque wrench, were shrink wrapped, using a hot air gun, to prevent the stack short circuiting the stack, by inadvertently connecting the two current collectors. Although this worked briefly, the shrink wrap made the bolts significantly thicker. The bolt holes were increased to accommodate for this; however, doing so decreased the distance between the nut and the border of the end plate, potentially decreasing its ability to hold the end plate in place.

To decrease the thickness of the shrink wrapped bolt, without decreasing the thickness of the bolt itself which could have potentially reduced the structural integrity when the stack was tightened, a different method to insulate the bolt was used. PTFE tape was wrapped around the bolts in place of the shrink wrap. The PTFE tape was much thinner than the shrink wrap and so the bolts fitted much better in the stack holes. Furthermore, the PTFE is known for its electrical insulation and chemical corrosion resistance which made it much more suitable than the shrink wrap. However, using the PTFE tape meant that it had to be re-wrapped between

each experiment due to tearing and unwrapping. Although the PTFE worked well, it was not a permanent solution.

To make the seals for the stack, a suitable material had to be used due to the corrosive nature of the electrolyte. EPDM was used due to its good chemical corrosion resistance. The very small dimensions (being 0.5 mm thick with an inner and outer diameter of 5 and 7 mm respectively) of the design and the flexibility of the EPDM sheet made it difficult to accurately cut the O-rings out of the sheet. Therefore, the O-rings were cut from the sheet using a laser cutter. This allowed for multiple O-rings to be manufactured, quickly and accurately. The thickness of the EPDM was slightly too thick for the laser cutter and so the cuts did not penetrate through to the entire sheet meaning that the O-rings had to be pried away from the bulk of the EPDM. Although having to manually separate the O-rings from the bulk of the EPDM took additional time, it prevented the O-rings from moving during the manufacturing process.

5.3.9 Fuel Cell Stack Construction

This section describes the fuel cell as a whole. The repeating cell, i.e. a single cell without the current collectors, is highlighted in Figure 2.2 and Figure 5.1. When the stack was constructed bolts were tightened to 2.5 N incrementally, to ensure the stack was sealed equally across the face of the stack, using a torque wrench. The stack sealed well with no electrolyte or air leakage during operation.

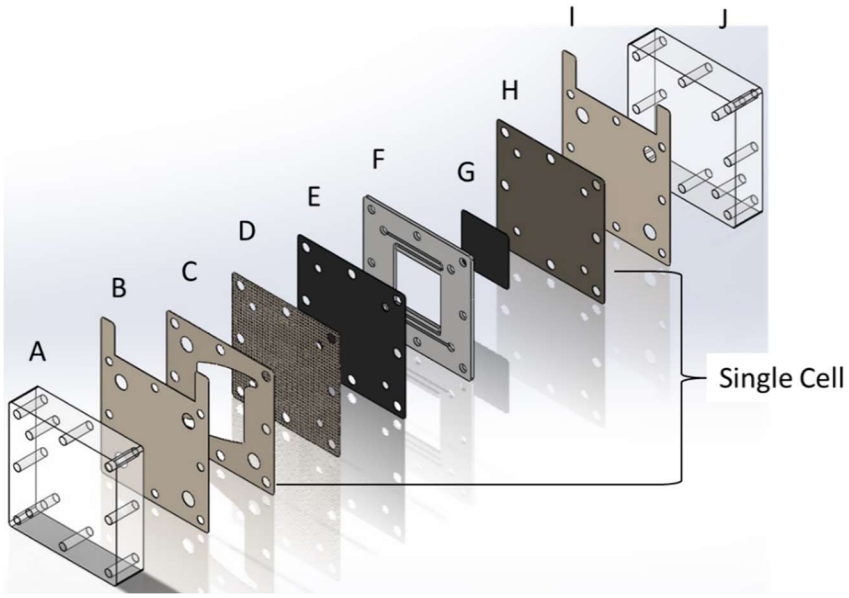

Figure 5.39 - CAD image of a single cell stack design showing the cathode end plate (A), cathode current collector (B), air plate (C), cathode substrate (D). GDL + cathode (E), electrolyte flow plate (F), an anode (G), anode substrate (H), anode current collector (I) and anode end plate (J).

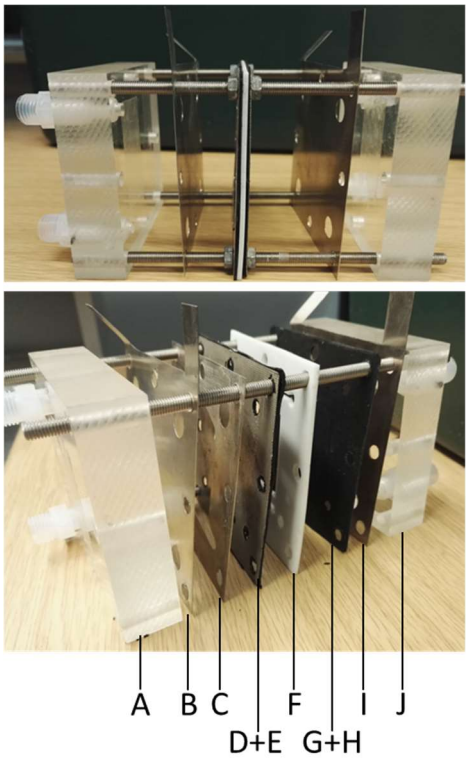

Figure 5.40 - Photo of constructed fuel cell showing the middle repeating unit (top) and exploded view (bottom) showing the cathode end plate (A), cathode current collector (B), air plate (C), cathode substrate (D). GDL + cathode (E), electrolyte flow plate (F), anode (G), anode substrate (H), anode current collector (I) and anode end plate (J).

5.3.9.1 *Cell Weight*

The weight of the stack, and therefore its components, was important, especially for portable applications. The weights of the individual components are highlighted in Table 5.7

Table 5.8 - Stack component and part percentage of total cell weight. and the percentage weight of the individual parts and components in Table 5.8.

Table 5.7 – Repeating unit component weights.

Component	Weight (g)
Air plate	10.7
Anode	0.5
Anode substrate	15.9
Carbon contact layer (CCL)	2.7
Cathode	0.5
Cathode substrate	11.1
Electrolyte Plate	FS = 21.0 PS = 18.3
GDL	2.7

Table 5.8 - Stack component and part percentage of total cell weight.

Component	FS (% wt.)	PS (% wt.)
Air plate	16.4	17.1
Anode Electrode	0.8	0.8
Anode substrate	24.4	25.5
CCL	4.1	4.3
Cathode Electrode	0.8	0.8
Cathode substrate	17.1	17.8
Electrolyte Plate	32.3	29.3
GDL	4.1	4.3
Anode	29.3	30.6
Electrolyte Plate	32.3	29.3
Cathode	22.0	22.9
Air Plate	16.4	17.1

It should be noted that the CCL was used in the calculation of the stack as a conservative figure. Due to the relatively low weight of the CCL, removing it from the stack would have only a small impact on the percent weight of the other components. Furthermore, the end plates and current collectors were not taken into consideration as, although important, could be considered less important compared to the cell components. This was because reducing the weight of the cell components would have a multiplier effect in a stack.

The weights, and by extension the percentage weights, of the components, show that the components responsible for the highest contributor of weight in the cell are the electrolyte plate > anode > cathode > air plate. This highlights which components of the stack could be developed to reduce their weight in future work. In the DBAFC stack developed in this work, the electrolyte plate was the heaviest component. This leads to the conclusion that, coupled with the results in Section 5.3.5, that the electrolyte plate was a component which requires possibly more research focus compared to the other components. Optimising the electrolyte plate to decrease the electrode thickness and altering the geometry, to reduce ionic leakage whilst increasing EESA, could potentially reduce the weight of the plate, and therefore the stack, significantly.

Depending on the stack configuration, i.e. the type of electrolyte plate and whether a CCL was required, the repeating unit weighed 60.2 - 65.1 g. Although this was only an increase of approximately 8 %, it was significant in a multi-cell stack. However, this would have to be balanced against the increase in electrical resistance, and therefore decreased ionic leakage, achieved with the FS design.

5.3.9.2 *Component Orientation*

The orientation of the electrolyte and air plate within the stake was important for uniform distribution across the cell. The air inlet had to be at the top of the stack and the outlet at the bottom (Figure 5.41). The amount of water in the air flowing through the stack could have increased, specifically with increased stack number and temperature, which may have eventually caused droplets to form.

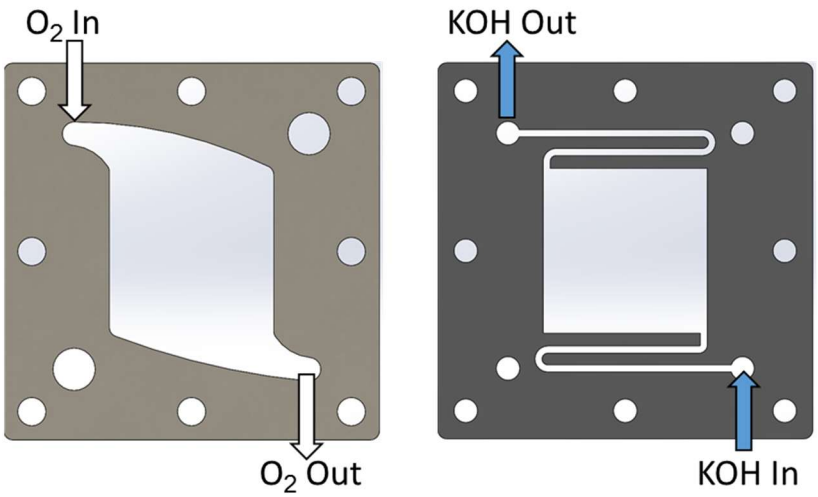

Figure 5.41 - Orientation of air (left) and electrolyte (right) plate.

Orienting the air flow plate with the outlet at the bottom allowed for the water to drop out of the air plate and out of the stack. Similarly, the electrolyte plate had to be in the opposite orientation to the air plate. As previously discussed, the hydrolysis of borohydride generates hydrogen gas. Having the electrolyte plate orientated with the outlet at the top reduced the volume of accumulated hydrogen gas pockets, reducing the borohydride flow and ion path to that area of the electrode. Furthermore, stagnant hydrogen gas could have potentially caused an explosion risk.

5.3.9.3 *Fuel Cell Compression*

The construction of the stack was simple with all the components slotting into each other without the need for any minor adjustments or any short circuiting, unlike the rig which required minor adjustments for the current collectors and electrodes for the plates to align. The stack was tightened to 2.5 N, incrementally at each bolt in order to ensure even pressure distribution which was important to ensure enhanced performance, current contact and various GDL properties [208]. However, this caused the end plates to flex and warp. This was most likely due to the strain of the bolt around the outer perimeter. Although there was no leakage out of the stack, there could have been some internal leakage allowing for fluid, both electrolyte and air, through the cells (Figure 5.42). There were a couple of ways which could have prevented this from happening. One method was to change the end plate material for

one which was stronger than acrylic. This could include a chemical corrosion resistant metal such as steel 901 or nichrome; however, it would have to be electrically insulated to prevent short circuiting. Although this would not require any more components for the system, it would not solve the distribution of compression across the face of the stack causing a reduction in the compression in the centre of the stack.

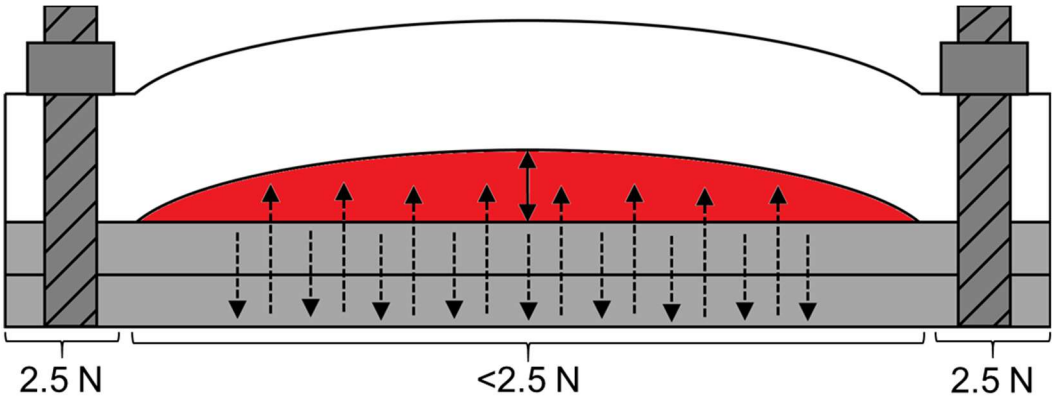

Figure 5.42 - Flex, and the void created (red), in stack end plate and diffusion of fluid through cell due to decrease compression.

Another method would be to apply compression through the centre of the stack (Figure 5.43). The bolts around the perimeter of the stack were screwed to the desired torque whilst a vice, which was fully insulated to prevent any electrical short circuiting, was placed in the middle of the end plate and screwed to the same torque. This would have prevented the end plate from warping due to better compression distribution across the face of the stack. However, this would have required the addition of another piece of equipment for the system.

Either altering the end plate material or using vice would have removed the end plate warping and prevented any internal leakage which could have led to the stack short circuiting via electrolyte crossover. The solution to prevent warping would depend on the application the DBAFC was used. For portable applications, the use of an insulated metallic end plate may provide enough central compression for there to be no internal leakage. Using a vice for portable applications would increase the bulkiness of the system which is undesirable. For a stationary application, both solutions could be used as the increased system size due to using a vice would unlikely be a problem. Alternatively, if viewing the inside of the fuel cell is not a

priority, other materials such as glass filled polymers or gas filled NORYL which are currently used for other low temperature fuel cells.

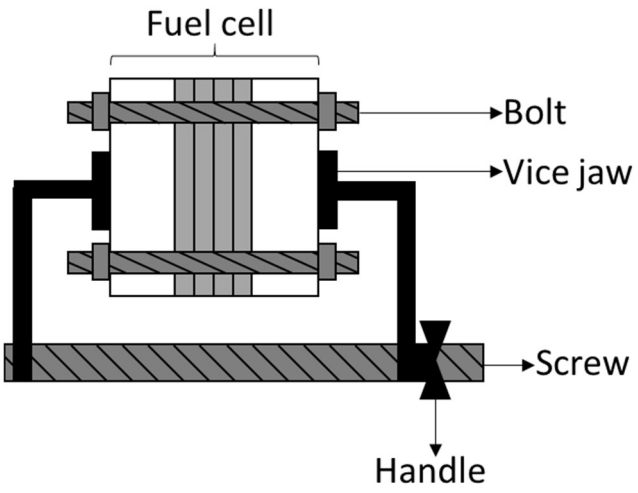

Figure 5.43 - Reduction of end plate warping via central compression using a vice.

5.4 Conclusions and Discussion

Overall the stack performed well with no leakage and good fluid distribution throughout the stack. The manufacture of most the components was simple, apart from the electrolyte plates which, due to the flexibility of PTFE and the small dimensions, required some alterations to the design. However, a minimum thickness of 2 mm PTFE with a finger length 2.5 mm was produced and used without finger flexing during operation. Although machining the PTFE plate using a jig worked, using a knife press could also achieve the small dimensions required. However, these small dimensions may not be desirable due to the flex in PTFE fingers. Due to their relatively simple design of the nickel current collectors, anode substrate and air plate plates were manufactured using drilling and automated machining CNC. The bolt holes and fluid transport channels on the cathode substrate were also manufactured in this way but the perforation was produced by the supplier via chemical etching which produced a suitable cathode substrate. The acrylic end plates bolt holes and fluid transport channels were drilled which worked well; however, if the plates were to be made thinner, i.e. to help decrease the stack weight, the end plates could potentially crack during manufacture due to being brittle. Using a laser cutter to manufacture the EPDM O-rings allowed for large quantities to be produced with minimal material wastage. Wrapping the bolts in PTFE tape allowed for a thin,

chemical and electrically insulating layer to be put over the bolts. Although this worked well, it was only temporary and another method, such as coating a thin layer on the bolts, may work better. Using bolts composed of just PTFE may not be suitable as and may break due to being soft and the relatively high torques used to tighten the stack. The manufacture of the electrodes was previously discussed in chapter 4, including their adhesion onto their respective substrates. Once the electrode was securely adhered onto the substrate a bolt was used to pierce the bolt hole and fluid transport channels which were covered either by a GDL or CCL.

The simulation of air flow through the air plate highlighted two low velocity regions (Figure 5.37). These starved regions could be rectified either by changing the design of the air plate or increasing the volumetric flow rate of air in the stack. Although it would be simpler to increase the volumetric flow rate of air, there are some disadvantages. Increasing volumetric flow rate of air would increase the amount of water being removed from the back of the GDL, which could lead to electrode degradation. Furthermore, should the stack be supplied with compressed oxygen instead of air, this would lead to a decrease in runtime as a higher volume of oxidant would be used. It is unlikely that the small starved regions, which is still supplied with air through with a much lower volumetric flow rate than the bulk of the electrode, will cause decreased power outputs. Furthermore, the cross-section of the air plate simulation showed that the flow of air had a typical laminar flow through a pipe profile with low velocities close to the walls, or in this case the back of the cathode substrate. The laminar flow velocity of air which can diffuse through to the cathode. As with the starved regions discussed although increasing the air volumetric flow rate would increase the air at the back of the cathode substrate, it would also affect the cost and water management. Another method could be used to distribute the air to the cathode which could include having the air flow perpendicular to the cathode substrate compared to the parallel used in this stack.

The results from the simulation of the air plate show good flow through the air plate. However, due to the laminar nature of the flow, the velocity of the air at the back of the cathode substrate is low. This could lead to not enough air getting through the cathode substrate and GDL to the cathode electrocatalyst. One method to overcome this is to make the air flow more turbulent.

5.5 Future Work

Although the stack worked well, with respect to leakage and fluid distribution, the design was not fully optimised. There are many aspects of the stack which could be improved, some of which are highlighted in the conclusions and discussion section above; however, there are aspects which when developed could have a significant impact on the cell's performance which is discussed here.

5.5.1 Electrolyte Flow Plates

There are two properties of the electrolyte flow plates which should be developed further; the geometry and the plate thickness. As previously mentioned the path in which the electrolyte flows between the electrodes is of great importance with respect to electrode-electrolyte exposure and ionic leakage.

Decreasing the thickness of the electrolyte flow plate would decrease the electrical resistance between the electrode. However, doing so would increase the manufacturing difficulty and decrease the rigidity of the PTFE. As previously mentioned PTFE is an ideal material for the use of an electrolyte flow plate due to its low cost, high chemical resistance and high electrical resistance. Another valuable, though not a necessary, property of PTFE is its ability to seal well against other parts. This property makes the PTFE soft and flexible which, along with the small dimensions of the geometry, makes it difficult to manufacture. Furthermore, the smaller the dimensions, the easier they will distort when the electrolyte is passed through the cell. Therefore, optimisation of the electrolyte flow plate needs to occur in three aspects:

- The reduction in electrical resistivity between electrodes – the thinner the plate the less the electrical resistance.
- The ease of plate manufacture and plate distortion – the thicker the plate, the increased ease of manufacture and decrease in plate distortion.
- Reduction in ionic leakage – increasing the resistance between the electrolyte inlet and outlet reduces the ionic leakage experienced in a stack with multiple cells.

There are several ways in which these aspects can be developed further. Although PTFE is suitable to be used for the electrolyte plate, changing the material to one which has increased structural hardness, when used in conjunction with a seal to prevent electrolyte leakage, could

potentially allow for a decrease in plate thickness and increase in ease of manufacturing. The geometry of the electrolyte flow path could be developed further through modelling a variety of designs and simulating the effects of the designs. Simulating the flow of electrolyte, the current density of the electrodes and the electrical resistance of the cells would give an indication of the effectiveness of the plates which would then be verified through empirical experimentation. However, this should only be done after the electrodes have been fully developed as the diffusion of electrolyte, which is affected by the electrode's porosity and wettability, would influence the ionic leakage of the electrolyte.

The simulations show that the cell adjacent to the inlet has the highest velocity, and therefore has the most amount of fuel being transported across the electrode's surface, potentially increasing the power output for that cell. This leaves the rest of the cells with a lower velocity which could inhibit power for the cells. One method that could rectify this to have multiple inlets at various points through the stack, feeding it electrolyte from a central reservoir. This increased the flow to the central cells; however, this would also increase stack construction and system complexity which could be potentially be mitigated by the additional power output or reduction in electrode degradation.

5.5.2 Reducing Cell Ohmic Resistance

It is important that the overall stack, and therefore the individual cell, ohmic resistance is low to make the efficiency of the stack as high as possible. One method of doing this is to reduce the ohmic resistance of the stack. Due to the stack being constructed out of a series of repeating plates, most of which were metallic, contact electrical resistance can become an important factor when trying to reduce the ohmic resistance. Depending on the manufacturing and materials used, this could be improved by one of two ways. Either methods to reduce the contact resistance by sintering plates together or by adapting the design of the plates so they can be manufactured out of one plate, removing the contact resistance completely, such as laser welding bipolar plates with different fluid distribution channels and depositing electrocatalyst on either side. Developing the plates and subsequent evaluation the effect of reducing the contact resistance between adjacent plates would have a significant improvement in the ohmic resistance of the stack, increasing overall efficiency.

5.5.3 Air Plate

Increasing the air being transported through the GDL could potentially be achieved by flowing the air perpendicular to the back of the cathode substrate compared to parallel. A simple perpendicular air plate setup is shown in Figure 5.44. In this case, the air plate is modulated with the first plate diffusing the air across an area equal to the electrode. The second plate contains channels which change the direction perpendicular to the electrode plate. The final plate diffuses the air across the back of the electrode and towards the outlet.

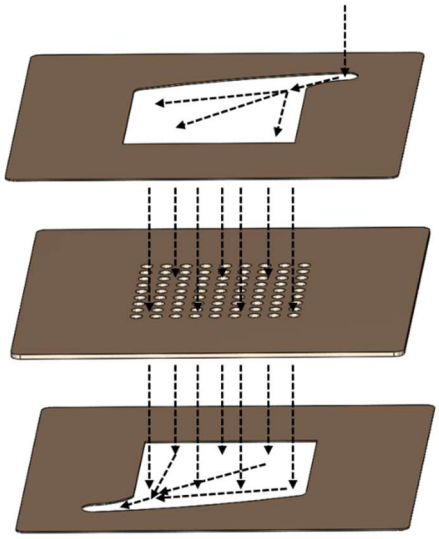

Figure 5.44 - Perpendicular air flow plate design which could potentially increase air distribution across the back of the cathode.

This design is not ideal as it increases the air plate by three times the one assessed in this work, causing an increase in cost, weight and electrical resistance. Having the air flow perpendicular would still contain areas of the starved electrode through it may increase the flow of air through the cathode substrate and GDL to the electrocatalyst. This would require further development to find an optimal air flow plate.

Alternatively, the nickel sheet could have a serpentine design. Although this would not direct the air flow through the GDL any more than the design used here, it would aid in distributing the air to all parts of the electrode, reducing the starved regions.

6 Fuel Cell System Design and Development

A fuel cell alone cannot produce electricity and therefore to operate successfully, a fuel cell requires the regulation of various parameters. Such parameters include the fuel and air at the inlet, the orientation of the fuel cell and the processing of the electrolyte at the outlet. This chapter describes the roles and requirements of fuel cell systems and the development of a scalable fuel cell system for a flowing electrolyte DBAFC. The systems were evaluated by operating the fuel cell under various conditions. In most system designs, the polarisation of the fuel cell could not be achieved due to operational challenges, for example, high temperatures and borohydride concentrations caused the cell to be blocked with hydrogen gas. As such, these observations have been described as well as potential solutions to technical challenges.

6.1 Role of a Fuel Cell System

The fuel cell system is the auxiliary equipment that enables the fuel cell to operate according to the design specifications. Different fuel cells and applications require their own unique system. For example, a system designed for a constant power stationary application would be different to a power on demand stationary application as well as constant power portable application. Hence, each system requires a variety of components, such as pumps, flow regulators, heating/cooling systems. The role of the system, specifically for flowing electrolyte fuel cells, along with its requirements are described in this section.

6.1.1 System Requirements

There is not one universal system which can be used, as different fuel cell types require different operating systems to generate the optimum amount of power. The minimum requirement for a system is to have the fuel cell, reductant and oxidant supplies. Another component which is common, but not for all fuel cells, is the regulation of fluid through the fuel cell. Most fuel cells utilise one or more gases during the redox reaction, although some fuel cells such as direct borohydride peroxide fuel cells use oxidants and reductants in a liquid phase, these are comparatively uncommon. A mass flow controller (MFC), a variable valve

which alters between the open and closed position to control the volumetric flow rates, is used to regulate the gas flow. Due to the issue of water management of fuel cells, it is typically important for the gas entering a low temperature fuel cell to have a controllable humidity. In alkaline based media, it is important for a carbon dioxide scrubber to be used on the oxidant gas entering the fuel cell to remove any carbon dioxide contaminating the gas, (unless pure oxygen is used instead of air), due to the challenges associated with the formation of solid carbonates in some fuel cells. Finally, efficiencies can be increased through balance of plant components. This can be in the form of a turbine which can increase overall efficiency using the unused exhaust fuel or combined heat power systems using waste heat from high temperature fuel cells [16, 209].

The nature of the electrolyte will determine the liquid management strategy around the fuel cell system. Fuel cells containing static electrolytes, which can be solid ceramic, i.e. SOFC, solid polymer, i.e. PEMFC, or a liquid, i.e. static AFC, do not require electrolyte transport around the system. However, other types of fuel cells, i.e. some AFC, which utilise flowing electrolyte require components to ensure adequate material transport through the fuel cell and stack. In the DBAFC developed in this work, the reductant was dissolved in the electrolyte, adding an additional complexity to the system over a reductant-free electrolyte system. Three main methods of liquid flow through a stack are single pass, recirculating and semi-recirculating (Figure 6.1). In all cases, chemically resistant pumps transport the electrolyte through the fuel cell.

In a single pass method, the electrolyte passes through the stack once. The reductant has a molar flow rate similar to that calculated by Faraday's equation (Equation 4.2). Due to the electrolyte only passing through the fuel cell once, the volumetric flow rates must be low to reduce waste. Conversely, in the recirculating method, the electrolyte is kept in a closed loop, passing through the stack continuously. This allows for the use of a variety of volumetric flow rates which gives the system more flexibility. Furthermore, high volumetric flow rates can remove by-products quickly from the electrode's surface to reduce potential electrocatalyst inhibition. To operate for prolonged periods of time, this requires the reductant concentration to be high. This can be challenging depending on the fuel cell, which may not be stable at high concentration and temperate thus being difficult to store. Also, any by-products produced will accumulate in the electrolyte, potentially inhibiting the further reaction. Finally, there is the

semi-recirculating method. The carrier electrolyte is circulated around the system whilst high reductant concentrations are injected before the fuel cell inlet, at low molar flow rates. This allows for high volumetric flow rates to be used for the carrier electrolyte. This presents the opportunity for a highly concentrated reductant to have a low volume, which could be easier to store compared to a fully recirculating electrolyte. Although this method could potentially have the benefits of both the single pass and recirculating system, the molar flow rate of reductant entering the cell must be monitored. Too much reductant entering the cell increases the reductant concentration within the carrier electrolyte. Too little reductant and cells within the stack may starve, reducing performance.

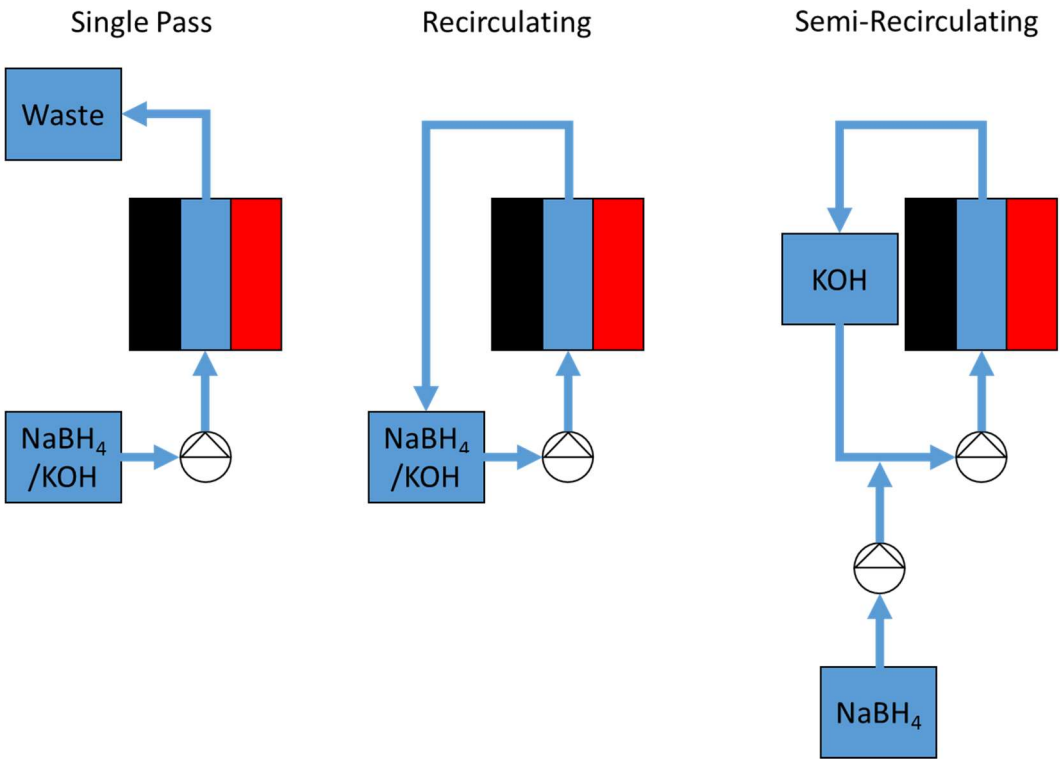

Figure 6.1 - Liquid fuel/electrolyte circulation methods.

Other transport components such as blowers, compressors and fans are used to transport gases around most fuel cell systems. These can be used with the reductant and/or oxidant flow streams or even in an auxiliary cooling circuit (see 6.1.3).

Each cell in a fuel cell produces heat due to inefficiencies. This generation of heat can be advantageous with high temperature fuel cells such as MCFC which generate high grade heat that can be used with combined heat and power (CHP) systems. However, heat can be an issue for lower operating temperature fuel cells. As such, stacks may require a method of cooling using a heat exchanger. This heat exchanger may initially heat the fuel cell at the beginning of startup to get the fuel cell to the desired operating temperature but then cool the stack once the temperature is self-sustaining. Various blowers, pumps and compressors used to regulate gas and liquid flow around the system require electrical motors which can be supplied by the fuel cell. Should the fuel cell be used in an automotive application then a motor would be used to drive the vehicle forward. However, this is based on a more complex powertrain, the architecture of which depends on the type of fuel cell, other energy storage and the type of electric motor used. The challenges of heat management are discussed further in Section 6.1.3.

The electricity generated by the fuel cell stack requires several electrical components to make it usable for the target application. This may include voltage regulators, possible inverter and electrical motors, depending on the application such as automobiles [65, 210]. The DC electricity generated from the fuel cell is unstable and will change depending on the degradation of electrodes and the overpotential applied to draw the current. Using an electrical regulator allows for a reduction in the voltage drop when the fuel cell is polarised and current needs to be drawn. Should the DC power delivered by the fuel cell not be suitable, an inverter is added to convert the DC to AC if required.

6.1.2 Water Management

Water management is a complex issue in fuel cells. Depending on the type of fuel cell, and the type of oxidant used, the redox reaction can have either a positive or negative net water value (see Section 2.3.3.3). Small quantities of water can also be lost through the GDL electrodes to the dry gas passing at the back of. Although the quantity of water is small, over a period of time it can build into a significant issue with electrode dehydrating and degrading [33]. Furthermore, the electrolyte contamination with carbon dioxide experienced in AFCs leads to the formation of carbonates through reaction with water causing changes in electrolyte volumes (see Section 2.3.2) [33]. The effect of this change in water and solution composition varies depending on the component and fuel cell type in question.

Solid polymer electrolyte fuel cells use either anion or proton exchange membranes which can facilitate water transport as a result of electro-osmosis or electro-osmotic drag whereby polar molecules migrate through a membrane in the presence of an applied potential, i.e. from the anode to the cathode [211]. In an alkali electrolyte fuel cell, the hydroxyl ions produced at the cathode migrate to the anode whilst water produced at the anode migrate to the cathode to complete the redox reaction as shown in Table 6.1. Unlike the hydroxyl ion whose concentration remains unchanged overall, more water is produced at the anode that is consumed at the cathode, leading to water accumulation at the anode. Furthermore, under electro-osmosis, the migration of hydroxyl ions from the cathode to the anode brings additional water molecules. This can lead to anode flooding, causing water to leak out to the back of the GDL and potentially causing electrical shortages. In addition, the lack of water on the cathode can reduce the rate of reaction affecting the efficiency of the cell [212]. In acidic media, i.e. PEMFC Table 6.1, the protons, water produced and water transported by electro-osmosis will migrate from the anode to the cathode. Although the cathode consumes the migrated water, it cannot consume the amount that is present and requires the careful control of gas humidity. However, this can still lead to too much water at the cathode, causing electrode flooding [213].

Table 6.1 - The production and consumption of water, hydroxyl ions and protons in an AFC and PEMFC.

Fuel Cell	Electrode	Reaction	H_2O Produced	OH^-/H^+ Produced
AFC	Anode	$2H_2 + 4OH^- \rightarrow 4H_2O + 4e^-$	+4	-4
	Cathode	$O_2 + 2H_2O + 4e^- \rightarrow 4OH^-$	-2	+4
PEMFC	Anode	$H_2 \rightarrow 2H^+ + 2e^-$	0	+2
	Cathode	$\frac{1}{2}O_2 + 2H^+ + 2e^- \rightarrow H_2O$	+1	-2

The effects of water accumulation across the fuel cell are not solely felt by the electrodes. Fuel cell electrolyte membranes, which are present in selected fuel cells such as PEMFCs (proton) and anion exchange membrane fuel cells (AEMFC), have a hydrated ion-conducting polymer structure which uses the dissociation of various ions within the polymer to conduct protons or

hydroxyl ions in acid and alkaline media respectively. The hydration of the membrane is of great importance to the performance of the membrane. Should the membrane become too dehydrated, the dissociation of ions in the membrane become impaired resulting in a lower ionic conductivity and increasing ohmic resistance across the cell [214]. A hydrated membrane is approximately 300 times more conductive than a dehydrated counterpart. The latter can become irreversibly damaged as a result, requiring it to be replaced [35].

In a fuel cell with a liquid electrolyte such as flowing AFCs, changes in the amount of water lead to alterations in chemical concentrations. Potassium hydroxide is a common electrolyte to use in AFCs due to its high conductivity. However, the conductivity of the electrolyte greatly depends on its concentration. For potassium hydroxide, the highest electrical conductivity is at 20 °C being 0.5697 $S.cm^{-1}$ using 6 M $KOH_{(aq.)}$ which decreases to 0.5603 $S.cm^{-1}$ and 0.5594 $S.cm^{-1}$ at 5 M and 7 M $KOH_{(aq.)}$ respectively [30]. Although this is only a decrease of about 2 % it would still undesired as it would increase ohmic resistance across the stack. Furthermore, in DFAFC such as DBAFC, alterations in the water content would alter the concentration of the reductant leading to a deviation in the fuel cell's optimal operating condition.

There are several ways in which water can be managed throughout the stack. The first and most common is through altering the gas humidity by manipulating the flow rate and temperature of the oxidant gas. For most fuel cells, air is usually preferred as the oxidant over pure oxygen because of the lower cost and availability. Increasing the air flow past the back of the cathode, any water generated can be removed as water vapour. For PEMFC, the exit humidity of the air leaving the cell must be approximately 100 % to prevent any electrode flooding [16]. Water management through this method is slightly more difficult for AFCs compared to PEMFC as the $KOH_{(aq.)}$ electrolyte has a lower vapour pressure than water and so the evaporation rate is slower although the vapour pressure slowly increases as water is produced and the concentration of $KOH_{(aq.)}$ decreases [16].

6.1.3 Heat Management

Controlling the temperature of a fuel cell and the stack is vital to operating at optimal performance. Different fuel cell technologies have different operating temperatures (summarised in Figure 6.2 [64]) to take advantage of different properties associated with that

temperature. For example, anode supported SOFC typically operate at approximately 800 °C which allows for the use of non-precious metals and faster kinetics. However, lower temperature fuel cells, such as AFCs, have faster startup times as the temperature of the fuel cell does not have to reach high temperatures before it can operate.

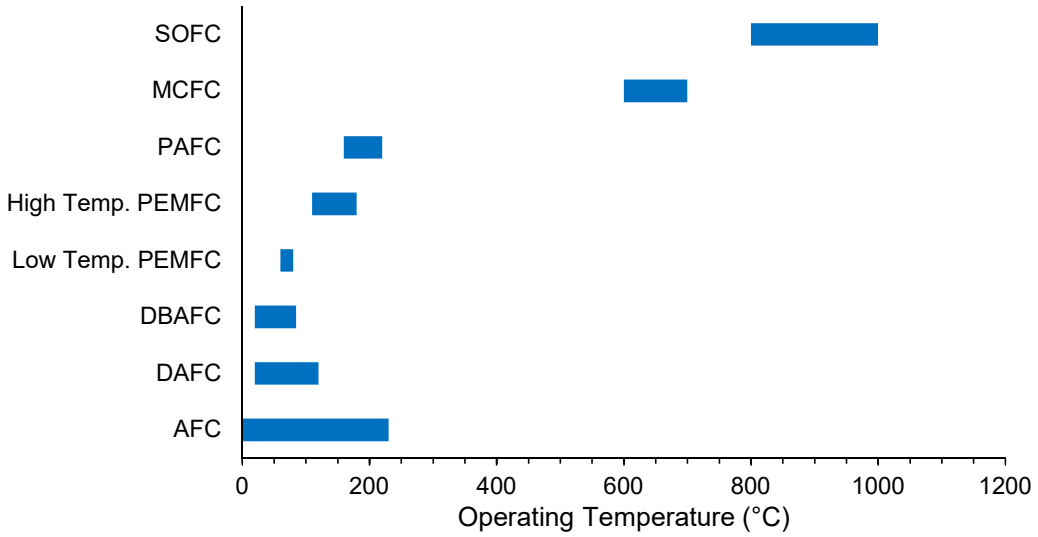

Figure 6.2 - Typical fuel cell operating temperature ranges.

Most fuel cells operate at elevated temperatures to reduce the activation energy loss, although some applications make running high temperature fuel cells impractical, such as for portable electronics. The temperature of the stack will most likely increase once the stack is in use, due to inter alia ohmic resistance, the heat of reaction, condensation of vapour and irreversible electrochemical production of heat. The impact of this increase in the temperature of the stack depends on the type and operating conditions of the fuel cell [215], as well as the number of cells in the stack and the current generated. In extreme cases, this may lead to the introduction of a cooling system to control the temperature of the system.

For fuel cells operating at low temperatures, such as PEMFC, cooling can be challenging because the operating temperature is close to ambient temperature, or worse lower than ambient temperature. Cooling can be affected by air cooling, liquid cooling or phase change [215, 216]. Air cooling circulates air through the stack to remove any heat that has been generated. The low heat transfer coefficient associated with gas means that only small

quantities of heat can be removed and this technique is thus only suitable for low power stacks (<5kW). However, it is the simplest and most cost-effective method of removing heat especially if air is used and can be passed through the cell/stack and exit the cell without the need for being recirculated.

Liquid cooling circulates water through pipes and through the bipolar plates in the stack. This is a common method of cooling due to the higher heat transfer coefficient compared to air/gas and is suitable for stacks with a higher power production (> 5 kW). The liquid passes through the stack, removing any heat, is cooled and then recirculated back into the stack. The temperature of the cooling liquid can be adjusted by controlling the temperature of the heat exchanger and flow rate of the liquid entering the stack. Careful design of the bipolar plate helps ensure adequate heat removal while the requirement for a pump reduces the net power output of the stack [217]. The nature of the liquid coolant must be such that it not to introduce ionic leakage, which would decrease the stack's efficiency (see Section 5.1.3.2).

Phase change is the removal of heat via the evaporation of a liquid. This principle is used for a variety of cooling systems, such as heat pipes, flow boiling and evaporative cooling, each with their benefits and disadvantages [216]. Using a phase change cooling system for fuel cells can be problematic due to the requirement of a specific coolant media and the introduction of two-phases [215].

6.1.4 Systems for Direct Borohydride Alkaline Fuel Cells

Several types of fuel cells use borohydride, including systems in which borohydride is a hydrogen storage material, known as indirect borohydride fuel cells (IBFC), direct borohydride-peroxide fuel cell (DBPFC), direct borohydride membraned fuel cell (DBMFC) and direct borohydride alkaline fuel cells (DBAFC). Although systems have been developed for borohydride fuel cells, these must not be mistaken for IBFC systems. The IBFCs use borohydride as a hydrogen carrier/storage material, whereby the borohydride is hydrolysed to release the hydrogen to be used by another fuel cell. An example of this is shown in Figure 6.3 [205, 218]. The hydrogen generated from the hydrolysis of borohydride is fed to a fuel cell where is it generates energy [49, 219-222] .Due to the indirect use of borohydride and the use

of another type of fuel cell, these are not within the scope of this project and will not be considered further.

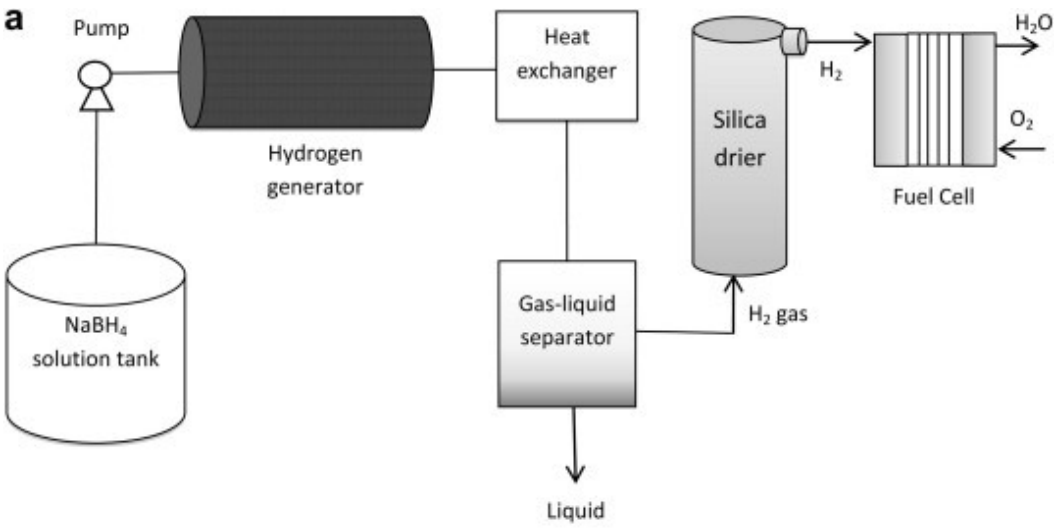

Figure 6.3 - Borohydride used in a fuel cell system [205].

The aim of this work was to use borohydride, via direct oxidation mechanism, to generate electricity rather than using borohydride as a precursor for another fuel cell. Borohydride as a reductant is often coupled with peroxide as an oxidant as its reduction potential is higher than that of oxygen (see Equation 6.1) [223].

$$\frac{1}{2}O_2 + H_2O + 2e^- \rightarrow 2OH^- \quad E_c = +0.4V\ vs\ SHE$$

$$H_2O_2 + 2e^- \rightarrow 2OH^- \quad E_c = +0.88V\ vs\ SHE$$

$$H_2O_2 + 2H^+ + 2e^- \rightarrow 2H_2O \quad E_c = +1.78V\ vs\ SHE$$

Equation 6.1 - Electroreduction of oxygen (top) and peroxide in alkaline (middle) and acidic (bottom) media.

In a DBPFC, the gas component on the cathode side is replaced by liquid hydrogen peroxide, thus removing all gas phase reactants such that DBPFC's become solid-liquid phase system and the reaction occurs at a double phase boundary, i.e. solid electrocatalyst and liquid peroxide/borohydride interface, compared to the triple phase boundary used in fuel cells with

a gas phase oxidant. As with the IBFC, peroxide can be used as an oxygen carrier and can decompose to release oxygen on the cathode [224]. DBPFC utilise both an acid and alkali media. The borohydride is dissolved in the alkali media due to its stability at high pHs (see Section 2.3.4.3) whilst the peroxide can be used in both acidic and alkali media. Regardless of whether acid or alkali is used with the peroxide, a membrane is used to separate the peroxide from the borohydride. This is to prevent fuel crossover as a reaction specific electrode would be required on both the anode and cathode. In a membraneless DBPFC, the peroxide channel is placed on the outside of the cathode, see Figure 6.6 [184], diffusing through the porous electrode where it is oxidised in a similar mechanism to gas phase oxidants diffusing through a GDL. The result is a fuel cell setup similar to that shown in Figure 6.4 [225] and Figure 6.5 [226].

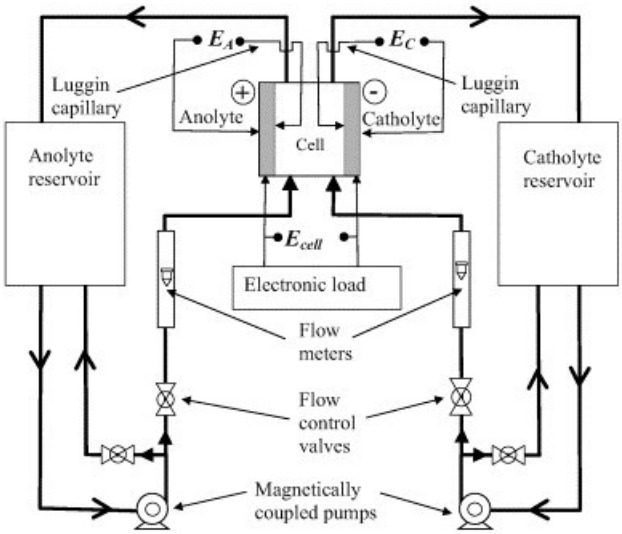

Figure 6.4 - DBPFC system using an acid catholyte by de Léon *et al.* [225].

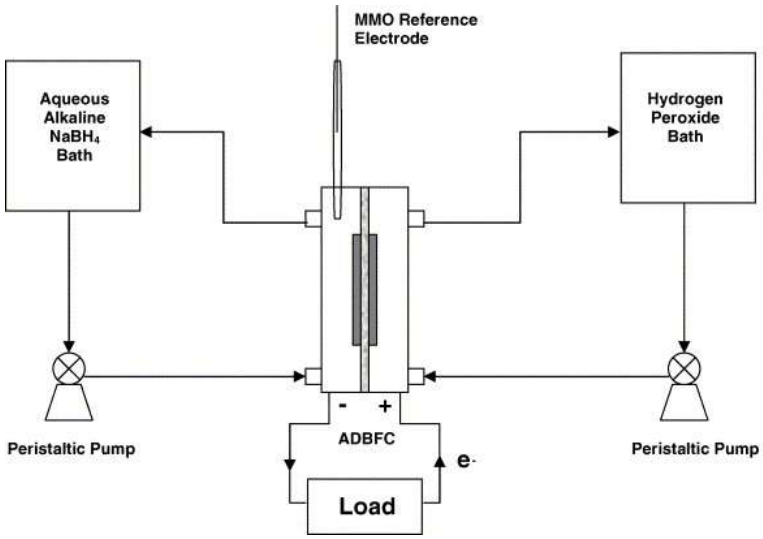

Figure 6.5 - DBPFC system using an alkaline catholyte by Choudhury *et al.* [226].

Both the anolyte (borohydride) and the catholyte (peroxide) are pumped through the fuel cell between the electrodes and membrane and is recirculated through to a reservoir. The benefits of this kind of setup are that the borohydride and peroxide flow rates can be independently controlled compared to a borohydride-peroxide-electrolyte mix. However, such systems are only designed for fuel cell testing and do not allow for the monitoring of the reduction of borohydride over time. Furthermore, these are based on membraned fuel cells, separating the two liquids. Although these are suitable for initial testing the system, they are unsuitable for scale up and offer little flexibility with respect to controlling the operating conditions.

Another type of DBFC is one which utilises a gaseous oxidant and a membrane, the DBMFC. In this type of DBFC, the oxidant has to be on the outside of the cathode (see Figure 6.6 [184]). This is due to membrane dehydration which would occur should the gas oxidant pass between the membrane and cathode and the removal, or reduction, of an ion conduction path. This is different from the DBPFC which can be present between the membrane and cathode. Due to the technology being in its infancy little research has been conducted on the system setup for any of these types of fuel cell.

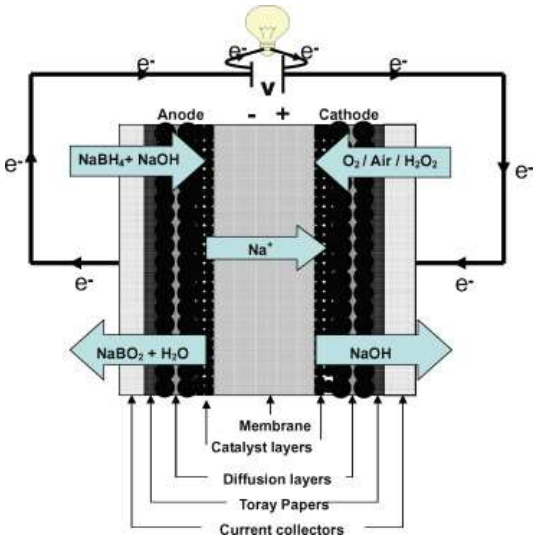

Figure 6.6 - DBMFC using oxygen, air or peroxide by Ma *et al.* [184].

Very little work has been conducted on the DBAFC, a membraneless DBFC. The fuel cell rig or system which has previously been published is by Verma *et al.* [88, 227, 228] and is shown in Figure 6.7. Although this system was suitable for cyclic voltammetry testing a fuel cell rig, with a single pass electrolyte at 1 mL.min^{-1} and 1-2 M $NaBH_4$/3 M $KOH_{(aq.)}$, the system was designed only for electrode testing, not for scale up or practical applications. The system features a fuel reservoir which is pumped through the fuel cell. The cell itself contains a magnetic bead between the electrodes to circulate the fuel to reduce the concentration gradient. The used fuel then leaves the fuel cell and is collected but a final reservoir.

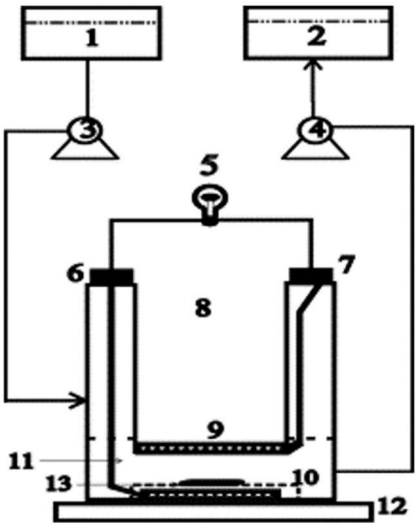

Number	Component
1	Fuel-electrolyte reservoir
2	Spent fuel-electrolyte
3+4	Peristatic pumps
5	Electronic load
6	Anode terminal
7	Cathode terminal
8	Air
9	Cathode
10	Anode
11	Fuel-electrolyte in fuel cell
12	Magnetic stirrer
13	Anode shield

Figure 6.7 - Flowing electrolyte DBAFC by Verma *et al.* [88, 227, 228].

The lack of development of DBAFC is likely due to the complicated oxidation mechanisms, leading to hydrolysis of borohydride and efficiency losses, and the requirement for electrocatalysts being specific to one reaction due to fuel crossover when a membrane is not used. However, this work looks to develop a versatile DBAFC system which is capable of both fuel cell testing and suitable for upscaling/real world applications.

6.1.5 Borohydride Recycling and Recovery

In the synthesis of sodium borohydride, borax is used as a precursor. Although borax ore supplies may currently be plentiful it is still a non-renewable source. Therefore, efforts must be made to find a method to economically recover any metaborate, the by-product of the decomposition of borohydride. This can be done either as part of the fuel cell system or separately. There have been several published methods by which borohydride can be recovered, here the term 'recovered' is used to represent the borohydride produced from outside of the system it was utilised. For example, this would include the removal of spent fuel and the converting of large quantities of metaborate back into borohydride to be sold back to the consumer. Methods for recovering borohydride and other borohydride synthesis methods are examined in detail by the work of Santos *et al.* [53, 229]. However, recycling the metaborate within the system would benefit the fuel cell system and potentially increase its efficiency. The most suitable method for metaborate recycling within the system is electrosynthesis, through various other methods are also described here.

Sanli *et al.* [61] investigated the electrosynthesis of borohydride using a silver mesh working electrode for the use of a DBPFC and determined that a reduction peak observed during cyclic voltammetry at +0.5 V (vs SCE) was related to the generation of borohydride from metaborate. Holding at this potential for 24 and 48 hour periods at room temperature in 0.1 M $NaBH_4$/1 M NaOH yielded 9 and 17 % borohydride synthesis respectively.

Similarly, the work of Park *et al.* [59] used a variety of different electrodes including Pd, Pt, Au and boron-doped diamond (BDD) to recycle borohydride. The white powder was produced using chronoamperometry and was then characterised using X-ray diffraction and Fourier

transform infra-red techniques and determined the powder to be borax. All electrodes produced pure borohydride through an electrochemical-thermal route. An example of an idealised system in which borohydride is recycled as part of an IDBFC, coupled with a PEMFC, for the hydrolysis and release of hydrogen is shown in Figure 6.8.

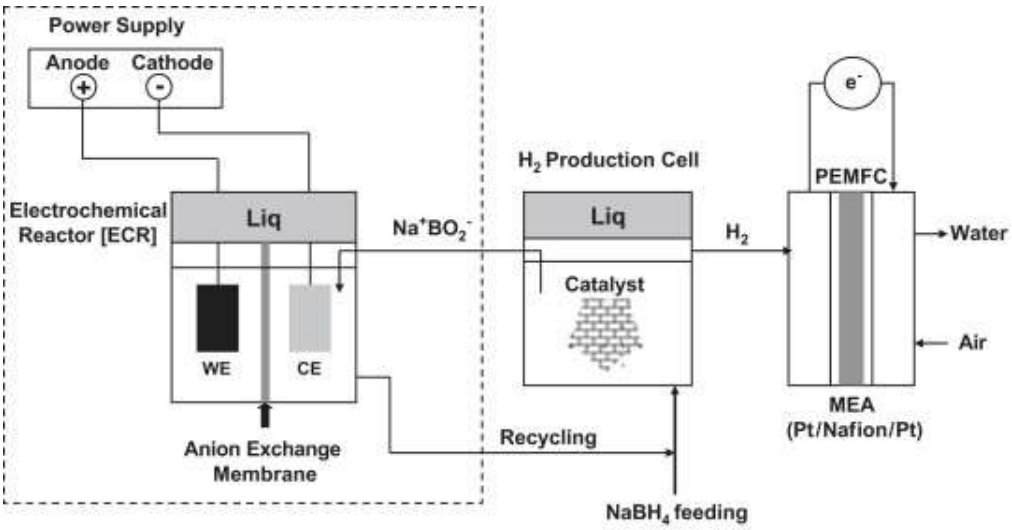

Figure 6.8 - Ideal system for borohydride recovery in an IDBFC taken from Park *et al.* [59].

Cooper, Dutcher, Sharifian and Hale [230, 231] submitted patents claiming to have converted borate to borohydride under aqueous conditions. However, the work of Gyenge *et al.* [232] attempted to recreate the results described in the patents with no success.

This is not to say that recycling borohydride from metaborate using electrosynthesis methods is unlikely to show any promise. The work of Santos *et al.* [229] showed borohydride formation using a two compartment electrochemical cell (Equation 6.2). Although the quantities were relatively low, for all electrosynthesis methods described, there are published technologies which work and have the potential to be developed and implemented into a fuel cell system.

$$NaBO_2 + 6H_2O + 8e^- \rightarrow NaBH_4 + 8OH^- \qquad E_0 = -1.24 \text{ V vs SHE}$$

$$8OH^- \rightarrow 2O_2 + 4H_2O + 8e^- \qquad E_0 = 0.40 \text{ V vs SHE}$$

Equation 6.2 - Santos *et al.* cell reaction [229].

6.1.6 Borohydride Utilisation

Determining and understanding how the borohydride is used in a fuel cell is important, especially when the fuel has a complex oxidation mechanism such as borohydride. In the case of DBAFCs, understanding how the borohydride is being oxidised can lead to a better understanding and comparison of different electrocatalysts and electrodes. As seen in the borohydride oxidation equation (Equation 2.7) four different components are produced from the decomposition of borohydride which includes metaborate, hydrogen, electrons and water (however, heat is also produced) any of which may be measured to give an estimate of the borohydride utilisation in a fuel cell.

The work of Wang *et al.* [233, 234] determined the utilisation percentage based on the rate of hydrogen generation. In Equation 6.3 the borohydride utilisation is represented as a function of the discharge electric power (E_{elect}) and the generated hydrogen energy (E_{H_2}).

$$Utilisation\ (\%) = \frac{E_{elect}}{E_{elect} + E_{H_2}}\ x\ 100$$

Equation 6.3 - Borohydride utilisation based on Wang *et al.*

Another similar method was used by Celik *et al.* [235] which calculated the fuel utilisation ratio (FUR) using the electrical energy (E_{elect}) and hydrogen energy (E_{H_2}); however, unlike Wang *et al.* it also incorporated the fuel on the cathode side that is not oxidised (E_C) and is represented in Equation 6.4.

$$FUR\ (\%) = \frac{E_{elect}}{E_{elect} + E_{H_2} + E_c}\ x\ 100$$

Equation 6.4 - Borohydride utilisation based on Celik *et al.*

These methods can be useful in approximating the utilisation of borohydride, though they do not provide information relating to the instantaneous borohydride hydrolysis and hydrogen oxidation. Measuring all the chemical species generated from the electrooxidation of borohydride, together with the electron potentials and heat produced, would still provide insufficient information to calculate an accurate utilisation percentage. The instantaneous hydrolysis-hydrogen oxidation that occurs at an electrode's surface is not insignificant, as described by Jamard *et al.* [236] who examined the effects of thiourea on hydrolysis inhibition for borohydride fuel cells. The results show that although the columbic efficiency increased, there was a decrease in specific power in the fuel cell. This means that the amount of instantaneous hydrolysis-hydrogen oxidation reaction occurring at the electrode cannot be considered insignificant or negligible and as such the methods of calculating utilisation percentage must be considered as approximations.

However, determining the total amount of borohydride that has been decomposed within the fuel cell can be achieved accurately by measuring the amount of borohydride that leaves the cell. Although this does not give any information pertaining to the mechanism of borohydride oxidation, it does give an indication of fuel cell performance. As such, determining the borohydride concentration was developed and is described in detail in Section 6.2.2.

6.2 Methods

A system was first designed containing the basic components required to run the DBAFC at room temperature and its fitness for purpose evaluated. Water was commonly pumped as a method to safely evaluate the system prior to the use of the fuel/electrolyte. This would identify if any leaks present in the fuel cell prior to using the electrolyte, which could have potentially leaked highly corrosive alkali media. Once the system appeared to show no issues, the fuel/electrolyte was pumped and the fuel cell was evaluated under the desired conditions. The following sections detail the programmes and methods developed to evaluate the properties of the system.

6.2.1 Mass Flow Meter LabVIEW Interface

A volumetric flow meter was used to monitor the flow of electrolyte through the system. The flow meter (BIO-Tech, FCH-M-PP-LC) used the Hall Effect to generate an electronic signal. An

interface between the flow meter and the computer was required to measure and record the signal needed to be designed. A simple program in LabVIEW was designed to measure the flow rate of future experiments.

The flow rate was calculated for a specific pump and voltage by measuring the amount of water passed over a period of time. From this, a power coefficient was calculated which was a function of the number of counts and a specific voltage. For example, 80 cm^3 of water would be pumped at 2 V over a period of approximately 16.8 s, giving a flow rate of 286 $cm^3.min^{-1}$. The number of counts was measured for the same voltage over a period of 20 s which was approximately 177 (526 $counts.min^{-1}$). Dividing the flow rate by the $counts.min^{-1}$ gave 0.543 $cm^3.count^{-1}$. This was done over a range of pump voltages to give a wide range of different flow rates. The different volumes per count are summarised below (Table 6.2).

Table 6.2 - Flow meter power coefficients.

Pump (V)	Liquid Flow Rate ($cm^3.min^{-1}$)	$Count.min^{-1}$	$Count.cm^{-3}$	Power Coefficient ($cm^3.Count^{-1}$)
2	286	526	1.84	0.543
4	657	1089	1.66	0.603
6	964	1689	1.75	0.571
8	1270	2012	1.58	0.631

The power coefficients in Table 6.2 show that the flow meter is not consistent, indicating that the flowmeter is not very accurate, though it may also be due to variations in the pressure drop from the pump even when the voltage was kept constant. As a result, the flow rates measured by the flow meter were treated as an indication only.

6.2.2 Determination of Borohydride Concentration using Cyclic Voltammetry

The work of Hou *et al.* [237] shows that the concentration of borohydride can be measured by cyclic voltammetry using a gold microelectrode. The background behaviour of the gold microelectrode in 6.6 M $KOH_{(aq.)}$ supporting electrolyte was recorded (shown in Figure 6.9).

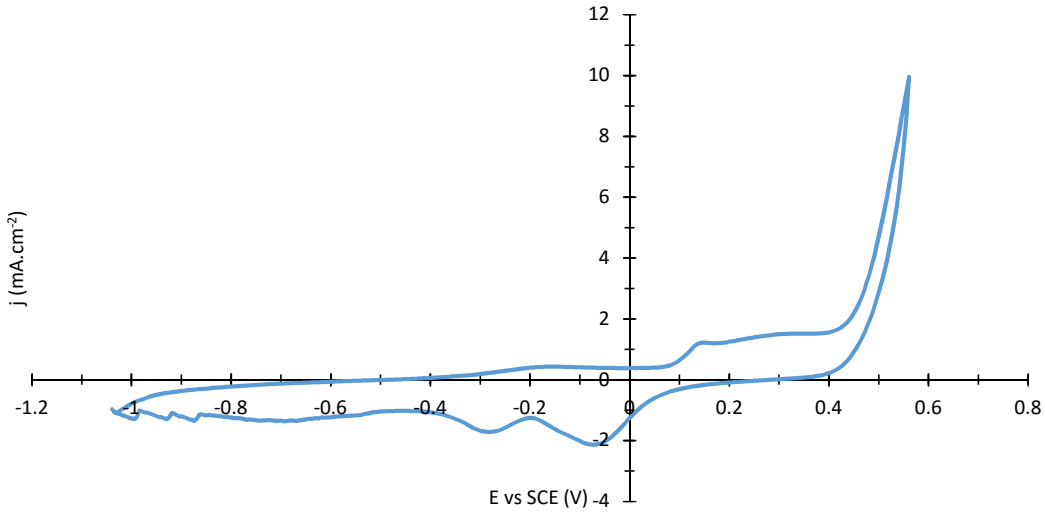

Figure 6.9 - CV of micro-gold electrode (50 µm diameter) in 6.6 M $KOH_{(aq.)}$ at 50 $mV.s^{-1}$ and 0 rpm.

A range of borohydride concentrations was prepared (10 µM,100 µM,1 mM,10 mM and 100 mM in 6.6 M KOH) and a cyclic voltammogram recorded under the same conditions as the background 6.6 M $KOH_{(aq.)}$ CV. Although the amount of current produced was relatively low (Figure 6.10 and Figure 6.11), large non-linear variations were observed between the borohydride concentration and the peak currents.

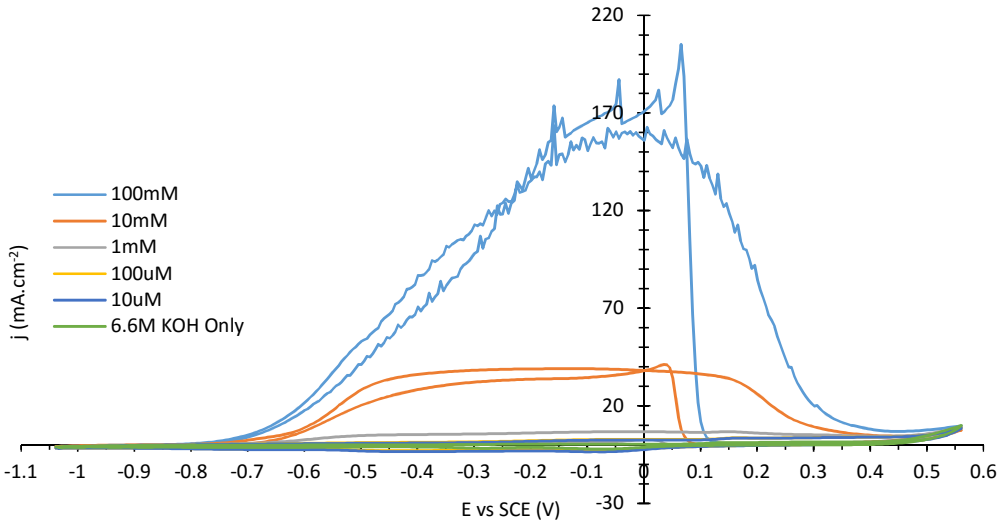

Figure 6.10 - CV showing the effect of borohydride concentration on current density using a micro-gold electrode (50 µm diameter) in various NaH_4/6.6 M $KOH_{(aq.)}$ concentrations at 50 $mV.s^{-1}$ and 0 rpm.

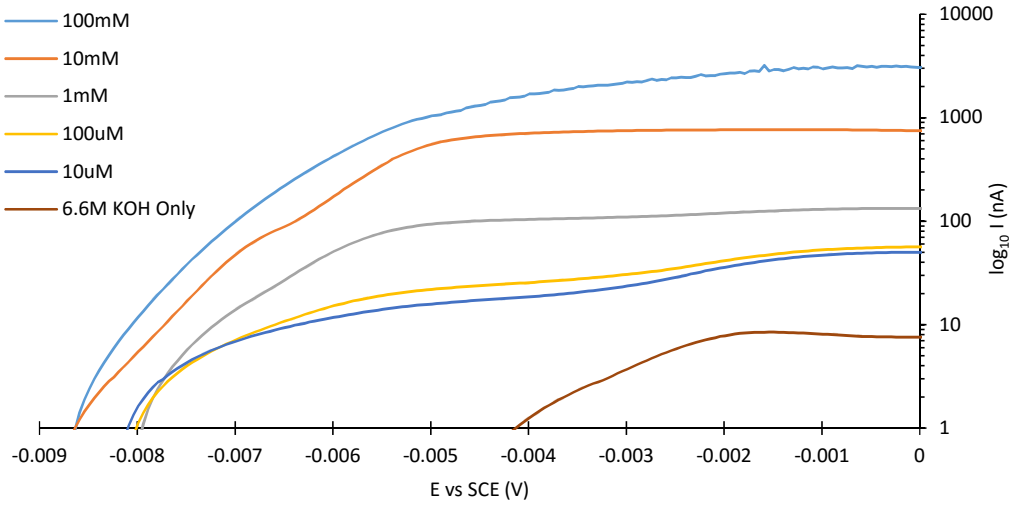

Figure 6.11 - The log_{10} current scale of borohydride at different concentrations using a micro-gold electrode (50 µm diameter) in various NaH_4/6.6 M $KOH_{(aq.)}$ concentrations at 50 $mV.s^{-1}$ and 0 rpm.

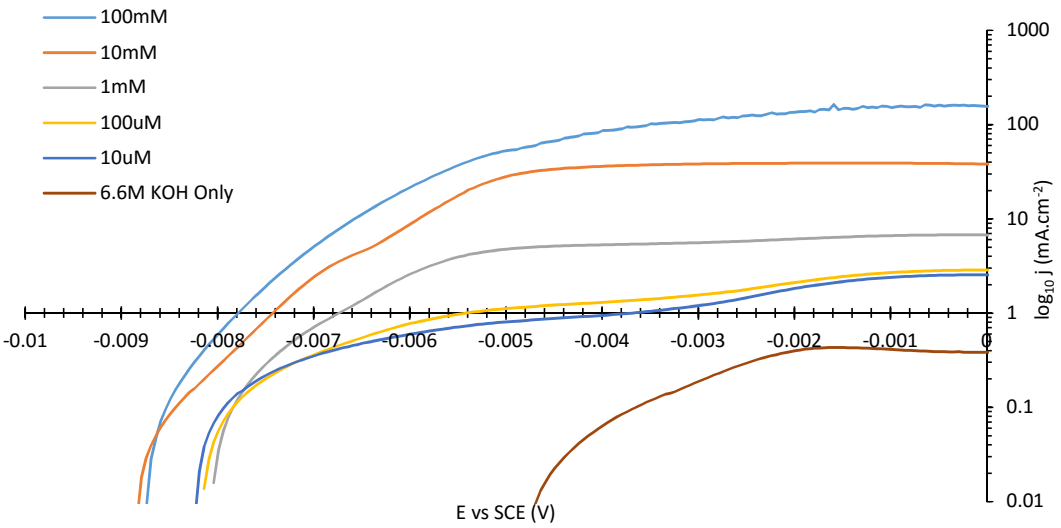

Figure 6.12 - The log_{10} current density scale of borohydride at different concentrations using a micro-gold electrode (50 µm diameter) in various NaH_4/6.6 M $KOH_{(aq.)}$ concentrations at 50 $mV.s^{-1}$ and 0 rpm.

Finally, the log_{10} peak currents were plotted against the log_{10} borohydride concentration (Figure 6.13). The results showed that there is a linear relationship between the log_{10} peak current and the log_{10} concentration between 0.1 - 10 mM borohydride. Therefore, within this range, the current produced is directly proportional to the amount of borohydride in the electrolyte. Outside of this range, the relationship is not linear and so the method would not be suitable for measuring borohydride concentrations.

Comparing the plots of current and current density (Figure 6.13 and Figure 6.14 respectively), there is a difference in the current densities generated in this work compared to the literature. Due to the same currents being generated for different sized electrodes (50 µm and 1 mm diameter electrodes for this work and the literature respectively), this would indicate that the electrodes were not mass transport limited and the current was based on the concentration of borohydride rather than the electrode size.

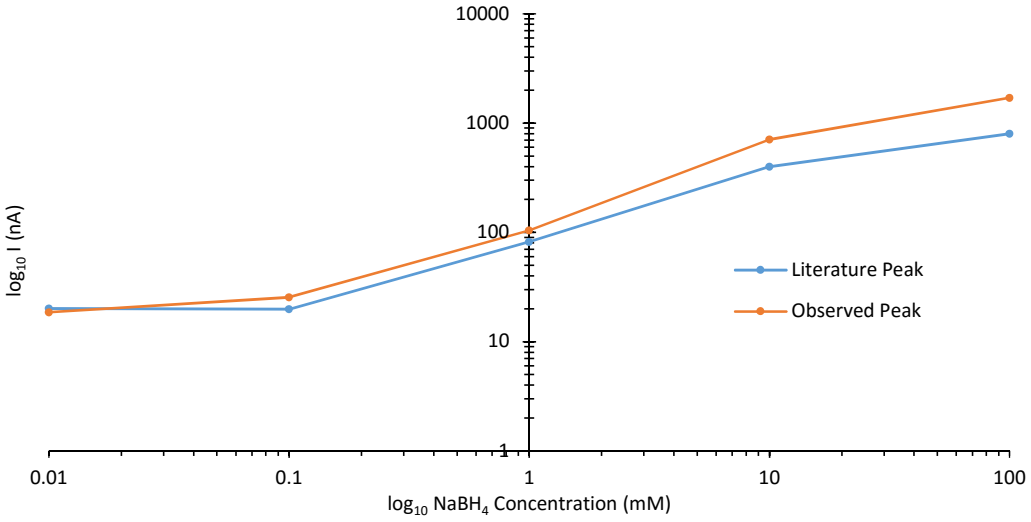

Figure 6.13 - Comparison of measured log_{10} peak currents of different borohydride concentrations (using a micro-gold electrode (50 µm diameter) in various NaH_4/6.6 M $KOH_{(aq.)}$ concentrations at 50 $mV.s^{-1}$ and 0 rpm.) with data replicated from Hou *et al. [237].*

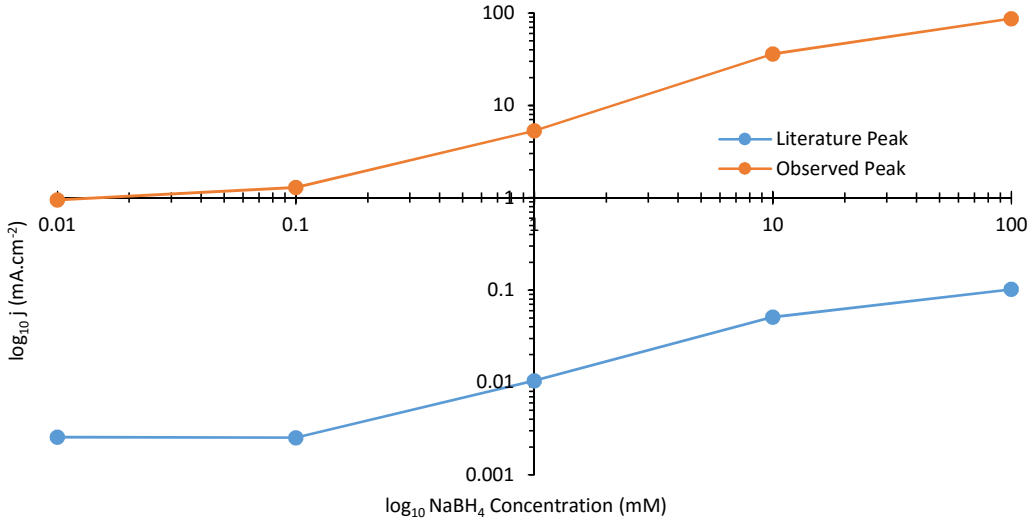

Figure 6.14 - Comparison of measured log_{10} peak currents densities of different borohydride concentrations (using a micro-gold electrode (50 µm diameter) in various NaH_4/6.6 M $KOH_{(aq.)}$ concentrations at 50 $mV.s^{-1}$ and 0 rpm.) with data replicated from Hou *et al.* [237] which used a 1 mm diameter electrode.

Using Faraday's equation, it is possible to calculate the molar flow rate of borohydride (see Equation 6.5) entering the cell and calculating the molar flow rates ($\dot{\eta}$) of the various by-products from the concentration (C) range of the borohydride, using a specified volumetric flow rate ($\dot{v}$), gives an outlet molar flow rate range that the can be detected using this method.

$$\dot{\eta} = C.\dot{v}$$

Equation 6.5 - Calculation of molar flow rate from concentration and volumetric flow rate.

Using Equation 6.5 at a fixed volumetric flow rate of 5 $cm^3.min^{-1}$, the molar flow rate of the upper (10 mM $NaBH_4$) and lower (0.1 mM $NaBH_4$) range of the electrochemical determination of borohydride concentration can be calculated (5 × 10^{-4} $mM.min^{-1}$, borohydride lower limit (BLL), and 5 × 10^{-2} $mM.min^{-1}$, borohydride upper limit (BUL), respectively). This was then used to calculate how much borohydride had decomposed using the molar flow rate of borohydride entering ($\dot{\eta}_{BH_4^-in}$) and leaving ($\dot{\eta}_{BH_4^-out}$) the fuel cell (using Equation 6.6).

$$Borohydride\ Decomposition\ (\%) = \frac{\dot{\eta}_{BH_4^-in} - \dot{\eta}_{BH_4^-out}}{\dot{\eta}_{BH_4^-in}}\ x\ 100$$

Equation 6.6 - Calculating the upper and lower borohydride decomposition limits.

Equation 6.6 relies on a known molar flow rate entering the fuel cell which was calculated using Faraday Equation (Equation 6.5) at a set current density. By altering the estimated current density, and therefore molar flow rate into the fuel cell, different upper and lower utilisation values were obtained. Table 6.3 summarises the various utilisation range of the fuel required for the borohydride exiting the fuel cell to fall within the observable range of 0.1 mM-10mM (or 8.333 × 10^{-9} and 8.333 × 10^{-7} $mol.s^{-1}$ at a volumetric flow rate of 5 $cm^3.min^{-1}$). For example, at a current density of 100 $mA.cm^{-2}$, this method allowed for the calculation of the amount of unused borohydride if the fuel cell utilised 47-99 % of the borohydride entering.

Table 6.3 – Upper and lower borohydride decomposition values based on different current and current densities (A_{geo} = 12.22 cm^2).

j (mA.cm^{-2})	I (A)	% Utilisation	
		Lower	Upper
100	1.222	47.4	99.5
200	2.444	73.7	99.7
400	4.888	86.8	99.9

At desired current densities (when j > 200 mA.cm^{-2}) this method requires the consumption of a large proportion of the fuel. However, requiring high fuel decomposition for those select current densities are for a A_{geo} = 12.22 cm^2. When applying Faraday's law to a fuel cell under constant conditions there are three variables, the charge number, molar flow rate and the current generated. Since the molar flow rate is known, the BUL molar flow rate based on the experiment (8.333 × 10^{-7} mol.s^{-1}), and the charge number is the same (n = 8), the A_{geo} can be calculated based on the total current generated. Substituting the known molar flow rate and the charge number into Equation 4.2 gives a total current of 0.6432 A. Therefore, any iteration of A_{geo} and current density which equates to 0.6432 A would give the widest utilisation range using this technique (up to 99% utilisation as the BLL is 1% of the BUL). Although it would be easier to simply change the flow rate so that the molar flow rate at the outlet lies within the detection range, this could potentially restrict the amount of fuel at the electrode, hindering performance.

Knowing what A_{geo} gives the widest decomposition percentage measurement range can be useful; however, it may not be necessary to have such a wide range. A fuel cell which decomposes a large amount of borohydride, either by direct oxidation or hydrolysis, would not require a large percentage range. Therefore, the usefulness of this technique would be based on the molar flow rate, borohydride decomposition and A_{geo}. Running an initial experiment with a fixed A_{geo} and measuring the approximate borohydride decomposition would determine the A_{geo} required for the measurement technique to be of use. Although in practice measuring the borohydride decomposition in this way would be very useful, altering the A_{geo} of the electrode for each electrocatalyst would require either a flexible fuel cell designed for the use of a wide range of electrode geometries or building a new fuel cell for each electrocatalyst for the borohydride leaving the fuel cell would fall within the range of the technique. This is because not every electrocatalyst would decompose the borohydride at the

same rate and therefore the molar flow rate of borohydride leaving the fuel cell may not fall in the detection range. Although this would be difficult, if a select few electrocatalysts were used with similar borohydride decomposition properties, a decomposition range could be selected which would accommodate all electrocatalysts with a single A_{geo}, allowing for the same fuel cell design to be used throughout.

6.3 Results

Initially, a simple system was developed to test various electrodes under specific conditions (system 1). However, as the fuel cell developed and a system was required to evaluate it under various conditions the simple system was no longer adequate and so the system had to be developed further. This section describes the evolution of the fuel cell system used to accommodate the desired requirements.

6.3.1 System 1 – Recirculating Electrolyte at Room Temperature

The recirculating electrolyte system was the first and most basic system designed (Figure 6.16). The electrolyte at the desired concentration (1 M $NaBH_4$/3 M KOH) was transported from a sealed bottle by means of a gear pump (Cole-Parmer miniature gear pump) to the fuel cell. The flow rate was determined by varying the voltage and measuring the volume of water pumped over a set time. From this, a flow meter was used to measure the real-time flow rate of the electrolyte using LabVIEW interface (see Section 6.2.1).

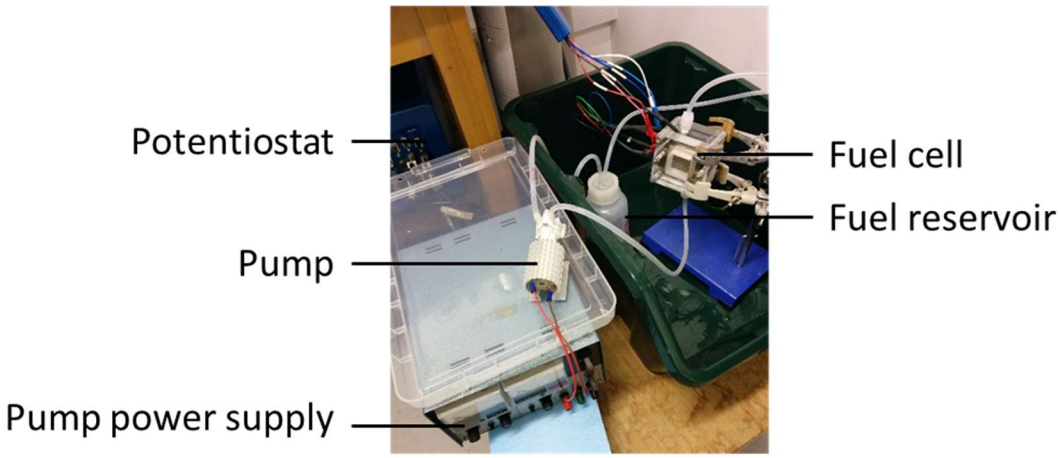

Figure 6.15 - System 1 with the open cathode end plate.

The compressed air was transported through a steel pipe (Swagelok), a mass flow controller (Alicat, MFC) and a non-return valve (Swagelok, NRV) through a sealed bottle containing carbon dioxide removal material (Sofnolime, CO_2 Absorb). The scrubbed air was then passed through the fuel cell out into the atmosphere. The fuel cell electrical performance was assessed using a potentiostat (Biologic SP-240 with booster) which was attached to the current collectors. Rigid plastic (PFA) tubing (Swagelok) was used for the air transportation and soft tubing (Tygon, RS Components) was used for the electrolyte transportation with Swagelok and SMC Pneumatics connectors used to the rigid plastic and soft plastic respectively. The electrolyte flow rate was measured using a flow meter (FM). Although the fuel cell is horizontal in Figure 6.16, during experimentation it was orientated so 45° on its corner. This allowed any hydrogen gas to rise to the electrolyte outlet, preventing accumulation.

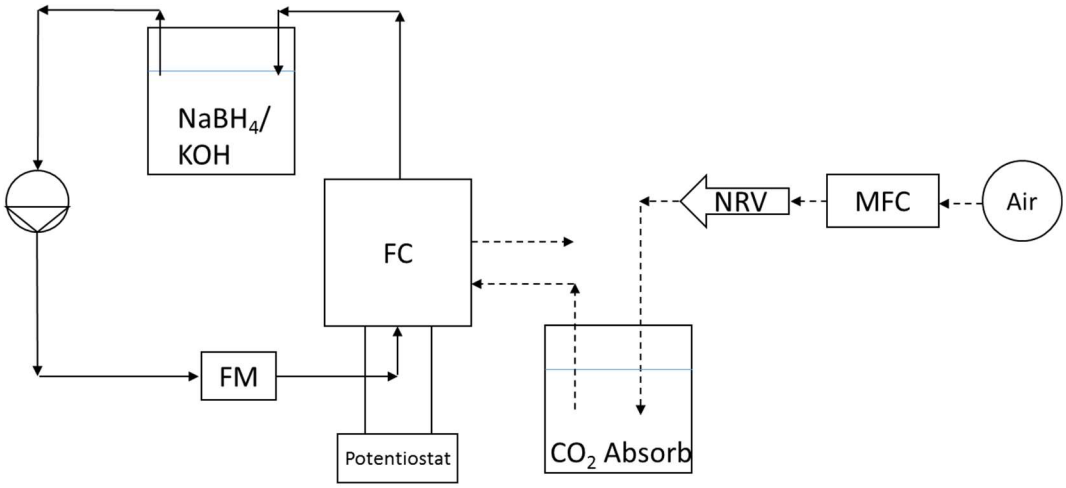

Figure 6.16 - System 1: Recirculating electrolyte at room temperature.

This system was evaluated under high volumetric and molar flow rate conditions. The high volumetric flow rates help prevent areas of the anode being starved of borohydride, facilitated the quick removal of potentially surface inhibiting by-products and prevent the build-up of hydrogen gas.

6.3.2 System 2 - Recirculating Electrolyte at Elevated Temperature

System 2 (Figure 6.18) was identical to system 1 with the addition of a hot plate to operate the fuel cell at elevated temperatures. The hot plate heated up the electrolyte around the system and through the fuel cell. The temperature of the electrolyte was restricted by the gear pump as increasing the electrolyte temperature caused the pump to short and stop pumping.

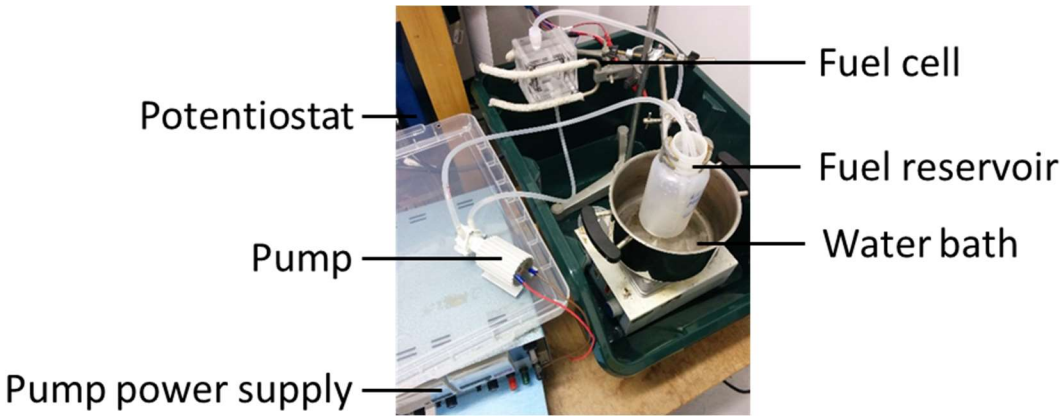

Figure 6.17 - System 2 with using the open cathode.

Adding the heating element to the system allowed for the evaluation of the fuel cell at elevated temperatures which was believed to improve power output, through an increase of the exchange current density, reducing activation losses. The fuel cell was placed into an oven and allowed to get up to the desired temperature prior to the experiment. The heat was supplied via a water bath which simultaneously mixed and heated the electrolyte leaving the fuel cell before it was pumped to the fuel cell once again. The reservoir vessel was sealed to prevent any evaporation of water and changes to borohydride and electrolyte concentrations.

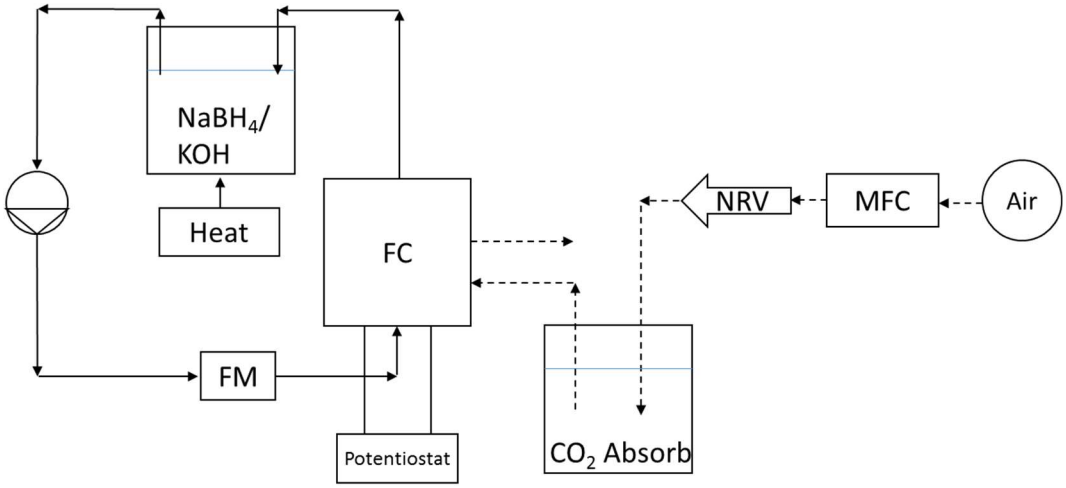

Figure 6.18 - System 2: Recirculating electrolyte at elevated temperature. FC = fuel cell, FM = flow meter, MFC = mass flow controller and NRV = non-return valve/check valve.

When the system was run at elevated temperatures, large quantities of hydrogen gas was evolved within the fuel cell which not only caused a safety issue but could have increased cell resistance and electrode weeping. Furthermore, increasing the temperature of the fuel/electrolyte reservoir could cause an increase in the pressure of the vessel.

6.3.3 System 3 – Semi-recirculating Electrolyte at High Flowrates

System 3 (Figure 6.19) introduced the concept of a semi-recirculating electrolyte, where the electrolyte acted as the "carrier" fluid within the system and governed the overall volumetric flow rate. The electrolyte was continuously circulated through the system at high flow rates (250 $cm^3.min^{-1}$) allowing for fast removal of by-products. Prior to reaching the fuel cell, the electrolyte was dosed with a high concentration borohydride solution (1 M $NaBH_4$/3 M KOH) at a slow flow rate (5 $cm^3.min^{-1}$) using a syringe pump (WPI AL-1,000) and mixed using an inline PTFE static mixer (ESSKA).

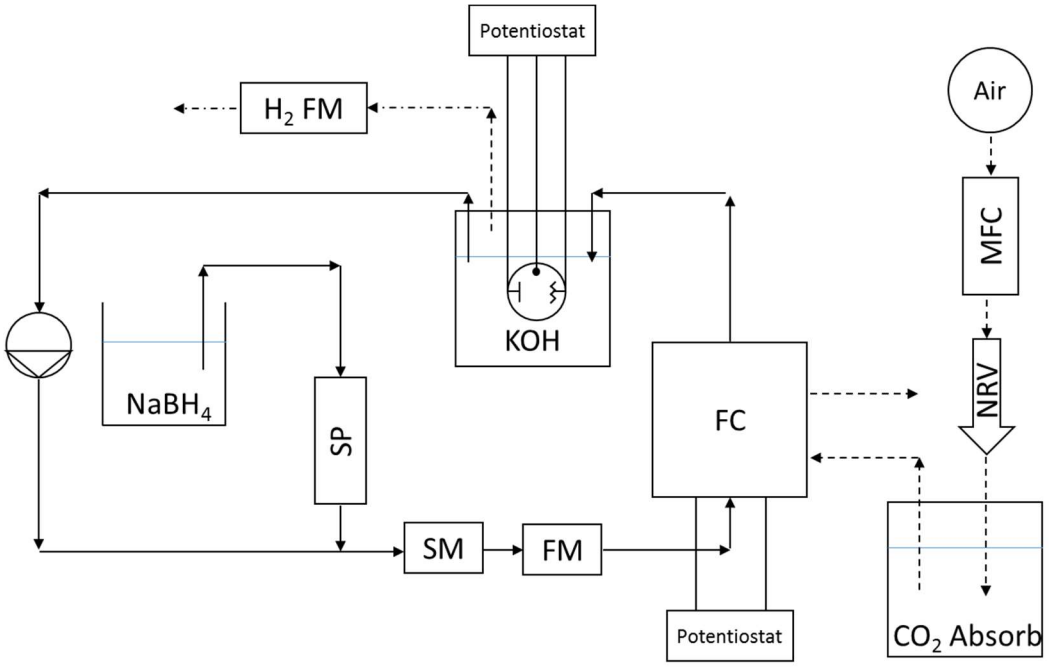

Figure 6.19 - System 3: Semi-recirculating electrolyte at high flowrates. FC = fuel cell, FM = flow meter, MFC = mass flow controller, NRV = non-return valve/check valve, SM = static mixer and SP = syringe pump.

System 3 introduced two important monitoring systems for (i) borohydride concentration, using the potentiostat see Section 6.2.2, and (ii) $H_{2(g)}$ using a flow meter connected to the fuel cell outlet. Using these measurements, an estimation to the fuel utilisation could be made. However, measuring these two properties was complicated and as such several configurations were designed and are reported in Section 6.3.9. Separating the $H_{2(g)}$ from the electrolyte proved difficult and so was developed from system to system. This is explained further in Section 6.3.9.

Although there are many benefits to the semi-recirculating system (see Section 6.1.4), not being able to measure the borohydride concentration leaving the fuel cell meant that it was impossible to determine whether the borohydride concentration was increasing in the carrier electrolyte after the fuel cell. Therefore, to ensure that there was a constant borohydride molar flow rate through the fuel cell during the entirety of all experiments a single pass was designed in place of the semi-recirculating.

6.3.4 System 4 – Single Pass Electrolyte at Low Flowrates

Developing a single pass system led to a large reduction in volumetric flow rate (5 $cm^3.min^{-1}$), thereby reducing the material waste observed in the semi-recirculating system. In place of the finite volume syringe was a fuel/electrolyte reservoir split across two vessels connected via a pump and overflow tube (Figure 6.20). The pump transported the fuel/electrolyte from the lower vessel up to the higher vessel. The higher vessel had two fuel/electrolyte outlets; one at the bottom which lead to the fuel cell and another larger one returning it into the lower vessel. As fuel/electrolyte leaves the top vessel to the fuel cell, the pump circulated the fuel/electrolyte around the two vessels ensuring that there was a constant head within the top vessel, so long as the pump volumetric flow rate was greater than that of the fuel cell outlet. The diameter of the overflow outlet and the pump volumetric flow rate was balanced so there is no deviation in the fuel/electrolyte head height. Another benefit of this system setup was the content pressure applied by the electrolyte due to a constant head height.

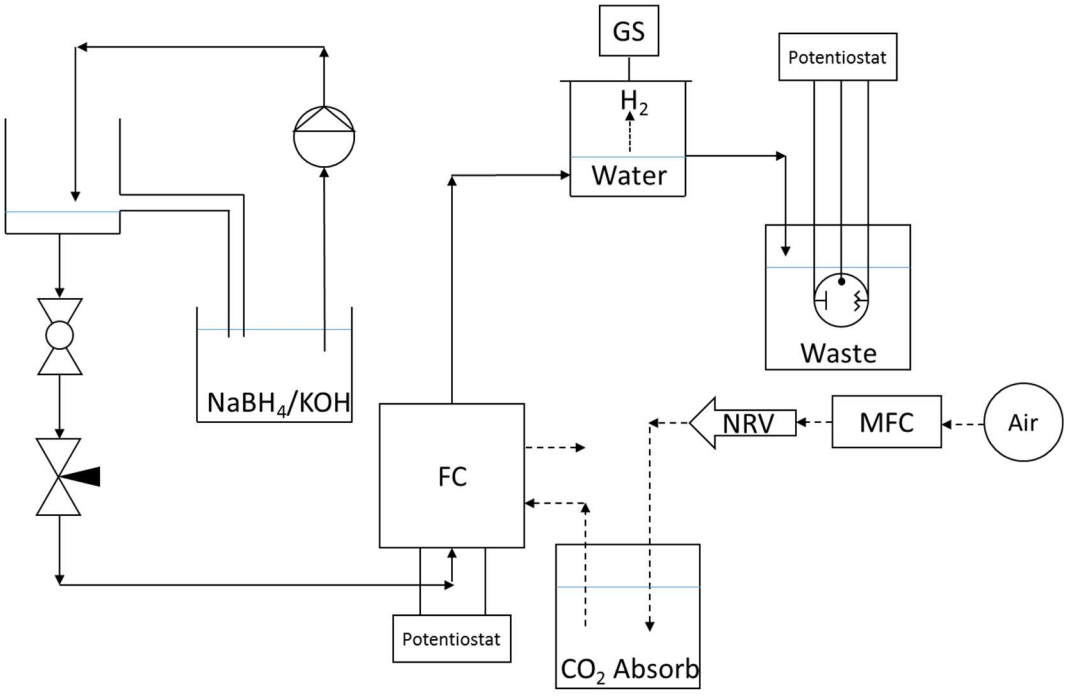

Figure 6.20 - System 4: single pass electrolyte at low flowrates. FC = fuel cell, FM = flow meter, MFC = mass flow controller, NRV = non-return valve/check valve and GS = gas syringe.

The fuel/electrolyte flow rate was controlled by a needle valve (Swagelok) which has a hand and a backboard divided into 360 °. This, along with calibrating the needle valve through flow rate experiments, allowed for more accurate flow rate adjustment. Furthermore, to ensure a

constant flow rate over various experiments a ball valve (Swagelok) was placed before the needle valve which was used to stop the fuel/electrolyte flow between experiments. By only opening and closing the ball valve and keeping the needle valve in the same position, the same flow rate between experiments was achieved.

6.3.5 System 5 – Single Pass with Coil Heater

The fuel/electrolyte tubing was extended, coiled and placed in a heated water bath, which allowed the fuel/electrolyte to reach the desired temperature. This also prevented issues of water evaporation and resulting concentration deviations that could occur in the system.

A humidity sensor (Omega Engineering, OM-EL-USB-2-PLUS) was added to the system at the air outlet of the fuel cell. This was used to monitor any increases in humidity, which may have arisen from the transport of water from the electrolyte through the GDL. Two thermocouples (TC Direct, 408-119) connected to a data logger (Thermosense Direct, HH-747UD) were used to determine the temperature of the electrolyte that of the fuel cell, the air outlet was scrubbed through a water bottle where a pH meter was used to detect any KOH leakage across the GDL (indicative of the formation of cracks) and an oxygen meter was also fitted to the scrubbing bottle to determine the oxygen content at the outlet of the fuel cell.

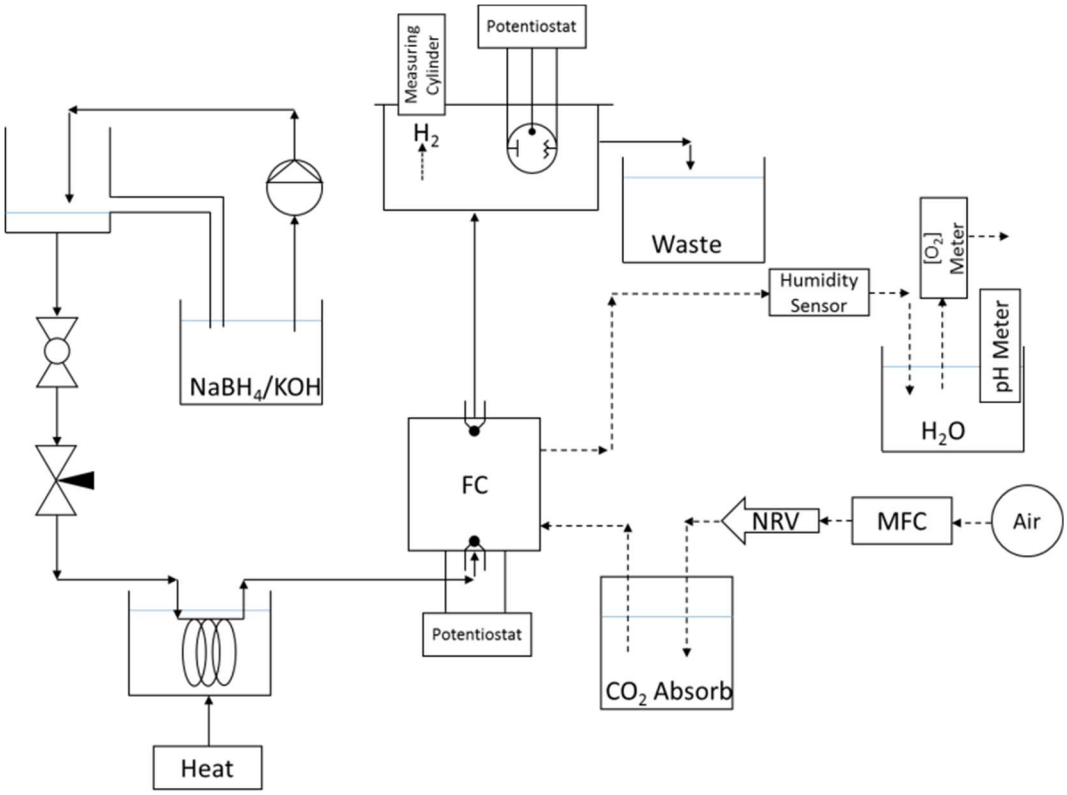

Figure 6.21 - System 5: single pass with coil heater. FC = fuel cell, FM = flow meter, MFC = mass flow controller and NRV = non-return valve/check valve.

Despite the greatly increased flow path between the valve and the fuel cell through the water bath, and the temperature of the bath close to 100 °C, the fuel/electrolyte did not get up to temperature due to the thermally insulating properties of the tubing.

The high borohydride concentration of the electrolyte would have normally expected to lead to the evolution of a large amount of hydrogen gas. In this case, the low volumetric flow rate led to a decrease in the in the molar flow rate through the fuel cell and consequentially a reduction in hydrogen evolution.

6.3.6 System 6 – Single Pass with Heating Column

To overcome the difficulties in bringing the fuel/electrolyte to the desired temperature, a new heating system was developed, which featured a heat exchanger made up of 3 Graham condensers connected in series. The fuel/electrolyte passed through the internal coil of the condensers while water from a heated water bath was circulated by means of a pump

(Superpak 607 MAX Bulk Fibre) through the external jacket in a counter-current configuration, the heated electrolyte at the desired temperature would then be allowed to flow to the fuel cell while the water was returned to the water bath (Figure 6.22).

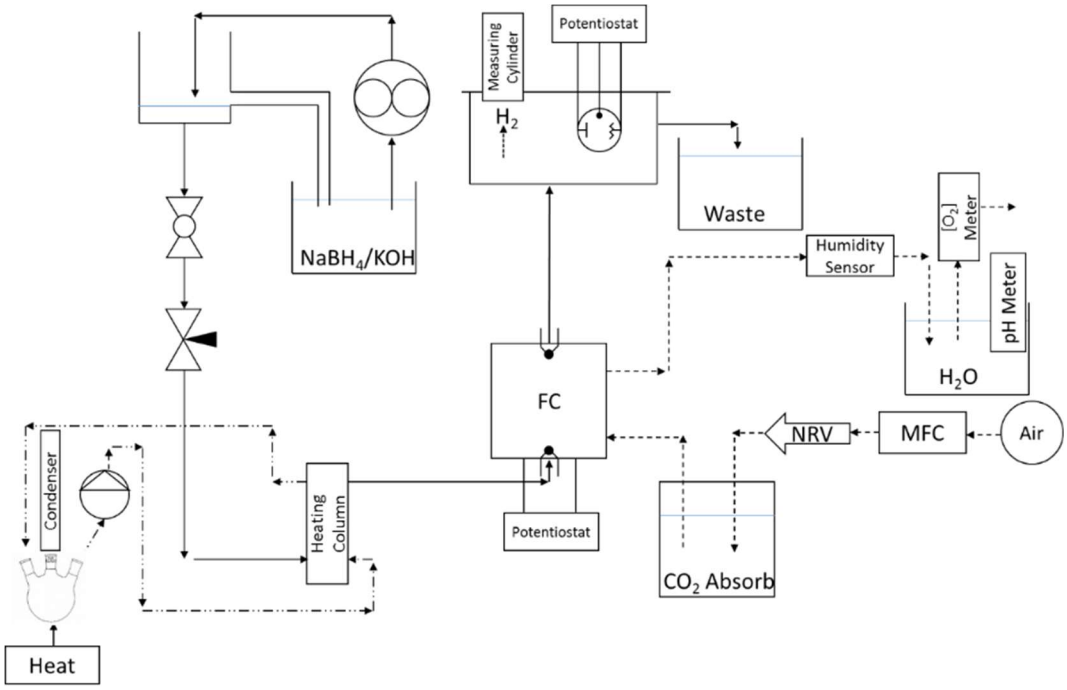

Figure 6.22 - System 6: single pass with heating column. FC = fuel cell, FM = flow meter, MFC = mass flow controller and NRV = non-return valve/check valve.

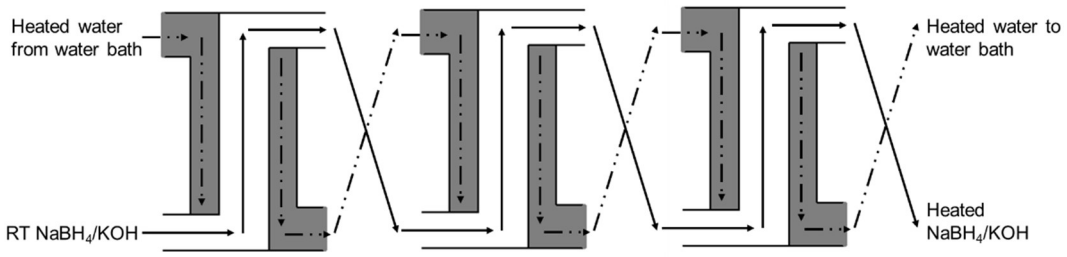

Figure 6.23 - the counter flow of heated water and fuel/electrolyte through the heating column.

Although this method allowed for increased temperatures to be reached compared to the heating coil in system 5 (Section 6.3.5), it was insufficient for the higher temperature of 70 °C. This problem could have been alleviated somewhat by increasing the temperature of the fuel/electrolyte prior to entering the heating column; however, doing so would have potentially led to issues mentioned in system 2 (Section 6.3.2), which included the evolution

of hydrogen gas and an increase in pressure. However, due to a large amount of hydrogen gas formed using system 2 it was believed that the fuel cell could not run at such an elevated temperature and so 50 °C would be adequate.

6.3.7 System 7 – Single Pass with Continuous Flow

One of the major limitation with system 6 was the lack of accuracy of the control of the flow rate afforded by the needle valves, despite the addition of the back plate, especially at very low volumetric flow rates. Furthermore, the needle valve was manufactured from stainless steel with poor corrosion resistance in caustic environments. In system 7, the overhead reservoir was replaced with two syringe pumps fitted with a 50 mL syringe (Norm-Ject Luer Lock) each. These were arranged in series with multiple NRVs (Bürkle, 8714-0060) allowing the electrolyte to be fed from a central fuel/electrolyte reservoir (Figure 6.24). The experiment was set up such that one of the syringe pumps fed the fuel/electrolyte through the NRV to the fuel cell. Concurrently, the second syringe pump would withdraw fuel/electrolyte from the central reservoir. After a set volume, the function of both syringes was reversed allowing for the experiment to run indefinitely as the central reservoir could be topped up when required, removing the limitations of fixed volumes and improving the accuracy at low flow over the needle valve setup.

The heating system described in System 6 (Section 6.3.6) was upgraded with additional flexible heating pads (RS Components, various sizes) between the insulation and the water reservoir, the fuel cell and heating column. The additional heating pads were used to increase the temperature of the water flowing through the heating column. Furthermore, the water bath was set to its maximum setting to get the fuel/electrolyte up to the desired temperature.

Although there were other low flow rate pumps which could have been used in place of a syringe pump without the volume limitations of a syringe pump, these had another issue which had to be taken into consideration. Other pumps such as peristaltic pumps deliver the liquid in “discrete pulses” due to the nature of the pump design. Should a pump like this be used, the fuel cell would receive the fuel/electrolyte in these discrete pulses with periods of time whereby no fuel/electrolyte. Although these durations without the fuel/electrolyte would be relatively short, at lower flow rates these durations are much longer. These longer durations

without fuel/electrolyte would not be long enough to cause any electrode starvation, but it would be long enough to cause fluctuations in current density and mechanical degradation which is undesirable.

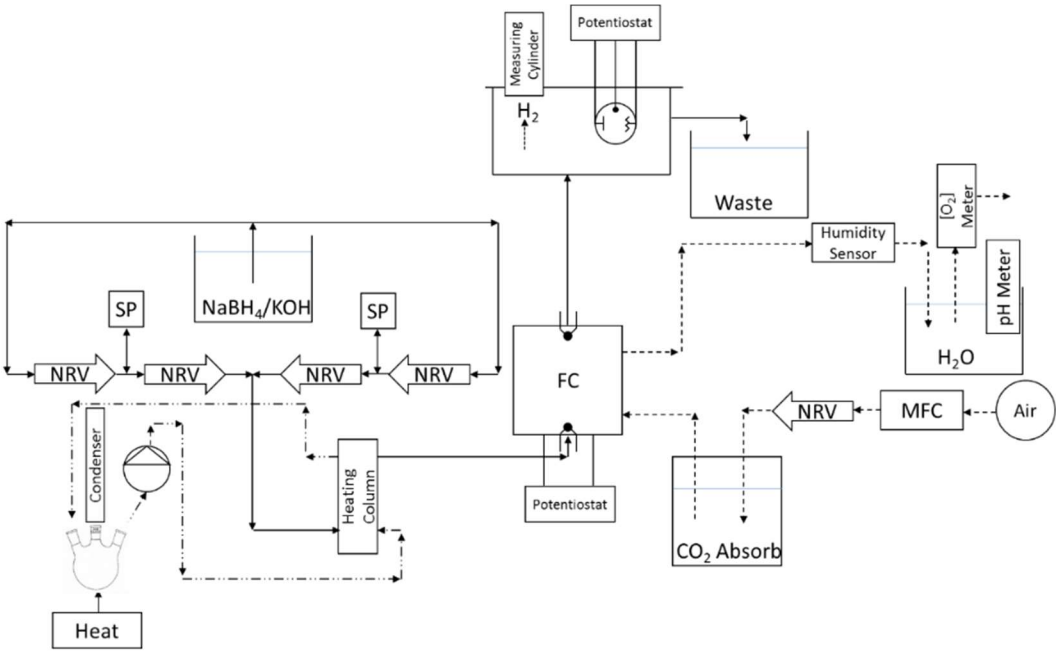

Figure 6.24 - System 7: single pass with continuous flow. FC = fuel cell, FM = flow meter, MFC = mass flow controller, SP = syringe pump and NRV = non-return valve/check valve.

Using the above setup, the circulating water was heated to about 80 °C, causing the pump's current density to increase, leading to the pump cutting out due to the internal parts of the pump expanding causing an increase in torque. This limited the temperature that could be reached in the heating column and its efficiency.

6.3.8 System 8 – Single Pass in Incubator

To limit the production of hydrogen gas in the system, borohydride concentration was decreased, which also allowed the operating temperature to be increased, potentially improving performance. To alleviate the issues encountered in the other systems developed in this work, the fuel cell was placed inside a low temperature oven (Stuart, HB-1D Hybridisation Oven). A section of the back of the oven was cut out and replaced with a large cork bung which had a series of holes drilled through to thread various fluid and electrical connections into the oven (Figure 6.25).

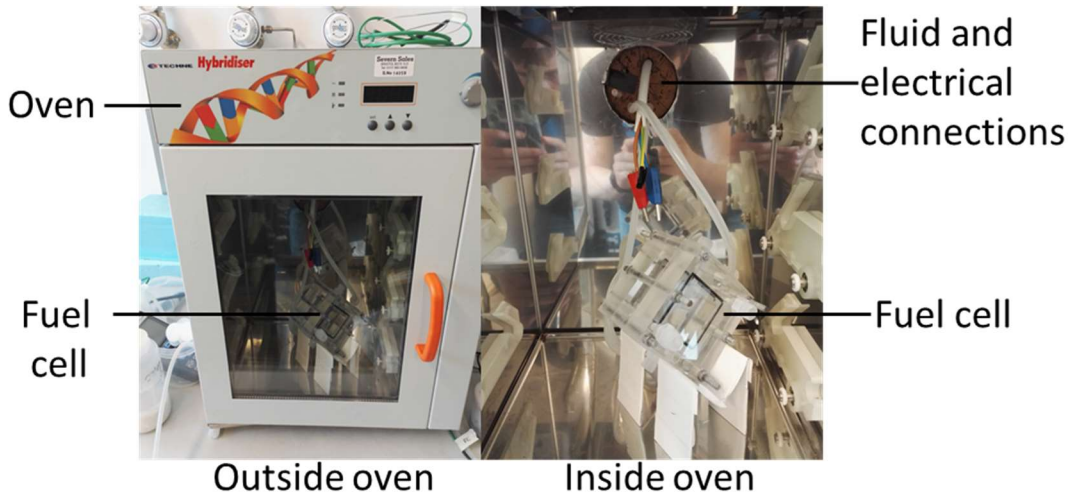

Figure 6.25 - A photo of the adapted oven (left) and the fuel cell inside (right).

The coil heat exchanger used in System 5, was further developed by replacing the plastic tubing with a corrosion resistant high chromium stainless steel (904L, Swagelok), which improved the rate of heat transfer between the fuel/electrolyte and the water bath while preventing the leaching of iron from other stainless steels. The coil (2 m long and 3 mm diameter), was coiled and bent to fit into the water bath (Figure 6.26). Additional thermocouples were fitted to the system to monitor the temperatures of the water bath, the fuel/electrolyte entering the fuel cell, the fuel cell and the oven (Figure 6.27). The fuel cell was placed in the oven prior to starting the experiment to allow it to reach the desired temperature.

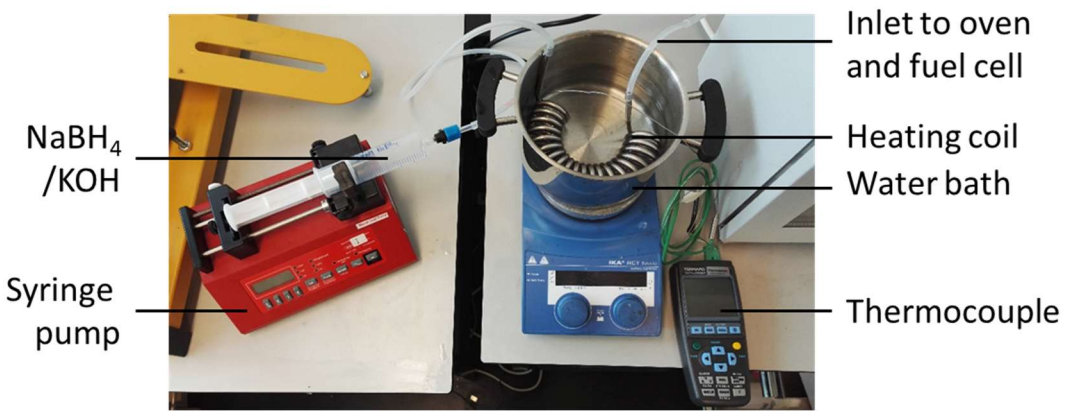

Figure 6.26 - The fuel/electrolyte flow path from the syringe pump, through the heating coil to the oven. A thermocouple in the water bath monitors steady state.

It was thought that the air entering the fuel cell, which enters at room temperature, could reduce the temperature of the fuel cell beyond that of which is desired. To test this hypothesis, the heating coil was submerged in 80 °C water and connected to a thermocouple and compressed air. The air was passed through the heating coil at volumetric flow rates equal to that of what would be used (0.4 $L.min^{-1}$) and the temperature of the air at the outlet was measured. During the experiment, the temperature of the air increased by only one degree compared to its temperature entering the coil. Although there are air heat exchangers which can be bought to increase the temperature of the air, it was concluded that the since there was only an increase in air temperature by a single degree it was unlikely to have a significant effect on the temperature of the fuel cell.

The performance of the electrodes was mostly investigated using system 8 due to its flexibility, although the oxygen meter, pH meter, hydrogen/electrolyte separator and borohydride concentration monitoring could not be implemented with this system (see Section 6.5).

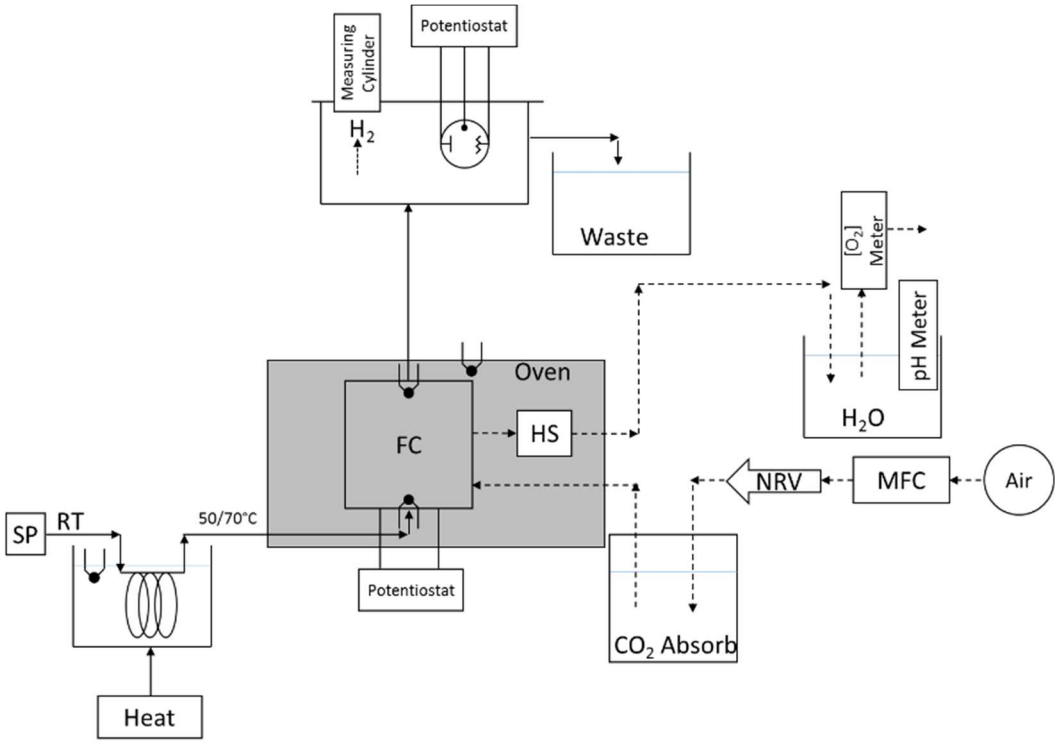

Figure 6.27 - System 8: single pass in the oven.

6.3.9 Borohydride and Hydrogen Separation Unit

Separating the spent fuel/electrolyte and the hydrogen gas, which had been evolved during the experiment, allowed for the measurement of the borohydride and hydrogen leaving the fuel cell. However, separating these two phases proved to be difficult. This section summaries the methods developed to achieve this.

6.3.9.1 *Separation Unit 1 – Measuring Total Hydrogen and Borohydride Measurement*

The initial setup used a vessel with an electrolyte/hydrogen inlet on the side, an upturned measuring cylinder was used to collect and measure the amount of hydrogen generated and a potentiostat was used to measure the concentration of borohydride (Figure 6.28).

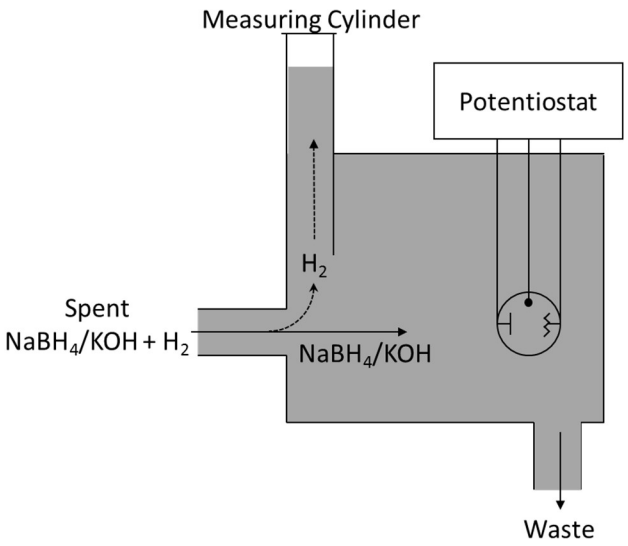

Figure 6.28 - Separation unit 1.

The unit measured the accumulated hydrogen at the end of an experiment which was allowed for the average flow rate to be determined, and consequently the borohydride decomposition percentage (see Section 6.1.6). However, the vessel had to be filled with liquid prior to the start of the experiment, resulting in a dilution of the borohydride leaving the fuel cell to a low concentration of 0.1 - 10 mM $NaBH_4$ (see Section 6.2.2), difficult to measure accurately.

6.3.9.2 *Separation Unit 2 – Continuous Hydrogen and Borohydride Measurement*

A second separation unit was designed which contained a sealed vessel with an inlet for the electrolyte and an outlet for the hydrogen (Figure 6.29). The unit contained a small "buffer" reservoir with the gold electrode. The buffer would fill with a small volume of electrolyte, with the hydrogen leaving the vessel through an outlet at the top with an attached hydrogen flow meter. As the electrolyte left the fuel cell, the buffer would overflow, expelling excess electrolyte into the waste section of the vessel below. With this setup, the buffer reservoir allowed for a more accurate determination of borohydride concentration, without the need for adjustments due to dilution.

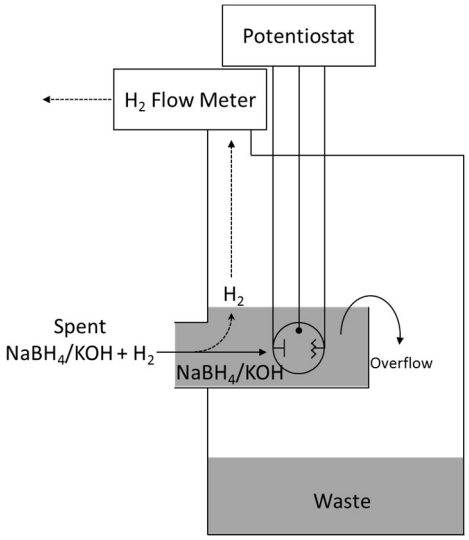

Figure 6.29 - Separation unit 2 introducing the "buffer" to separate the electrolyte and hydrogen gas.

Limitations of this design included the smaller, but non-negligible, dilution effect on the borohydride concentration while the volume of the buffer reservoir volume was being slowly replaced. In addition, the introduction of the electrolyte into the sealed vessel increased the pressure with consequently would increase the hydrogen velocity through the flow meter making the hydrogen flow measurement unreliable.

6.3.9.3 *Separation Unit 3 – Inline Separation and Continuous Measurement*

As a way of overcoming the drawbacks associated with unit 2, an inline unit placed at the outlet of the fuel cell was developed (Figure 6.30). The unit flow path was narrow and tall, allowing for easy phase separation. The electrolyte then travelled to the gold electrode, allowing for concentration measurements, and the hydrogen leaves through the hydrogen flow meter.

This inline method of phase separation and their subsequent measurement required an outlet with a variable diameter to control the volume within the separation unit. An open outlet would allow an escape route for the hydrogen, giving inaccurate results. Conversely, having a sealed vessel would give rise to issues similar to that of unit 2. Although it was possible for a fixed diameter outlet to sustain a constant volume in the unit, any deviations in volume created by the inconsistent evolution of hydrogen within the fuel cell could cause the

electrolyte to start moving towards the hydrogen flow meter. Therefore, a variable sized outlet would best suit this kind of separating unit.

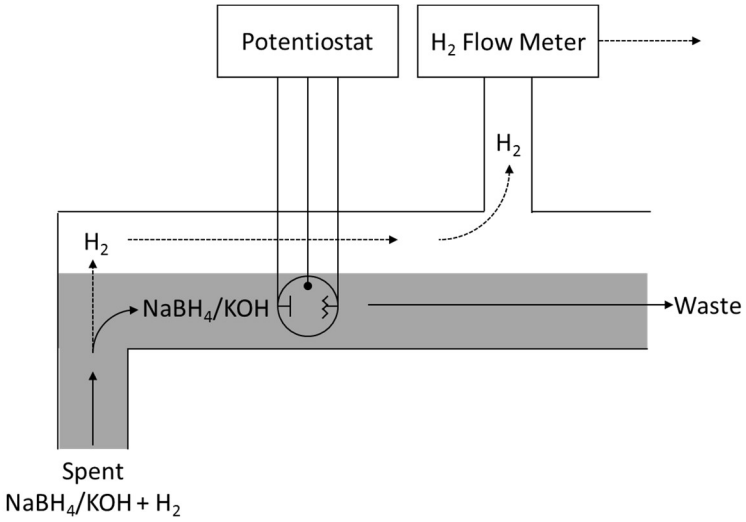

Figure 6.30 - Separation unit 3.

Unfortunately, this unit was not constructed or tested and so further development of the separating unit is required.

6.4 Conclusions and Discussion

This chapter describes the evolution of the design and implemented to test a DBAFC under a variety of conditions. A summary of the operating conditions is given in Table 6.4

Table 6.5 - Summary of the different systems showing the benefits compared to the previous system and challenges. while Table 6.5 summarises the advantages and drawbacks of each setup.

Table 6.4 - The change in operating conditions with the development of the system design.

System	[$NaBH_4$] (M)	$\dot{v}$ ($cm^3.min^{-1}$)	$NaBH_4$ $\dot{n}$ ($mol.min^{-1}$)	Temp. (°C)
1	1	250	0.25	RT
2	1	250	0.25	70
3	1	250	0.25	RT

4	0.1	50	5.0E-03	RT
5	0.1	50	5.0E-03	50
6	0.1	50	5.0E-03	50
7	0.1	5	5.0E-04	50
8	0.038	5	1.9E-04	70

Table 6.5 - Summary of the different systems showing the benefits compared to the previous system and challenges.

System	Benefits	Challenges
1	• Fast removal of by-products.	• No temperature control.
2	• Can be used at increased temperatures.	• Large quantities of hydrogen generation.
3	• Potential reduction in hydrogen generation. • Monitoring of borohydride and hydrogen concentrations.	• The semi-circulating electrolyte can cause issues with respect to keeping a constant known borohydride concentration through the fuel cell. • High flow rates not possible with single pass due to material wastage.
4	• Slower flow rates. • Constant pressure. • Measurement of H_2 generation.	• No temperature control. • H_2 measurement difficult due to low pressure.
5	• Can be used at increased temperatures. • Measurement of air outlet humidity.	• The heating coil could not increase electrolyte to desired temperatures.
6	• Heating column used to increase electrolyte temperature.	• Heating coil could not increase electrolyte to desired temperatures. • Accurately setting electrolyte flow difficult due to the needle valve. • Needle valve material unstable in alkali conditions.
7	• Removal of unstable materials. • Allows for accurate low flow rates.	• Heating column unable to increase electrolyte temperature despite low flow rates.
8	• Corrosive resistant stainless steel coil used to increase electrolyte temperature.	• Heater was unable to bring air up to temperature.

	• Fuel cell placed in the oven to further control operating temperature. • Air heater added to the system to bring air up to the desired temperature.	

The systems designed in this chapter were focused on DBAFC testing compared to being specifically for continuous power (CP) or power on demand (PoD). The main difference was that the testing system had to be flexible in its ability to be used in a wide range of operating conditions, easy to customise, adapted if needed and contain a range of sensors so that the desired data can be generated in each experiment. Although systems designed for CP and PoD would require some flexibility and measurement of various system properties, it would not require as much as the optimised systems would have been fully developed prior to their use and only minor alterations to operating conditions would be required, i.e. flow rate. The number of data measurements may also be reduced as only certain system properties may only be classed as essential, i.e. system temperature and flow rate, whilst others provide additional information not required for the overall running of the system, i.e. humidity of exhaust oxidant which may give and an indication of the conditions at the electrode and any degradation. Furthermore, operating systems do not require customisability once the system has been optimised and additional monitoring system would increase cost without delivering additional value. The development of optimal CP and PoD systems was considered out of scope for this project; however, for DBAFC power outputs and applications a PoD system would be more suitable than for CP due to the power range being low compared to other types of fuel cells, see Figure 6.2, and their relatively low operating temperatures allow for fast startup.

System 8 offered the most versatility to the required fuel cell testing under a variety of conditions. It allowed for control over temperature, reductant and oxidant flow rates and orientations. Hydrogen gas production from borohydride hydrolysis leads to decreased electrical efficiencies and its accumulation within the fuel cell presents a safety risk [57]. Furthermore, gas generation makes it difficult to measure key system properties, such as borohydride concentration, and the system, therefore, required a separate liquid-gas phase separation unit to prevent hydrogen bubbles causing noise in the voltammogram or restricting access to the surface of the microelectrode. This design could have been improved by the

addition of an inline borohydride concentration monitoring method in the presence of hydrogen gas.

Hydrogen generation was a challenge for the development of the system, as it decreased the efficiency of the system. In addition, the liquid electrolyte could have become contaminated with carbon dioxide, leading to the production of potassium carbonate and sodium metaborate, as the borohydride oxidation by-product, both of which could have accumulated and reduced the system efficiency. As mentioned in background chapter, the production of carbonates is an important challenge for liquid flowing AFC, due to the increase in ionic resistance, and various methods could be employed to prevent and treat it. However, the effects of metaborate accumulation are not as fully understood. Long term stability experiments on DBAFC have not been conducted and the effects of metaborate on electrocatalyst poisoning and other fuel cell properties are not known and can only be determined through experimentation.

6.5 Future Work

Following the development of the fuel cell testing system, a suitable system was designed to test the fuel cell at a variety of conditions. Although this system setup was adequate for much of the testing, the system could be developed further. Figure 6.31 shows such a system, which builds on what has previously been developed.

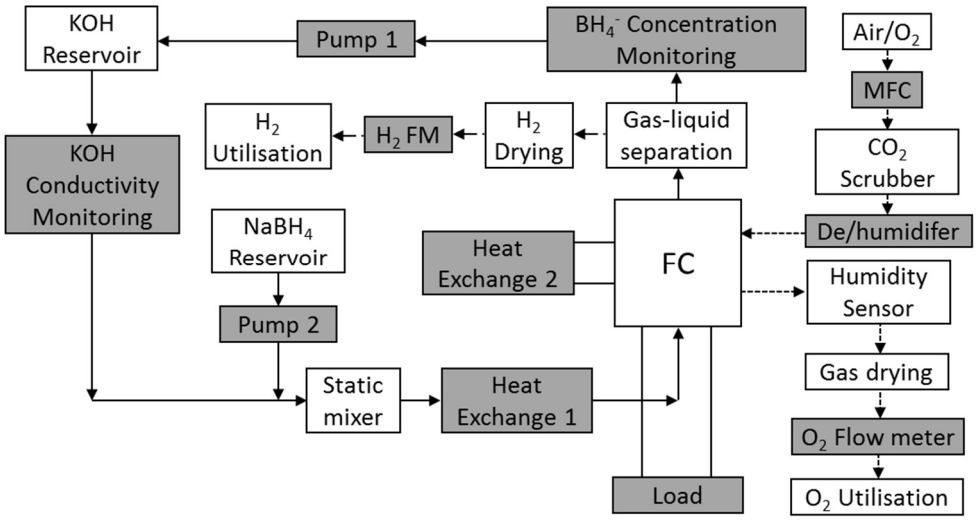

Figure 6.31 - An ideal semi-recirculating system for running a DBAFC/stack. Components in grey are connected to a PC and automated.

In addition to the features discussed for system 9, the system in Figure 6.31 includes the automation of several components. Two control systems are introduced to regulate the current generated using the data collected from the electronic load, a H_2 flow meter and borohydride concentration potentiostat using the fuel pump. When the system starts, a current is drawn from the fuel cell, leading to the utilisation of some of the borohydride. Any unoxidised borohydride leaving the fuel cell is recirculated, and its concentration is adjusted using pump 2. To ensure proper control of the fuel concentration, and reduce the likelihood of processing issues especially at increased temperatures, a feedback control measuring the borohydride concentration at the outlet of the fuel cell would be used to regulate the amount of borohydride injected from the reservoir to compensate for the unoxidised fuel in the electrolyte. Any changes in the concentration of borohydride leaving the fuel cell could be compensated for by altering the volumetric flow rate of the fuel reservoir pump and therefore changing the molar flow rate of borohydride.

Testing the fuel cell at increased temperature requires careful control over the thermocouple located at the electrolyte inlet. This information can be fed through the system to the heat exchanger to adjust the electrolyte temperature accordingly.

The system can also be fitted with a de/humidifier attached to the air line into the fuel cell. Air with a high volumetric flow rate or a low humidity can lead to the dehydration of the GDL which causes potassium hydroxide crystals to form and block the channels, reducing air flow through the GDL. Furthermore, potassium hydroxide crystals can grow between the GDL and the substrate causing the GDL to peel away. In both cases, this can lead to permanent damage to the GDL.

The ideal system would also contain a hydrogen and oxygen utilisation component. Hydrogen that is generated from any hydrolysis of borohydride could also be captured and used in another type of fuel cell, i.e. PEMFC.

7 Summary, Discussion and Future Work

7.1 Summary

Direct borohydride alkaline fuel cells offer a safer, more practical and potentially higher performing alternative to the more established low temperature fuel cells. Furthermore, the removal of the membrane allows for the elimination of a dedicated cooling system. However, despite their many benefits, DBAFC must be developed further if they are to be considered comparable to other fuel cells such as the complex BOR, with inefficient oxidation pathways and the generation of hydrogen. In this work, various aspects of the DBAFC were developed as a proof of concept, to outline any advantages, challenges and direction for future development.

The electrocatalyst is key to the efficiency of a fuel cell, especially so for a DBAFC as the electrocatalyst needs to be specific to the direct oxidation pathway. Furthermore, as the cathode is in the presence of both fuel and oxidant, it must have an affinity to the ORR only, as oxidising the borohydride would result in inefficiencies. The Ru on activated C had the highest performance out of the electrocatalysts evaluated, with acceptable kinetics and current densities. When developed into a multi-layered screen printable anode, it outperformed a commercially available electrode. A novel screen printed cathode was developed using a commercially used spinel electrocatalyst. Despite the cathode formulation resulting in defects on the electrode surface during printing, the electrode was repairable during the subsequent lamination step, producing an electrode which could be used for DBAFCs.

To determine the performance of the electrodes under various operating conditions, a fuel cell stack and system was designed. The stack was specifically designed for a membraneless-DBAFC, allowing the flow of electrolyte and reductant whilst reducing the ionic leakage without sacrificing performance. Both computational simulation and experimentation were used to validate the electrolyte and air plates to optimise fluid flow. A combination of screen printing electrodes and the use of efficient and lightweight materials produced a light weight cell suitable for mobile applications. Finally, the fuel cell stack was incorporated into a flexible testing system which allowed the monitoring of hydrogen evolution, air humidity and pH

changes over a wide temperature and flow rate range during experimentation. Various system designs, including circulating, semi-circulating and single pass systems, were evaluated for the use with a membraneless-DBAFC to determine the optimum system to use for fuel cell evaluation and operation under a variety of conditions, with the single pass system being favoured due to its ability to remove oxidation by-products and consistent concentration during experimentation.

7.2 Discussion

Membraneless-DBAFCs have many advantages over other low temperature fuel cells, including AFCs and PEMFCs; however, there are several challenges which need to be overcome, principally with the electrocatalysts. In addition to the desired properties, including increased stability and performance, the anode electrocatalyst must be specific to the direct oxidation of borohydride. Furthermore, the cathode must be specific in the presence of both fuel and oxidant to prevent an effective short-circuit. Producing an electrocatalyst which is specific to a particular reaction makes its development more complex compared to other fuel cell types. Hydrogen evolution as a product of indirect borohydride oxidation, may still be recycled within the system to another type of fuel cell to ensure good overall system efficiency.

Screen printed electrodes were evaluated and produced relatively low current densities compared to the literature, despite outperforming the commercial anode, the electrodes developed here were suitable as a base formulation. From this, the anode and cathode ink formulae could be developed further into more effective electrodes as a method for electrode mass production.

Arguably, the most important parameter in the use of membraneless-DBAFCs as an energy generating device is the availability of borohydride fuel. Many fuel cells use hydrogen or other natural gasses which have been studied extensively and multiple renewable methods for fuel generation are available. Ultimately, borohydride is produced from borax ore which, although is naturally occurring and abundant, is not renewable. Due to borohydride's use as a hydrogen storage material for other types of fuel cells, studies on recycling metaborate (the borohydride oxidation product) using electrochemical methods have been conducted. Using these

electrochemical methods, using electricity produced by renewable sources can offer a renewable and clean method of borohydride generation.

7.3 Future Work

The primary focus of further work regarding DBAFCs would involve the continuation of the identification and development of a suitable electrocatalyst. This is the most complex area of DBAFC development and constitutes a “bottleneck” to this research. Identifying an electrocatalyst which has a good kinetics and a high affinity would generate increased power outputs which would suppress the evolved hydrogen gas challenged of the BOR. The Ru based electrocatalysts performed well in this work which would warrant further investigation; however, the literature highlighted other materials which appeared to have a better performance, with respect to power density. Other areas of future work include the development of a suitable manufacturing method, stack and system design are also of importance but with more limited impact.

Regarding long term future work, there are three key areas; increasing fuel cell performance, developing renewable/green energy sources and the energy infrastructure. Although integrating the fuel cell technology and its requirements into the current infrastructure, i.e. replacing car engines with fuel cells and having borohydride accessible to replace spent fuel, and determining a suitable method to recover the spent fuel would be difficult, the development of the fuel cell itself would arguably be the most challenging. Increasing fuel cell performance for specific applications whilst reducing the cost to make the technology commercially viable is a massive challenge which continues to drive research focus. Although other technologies, such as high efficiency solar cells coupled with high energy density batteries, may in the future be the ultimate goal in green renewable energy, the performance isn’t currently sufficient. There requires an intermediate technology, one which can reduce our impact on the environment now, but possibly not as much as future technologies. Therefore, out of the key areas mentioned it is the fuel cell development which requires more attention. Once a suitable fuel cell has been developed, researching renewable sources for the fuels and integrating the solution current infrastructure should follow.

The membraneless-DBAFCs are suitable for many low temperature applications, including portable electronics. Implementation will require further research into DBAFC and borohydride recycling. This may increase interest in the technology.

8 References

[1] B. Group, 2014, BP Statistical Review of World Energy June 2014, http://www.bp.com/content/dam/bp-country/de_de/PDFs/brochures/BP-statistical-review-of-world-energy-2014-full-report.pdf, 20 Dec 2016: 20 Dec 2016

[2] D.o.E.a.S.A. United Nations, Population Division 2015, World Population Prospects The 2015 Revision: Key Findings and Advance Tables https://esa.un.org/unpd/wpp/publications/files/key_findings_wpp_2015.pdf,

[3] Chapter 2 Hydrogen from Fossil Fuels and Biomass, in: Hydrogen Energy: Challenges and Prospects, The Royal Society of Chemistry, 2008, pp. 34-66.

[4] D.J. Wuebbles, A.K. Jain, Fuel Processing Technology, 71 (2001) 99-119.

[5] S.A. Abbasi, N. Abbasi, Applied Energy, 65 (2000) 121-144.

[6] S. Speidel, T. Bräunl, Renewable and Sustainable Energy Reviews, 60 (2016) 1213-1224.

[7] J.-M. Tarascon, Key challenges in future Li-battery research, 2010.

[8] Y. Lin, S. Tanaka, Appl Microbiol Biotechnol, 69 (2006) 627-642.

[9] J.D. Holladay, J. Hu, D.L. King, Y. Wang, Catalysis Today, 139 (2009) 244-260.

[10] L. Zhou, Renewable and Sustainable Energy Reviews, 9 (2005) 395-408.

[11] J.L. Tirado, Materials Science and Engineering: R: Reports, 40 (2003) 103-136.

[12] J. Van Mierlo, G. Maggetto, Fuel Cells, 7 (2007) 165-173.

[13] U. Lucia, Renewable and Sustainable Energy Reviews, 30 (2014) 164-169.

[14] J.M. Andújar, F. Segura, Renewable and Sustainable Energy Reviews, 13 (2009) 2309-2322.

[15] M. Warshay, P.R. Prokopius, Journal of Power Sources, 29 (1990) 193-200.

[16] J. Larminie, A. Dicks, in, John Wiley & Sons, 2000, pp. 308.

[17] D.G. Epp, R.M. Baumert, 2000, Integrated fuel cell electric power generation system for submarine applications, US 6063515 A, Ballard Power Systems Inc.

[18] A. Psoma, G. Sattler, Journal of Power Sources, 106 (2002) 381-383.

[19] Fuel Cells Bulletin, 2015 (2015) 2.

[20] Fuel Cells Bulletin, 2014 (2014) 2.

[21] B.C.H. Steele, A. Heinzel, Nature, 414 (2001) 7.

[22] A. Folkesson, C. Andersson, P. Alvfors, M. Alaküla, L. Overgaard, Journal of Power Sources, 118 (2003) 349-357.

[23] N.Q. Minh, Solid State Ionics, 174 (2004) 271-277.

[24] M.L. Perry, T.F. Fuller, Journal of The Electrochemical Society, 149 (2002) S59-S67.

[25] F.T. Bacon, Electrochimica Acta, 14 (1969) 569-585.

[26] S. Barrett, Fuel Cells Bulletin, 2015 (2015) 12-15.
[27] X. Li, G. Liu, B.N. Popov, Journal of Power Sources, 195 (2010) 6373-6378.
[28] X. Li, B.N. Popov, T. Kawahara, H. Yanagi, Journal of Power Sources, 196 (2011) 1717-1722.
[29] I. Kruusenberg, L. Matisen, Q. Shah, A.M. Kannan, K. Tammeveski, International Journal of Hydrogen Energy, 37 (2012) 4406-4412.
[30] R.J. Gilliam, J.W. Graydon, D.W. Kirk, S.J. Thorpe, International Journal of Hydrogen Energy, 32 (2007) 359-364.
[31] M.A. Al-Saleh, S. Gültekin, A.S. Al-Zakri, H. Celiker, J Appl Electrochem, 24 (1994) 575-580.
[32] I. Verhaert, S. Verhelst, G. Janssen, G. Mulder, M. De Paepe, International Journal of Hydrogen Energy, 36 (2011) 11011-11024.
[33] G.F. McLean, T. Niet, S. Prince-Richard, N. Djilali, International Journal of Hydrogen Energy, 27 (2002) 507-526.
[34] S.A. Mousavi Shaegh, N.-T. Nguyen, S.H. Chan, International Journal of Hydrogen Energy, 36 (2011) 5675-5694.
[35] M. Ji, Z. Wei, Energies, 2 (2009) 1057.
[36] G. Merle, M. Wessling, K. Nijmeijer, Journal of Membrane Science, 377 (2011) 1-35.
[37] J.R. Varcoe, R.C.T. Slade, Fuel Cells, 5 (2005) 187-200.
[38] T.Q. Hua, R.K. Ahluwalia, J.K. Peng, M. Kromer, S. Lasher, K. McKenney, K. Law, J. Sinha, International Journal of Hydrogen Energy, 36 (2011) 3037-3049.
[39] E.H. Yu, X. Wang, U. Krewer, L. Li, K. Scott, Energy & Environmental Science, 5 (2012) 5668-5680.
[40] J.M. Ogden, M.M. Steinbugler, T.G. Kreutz, Journal of Power Sources, 79 (1999) 143-168.
[41] P.S. Nigam, A. Singh, Progress in Energy and Combustion Science, 37 (2011) 52-68.
[42] E. Herrero, W. Chrzanowski, A. Wieckowski, The Journal of Physical Chemistry, 99 (1995) 10423-10424.
[43] M.H. Haider, N.F. Dummer, D.W. Knight, R.L. Jenkins, M. Howard, J. Moulijn, S.H. Taylor, G.J. Hutchings, Nat Chem, 7 (2015) 1028-1032.
[44] C.N. Hamelinck, A.P.C. Faaij, Journal of Power Sources, 111 (2002) 1-22.
[45] B.S. Dien, M.A. Cotta, T.W. Jeffries, Appl Microbiol Biotechnol, 63 (2003) 258-266.
[46] S.Y. Shen, T.S. Zhao, J.B. Xu, International Journal of Hydrogen Energy, 35 (2010) 12911-12917.
[47] Y. Kojima, T. Haga, International Journal of Hydrogen Energy, 28 (2003) 989-993.
[48] S.-C. Li, F.-C. Wang, International Journal of Hydrogen Energy, 41 (2016) 3038-3051.

[49] T. Kim, Energy, 69 (2014) 721-727.
[50] A. Chinnappan, J.M.C. Puguan, W.-J. Chung, H. Kim, Journal of Power Sources, 293 (2015) 429-436.
[51] Y. Chen, Y. Shi, X. Liu, Y. Zhang, Fuel, 140 (2015) 685-692.
[52] D. Schubert, D. Neiner, M. Bowden, S. Whittemore, J. Holladay, Z. Huang, T. Autrey, Journal of Alloys and Compounds, 645, Supplement 1 (2015) S196-S199.
[53] D.M.F. Santos, C.A.C. Sequeira, Renewable and Sustainable Energy Reviews, 15 (2011) 3980-4001.
[54] H.I. Schlesinger, H.C. Brown, A.E. Finholt, Journal of the American Chemical Society, 75 (1953) 205-209.
[55] A. Mergen, M.H. Demirhan, M. Bilen, Advanced Powder Technology, 14 (2003) 279-293.
[56] H.I. Schlesinger, H.C. Brown, A.E. Finholt, J.R. Gilbreath, H.R. Hoekstra, E.K. Hyde, Journal of the American Chemical Society, 75 (1953) 215-219.
[57] G. Rostamikia, M.J. Janik, Energy & Environmental Science, 3 (2010) 1262-1274.
[58] C. Coutanceau*, S. Baranton, M. Simoes, Chapter 5 Nanocatalysts for Direct Borohydride Oxidation in Alkaline Media, in: Catalysts for Alcohol-Fuelled Direct Oxidation Fuel Cells, The Royal Society of Chemistry, 2012, pp. 158-205.
[59] E.H. Park, S. Uk Jeong, U. Ho Jung, S.H. Kim, J. Lee, S. Woo Nam, T. Hoon Lim, Y. Jun Park, Y. Ho Yu, International Journal of Hydrogen Energy, 32 (2007) 2982-2987.
[60] Z.P. Li, B.H. Liu, K. Arai, N. Morigazaki, S. Suda, Journal of Alloys and Compounds, 356–357 (2003) 469-474.
[61] A.E. Sanli, İ. Kayacan, B.Z. Uysal, M.L. Aksu, Journal of Power Sources, 195 (2010) 2604-2607.
[62] A. Kantürk Figen, S. Pişkin, International Journal of Hydrogen Energy, 38 (2013) 3702-3709.
[63] S. Park, J.M. Vohs, R.J. Gorte, Nature, 404 (2000) 265-267.
[64] O.Z. Sharaf, M.F. Orhan, Renewable and Sustainable Energy Reviews, 32 (2014) 810-853.
[65] A.L. Dicks, Current Opinion in Solid State and Materials Science, 8 (2004) 379-383.
[66] B. Timurkutluk, C. Timurkutluk, M.D. Mat, Y. Kaplan, Renewable and Sustainable Energy Reviews, 56 (2016) 1101-1121.
[67] J.K. Nørskov, J. Rossmeisl, A. Logadottir, L. Lindqvist, J.R. Kitchin, T. Bligaard, H. Jónsson, The Journal of Physical Chemistry B, 108 (2004) 17886-17892.
[68] C. Lamy, A. Lima, V. LeRhun, F. Delime, C. Coutanceau, J.-M. Léger, Journal of Power Sources, 105 (2002) 283-296.

[69] Z. Fu, Q.M. Huang, X.D. Xiang, Y.L. Lin, W. Wu, S.J. Hu, W.S. Li, International Journal of Hydrogen Energy, 37 (2012) 4704-4709.
[70] F. Bidault, D.J.L. Brett, P.H. Middleton, N.P. Brandon, Journal of Power Sources, 187 (2009) 39-48.
[71] E. Antolini, E.R. Gonzalez, Journal of Power Sources, 195 (2010) 3431-3450.
[72] Y. Wang, G. Li, J. Jin, S. Yang, International Journal of Hydrogen Energy, 42 (2017) 5938-5947.
[73] P.-Y. Olu, N. Job, M. Chatenet, Journal of Power Sources, 327 (2016) 235-257.
[74] N.A. Choudhury, J. Ma, Y. Sahai, Journal of Power Sources, 210 (2012) 358-365.
[75] X. Yang, Y. Liu, S. Li, X. Wei, L. Wang, Y. Chen, Scientific Reports, 2 (2012) 567.
[76] C.-C. Huang, Y.-L. Liu, W.-H. Pan, C.-M. Chang, C.-M. Shih, H.-Y. Chu, C.-H. Chien, C.-H. Juan, S.J. Lue, Journal of Polymer Science Part B: Polymer Physics, 51 (2013) 1779-1789.
[77] H. Qin, S. Lao, Z. Liu, J. Zhu, Z. Li, International Journal of Hydrogen Energy, 35 (2010) 1872-1878.
[78] D. Cao, D. Chen, J. Lan, G. Wang, Journal of Power Sources, 190 (2009) 346-350.
[79] H. Liu, C. Song, L. Zhang, J. Zhang, H. Wang, D.P. Wilkinson, Journal of Power Sources, 155 (2006) 95-110.
[80] B. Šljukić, J. Milikić, D.M.F. Santos, C.A.C. Sequeira, Electrochimica Acta, 107 (2013) 577-583.
[81] N.A. Karim, S.K. Kamarudin, Applied Energy, 103 (2013) 212-220.
[82] G.Q. Sun, J.T. Wang, R.F. Savinell, J Appl Electrochem, 28 (1998) 1087-1093.
[83] M.A. Thorseth, C.E. Tornow, E.C.M. Tse, A.A. Gewirth, Coordination Chemistry Reviews, 257 (2013) 130-139.
[84] J. Ma, J. Wang, Y. Liu, Journal of Power Sources, 172 (2007) 220-224.
[85] A. Hamnett, Catalysis Today, 38 (1997) 445-457.
[86] C.W.B. Bezerra, L. Zhang, K. Lee, H. Liu, A.L.B. Marques, E.P. Marques, H. Wang, J. Zhang, Electrochimica Acta, 53 (2008) 4937-4951.
[87] C. Xu, Z. Tian, P. Shen, S.P. Jiang, Electrochimica Acta, 53 (2008) 2610-2618.
[88] A. Verma, A.K. Jha, S. Basu, Journal of Power Sources, 141 (2005) 30-34.
[89] L. Mao, Sotomura, T., Nakatsu, K., Koshiba, N., Zhang, D. and Ohsaka, T., Journal of Then Electrochemical Society, 149 (2002) A504-A507.
[90] P.V. Samant, J.B. Fernandes, Journal of Power Sources, 79 (1999) 114-118.
[91] C.S. Johnson, D.W. Dees, M.F. Mansuetto, M.M. Thackeray, D.R. Vissers, D. Argyriou, C.K. Loong, L. Christensen, Journal of Power Sources, 68 (1997) 570-577.
[92] C. Xu, P.K. Shen, Chemical Communications, 0 (2004) 2238-2239.

[93] P.K. Shen, C. Xu, Electrochemistry Communications, 8 (2006) 184-188.
[94] X. Wei, X. Yang, S. Li, Y. Chen, Y. Liu, Electrochimica Acta, 56 (2011) 7523-7529.
[95] J.a.O. Bockris, T., Journal of The Electrochemical Society, 131 (1984) 290-302.
[96] K. Miyazaki, N. Sugimura, K. Matsuoka, Y. Iriyama, T. Abe, M. Matsuoka, Z. Ogumi, Journal of Power Sources, 178 (2008) 683-686.
[97] V. Hermann, D. Dutriat, S. Müller, C. Comninellis, Electrochimica Acta, 46 (2000) 365-372.
[98] M. Lo Faro, M. Minutoli, G. Monforte, V. Antonucci, A.S. Aricò, Biomass and Bioenergy, 35 (2011) 1075-1084.
[99] T. Nissinen, T. Valo, M. Gasik, J. Rantanen, M. Lampinen, Journal of Power Sources, 106 (2002) 109-115.
[100] E. Rios, J.L. Gautier, G. Poillerat, P. Chartier, Electrochimica Acta, 44 (1998) 1491-1497.
[101] H. Liu, X. Zhu, M. Cheng, Y. Cong, W. Yang, International Journal of Hydrogen Energy, 38 (2013) 1052-1057.
[102] F. Deng, Q. Zheng, Acta Mechanica Solida Sinica, 22 (2009) 1-17.
[103] K. Gong, F. Du, Z. Xia, M. Durstock, L. Dai, Science, 323 (2009) 760-764.
[104] S. Liu, H. Zhang, Z. Xu, H. Zhong, H. Jin, International Journal of Hydrogen Energy, 37 (2012) 19065-19072.
[105] P. Ayala, R. Arenal, M. Rümmeli, A. Rubio, T. Pichler, Carbon, 48 (2010) 575-586.
[106] T.C. Nagaiah, S. Kundu, M. Bron, M. Muhler, W. Schuhmann, Electrochemistry Communications, 12 (2010) 338-341.
[107] D. Ham, J. Lee, Energies, 2 (2009) 873-899.
[108] A. Serov, C. Kwak, Applied Catalysis B: Environmental, 90 (2009) 313-320.
[109] D.R. McIntyre, G.T. Burstein, A. Vossen, Journal of Power Sources, 107 (2002) 67-73.
[110] M. Nagai, M. Yoshida, H. Tominaga, Electrochimica Acta, 52 (2007) 5430-5436.
[111] H. Zhong, H. Zhang, G. Liu, Y. Liang, J. Hu, B. Yi, Electrochemistry Communications, 8 (2006) 707-712.
[112] H. Wu, W. Chen, Journal of the American Chemical Society, 133 (2011) 15236-15239.
[113] O.T.M. Musthafa, S. Sampath, Chemical Communications, 0 (2008) 67-69.
[114] K. Lee, L. Zhang, J. Zhang, Electrochemistry Communications, 9 (2007) 1704-1708.
[115] D. Cao, A. Wieckowski, J. Inukai, N. Alonso-Vante, Journal of The Electrochemical Society, 153 (2006) A869-A874.
[116] K. Lee, L. Zhang, J. Zhang, Journal of Power Sources, 165 (2007) 108-113.
[117] Y. Gochi-Ponce, G. Alonso-Nuñez, N. Alonso-Vante, Electrochemistry Communications, 8 (2006) 1487-1491.

[118] R.W. Reeve, P.A. Christensen, A. Hamnett, S.A. Haydock, S.C. Roy, Journal of The Electrochemical Society, 145 (1998) 3463-3471.
[119] B. Braunchweig, D. Hibbitts, M. Neurock, A. Wieckowski, Catalysis Today, 202 (2013) 197-209.
[120] Y. Zhao, X. Yang, J. Tian, F. Wang, L. Zhan, International Journal of Hydrogen Energy, 35 (2010) 3249-3257.
[121] M. Chatenet, M.B. Molina-Concha, N. El-Kissi, G. Parrour, J.P. Diard, Electrochimica Acta, 54 (2009) 4426-4435.
[122] A.J. Bard, L.R. Faulkner, Electrochemical Methods: Fundamentals and Applications, Wiley, 2000.
[123] R. Zhou, Y. Zheng, M. Jaroniec, S.-Z. Qiao, ACS Catalysis, 6 (2016) 4720-4728.
[124] S.-A. Sheppard, S. A. Campbell, J. R. Smith, G. W. Lloyd, F. C. Walsh, T. R. Ralph, Analyst, 123 (1998) 1923-1929.
[125] E. Gyenge, Electrochimica Acta, 49 (2004) 965-978.
[126] J.I. Martins, M.C. Nunes, R. Koch, L. Martins, M. Bazzaoui, Electrochimica Acta, 52 (2007) 6443-6449.
[127] F.G.B. San, O. Okur, K. Ç. İyigün, I.I. Gülsaç, E. Okumuş, in: 2013 3rd International Conference on Electric Power and Energy Conversion Systems, 2013, pp. 1-4.
[128] M. Martins, B. Šljukić, C.A.C. Sequeira, Ö. Metin, M. Erdem, T. Sener, D.M.F. Santos, International Journal of Hydrogen Energy, 41 (2016) 10914-10922.
[129] C. Grimmer, M. Grandi, R. Zacharias, B. Cermenek, H. Weber, C. Morais, T.W. Napporn, S. Weinberger, A. Schenk, V. Hacker, Applied Catalysis B: Environmental, 180 (2016) 614-621.
[130] M. Łukaszewski, M. Soszko, A. Czerwiński, Int. J. Electrochem. Sci, 11 (2016) 4442-4469.
[131] N. Duteanu, G. Vlachogiannopoulos, M.R. Shivhare, E.H. Yu, K. Scott, J Appl Electrochem, 37 (2007) 1085-1091.
[132] C. Grimmer, R. Zacharias, M. Grandi, B. Cermenek, A. Schenk, S. Weinberger, F.-A. Mautner, B. Bitschnau, V. Hacker, The Journal of Physical Chemistry C, 119 (2015) 23839-23844.
[133] F.A. de Bruijn, V.A.T. Dam, G.J.M. Janssen, Fuel Cells, 8 (2008) 3-22.
[134] M.R. Somalu, V. Yufit, N.P. Brandon, International Journal of Hydrogen Energy, 38 (2013) 9500-9510.
[135] D. Shou, Y. Tang, L. Ye, J. Fan, F. Ding, International Journal of Hydrogen Energy, 38 (2013) 10519-10526.
[136] L. Espinal, Porosity and Its Measurement, in: Characterization of Materials, John Wiley & Sons, Inc., 2002.

[137] O. Lanzi, U. Landau, Journal of The Electrochemical Society, 137 (1990) 585-593.
[138] N.A. Choudhury, Y. Sahai, R.G. Buchheit, Journal of The Electrochemical Society, 158 (2011) B712-B716.
[139] J. Ma, Y. Sahai, R.G. Buchheit, Journal of Power Sources, 202 (2012) 18-27.
[140] J. Ma, N.A. Choudhury, Y. Sahai, R.G. Buchheit, Journal of Power Sources, 196 (2011) 8257-8264.
[141] M.R. Somalu, V. Yufit, I.P. Shapiro, P. Xiao, N.P. Brandon, International Journal of Hydrogen Energy, 38 (2013) 6789-6801.
[142] M.R. Somalu, N.P. Brandon, Journal of the American Ceramic Society, 95 (2012) 1220-1228.
[143] J.H. Sung, J.Y. Lee, S. Kim, J. Suh, J. Kim, K.H. Ahn, S.J. Lee, Journal of Materials Science, 45 (2010) 2466-2473.
[144] J. Piao, K. Sun, N. Zhang, S. Xu, Journal of Power Sources, 175 (2008) 288-295.
[145] J.W. Phair, Journal of the American Ceramic Society, 91 (2008) 2130-2137.
[146] L. Nie, J. Liu, Y. Zhang, M. Liu, Journal of Power Sources, 196 (2011) 9975-9979.
[147] N. Rajalakshmi, K.S. Dhathathreyan, Chemical Engineering Journal, 129 (2007) 31-40.
[148] C.-H. Wan, C.-H. Lin, Journal of Power Sources, 186 (2009) 229-237.
[149] C.H. Hsu, C.C. Wan, Journal of Power Sources, 115 (2003) 268-273.
[150] R. Fernández, P. Ferreira-Aparicio, L. Daza, Journal of Power Sources, 151 (2005) 18-24.
[151] J. Kivisaari, J. Lamminen, M.J. Lampinen, M. Viitanen, Journal of Power Sources, 32 (1990) 233-241.
[152] E. De Geeter, M. Mangan, S. Spaepen, W. Stinissen, G. Vennekens, Journal of Power Sources, 80 (1999) 207-212.
[153] K. Bolwin, E. Gülzow, D. Bevers, W. Schnurnberger, Solid State Ionics, 77 (1995) 324-330.
[154] T. Bayer, H.C. Pham, K. Sasaki, S.M. Lyth, Journal of Power Sources, 327 (2016) 319-326.
[155] A.D. Taylor, E.Y. Kim, V.P. Humes, J. Kizuka, L.T. Thompson, Journal of Power Sources, 171 (2007) 101-106.
[156] V. Mehta, J.S. Cooper, Journal of Power Sources, 114 (2003) 32-53.
[157] J. Roller, R. Maric, K. Fatih, R. Neagu, 2015, Catalytic materials for fuel cell electrodes and method for their production, US 8993472 B2, National Research Council Of Canada
[158] T. Soboleva, X. Zhao, K. Malek, Z. Xie, T. Navessin, S. Holdcroft, ACS applied materials & interfaces, 2 (2010) 375-384.
[159] I.-S. Park, W. Li, A. Manthiram, Journal of Power Sources, 195 (2010) 7078-7082.

[160] H. Ito, Y. Heo, M. Ishida, A. Nakano, S. Someya, T. Munakata, Journal of Power Sources, 342 (2017) 393-404.
[161] S. Latorrata, R. Balzarotti, P. Gallo Stampino, C. Cristiani, G. Dotelli, M. Guilizzoni, Progress in Organic Coatings, 78 (2015) 517-525.
[162] S. Latorrata, P.G. Stampino, C. Cristiani, G. Dotelli, Fuel Cells, 15 (2015) 463-471.
[163] S. Latorrata, P.G. Stampino, E. Amici, R. Pelosato, C. Cristiani, G. Dotelli, Solid State Ionics, 216 (2012) 73-77.
[164] T.M. Sullivan, S. Middleman, Journal of Non-Newtonian Fluid Mechanics, 21 (1986) 13-38.
[165] J.W. Ihm, H. Ryu, J.S. Bae, W.K. Choo, D.K. Choi, Journal of Materials Science, 39 (2004) 4647-4649.
[166] A. Datz, B. Schricker, M. Waidhas, 2005, Gas diffusion electrode and method for its production, Siemens Aktiengesellschaft
[167] G. Velayutham, International Journal of Hydrogen Energy, 36 (2011) 14845-14850.
[168] C. Xia, F. Chen, M. Liu, Electrochemical and Solid-State Letters, 4 (2001) A52-A54.
[169] D. Rotureau, J.P. Viricelle, C. Pijolat, N. Caillol, M. Pijolat, Journal of the European Ceramic Society, 25 (2005) 2633-2636.
[170] Y.-G. Wang, Y.-Y. Xia, Electrochemistry Communications, 8 (2006) 1775-1778.
[171] J. Ma, Y. Liu, Y. Liu, Y. Yan, P. Zhang, Fuel Cells, 8 (2008) 394-398.
[172] F.G. Boyacı San, O. Okur, Ç. İyigün Karadağ, I. Isik-Gulsac, E. Okumuş, Energy, 71 (2014) 160-169.
[173] M.R. Somalu, A. Muchtar, W.R.W. Daud, N.P. Brandon, Renewable and Sustainable Energy Reviews.
[174] L. Giorgi, E. Antolini, A. Pozio, E. Passalacqua, Electrochimica Acta, 43 (1998) 3675-3680.
[175] H. Tawfik, Y. Hung, D. Mahajan, Journal of Power Sources, 163 (2007) 755-767.
[176] X. Li, I. Sabir, International Journal of Hydrogen Energy, 30 (2005) 359-371.
[177] R. Wlodarczyk, D. Zasada, S. Morel, A. Kacprzak, International Journal of Hydrogen Energy, 41 (2016) 17644-17651.
[178] A. Woodman, K. Jayne, E. Anderson, M.C. Kimble, in: AESF SUR FIN-PROCEEDINGS-, American Electroplaters and Surface Finishers Society Inc, 1999, pp. 717-726.
[179] H. Liu, P. Li, D. Juarez-Robles, K. Wang, A. Hernandez-Guerrero, Frontiers in Energy Research, 2 (2014).
[180] Y. Wang, S. Basu, C.-Y. Wang, Journal of Power Sources, 179 (2008) 603-617.

[181] C.K. Dyer, P.T. Moseley, Z. Ogumi, D.A.J. Rand, B. Scrosati, J. Garche, Encyclopedia of Electrochemical Power Sources, Elsevier Science, 2013.
[182] A. Hermann, T. Chaudhuri, P. Spagnol, International Journal of Hydrogen Energy, 30 (2005) 1297-1302.
[183] R. Taherian, Journal of Power Sources, 265 (2014) 370-390.
[184] J. Ma, N.A. Choudhury, Y. Sahai, Renewable and Sustainable Energy Reviews, 14 (2010) 183-199.
[185] N. Luo, G.H. Miley, J. Mather, R. Burton, G. Hawkins, E. Byrd, F. Holcomb, J. Rusek, Journal of Power Sources, 185 (2008) 356-362.
[186] C. Kim, K.-J. Kim, M.Y. Ha, Journal of Power Sources, 180 (2008) 114-121.
[187] C.G. Arges, V. Ramani, P.N. Pintauro, Electrochemical Society Interface, (2010) 31.
[188] J.R. Varcoe, P. Atanassov, D.R. Dekel, A.M. Herring, M.A. Hickner, P.A. Kohl, A.R. Kucernak, W.E. Mustain, K. Nijmeijer, K. Scott, T. Xu, L. Zhuang, Energy & Environmental Science, 7 (2014) 3135-3191.
[189] E. Agel, J. Bouet, J.F. Fauvarque, Journal of Power Sources, 101 (2001) 267-274.
[190] D. Dunwoody, J. Leddy, Interface-Electrochemical Society, 14 (2005) 37-40.
[191] J. Ran, L. Wu, Y. He, Z. Yang, Y. Wang, C. Jiang, L. Ge, E. Bakangura, T. Xu, Journal of Membrane Science, 522 (2017) 267-291.
[192] E.R. Choban, L.J. Markoski, A. Wieckowski, P.J.A. Kenis, Journal of Power Sources, 128 (2004) 54-60.
[193] X. Yu, E.J. Pascual, J.C. Wauson, A. Manthiram, Journal of Power Sources, 331 (2016) 340-347.
[194] E. Kjeang, N. Djilali, D. Sinton, Journal of Power Sources, 186 (2009) 353-369.
[195] F. Bidault, D.J.L. Brett, P.H. Middleton, N. Abson, N.P. Brandon, International Journal of Hydrogen Energy, 34 (2009) 6799-6808.
[196] D. Cao, Y. Gao, G. Wang, R. Miao, Y. Liu, International Journal of Hydrogen Energy, 35 (2010) 807-813.
[197] J. Nor, 2008, Electrode structure for stacked alkaline fuel cells, EP 1997172 A1, MKU Cyprus Limited
[198] J. Nor, 2008, Electrode structure for stacked alkaline fuel cells, US 7354674 B2, Astris Energi Inc.
[199] J. Nor, 2007, Electrode structure for stacked alkaline fuel cells, CA 2644201 A1, MKU Cyprus Limited
[200] S.R. Ovshinsky, S. Venkatesan, B. Aladjov, R.T. Young, T. Hopper, 2002, Alkaline fuel cell, US 6447942 B1, Energy Conversion Devices, Inc.

[201] L.F. Urry, 1997, Current collectors for alkaline cells, US 5639578 A, Eveready Battery Company

[202] L. Zhang, H. Liu, J. Zhang, D. Ghosh, J.C.Y. Jung, B. Downing, 2007, Air diffusion cathodes for fuel cells, WO 2007112563 A1, Magpower Systems Inc., National Research Council Of Canada

[203] N.M. Abson, P.H. Middleton, 2006, Novel materials for alkaline fuel cells, EP 1715538 A1, Nicholas M. Abson, Peter Hugh Middleton

[204] I.D. Zaytsev, G.G. Aseyev, Properties of Aqueous Solutions of Electrolytes, Taylor & Francis, 1992.

[205] I. Merino-Jiménez, C. Ponce de León, A.A. Shah, F.C. Walsh, Journal of Power Sources, 219 (2012) 339-357.

[206] D. Ouellette, U. Gencalp, C.O. Colpan, International Journal of Hydrogen Energy, 42 (2017) 2680-2690.

[207] F. Goodridge, K. Scott, Electrochemical Process Engineering: A Guide to the Design of Electrolytic Plant, Springer US, 2013.

[208] M. Mikkola, T. Tingelöf, J.K. Ihonen, Journal of Power Sources, 193 (2009) 269-275.

[209] F.J. Barclay, Fuel Cells, Engines and Hydrogen: An Exergy Approach, Wiley, 2006.

[210] H. Fadali, 2008, 'Fuel cell distributed generation: power conditioning, control and energy management', University of Waterloo, Dec 2016, Dec 2016, https://www.researchgate.net/file.PostFileLoader.html?id=58984b073d7f4b4c6d54abc5&assetKey=AS%3A458707034218496%401486375687024

[211] J. Daintith, Dictionary of Chemistry (6th Edition), 6th ed., Oxford University Press.

[212] S. Huo, H. Deng, Y. Chang, K. Jiao, International Journal of Hydrogen Energy, 37 (2012) 18389-18402.

[213] Z. Luo, Z. Chang, Y. Zhang, Z. Liu, J. Li, International Journal of Hydrogen Energy, 35 (2010) 3120-3124.

[214] H. Li, Y. Tang, Z. Wang, Z. Shi, S. Wu, D. Song, J. Zhang, K. Fatih, J. Zhang, H. Wang, Z. Liu, R. Abouatallah, A. Mazza, Journal of Power Sources, 178 (2008) 103-117.

[215] G. Zhang, S.G. Kandlikar, International Journal of Hydrogen Energy, 37 (2012) 2412-2429.

[216] A. Fly, R.H. Thring, International Journal of Hydrogen Energy, 41 (2016) 14217-14229.

[217] P.T. Garrity, J.F. Klausner, R. Mei, Heat Transfer Engineering, 28 (2007) 877-884.

[218] Q. Zhang, G. Smith, Y. Wu, R. Mohring, International Journal of Hydrogen Energy, 31 (2006) 961-965.

[219] T. Kim, S. Kwon, International Journal of Hydrogen Energy, 37 (2012) 615-622.

[220] J.B. Lakeman, A. Rose, K.D. Pointon, D.J. Browning, K.V. Lovell, S.C. Waring, J.A. Horsfall, Journal of Power Sources, 162 (2006) 765-772.
[221] K. Kim, T. Kim, K. Lee, S. Kwon, Journal of Power Sources, 196 (2011) 9069-9075.
[222] B.S. Richardson, J.F. Birdwell, F.G. Pin, J.F. Jansen, R.F. Lind, Journal of Power Sources, 145 (2005) 21-29.
[223] L. An, T. Zhao, X. Yan, X. Zhou, P. Tan, Science Bulletin, 60 (2015) 55-64.
[224] G. Selvarani, S.K. Prashant, A.K. Sahu, P. Sridhar, S. Pitchumani, A.K. Shukla, Journal of Power Sources, 178 (2008) 86-91.
[225] C.P. de León, F.C. Walsh, A. Rose, J.B. Lakeman, D.J. Browning, R.W. Reeve, Journal of Power Sources, 164 (2007) 441-448.
[226] N.A. Choudhury, R.K. Raman, S. Sampath, A.K. Shukla, Journal of Power Sources, 143 (2005) 1-8.
[227] A. Verma, S. Basu, Journal of Power Sources, 168 (2007) 200-210.
[228] A. Verma, S. Basu, Journal of Power Sources, 174 (2007) 180-185.
[229] D.M.F. Santos, C.A.C. Sequeira, International Journal of Hydrogen Energy, 35 (2010) 9851-9861.
[230] H. Cooper, 1973, Electrolytic process for the production of alkali metal borohydrides, US 3734842 A, Cooper, H
[231] C.H. Hale, H. Sharifian, 1990, Production of metal borohydrides and organic onium borohydrides, Southwestern Analytical Chemicals, Inc.
[232] E.L. Gyenge, C.W. Oloman, J Appl Electrochem, 28 (1998) 1147-1151.
[233] L. Wang, C. Ma, Y. Sun, S. Suda, Journal of Alloys and Compounds, 391 (2005) 318-322.
[234] L. Wang, C.-a. Ma, X. Mao, Journal of Alloys and Compounds, 397 (2005) 313-316.
[235] C. Celik, F.G. Boyaci San, H.I. Sarac, International Journal of Hydrogen Energy, 35 (2010) 8678-8682.
[236] R. Jamard, A. Latour, J. Salomon, P. Capron, A. Martinent-Beaumont, Journal of Power Sources, 176 (2008) 287-292.
[237] J. Hou, M.W. Ellis, R.B. Moore, Electrochemical and Solid-State Letters, 15 (2012) B39-B43.